

Vol. 23, no. 3, 2023

eISSN 2687-1653

PEER-REVIEWED SCIENTIFIC AND PRACTICAL JOURNAL

Advanced Engineering Research (Rostov-on-Don)

Mechanics

Machine Building
and Machine Science

Information Technology,
Computer Science
and Management



www.vestnik-donstu.ru
DOI 10.23947/2687-1653



Advanced Engineering Research (Rostov-on-Don)

Peer-reviewed scientific and practical journal (published since 2000)

eISSN 2687–1653

DOI: 10.23947/2687–1653

Vol. 23, no. 3, 2023

The journal is aimed at informing the readership about the latest achievements and prospects in the field of mechanics, mechanical engineering, computer science and computer technology. The publication is a forum for cooperation between Russian and foreign scientists, it contributes to the convergence of the Russian and world scientific and information space.

The journal is included in the List of the leading peer-reviewed scientific publications (Higher Attestation Commission under the Ministry of Science and Higher Education of the Russian Federation), where basic scientific results of dissertations for the degrees of Doctor and Candidate of Science in scientific specialties and their respective branches of science should be published.

The journal publishes articles in the following fields of science:

- Theoretical Mechanics, Dynamics of Machines (Engineering Sciences)
- Deformable Solid Mechanics (Engineering, Physical and Mathematical Sciences)
- Mechanics of Liquid, Gas and Plasma (Engineering Sciences)
- Mathematical Simulation, Numerical Methods and Program Systems (Engineering Sciences)
- System Analysis, Information Management and Processing, Statistics (Engineering Sciences)
- Automation and Control of Technological Processes and Productions (Engineering Sciences)
- Software and Mathematical Support of Machines, Complexes and Computer Networks (Engineering Sciences)
- Computer Modeling and Design Automation (Engineering, Physical and Mathematical Sciences)
- Computer Science and Information Processes (Engineering Sciences)
- Machine Science (Engineering Sciences)
- Machine Friction and Wear (Engineering Sciences)
- Technology and Equipment of Mechanical and Physicotechnical Processing (Engineering Sciences)
- Engineering Technology (Engineering Sciences)
- Welding, Allied Processes and Technologies (Engineering Sciences)
- Methods and Devices for Monitoring and Diagnostics of Materials, Products, Substances and the Natural Environment (Engineering Sciences)
- Hydraulic Machines, Vacuum, Compressor Equipment, Hydraulic and Pneumatic Systems (Engineering Sciences)

Indexing and archiving

RISC, CyberLeninka, EBSCO, Dimensions, DOAJ, Index Copernicus, Internet Archive, Google Scholar

Name of the body that registered the publication

Mass media registration certificate ЭЛ № ФС 77 – 78854 dated August 07, 2020, issued by the Federal Service for Supervision of Communications, Information Technology and Mass Media

Founder and publisher

Federal State Budgetary Educational Institution of Higher Education Don State Technical University (DSTU)

Periodicity

4 issues per year

Address of the founder and publisher

1, Gagarin sq., Rostov-on-Don, 344003, Russian Federation

E-mail

vestnik@donstu.ru

Telephone

+7 (863) 2–738–372

Website

<http://vestnik-donstu.ru/>

Date of publication

30.09.2023





Advanced Engineering Research (Rostov-on-Don)

Рецензируемый научно-практический журнал (издается с 2000 года)

eISSN 2687–1653

DOI: 10.23947/2687–1653

Том 23, № 3, 2023

Создан в целях информирования читательской аудитории о новейших достижениях и перспективах в области механики, машиностроения, информатики и вычислительной техники. Издание является форумом для сотрудничества российских и иностранных ученых, способствует сближению российского и мирового научно-информационного пространства.

Журнал включен в перечень рецензируемых научных изданий, в котором должны быть опубликованы основные научные результаты диссертаций на соискание ученой степени кандидата наук, на соискание ученой степени доктора наук (Перечень ВАК) по следующим научным специальностям:

- 1.1.7 – Теоретическая механика, динамика машин (технические науки)
- 1.1.8 – Механика деформируемого твердого тела (технические, физико-математические науки)
- 1.1.9 – Механика жидкости, газа и плазмы (технические науки)
- 1.2.2 – Математическое моделирование, численные методы и комплексы программ (технические науки)
- 2.3.1 – Системный анализ, управление и обработка информации, статистика (технические науки)
- 2.3.3 – Автоматизация и управление технологическими процессами и производствами (технические науки)
- 2.3.5 – Математическое и программное обеспечение вычислительных систем, комплексов и компьютерных сетей (технические науки)
- 2.3.7 – Компьютерное моделирование и автоматизация проектирования (технические, физико-математические науки)
- 2.3.8 – Информатика и информационные процессы (технические науки)
- 2.5.2 – Машиноведение (технические науки)
- 2.5.3 – Трение и износ в машинах (технические науки)
- 2.5.5 – Технология и оборудование механической и физико-технической обработки (технические науки)
- 2.5.6 – Технология машиностроения (технические науки)
- 2.5.8 – Сварка, родственные процессы и технологии (технические науки)
- 2.5.9 – Методы и приборы контроля и диагностики материалов, изделий, веществ и природной среды (технические науки)
- 2.5.10 – Гидравлические машины, вакуумная, компрессорная техника, гидро- и пневмосистемы (технические науки)

<i>Индексация и архивация:</i>	РИНЦ, CyberLeninka, CrossRef, Dimensions, DOAJ, EBSCO, Index Copernicus, Internet Archive, Google Scholar
<i>Наименование органа, зарегистрировавшего издание</i>	Свидетельство о регистрации средства массовой информации ЭЛ № ФС 77 – 78854 от 07 августа 2020 г., выдано Федеральной службой по надзору в сфере связи, информационных технологий и массовых коммуникаций
<i>Учредитель и издатель</i>	Федеральное государственное бюджетное образовательное учреждение высшего образования «Донской государственный технический университет» (ДГТУ)
<i>Периодичность</i>	4 выпуска в год
<i>Адрес учредителя и издателя</i>	344003, Российская Федерация, г. Ростов-на-Дону, пл. Гагарина, 1
<i>E-mail</i>	vestnik@donstu.ru
<i>Телефон</i>	+7 (863) 2–738–372
<i>Сайт</i>	http://vestnik-donstu.ru/
<i>Дата выхода в свет</i>	30.09.2023



Editorial Board

Editor-in-Chief: Alexey N. Beskopylny, Dr.Sci. (Eng.), Professor, Don State Technical University (Rostov-on-Don, Russian Federation);

Deputy Chief Editor: Alexandr I. Sukhinov, Corresponding Member, Russian Academy of Sciences, Dr.Sci. (Phys.-Math.), Professor, Don State Technical University (Rostov-on-Don, Russian Federation);

Executive Editor: Manana G. Komakhidze, Cand.Sci. (Chemistry), Don State Technical University (Rostov-on-Don, Russian Federation);

Executive Secretary: Nadezhda A. Shevchenko, Don State Technical University (Rostov-on-Don, Russian Federation);

Sergey M. Aizikovitch, Dr.Sci. (Phys.-Math.), Professor, Don State Technical University (Rostov-on-Don, Russian Federation);

Kamil S. Akhverdiev, Dr.Sci. (Eng.), Professor, Rostov State Transport University (Rostov-on-Don, Russian Federation);

Imad R. Antipas, Cand.Sci. (Eng.), Don State Technical University (Rostov-on-Don, Russian Federation);

Hubert Anysz, PhD (Eng.), Assistant Professor, Warsaw University of Technology (Republic of Poland);

Ahilan Appathurai, National Junior Research Fellow, Anna University Chennai (India);

Gultekin Basmaci, PhD (Eng.), Professor, Burdur Mehmet Akif Ersoy University (Turkey);

Yuri O. Chernyshev, Dr.Sci. (Eng.), Professor, Don State Technical University (Rostov-on-Don, Russian Federation);

Evgenii A. Demekhin, Dr.Sci. (Phys.-Math.), Professor, Financial University under the RF Government, Krasnodar branch (Krasnodar, Russian Federation);

Oleg V. Dvornikov, Dr.Sci. (Eng.), Professor, Belarusian State University (Belarus);

Karen O. Egiazaryan, Dr.Sci. (Eng.), Professor, Tampere University of Technology (Finland);

Victor A. Eremeev, Dr.Sci. (Phys.-Math.), Professor, Southern Scientific Center of RAS (Rostov-on-Don, Russian Federation);

Nikolay E. Galushkin, Dr.Sci. (Eng.), Professor, Institute of Service and Business, DSTU branch (Shakhty, Russian Federation);

LaRoux K. Gillespie, Dr.Sci. (Eng.), Professor, President-Elect of the Society of Manufacturing Engineers (USA);

Ali M. Hasan, PhD (Computer Engineering), Al Nahrain University (Baghdad, Iraq);

Huchang Liao, Professor, IAAM Fellow, IEEE Business School Senior Fellow, Sichuan University (China);

Hamid A. Jalab, PhD (Computer Science & IT), University of Malaya (Malaysia);

Revaz Z. Kavtaradze, Dr.Sci. (Eng.), Professor, Raphiel Dvali Institute of Machine Mechanics (Georgia);

Janusz Witalis Kozubal, Dr.Sci. (Eng.), Wroclaw Polytechnic University (Republic of Poland);

Ilya I. Kudish, PhD (Phys.-Math.), Kettering University (USA);

Victor M. Kureychik, Dr.Sci. (Eng.), Professor, Southern Federal University (Rostov-on-Don, Russian Federation);

Geny V. Kuznetsov, Dr.Sci. (Phys.-Math.), Professor, Tomsk Polytechnic University (Tomsk, Russian Federation);

Vladimir I. Lysak, Dr.Sci. (Eng.), Professor, Volgograd State Technical University (Volgograd, Russian Federation);

Vladimir I. Marchuk, Dr.Sci. (Eng.), Professor, Institute of Service and Business, DSTU branch (Shakhty, Russian Federation);

Vladimir M. Mladenovic, Dr.Sci. (Eng.), Professor, University of Kragujevac (Serbia);

Murman A. Mukutadze, Dr.Sci. (Eng.), Professor, Rostov State Transport University (Rostov-on-Don, Russian Federation);

Andrey V. Nasedkin, Dr.Sci. (Phys.-Math.), Professor, Southern Federal University (Rostov-on-Don, Russian Federation);

Tamaz M. Natriashvili, Academician, Raphiel Dvali Institute of Machine Mechanics (Georgia);

Nguyen Dong Ahn, Dr.Sci. (Phys.-Math.), Professor, Academy of Sciences and Technologies of Vietnam (Vietnam);

Nguyen Xuan Chiem, Dr.Sci. (Eng.), Le Quy Don Technical University (Vietnam);

Sergey G. Parshin, Dr.Sci. (Eng.), Associate Professor, St. Petersburg Polytechnic University (St. Petersburg, Russian Federation);

Konstantin V. Podmaster'ev, Dr.Sci. (Eng.), Professor, Orel State University named after I.S. Turgenev (Orel, Russian Federation);

Roman N. Polyakov, Dr.Sci. (Eng.), Associate Professor, Orel State University named after I.S. Turgenev (Orel, Russian Federation);

Valentin L. Popov, Dr.Sci. (Phys.-Math.), Professor, Berlin University of Technology (Germany);

Nikolay N. Prokopenko, Dr.Sci. (Eng.), Professor, Don State Technical University (Rostov-on-Don, Russian Federation);

José Carlos Quadrado, PhD (Electrical Engineering and Computers), DSc Habil, Polytechnic Institute of Porto (Portugal);

Alexander T. Rybak, Dr.Sci. (Eng.), Professor, Don State Technical University (Rostov-on-Don, Russian Federation);

Muzafer H. Saračević, Full Professor, Novi Pazar International University (Serbia);

Arestak A. Sarukhanyan, Dr.Sci. (Eng.), Professor, National University of Architecture and Construction of Armenia (Armenia);

Vladimir N. Sidorov, Dr.Sci. (Eng.), Russian University of Transport (Moscow, Russian Federation);

Arkady N. Solovyev, Dr.Sci. (Phys.-Math.), Professor, Don State Technical University (Rostov-on-Don, Russian Federation);

Mezhlum A. Sumbatyan, Dr.Sci. (Phys.-Math.), Professor, Southern Federal University (Rostov-on-Don, Russian Federation);

Mikhail A. Tamarkin, Dr.Sci. (Eng.), Professor, Don State Technical University (Rostov-on-Don, Russian Federation);

Murat Tezer, Professor, Near East University (Turkey);

Bertram Torsten, Dr.Sci. (Eng.), Professor, TU Dortmund University (Germany);

Vyacheslav G. Tsybulin, Dr.Sci. (Phys.-Math.), Associate Professor, Southern Federal University (Rostov-on-Don, Russian Federation);

Umid M. Turdaliev, Dr.Sci. (Eng.), Professor, Andijan Machine-Building Institute (Uzbekistan);

Ahmet Uyumaz, PhD (Eng.), Professor, Burdur Mehmet Akif Ersoy University (Turkey);

Valery N. Varavka, Dr.Sci. (Eng.), Professor, Don State Technical University (Rostov-on-Don, Russian Federation);

Igor M. Verner, PhD (Eng.), Professor, Technion — Israel Institute of Technology (Israel);

Sergei A. Voronov, Dr.Sci. (Eng.), Associate Professor, Russian Foundation of Fundamental Research (Moscow, Russian Federation);

Batyr M. Yazyev, Dr.Sci. (Eng.), Professor, Don State Technical University (Rostov-on-Don, Russian Federation);

Vilor L. Zakovorotny, Dr.Sci. (Eng.), Professor, Don State Technical University (Rostov-on-Don, Russian Federation).

Редакционная коллегия

Главный редактор: Бескопыйный Алексей Николаевич, доктор технических наук, профессор, Донской государственный технический университет (Ростов-на-Дону, Российская Федерация);

заместитель главного редактора: Сухинов Александр Иванович, член-корреспондент РАН, доктор физико-математических наук, профессор, Донской государственный технический университет (Ростов-на-Дону, Российская Федерация);

ответственный редактор: Комахидзе Манана Гивиевна, кандидат химических наук, Донской государственный технический университет (Ростов-на-Дону, Российская Федерация);

ответственный секретарь: Шевченко Надежда Анатольевна, Донской государственный технический университет (Ростов-на-Дону, Российская Федерация);

Айзикович Сергей Михайлович, доктор физико-математических наук, профессор, Донской государственный технический университет (Ростов-на-Дону, Российская Федерация);

Антибас Имад Ризакалла, кандидат технических наук, Донской государственный технический университет (Ростов-на-Дону, Российская Федерация);

Ахилан Аппатурай, младший научный сотрудник, Инженерно-технологический колледж PSN, Университет Анны Ченнаи (Индия);

Ахвердиев Камил Самед Оглы, доктор технических наук, профессор, Ростовский государственный университет путей сообщения (Ростов-на-Дону, Российская Федерация);

Варавка Валерий Николаевич, доктор технических наук, профессор, Донской государственный технический университет (Ростов-на-Дону, Российская Федерация);

Вернер Игорь Михайлович, доктор технических наук, профессор, Технологический институт в Израиле (Израиль);

Воронов Сергей Александрович, доктор технических наук, доцент, Российский фонд фундаментальных исследований (Москва, Российская Федерация);

Галушкин Николай Ефимович, доктор технических наук, профессор, Институт сферы обслуживания и предпринимательства, филиал ДГТУ (Шахты, Российская Федерация);

Лару Гиллеспи, доктор технических наук, профессор, Президент Общества машиностроителей (США);

Аныш Губерт, доктор наук, доцент, Варшавский технологический университет (Польша);

Басмачи Гюльтекин, доктор наук, профессор, Университет Бурдура Мехмета Акифа Эрсоа (Турция);

Дворников Олег Владимирович, доктор технических наук, профессор, Белорусский государственный университет (Беларусь);

Демехин Евгений Афанасьевич, доктор физико-математических наук, профессор, Краснодарский филиал Финансового университета при Правительстве РФ (Краснодар, Российская Федерация);

Хамид Абдулла Джалаб, доктор наук (информатика и ИТ), университет Малайя (Малайзия);

Егназарян Карен Оникович, доктор технических наук, профессор, Технологический университет Тампере (Финляндия);

Еремеев Виктор Анатольевич, доктор физико-математических наук, профессор, Южный научный центр РАН (Ростов-на-Дону, Российская Федерация);

Заковоротный Вилор Лаврентьевич, доктор технических наук, профессор, Донской государственный технический университет (Ростов-на-Дону, Российская Федерация);

Кавтарадзе Реваз Зурабович, доктор технических наук, профессор, Институт механики машин им. Р. Двали (Грузия);

Козубал Януш Виталис, доктор технических наук, профессор, Вроцлавский технический университет (Польша);

Хосе Карлос Куадрадо, доктор наук (электротехника и компьютеры), Политехнический институт Порту (Португалия);

Кудиш Илья Исаилович, доктор физико-математических наук, Университет Кеттеринга (США);

Кузнецов Генний Владимирович, доктор физико-математических наук, профессор, Томский политехнический университет (Томск, Российская Федерация);

Курейчик Виктор Михайлович, доктор технических наук, профессор, Южный федеральный университет (Ростов-на-Дону, Российская Федерация);

Лысак Владимир Ильич, доктор технических наук, профессор, Волгоградский государственный технический университет (Волгоград, Российская Федерация);

Марчук Владимир Иванович, доктор технических наук, профессор, Институт сферы обслуживания и предпринимательства, филиал ДГТУ (Шахты, Российская Федерация);

Владимир Младенович, доктор технических наук, профессор, Крагуевацкий университет (Сербия);

Мукутадзе Мурман Александрович, доктор технических наук, доцент, Ростовский государственный университет путей сообщения (Ростов-на-Дону, Российская Федерация);

Наседкин Андрей Викторович, доктор физико-математических наук, профессор, Южный федеральный университет (Ростов-на-Дону, Российская Федерация);

Натришвили Тамаз Мамиевич, академик, Институт механики машин им. Р. Двали (Грузия);

Нгуен Донг Ань, доктор физико-математических наук, профессор, Институт механики Академии наук и технологий Вьетнама (Вьетнам);

Нгуен Суан Тьем, доктор технических наук, Вьетнамский государственный технический университет им. Ле Куй Дона (Вьетнам);

Паршин Сергей Георгиевич, доктор технических наук, доцент, Санкт-Петербургский политехнический университет (Санкт-Петербург, Российская Федерация);

Подмастерьев Константин Валентинович, доктор технических наук, профессор, Орловский государственный университет им. И. С. Тургенева (Орел, Российская Федерация);

Поляков Роман Николаевич, доктор технических наук, доцент, Орловский государственный университет им. И. С. Тургенева (Орел, Российская Федерация);

Попов Валентин Леонидович, доктор физико-математических наук, профессор, Институт механики Берлинского технического университета (Германия);

Прокопенко Николай Николаевич, доктор технических наук, профессор, Донской государственный технический университет (Ростов-на-Дону, Российская Федерация);

Рыбак Александр Тимофеевич, доктор технических наук, профессор, Донской государственный технический университет (Ростов-на-Дону, Российская Федерация);

Музафер Сарачевич, доктор наук, профессор, Университет Нови-Пазара (Сербия);

Саруханян Арестак Арамаисович, доктор технических наук, профессор, Национальный университет архитектуры и строительства Армении (Армения);

Сидоров Владимир Николаевич, доктор технических наук, Российский университет транспорта (Москва, Российская Федерация);

Соловьёв Аркадий Николаевич, доктор физико-математических наук, профессор, Донской государственный технический университет (Ростов-на-Дону, Российская Федерация);

Сумбатян Междум Альбертович, доктор физико-математических наук, профессор, Южный федеральный университет (Ростов-на-Дону, Российская Федерация);

Тамаркин Михаил Аркадьевич, доктор технических наук, профессор, Донской государственный технический университет (Ростов-на-Дону, Российская Федерация);

Мурат Тезер, профессор, Ближневосточный университет (Турция);

Бертрам Торстен, доктор технических наук, профессор, Технический университет Дортмунда (Германия);

Турдалиев Умид Мухтаралиевич, доктор технических наук, профессор, Андижанский машиностроительный институт (Узбекистан);

Ахмет Уюмаз, доктор технических наук, профессор, университет Бурдура Мехмета Акифа Эрсоа (Турция);

Али Маджид Хасан Алвазли, доктор наук (компьютерная инженерия), доцент, Университет Аль-Нахрейн (Ирак);

Цибулин Вячеслав Георгиевич, доктор физико-математических наук, доцент, Южный федеральный университет (Ростов-на-Дону, Российская Федерация);

Чернышев Юрий Олегович, доктор технических наук, профессор, Донской государственный технический университет (Ростов-на-Дону, Российская Федерация);

Хучан Ляо, профессор, научный сотрудник ИААМ; Старший член Школы бизнеса IEEE, Университет Сычуань (Китай);

Языев Батыр Меретович, доктор технических наук, профессор, Донской государственный технический университет (Ростов-на-Дону, Российская Федерация).

Contents

MECHANICS

Influence of the Sphero-Cylindrical Tool Orientation Angles on Roughness under Processing Complex-Profile Surfaces	231
<i>MR Gimadeev, AV Nikitenko, VO Berkun</i>	
Study on Dynamic Response Characteristics of Different Asphalt Pavement Structures Based on ALF Test	241
<i>Ni Guangcong, AN Tiraturyan, EV Uglova, AV Vorobev</i>	
Buckling of Rectangular Plates under Nonlinear Creep	257
<i>SB Yazyev, AS Chepurnenko</i>	

MACHINE BUILDING AND MACHINE SCIENCE

Optimization of Geometric Characteristics of Cycloidal Profiles of Gerotor Hydraulic Machines	269
<i>SO Kireyev, AR Lebedev, MV Korchagina</i>	
Investigation of Dynamic Characteristics of an Automated Position Long-Stroke Pneumatic Actuator of Fabrication System	283
<i>DA Korotych, VS Sidorenko, SP Prikhodko</i>	

INFORMATION TECHNOLOGY, COMPUTER SCIENCE AND MANAGEMENT

GATCGGenerator: New Software for Generation of Quasirandom Nucleotide Sequences	296
<i>OYu Kiryanova, RR Garafutdinov, IM Gubaydullin, AV Chemeris</i>	
Sensitivity of Diffusion-Weighted Image Combined with T2 Turbo Inversion Recovery Magnitude Sequence and as an Alternative to Contrast-Enhanced MRI in the Detection of Perianal Fistula.....	307
<i>Noor Fadhil Baqir, Rasha Sabeeh Ahmed, Khaleel Ibraheem Mohsen</i>	
3D Human Motion Capture Method Based on Computer Vision	317
<i>AD Obukhov, DL Dedov, EO Surkova, IL Korobova</i>	
Model of a Parallel-Pipeline Computational Process for Solving a System of Grid Equations	329
<i>VN Litvinov, NB Rudenko, NN Gracheva</i>	

Содержание

МЕХАНИКА

Влияние углов ориентации сфероцилиндрического инструмента на шероховатость при обработке сложнопрофильных поверхностей	231
<i>М.Р. Гимадеев, А.В. Никитенко, В.О. Беркун</i>	
Исследование характеристик динамического отклика дорожных конструкций при ускоренном тестировании.....	241
<i>Ни Гуанцунг, А.Н. Тиратуриян, Е.В. Углова, А.В. Воробьев</i>	
Выпучивание прямоугольных пластин при нелинейной ползучести	257
<i>С.Б. Языев, А.С. Чепурненко</i>	

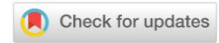
МАШИНОСТРОЕНИЕ И МАШИНОВЕДЕНИЕ

Оптимизация геометрических характеристик циклоидальных профилей героторных гидромашин	269
<i>С.О. Киреев, А.Р. Лебедев, М.В. Корчагина</i>	
Исследование динамических характеристик автоматизированного позиционного длинноходового пневмопривода технологического оборудования	283
<i>Д.А. Коротыч, В.С. Сидоренко, С.П. Приходько</i>	

ИНФОРМАТИКА, ВЫЧИСЛИТЕЛЬНАЯ ТЕХНИКА И УПРАВЛЕНИЕ

GATCGGenerator: новый генератор для создания квазислучайных нуклеотидных последовательностей	296
<i>О.Ю. Кирьянова Р.Р. Гарафутдинов, И.М. Губайдуллин, А.В. Чемерис</i>	
Чувствительность диффузионно-взвешенного изображения в сочетании с последовательностью восстановления турбо-инверсии T2 в качестве альтернативы МРТ с контрастным усилением при обнаружении параректального свища (на англ. языке)	307
<i>Noor Fadhil Baqir, Rasha Sabeeh Ahmed, Khaleel Ibraheem Mohsen</i>	
Метод трехмерного захвата движений человека на основе компьютерного зрения	317
<i>А.Д. Обухов, Д.Л. Дедов, Е.О. Суркова, И.Л. Коробова</i>	
Разработка модели параллельно-конвейерного вычислительного процесса для решения системы сеточных уравнений	329
<i>В.Н. Литвинов, Н.Б. Руденко, Н.Н. Грачева</i>	

MECHANICS



UDC 621.914.1:517

Original article

<https://doi.org/10.23947/2687-1653-2023-23-3-231-240>

Influence of the Sphero-Cylindrical Tool Orientation Angles on Roughness under Processing Complex-Profile Surfaces

Mikhail R. Gimadeev¹ , Aleksandr V. Nikitenko¹ , Vera O. Berkun^{1,2}
¹ Pacific National University, Khabarovsk, Russian Federation² “PromMash” LLC, Khabarovsk, Russian Federation✉ 009063@pnu.edu.ru, j_l_wiegott@list.ru

Abstract

Introduction. When milling complex-profile surfaces of parts, the selection of tool trajectories and orientations affect the roughness parameters. However, in the studies devoted to the formation of trajectories, recommendations to provide the quality of microgeometry of surfaces were not taken into account. Moreover, when writing programs for CNC equipment in CAM systems, the limitations of cutting modes were determined exclusively using a geometric approach. It did not take into account the influence of the orientation angles of the sphero-cylindrical tool relative to the normal plane on the quality of surface treatment, namely on roughness. The work was aimed at the creation of the methodology for selecting the limiting values of the orientation angles of a sphero-cylindrical tool to optimize the process of machining spatially complex surfaces. The tasks included achieving the minimum values of the amplitude roughness parameter R_z and determining the effectiveness of various machining paths.

Materials and Methods. Methods of correlation and regression analysis were used, the results were compared and generalized. The least-squares method was applied to estimate the parameters of the regression equation. The DMU 50 ecoline processing center was used for the experimental studies. Roughness was measured on a Surfcam 1800 D profilometer. The material of the samples was steel 12X18N10T. The material of the tool was hard alloy 1620 Sandvik with PVD coating (physical vapor deposition, the closest domestic analogue is T15K6).

Results. It has been shown in detail how roughness parameters R_z depend on the angle of inclination and the diameter of the tool. Twenty examples were summarized in a table. Natural regression coefficients were calculated using linear and hyperbolic models. It was found that the diameter of the tool had a greater effect on the formation of roughness parameter R_z than the angle of inclination. For a detailed description of the influence features, the coefficients of multiple, partial, paired correlation and multiple determination were compared. The limitations associated with the angles of inclination of the tool when processing complex surfaces were determined. A scheme for calculating the angle of the normal was visualized, which included the selected step along the axis to determine the lengths of the segments of the broken curve. The profilograms of surfaces obtained with different shaping trajectories were given in the form of drawings. This allowed us to conclude that milling from top to bottom is unsuitable when the tool is tilted 5° – 35° . A map has been compiled by which it is possible to judge the roughness, knowing the type of milling and the inclination angle (from 5° to 80°). The dependence of the roughness parameter on the processing speed and the use of coolant was represented graphically. The calculated parameters for determining the optimal angle of inclination of the tool were tabulated. Their analysis proved the adequacy of the proposed method of preparing control information.

Discussion and Conclusion. The presented technique made it possible to determine the optimal values of the orientation angles of the sphero-cylindrical tool, taking into account the cutting speed and the minimum possible amplitude roughness parameter R_z . The pattern of feeding $f_z = 0.4$ mm/tooth for surface areas with a total angle of

5–50° was considered. In this case, processing along trajectories in the passing, opposite and bottom-top directions, provided roughness in the range of 3–6 μm according to parameter R_z . The top-down toolpath is not recommended for use in final operations due to the significant height of parameter R_z .

Keywords: amplitude roughness parameter, orientation of a sphero-cylindrical tool, milling of complex-profile surfaces, spatially complex surfaces

Acknowledgments: the authors would like to thank V.M. Davydov, Dr.Sci. (Engineering), Professor, Head of the Technical Informatics and Information Systems Department, Pacific National University, Khabarovsk, for significant comments and important tips when conducting research and designing the article.

For citation. Gimadeev MR, Nikitenko AV, Berkun VO. Influence of the Sphero-Cylindrical Tool Orientation Angles on Roughness under Processing Complex-Profile Surfaces. *Advanced Engineering Research (Rostov-on-Don)*. 2023;23(3):231–240. <https://doi.org/10.23947/2687-1653-2023-23-3-231-240>

Научная статья

Влияние углов ориентации сфероцилиндрического инструмента на шероховатость при обработке сложнопрофильных поверхностей

М.Р. Гимадеев¹  , А.В. Никитенко¹ , В.О. Беркун^{1,2} 

¹ Тихоокеанский государственный университет, г. Хабаровск, Российская Федерация

² Общество с ограниченной ответственностью «ПромМаш», г. Хабаровск, Российская Федерация

 009063@pnu.edu.ru, jl_wiegott@list.ru

Аннотация

Введение. При фрезеровании сложных поверхностей деталей выбор траекторий и ориентации инструмента влияют на параметры шероховатости. Однако в исследованиях, посвященных формированию траекторий, не учитываются рекомендации, позволяющие обеспечить качество микрогеометрии поверхностей. К тому же при написании программ для оборудования с ЧПУ в САМ-системах (от англ. computer-aided manufacturing — автоматизированное производство) ограничения режимов резания определяются исключительно с помощью геометрического подхода. Он не учитывает влияние углов ориентации сфероцилиндрического инструмента относительно плоскости нормали на качество обработки поверхностей, а именно на шероховатость. Цель работы — создание методики по выбору предельных значений углов ориентации сфероцилиндрического инструмента для оптимизации процесса механической обработки пространственно-сложных поверхностей. Задачи: достижение минимальных значений амплитудного параметра шероховатости R_z и определение эффективности различных траекторий обработки.

Материалы и методы. Использовались методы корреляционного и регрессионного анализа, результаты сравнивались и обобщались. Для оценки параметров уравнения регрессии применялся метод наименьших квадратов. Для экспериментальных исследований задействовали обрабатывающий центр DMU 50 ecoline. Шероховатость измеряли на профилометре Surfcom 1800 D. Материал образцов — сталь 12X18H10T. Материал инструмента — твердый сплав 1620 Sandvik с PVD-покрытием (от англ. physical vapor deposition — физическое осаждение паров металлов, ближайший отечественный аналог — Т15К6).

Результаты исследования. Детально показано, как параметры шероховатости R_z зависят от угла наклона и диаметра инструмента. Двадцать примеров представлены в виде таблицы. Естественные коэффициенты регрессии рассчитаны по линейной и гиперболической моделям. Установлено, что диаметр инструмента больше влияет на формирование параметра шероховатости R_z , чем угол наклона. Для детального описания особенностей влияния сравнивались коэффициенты множественной, частной, парной корреляции и множественной детерминации. Определены ограничения, связанные с углами наклона инструмента при обработке сложных поверхностей. Визуализирована схема для расчета угла нормали, которая включает выбранный шаг по оси для определения длин отрезков ломаной кривой. Даны в виде рисунков профилограммы

поверхностей, полученные при различных траекториях формообразования. Это позволило сделать вывод о непригодности фрезерования сверху вниз при наклоне инструмента 5° – 35° . Составлена карта, по которой можно судить о шероховатости, зная вид фрезерования и угол наклона (от 5° до 80°). Графически показана зависимость параметра шероховатости от скорости обработки и применения охлаждающей жидкости. Сведены в таблицу расчетные параметры для определения оптимального угла наклона инструмента. Их анализ доказал адекватность предложенного метода подготовки управляющей информации.

Обсуждение и заключение. Представленная методика позволила определить оптимальные значения углов ориентации сфероцилиндрического инструмента с учетом скорости резания и достижения минимально возможного амплитудного параметра шероховатости R_z . Рассмотрена ситуация подачи $f_z = 0.4$ мм/зуб для участков поверхности с суммарным углом 5° – 50° . В этом случае обработка по траекториям в попутном, встречном направлении и снизу вверх обеспечила шероховатость в диапазоне 3–6 мкм по параметру R_z . Траектория движения сверху вниз не рекомендована к применению на окончательных операциях из-за значительной высоты параметра R_z .

Ключевые слова: амплитудный параметр шероховатости, ориентация сфероцилиндрического инструмента, фрезерование сложных поверхностей, пространственно сложные поверхности

Благодарности: авторы выражают благодарность В.М. Давыдову, д.т.н., профессору, заведующему кафедрой «ТИИС» (ФГБОУ ВО ТОГУ, г. Хабаровск) за значимые замечания и важные советы при проведении исследования и оформлении статьи.

Для цитирования. Гимадеев М.Р., Никитенко А.В., Беркун В.О. Влияние углов ориентации сфероцилиндрического инструмента на шероховатость при обработке сложнопрофильных поверхностей. *Advanced Engineering Research (Rostov-on-Don)*. 2023;23(3):231–240. <https://doi.org/10.23947/2687-1653-2023-23-3-231-240>

Introduction. The reliability of machine parts is determined by such performance properties (PP) of surfaces as wear resistance, tightness, strength, quality of coatings [1]. These PP depend on the physico-mechanical and geometric parameters of functional surfaces, including roughness [2–4].

The analysis of the scientific literature suggests a growing interest in the topic of providing the necessary roughness parameters due to the reasonable selection of trajectories of shaping movements and orientation of the sphero-cylindrical tool when milling spatially complex surfaces (SCS) [5–7]. Examples of such parts are forming elements of die tooling, master models for casting, executive surfaces of gearing [8–10].

A number of authors studied the influence of strategies under the milling of SCS and methods of optimizing machining [10–12]. However, knowledge about the formation of trajectories does not take into account the recommendations for providing the quality of microgeometry of the surfaces of the part. It should also be noted that when creating programs for CNC equipment in CAM systems, the limitations of cutting modes are determined exclusively using a geometric approach [13, 14]. It does not take into account the influence of the orientation angles of the sphero-cylindrical tool relative to the normal plane on the quality of surface treatment, namely on roughness. The method of selecting the angles of tool orientation based on empirical models can overcome these disadvantages. Its advantages:

- influence of the tool orientation angles on the surface roughness is taken into account;
- ability to reasonably select processing paths is supported.

The study was aimed at the creation of a methodology for selecting the limiting values of the orientation angles of a sphero-cylindrical tool to optimize the process of machining spatially complex surfaces. The tasks included achieving the minimum values of the amplitude roughness parameter R_z and determining the effectiveness of various machining trajectories.

Materials and Methods. Thus, CAM systems provide forming multi-coordinate machining trajectories with tracking of additional parameters, such as collisions, the point of contact between the tool and the part, etc. The sphero-

cylindrical tool touches the part at point $P_i(x_i, y_i, z_i) = P_d(x_d, y_d, z_d)$. At the same time, it is required to avoid machining with the center of the cutter and orient the tool with an angle of inclination of at least 5° – 15° .

In the final operations, the effective cutting speed is determined by the effective diameter. At an equal rotational speed, it grows with the increase in the angle of inclination of the tool to the workpiece. An increase in the cutting speed generally causes a decrease in the microhardness of the surface, and with an increase in $V > 75$ m/min, the microhardness parameters change slightly [12]. The dissipation rate strongly depends on the cutting speed and the volume of the material being removed; therefore, cutting-tool lubricant (CTL) is needed to intensify the cutting process [15].

For the experiments, technological equipment with CNC was used, a five-axis machining center DMU 50 ecoline with a maximum spindle frequency of 8,000 rpm. The surface roughness was measured by a Surfcom 1800 D profilometer. Sandvik end mills of the R216 series were used for processing 12X18H10T steel. The material was hard alloy 1620 with PVD coating (the closest domestic analogue is T15K6). The diameter was 8 mm, the number of teeth — 2. To provide a uniform allowance ($a_p = 0.2$ mm), mechanical treatment with sphero-cylindrical cutters was carried out before the final milling operation.

Research Results. Before determining the angles of inclination, it was required to establish how variable factors affected the response function. In this case, we are talking about the surface roughness according to parameter Rz (μm). To find empirical mathematical models of milling with a sphero-cylindrical tool, we took the independent variables: X_1 — diameter (D , mm) and X_2 — the angle of the tool inclination (γ , $^\circ$). The initial data for the analysis were considered in previous studies (when applied to tooth $f_z = 0.4$ mm/tooth) [16–19] (Table 1).

Table 1

Roughness parameters Rz depending on the angle of inclination and diameter of the tool

Angle, $^\circ$	Tool diameter, mm			
	6	8	10	12
10	9.33	7.66	5.99	4.33
20	8.59	7.06	5.53	4.01
30	7.85	6.46	5.07	3.69
40	7.11	5.86	4.61	3.37
50	6.37	5.26	4.15	3.05

Based on theoretical data on significant factors affecting roughness, linear (1.1) and hyperbolic (1.2) models were adopted:

$$Rz = Y = a + b_1 X_1 + b_2 X_2, \quad (1.1)$$

$$Rz = Y' = a' + b_1' X_1 + \frac{b_2'}{X_2}. \quad (1.2)$$

Here are the calculated natural regression coefficients: $a = 13.37$; $a' = 10.25$; $b_1 = -0.66$; $b_2 = -0.58$; $b_2' = 0.51$.

The parameters of the two-factor regression equation were estimated using the standard least squares method; therefore, for simplicity of presentation, we omitted the formulas indicating the coefficients. Standardized β -coefficients: $\beta_1' = -0.79$; $\beta_2 = -0.58$; $\beta_2' = -0.51$. Comparison of the modules of the values of standardized regression coefficients β allowed us to conclude that factor X_1 (tool diameter) had more effect on the formation of the roughness parameter Rz than X_2 (inclination angle). Coefficients of multiple, partial, paired correlation and multiple determination:

$$R_{YX_1 X_2} = 0.98; r_{YX_1 X_2} = -0.98; r_{YX_2 X_1} = -0.97; r_{X_1 X_2 Y} = -0.95;$$

$$R_{Y' X_1 X_2} = 0.95; r_{Y' X_1 X_2} = -0.93; r_{Y' X_2 X_1} = 0.85; r_{X_1 X_2 Y'} = 0.79;$$

$$r_{YX_1} = -0.79; r_{YX_2} = -0.58; r_{X_1 X_2} = 0.00; r_{YX_2'} = 0.51;$$

$$r_{X_1 X_2'} = 0.00; R^2(Y) = 0.95; R^2(Y') = 0.90.$$

Comparing the coefficients, we drew the following conclusions.

When factor X_2 was fixed at a constant level, factor X_1 most strongly affected ($|0.98| > |0.79|$). When comparing the coefficients of the hyperbolic model, ($|0.93| > |0.79|$).

When factor X_1 was fixed, the effect of factor X_2 on R_z increased for both models: linear $|0.97| > |0.58|$, hyperbolic $|0.93| > |0.51|$.

To ensure the uniformity of the microrelief of the surface, the dependence of the feed and the effective diameter of the tool (D_{cap}) was established, which varied depending on the angle of processing. We defined the limitations associated with the angles of the tool inclination when processing the SCS. To do this, the surface of the part was to be divided into sections and the normal angles calculated. If $z = f(x, y)$, then, in general, the orientation of the tool to the surface was set by selecting the direction of the normal.

At $\cos \gamma = 1 / |N|$:

$$N = \left(-\frac{\delta f}{\delta x}, -\frac{\delta f}{\delta y}, 1 \right). \quad (2.1)$$

At $\cos \gamma = -1 / |N|$:

$$N = \left(\frac{\delta f}{\delta x}, \frac{\delta f}{\delta y}, -1 \right). \quad (2.2)$$

To determine the inclination angle of the tangent plane, the following equation was used:

$$\tan \alpha = |grad(z)_A| = \sqrt{\left(\frac{\delta z}{\delta x} \right)^2 + \left(\frac{\delta z}{\delta y} \right)^2}, \quad (3)$$

where $\alpha = |90^\circ - \gamma|$.

AV Nikitenko [20] presented a model for optimizing the orientation angle of a part with corrective angles of inclination A and B relative to X and Y axes:

$$\tan \alpha' = \sqrt{\left(\frac{\delta z}{\delta x} + \tan B \right)^2 + \left(\frac{\delta z}{\delta y} + \tan A \right)^2}. \quad (4)$$

For a special case (Fig. 1), determination of angle λ to normal N :

$$\lambda = \arctan \frac{\Delta z}{\Delta x}. \quad (5)$$

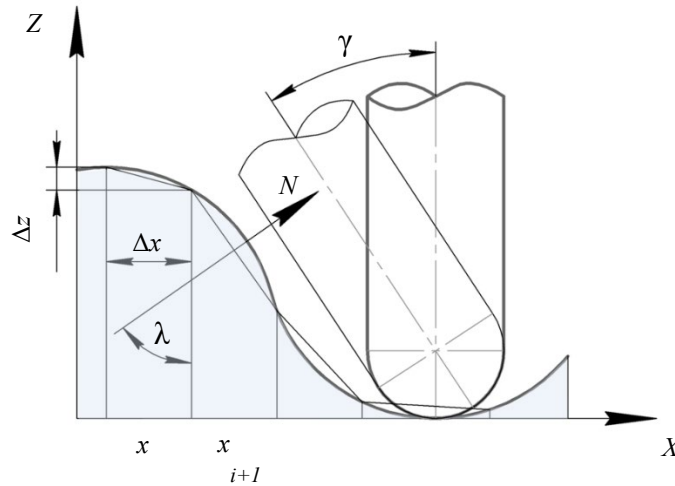


Fig. 1. Scheme for calculating the angle of the normal: N — normal; λ — angle to the normal; Δx — selected step along X axis to calculate the lengths of the polyline curve segments, mm; Δz — distance along Z axis, depending on the step along X axis, mm

With a discretely defined surface profile, the length of the curve describing the profile geometry:

$$S_n = \sum_{i=1}^n \Delta S_i. \quad (6)$$

Here, the length of the polyline section $\Delta S_i = \sqrt{\Delta x^2 + \Delta z^2}$.

The roughness of R_z was considered as an output parameter (Fig. 2), taking into account the limitations associated with the trajectories of motion and the angles of inclination of the sphero-cylindrical tool.

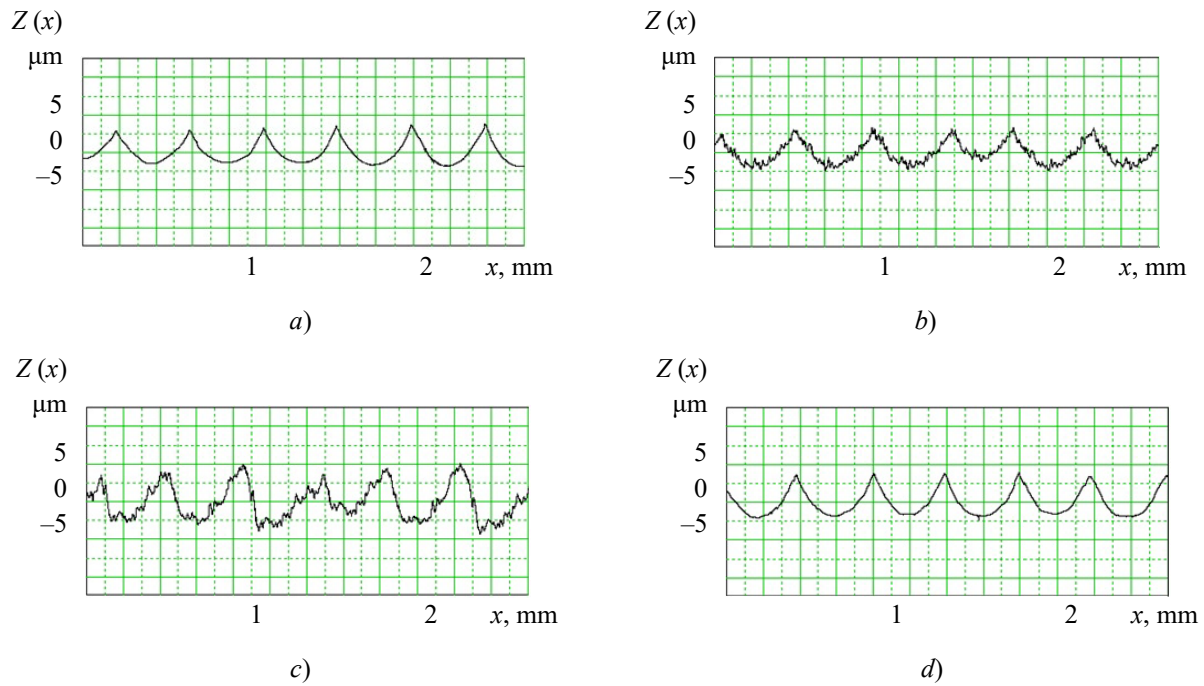


Fig. 2. Profilograms of surfaces obtained with different shaping trajectories at $\Gamma = 35^\circ\text{--}45^\circ$:
 a — passing milling; b — counter milling; c — top-bottom milling; d — bottom-up milling

Top-bottom milling is characterized by the greatest amplitude, the unevenness of the resulting surface profile, and is not recommended for shaping with a tool tilted at an angle of $5^\circ\text{--}35^\circ$.

The roughness selection map (Fig. 3) for R_z parameter is based on the results of the given and previous studies [16–19].

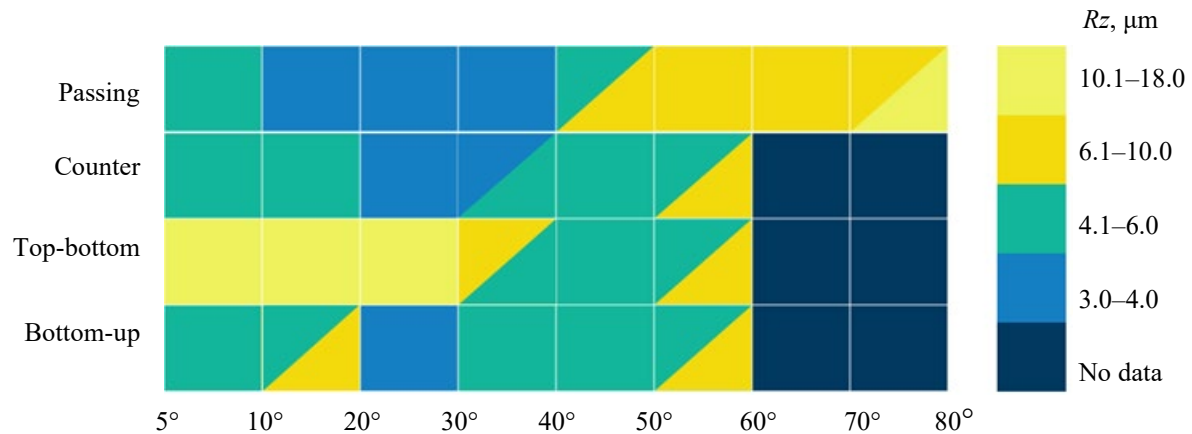


Fig. 3. Roughness selection map

When using CTL, a film was formed on the contact surfaces of the tool and the workpiece material, which helped to reduce adhesive wear. At the cutting speed $V > 70$ m/min, the effect of dynamic friction was reduced. At the same time, the duration of the physico-chemical effect of the medium on the contact surfaces went down, which limited the effect of the use of the CTL (Fig. 4).

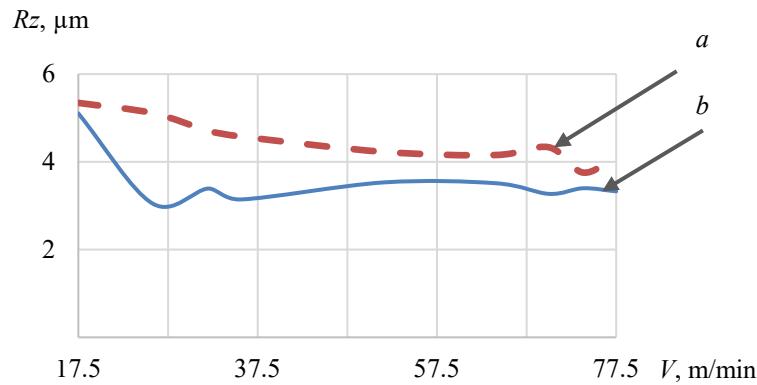


Fig. 4. Dependence of roughness parameter Rz on the machining speed: a — without CTL; b — with the use of CTL

The considered technique was aimed not at establishing critical values of possible orientation angles of a sphero-cylindrical tool for a specific object, but at achieving roughness parameters taking into account the effective cutting speed, feed, and inclination angles for a wide range of parts with concave-convex and linear sections. This approach could provide generalizing and clarifying the ways of optimizing machining. In addition to roughness, the limitations of the minimum effective cutting speed, depending on the effective diameter of the tool, were analyzed. At the same time, the minimum recommended effective cutting speed was (V_{cap}) — 75 m/min.

According to the feed and lateral pitch, the angle of orientation of the tool can correspond to positive and negative values. When calculating, it was considered modulo. Based on the calculated data (Table 2), the surface profile (Fig. 1) was divided into sections. The normal angles were determined, and the trajectories of the shaping movements were assigned to provide the required roughness, taking into account the angles of inclination of the tool.

Table 2

Design parameters for determining the optimal angle of inclination of the tool

n	$\Delta z, \text{ mm}$	$\Delta x, \text{ mm}$	$\lambda, ^\circ$	$\Gamma = \lambda + \gamma, ^\circ$			V_{cap} at $\gamma = 5$
				$\gamma = 1$	$\gamma = 3$	$\gamma = 5$	
1	0.16	0.25	3.59	4.59	6.59	8.59	68.0
2	0.48		10.83	11.83	13.83	15.83	84.4
3	0.82		18.25	19.25	21.25	23.25	99.8
4	1.22		26.01	27.01	29.01	31.01	114.2
5	1.71		34.34	35.34	37.34	39.34	127.2
6	2.38		43.64	44.64	46.64	48.64	138.6
7	3.55		54.82	55.82	57.82	59.82	147.5
8	6.59		69.21	70.21	72.21	74.21	150.7
9	4.56		61.26	62.26	64.26	66.26	150.1
10	2.81		48.39	49.39	51.39	53.39	143.1
11	1.98		38.41	39.41	41.41	43.41	132.7
12	1.43		29.71	30.71	32.71	34.71	120.3
13	1.00		21.73	22.73	24.73	26.73	106.5
14	0.63		14.17	15.17	17.17	19.17	91.5
15	0.30		6.87	7.87	9.87	11.87	75.5
16	0.01		0.32	1.32	3.32	5.32	60.2
17	0.33		7.52	8.52	10.52	12.52	77.0
...
n_i	1.03		22.43	23.43	25.43	27.43	107.8
n_{i+1}	1.47		30.46	31.46	33.46	35.46	121.5

The measured roughness values, taking into account the recommended angles of inclination of the sphero-cylindrical tool and the movement trajectory, are minimal with respect to Rz parameter (from 3 to 6 μm). At the same

time, these values correlate with data from other studies (Fig. 3). This allows us to conclude that the proposed method of preparing control information is adequate.

Discussion and Conclusion. The presented technique of selecting the limit values of the orientation angles of a sphero-cylindrical tool can be used to process the SCS with one tool without replacement, taking into account the accepted restrictions. The proposed approach makes it possible to determine the optimal values of the orientation angles of a sphero-cylindrical tool, allowing for the cutting speed and achieving the minimum possible amplitude parameter of roughness R_z .

We considered the situation for surface areas with a total angle of 5° – 50° at feed $f_z = 0.4$ mm/tooth. In this case, machining along trajectories in the passing direction, from bottom to top and in the opposite direction allowed for roughness in the range of 3 – 6 μm according to R_z parameter. This was less than the maximum values obtained by 15 – 30 %. At angles of 10° – 40° and the passing processing direction, the minimum values of R_z — 3 – 4 μm were recorded. The trajectory of top-bottom movement was not recommended for use in final operations due to the significant height of the R_z profile. At the same time, the values of 4.1 – 6 μm for this trajectory were achieved in a narrow range of angles — 40° – 50° .

References

1. Suslov AG, Federov VP, Nagorkin MN, Pyrikov IL. Complex Approach to Experimental Investigations of Metal Working Technological Systems to Ensure Parameters of Quality and Operation Properties of Machinery Surfaces. *Science Intensive Technologies in Mechanical Engineering*. 2018;(10):3–13. https://doi.org/10.30987/article_5bb4b1f9abbc54.46761484
2. Ponomarev BB, Suong H Nguyen. Evaluation of Surface Roughness in Five-Axis Ball-End Milling. *Proceedings of Higher Educational Institutions. Machine Building*. 2020;5(722):21–31. <https://doi.org/10.18698/0536-1044-2020-5-21-31>
3. Pimenov D, Hassui A, Wojciechowski S, Mia M, Magri A, Suyama DI, et al. Effect of the Relative Position of the Face Milling Tool towards the Workpiece on Machined Surface Roughness and Milling Dynamics. *Applied Sciences*. 2019;9(5):842. <https://doi.org/10.3390/app9050842>
4. Averchenkov VI, Filippova LB, Pugach LI. Determination of Software Tool Compensation Values in the Preparation of Automated Production of the Use of Active Control Sensor Tool. *Izvestiya Tula State University*. 2013;(7–1):70–78. URL: https://tidings.tsu.tula.ru/tidings/pdf/web/file/tsu_izv_technical_sciences_2013_07_part_1.pdf (accessed: 05.04.2023).
5. İzol P, Vrabel M, Maňková I. Comparison of Milling Strategies when Machining Freeform Surfaces. *Materials Science Forum*. 2016;862:18–25. [10.4028/www.scientific.net/MSF.862.18](https://doi.org/10.4028/www.scientific.net/MSF.862.18)
6. Hassanpour H, Shajari S, Rasti A, Sadeghi MH. Investigation of Milling Strategies Effect on Microhardness of a Typical Curved Surface. *Modares Mechanical Engineering*. 2015;15(2):34–40. URL: https://www.researchgate.net/publication/270449928_Investigation_of_milling_strategies_effect_on_microhardness_of_a_typical_curved_surface (accessed: 05.04.2023).
7. Shajari S, Sadeghi MH, Hassanpour H. The Influence of Tool Path Strategies on Cutting Force and Surface Texture during Ball End Milling of Low Curvature Convex Surfaces. *The Scientific World Journal*. 2014;2014:374526. <https://doi.org/10.1155/2014/374526>
8. Matras A, Kowalczyk R. Analysis of Machining Accuracy during Free Form Surface Milling Simulation for Different Milling Strategies. *Proceedings of the SPIE*. 2014;9290:1–7. <https://doi.org/10.1117/12.2075081>
9. Ponomarev BB, Nguyen Sy Hien. The Influence of Tool Orientation on Cutting Forces during End Milling. *Proceedings of Higher Educational Institutions. Machine Building*. 2019;3(708):11–20. <https://doi.org/10.18698/0536-1044-2019-3-11-20>
10. Mali RA, Gupta TVK, Ramkumar J. A Comprehensive Review of Free-Form Surface Milling — Advances over a Decade. *Journal of Manufacturing Processes*. 2021;62:132–167. <https://doi.org/10.1016/j.jmapro.2020.12.014>
11. Xiurong Zhu, Yeu Wang. Process Analysis and Parameter Optimization of Five Axis NC Machine for Machining Complex Curved Surface Impellers. In: *Proc. International Conference on Intelligent Transportation. Big Data & Smart City (ICITBS)*. New York: IEEE; 2019. P. 122–124. <https://doi.org/10.1109/ICITBS.2019.00036>
12. Zhidyaev AN, Masheryakov AV, Pronichev ND, Shulepov AP. Milling and Microballs Strengthening Conditions Influence on High-Temperature Alloys and Steels Parts' Coating Surface Quality Experimental Investigation. *VESTNIK of Samara University. Aerospace and Mechanical Engineering*. 2012;(5–2(36)):245–251. URL: <https://cyberleninka.ru/article/n/eksperimentalnoe-issledovanie-vliyaniya-rezhimov-frezirovaniya-i-uprochneniya-na-parametry-kachestva-poverhnostnogo-sloya-detaley-iz/viewer> (accessed: 05.04.2023).

13. Lapshin VP, Khristoforova VV, Nosachev SV. Relationship of Temperature and Cutting Force with Tool Wear and Vibration in Metal Turning. *Obrabotka Metallov (Metal Working and Material Science)*. 2020;22(3):44–58. <https://doi.org/10.17212/1994-6309-2020-22.3-44-58>
14. Blau P, Busch K, Dix M, Hochmuth C, Stoll A, Wertheim R. Flushing Strategies for High Performance, Efficient and Environmentally Friendly Cutting. *Procedia CIRP*. 2015;26:361–366. <https://doi.org/10.1016/j.procir.2014.07.058>
15. Kuscheva ME, Klauch DN, Kobelev OA. Principles of Selection of Cutting Technological Mediums for Metal Cutting. *Izvestiya MGTU "MAMI"*. 2014;8(1–2):73–76. <https://doi.org/10.17816/2074-0530-67737>
16. Gimadeev MR, Li AA. Analysis of Systems for Automated Provision of Surface Roughness Parameters Based on Dynamic Monitoring. *Advanced Engineering Research (Rostov-on-Don)*. 2022;22(2):116–129. <https://doi.org/10.23947/2687-1653-2022-22-2-116-129>
17. Davydov VM, Gimadeev MR, Nikitenko AV, Sarygin AV. Formation of Roughness Parameters Based on Correlation Relations during Finishing Milling of Spatially Complex Surfaces. *Strengthening Technologies and Coatings*. 2019;15(6(174)):243–249. URL: https://www.mashin.ru/files/2019/up619_web.pdf (accessed: 05.04.2023).
18. Gimadeev MR, Davydov VM. Correlation of the Roughness in Milling of Spherical Tool. *Assembling in Mechanical Engineering and Instrument-Making*. 2019;(5):219–224.
19. Gimadeev MR, Li AA, Berkun VO, Stelmakov VA. Experimental Study of the Dynamics of the Machining Process by Ball-End Mills. *Obrabotka Metallov (Metal Working and Material Science)*. 2023;25(1):44–56. <https://doi.org/10.17212/1994-6309-2023-25.1-44-56>
20. Nikitenko AV. Development of a Model of Optimization of Angle of Orientation of a Workpiece when Processing Difficult Surfaces. *Uchenye zametki TOGU*. 2021;12(2):66–69. URL: https://pnu.edu.ru/media/ejournal/articles-2021/TGU_12_71.pdf (accessed: 05.04.2023).

Received 26.05.2023

Revised 23.06.2023

Accepted 27.06.2023

About the Authors:

Mikhail R. Gimadeev, Cand.Sci. (Eng.), Associate Professor of the Technological Informatics and Information Systems Department, Pacific National University (136, Tihookeanskaya St., Khabarovsk, 680035, RF), [ScopusID](#), [AuthorID](#), [ORCID, 009063@pnu.edu.ru](mailto:009063@pnu.edu.ru), jl_wiegott@list.ru

Aleksandr V. Nikitenko, Cand.Sci. (Eng.), Associate Professor of the Technological Informatics and Information Systems Department, Pacific National University (136, Tihookeanskaya St., Khabarovsk, 680035, RF), [AuthorID](#), [ORCID](#), a.v.nikitenko@mail.ru

Vera O. Berkun, Design engineer, “PromMash” LLC (11, 42a, R. Matveevskoe, Khabarovsk, 680031, RF), Postgraduate of the Technological Informatics and Information Systems Department, Pacific National University (136, Tihookeanskaya St., Khabarovsk, 680035, RF), [AuthorID](#), [ORCID](#), vera.berkun.2017@gmail.com

Claimed contributorship:

MR Gimadeev: basic research concept formulation, determination of the system of equations, experiment planning, critical analysis of materials, formulation of conclusions.

AV Nikitenko: solving research problems, conducting an experiment, finalizing the text. correcting conclusions.

VO Berkun: conducting experiments and calculations. collecting and processing materials, analyzing and supplementing the text.

Conflict of interest statement: the authors do not have any conflict of interest.

All authors have read and approved the final manuscript.

Поступила в редакцию 26.05.2023

Поступила после рецензирования 23.06.2023

Принята к публикации 27.06.2023

Об авторах:

Михаил Радикович Гимадеев, кандидат технических наук, доцент кафедры технологической информатики и информационных систем Тихоокеанского государственного университета (680035, РФ, г. Хабаровск, ул. Тихоокеанская, 136), [ScopusID](#), [AuthorID](#), [ORCID](#), 009063@pnu.edu.ru, jl_wiegott@list.ru

Александр Васильевич Никитенко, кандидат технических наук, доцент кафедры технологической информатики и информационных систем Тихоокеанского государственного университета (680035, РФ, г. Хабаровск, ул. Тихоокеанская, 136), [AuthorID](#), [ORCID](#), a.v.nikitenko@mail.ru

Вера Олеговна Беркун, инженер-конструктор ООО «ПромМаш» (680031, РФ, г. Хабаровск, ш. Матвеевское, 42 а, л 1), аспирант кафедры технологической информатики и информационных систем Тихоокеанского государственного университета (680035, РФ, г. Хабаровск, ул. Тихоокеанская, 136), [AuthorID](#), [ORCID](#), vera.berkun.2017@gmail.com

Заявленный вклад соавторов:

М.Р. Гимадеев — формирование основной концепции исследования, определение системы уравнений, планирование эксперимента, критический анализ материалов, формулирование выводов.

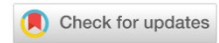
А.В. Никитенко — решение задач исследования, проведение эксперимента, доработка текста, корректировка выводов.

В.О. Беркун — проведение эксперимента и расчетов, сбор и обработка материалов, анализ и дополнение текста.

Конфликт интересов: авторы заявляют об отсутствии конфликта интересов.

Все авторы прочитали и одобрили окончательный вариант рукописи.

MECHANICS



UDC 625.7/8

Original article

<https://doi.org/10.23947/2687-1653-2023-23-3-241-256>

Study on Dynamic Response Characteristics of Different Asphalt Pavement Structures Based on ALF Test

Ni Guangcong¹ , Artem N. Tiraturyan² , Evgeniya V. Uglova² , Andrey V. Vorobev²

¹ ShanDong JiaoTong University, Jinan, China

² Don State Technical University, Rostov-on-Don, Russian Federation

✉ tiraturjan@list.ru

Abstract

Introduction. In recent years, one of the main trends in the field of testing road structures has become field study of their large-scale models at the accelerated load facility (ALF). It can significantly reduce the cost of selecting the most economical and durable pavement designs. However, the results obtained on the ALF are often relative, since they practically do not correlate with the results of laboratory and field tests on real objects. This study is aimed at a comprehensive investigation of the response of a road structure to a dynamic load, the establishment of patterns of fatigue failure of asphalt concrete layers during the accelerated testing and full-scale tests on real objects.

Materials and Methods. During testing, an accelerated load facility was used, located on the territory of the ShanDong Transport University. When conducting field tests, a dynamic loading unit with a falling weight FWD Primax 1500 was used, which recorded the deflection bowl on the surface of the structure under study. To record the dynamic response in the arrangement of the road structure, a complex of strain gauge sensors was used, which made it possible to register both compressive stresses and tensile strains in different layers. The results obtained under natural conditions were compared to the results obtained on the mathematical FEM model.

Results. The research results have shown that the thickness of the lower coating layer is the main factor affecting the amount of vertical deformation of the pavement, which must be taken into account at the design stage of the pavement structure. Thus, with a thickness of the upper layer of the base of 10 cm, the vertical deformation was 100 μm , and with a thickness of 20 cm – 55 μm , provided that the overall strength of the structure was ensured. The number of load application cycles on the ALF had a minimal effect on the selected asphalt concrete samples during split tensile tests.

Discussion and Conclusion. The adequacy of the results obtained in the course of accelerated testing of road structures was shown through a comprehensive comparison of numerical simulation data and full-scale tests, and the adequacy of the applied calculation methods was validated. The results of the study can be further applied in the road industry to develop and improve the regulatory framework for the design of non-rigid pavement under conditions of increased loads and heavy traffic.

Keywords: asphalt concrete pavement, accelerated loading test, multilayered half-space, stress-strain, temperature correction, dynamic response model

Acknowledgements: the authors appreciate the staff of the Road-testing laboratory, ShanDong Transport University, for their assistance in carrying out research at the ALF installation, as well as the respected reviewers for the time and effort spent on reviewing this article.

Funding information. The research was carried out within the framework of a grant from President of the Russian Federation on State support for young Russian scientists — Candidates of science (application MK–242.2022.4).

For citation. Guangcong Ni, Tiraturyan AN, Uglova EV, Vorobev AV. Study on Dynamic Response Characteristics of Different Asphalt Pavement Structures Based on ALF Test. *Advanced Engineering Research (Rostov-on-Don)*. 2023;23(3):241–256. <https://doi.org/10.23947/2687-1653-2023-23-3-241-256>

Научная статья

Исследование характеристик динамического отклика дорожных конструкций при ускоренном тестировании

Ни Гуанцунг¹ , А.Н. Тиратурян²  , Е.В. Углова² , А.В. Воробьев² 

¹ Шаньдунский транспортный университет, г. Цзинань, провинция Шаньдун, Китайская Народная Республика

² Донской государственный технический университет, г. Ростов-на-Дону, Российская Федерация

 tiraturjan@list.ru

Аннотация

Введение. Одним из главных трендов в области испытаний дорожных конструкций в последние годы стали натурные исследования их крупномасштабных моделей на установках ускоренного тестирования (ALF). Это позволяет значительно уменьшить затраты на выбор наиболее экономичных и долговечных конструкций дорожных одежд. Однако результаты, полученные на установках ALF, зачастую являются относительными, так как практически не увязываются с результатами лабораторных и полевых испытаний на реальных объектах. Поэтому целью данного исследования явилось комплексное изучение отклика дорожной конструкции на динамическую нагрузку, установление закономерностей усталостного разрушения асфальтобетонных слоев при испытаниях на ускоренное тестирование и при натурных испытаниях на реальных объектах.

Материалы и методы. При проведении испытаний использовалась установка ускоренного тестирования, находящаяся в Шаньдунском транспортном университете. Полевые испытания проходили с применением установки динамического нагружения с падающим грузом FWD Primax 1500, которая осуществляет регистрацию чаши прогиба на поверхности обследуемой конструкции. Для регистрации динамического отклика в структуре дорожной конструкции использовался комплекс тензометрических датчиков, позволяющих отмечать как сжимающие напряжения, так и растягивающие деформации в различных слоях. Результаты, полученные в натурных условиях, были сопоставлены с результатами, полученными на математической МКЭ-модели.

Результаты исследования. Результаты исследования показали, что толщина верхнего слоя основания является основным фактором, влияющим на величину вертикальной деформации дорожного покрытия, который необходимо учитывать на стадии проектирования конструкции дорожной одежды. При толщине верхнего слоя основания в 10 см вертикальная деформация — 100 мкм, а при толщине в 20 см — 55 мкм при условии обеспеченности общей равнопрочности конструкции. Количество циклов приложения нагрузки на установке ускоренного нагружения имеет минимальное влияние на отобранные образцы асфальтобетона при испытаниях прочности на раскол.

Обсуждение и заключение. Путем комплексного сопоставления данных численного моделирования и натурных испытаний показана их тождественность результатам, полученным в ходе ускоренного тестирования дорожных конструкций, обоснована адекватность применяемых расчетных методик. Результаты исследования могут быть применены в дорожной отрасли для разработки и совершенствования нормативной базы при проектировании жестких дорожных одежд в условиях повышенных нагрузок и интенсивного движения транспорта.

Ключевые слова: асфальтобетонное покрытие, установки ускоренного тестирования, многослойное полупространство, напряженно-деформированное состояние, температурная корректировка, модель динамического отклика

Благодарности: авторы статьи выражают искреннюю благодарность сотрудникам дорожно-испытательной лаборатории Шаньдунского транспортного университета за содействие в выполнении исследований на установке ускоренного тестирования (ALF), а также уважаемым рецензентам за время и силы, затраченные на рассмотрение данной статьи.

Финансирование. Исследования проводились в рамках гранта президента Российской Федерации для государственной поддержки молодых российских ученых — кандидатов наук (заявка МК-242.2022.4).

Для цитирования. Гуанцунг Ни, Тиратурян А.Н., Углова Е.В., Воробьев А.В. Исследование характеристик динамического отклика дорожных конструкций при ускоренном тестировании. *Advanced Engineering Research (Rostov-on-Don)*. 2023;23(3):241–256. <https://doi.org/10.23947/2687-1653-2023-23-3-241-256>

Introduction. Fatigue damage is one of the main forms of damage to exploited asphalt concrete pavements [1, 2]. As a rule, it is associated with alternating loading from the intense multi-cycle impact of the traffic flow. This type of destruction is characteristic of highways all over the world and is one of the challenges to which road scientists are trying to respond. One of the priorities of modern research in the field of fatigue failure forecasting is the testing of road structures at the accelerated load facilities. A certain contribution to the solution of this problem was made by Chinese scientists who analyzed the law of variation in the elasticity modulus of the asphalt concrete layer and its deformation during accelerated loading [3, 4]. The mechanism of destruction and fatigue characteristics of asphalt concrete mixture during operation were investigated in [5]. Its authors obtained a correction factor that took into account the difference in the mechanisms of deformation of the road structure under the influence of a test load on accelerated testing installations and during real field tests.

In general, it should be noted that, despite the sufficiently effective simulation of the passage of single loads from the traffic flow, reproduced on ALF, difficulties arise with modeling the load distribution over the width of the carriageway, under environmental conditions, soil-geological conditions, etc. Thus, the test results at ALF cannot be directly used to assess the fatigue characteristics of the actual road surface. They require additional validation under real conditions.

The authors [6–8] studied the responses of road structures to the dynamic impact of the test load, compared and analyzed their changes. The researchers applied methods combining real-time visual observation, instrumental tests for deflection, and fatigue failure resistance during loading, and also carried out work to establish relationships between stresses, deformations in the pavement structure and the temperature of various pavement structures.

It should also be noted that similar studies are being conducted in other countries, besides the PR China, including the Russian Federation, European countries, and the USA. The results of active research aimed at comparing laboratory loading modes to the loading modes corresponding to real road conditions were considered in [9–11]. At the same time, there are no similar comparisons of the results of field and laboratory studies to the results obtained on large-scale models in a controlled experiment. The results of experimental studies in the field of predicting fatigue failure of asphalt concrete layers were given in [12–14]. They comprehensively considered the issues of determining the empirical coefficients required to predict the fatigue failure of asphalt concrete layers according to field visual observations, as well as standard methods of testing asphalt concrete for fatigue when applying a four-point load or indirect stretching. However, the issues of research on large-scale models were also not addressed in them. A number of works deal directly with large-scale modeling, but for roadway paving of different designs [15–17]. The comparison of equal-strength structures to different layers and their thicknesses is the most interesting from a research point of view, since it will provide establishing patterns in the processes of deformation of asphalt concrete associated with its fatigue failure.

Materials and Methods. Accelerated Load Facility. The Accelerated Load Facility (ALF) is located on the territory of ShanDong Transport University. It is a set of equipment for complex testing of road structures (Fig. 1). At the moment, it is one of the modeling methods closest to the real conditions for reproducing a moving transport load. ALF is used to

study the characteristics of asphalt concrete coatings under plastic deformations, fatigue cracking and downward cracking. On the ALF, the axle load and the speed of its movement can be adjusted, which provides the best of all types of test equipment compliance with real deformation conditions.



Fig. 1. Accelerated Load Facility [8]

Three typical designs of the roadway paving for the device on the test track were selected to study the fatigue resistance of asphalt concrete mixtures while in operation and pavement defects in different regions. The test section of the road is 12 m long and 4 m wide. The road structure is a working layer of the soil of the roadbed, reinforced with cement, with a coating of three different types of asphalt concrete: S1, S2, and S3, respectively (Fig. 2). The calculated load reproduced by the ALF system is a semi-axial load transmitted through two wheels — BZZ-100. The reproducible load range is 80-200 kN, the load step is 20 kN, the time interval between load applications is 9 s.

4 m	4 m	4 m
←→	←→	←→
5 cm SMA-13		
5 cm AC-20	10 cm AC-20	15 cm AC-20
20 cm AC-25	15 cm AC-25	10 cm AC-25
Soil treated with cement 6 %		
Soil treated with cement 4 %		
Earth road		

Fig. 2. Road structure at the test road section

A set of equipment was assembled from soil pressure, deformation and temperature sensors installed parallel and perpendicular to the direction of loading to provide real-time monitoring of the dynamic response of the structure during the construction of the test section of the road (Fig. 3, 4). In the lower part of the monolithic asphalt concrete layer there were four sensors of horizontal and longitudinal deformation (Fig. 5). The data collection channel of the corresponding sensor and its location are indicated in Table 1. This arrangement of equipment was validated by world experience in monitoring the stress-strain state (SSS) of road structures and was described in [18–19].



Fig. 3. Sensor for registering pressure in the soil and on the surface of the base layers [18]



Fig. 4. Sensor for recording relative tensile strain [18]

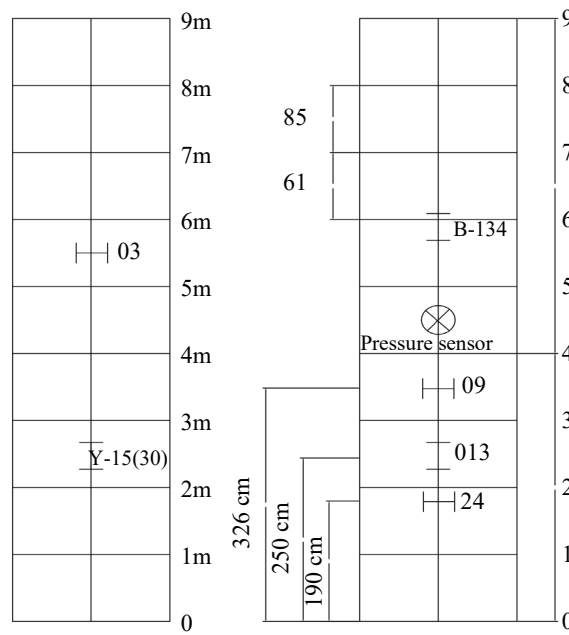


Fig. 5. The depth of each sensor

Table 1

Sensor number and location		
No.	Model	Location
W1	B-134	6 m
W2	013	2.5 m
W3	24	2 m
W4	09	3.2 m
W5	Y-15	2.5 m
W6	03	5.5 m
F1	Soil pressure sensor	4.5 m

To register the dynamic response on the surface of the road structure, in addition to the ALF, a dynamic loading unit with a falling load FWD PRIMAX 1500 was used. This unit is a pulse dynamic meter of surface movements of the coating, which provides determining the history of movements on the pavement surface under impact by means of installed geophone sensors (Fig. 6). Studies have shown that FWD can be used to determine the elastic modulus of pavement layers during testing at the ALF [20]. In the course of the research, measurements with the FWD were carried out every time after 70,000 cycles on the ALF. The measurement scheme is shown in Figure 7.



Fig. 6. Falling Weight Deflectometer (FWD) [20]

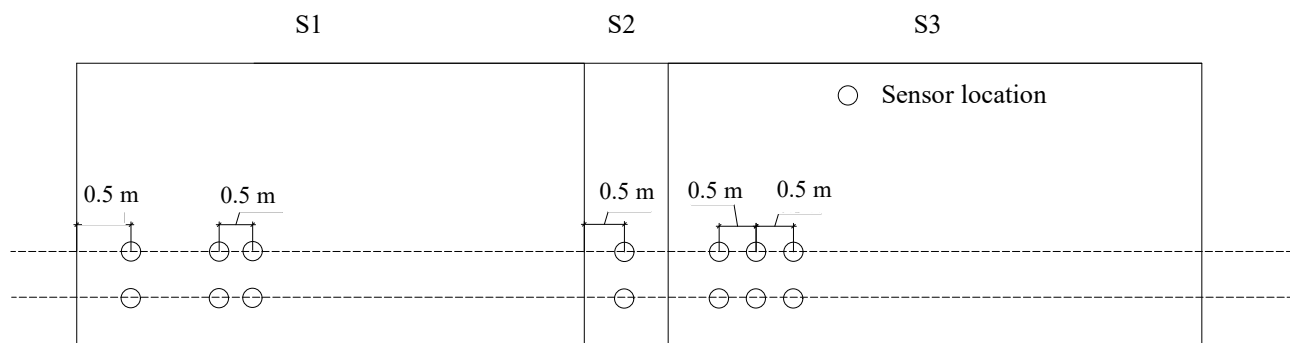


Fig. 7. Schematic diagram of measurements by the FWD

Split Tensile Tests. To obtain comparable results within the framework of this study, laboratory tests for fatigue durability were carried out at the MTS asphalt concrete testing facility [21–24] (Fig. 8). The tests were performed on asphalt concrete samples selected from the accelerated testing site in accordance with the PR China standard — JTG E20-2011¹. When testing asphalt concrete for splitting, the temperature was 15 °C, the loading speed was 50 mm/min. Each type of asphalt concrete mix was subjected to four parallel tests. When tested for fatigue durability under controlled voltage conditions, the waveform was half-sinusoid with a frequency of 10 Hz. The complete destruction of the sample was taken as the criterion of destruction. Each test was carried out for three stress levels and three samples of asphalt concrete mix.

¹ Ministry of Transport of the People's Republic of China. JTG E20-2011 “Test Regulations of Asphalt and Asphalt Mixture for Highway Engineering” [JTG E20-2011 English PDF \(JTGE20-2011\)](http://www.chinesestandard.net). (chinesestandard.net) [S].



Fig. 8. Installation of a material testing system [21]

Research Results. The temperature condition of the road structure operation at the accelerated testing section.

Temperature sensors were mounted in the test structures of the roadway paving at a depth of 0.2 and 6 cm from the road surface, respectively (Fig. 9).

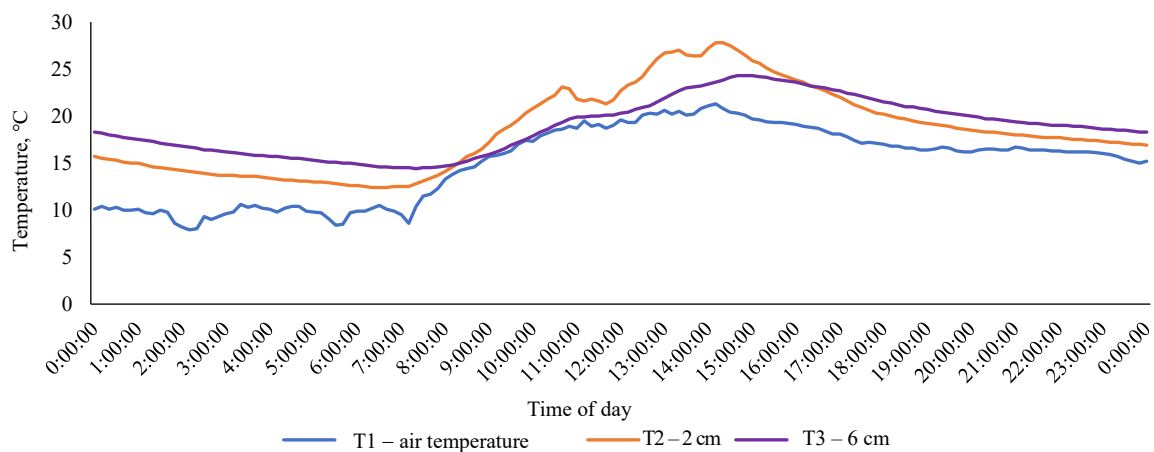


Fig. 9. Temperature variation diagram of asphalt concrete layers at different depths

Automatic data collection was carried out every 15 minutes. Figure 9 shows the curve of temperature variation at different depths of the pavement structure. It can be seen that the temperature here changes together with the change in ambient temperature. The temperature at a depth of 2 cm from the coating surface is almost during the entire observation period above the air temperature and the temperature at a depth of 6 cm.

Analysis of temperature, stresses and deformations in the lower layer of asphalt concrete. During the tests at the ALF, data on tensile deformations at the lower boundary of the lower asphalt concrete layer were collected during each test day. To provide the accuracy and reliability of the deformation data, its registration was carried out using a channel with a transmission frequency of 2,000 Hz and continuous recording of the response lasting at least three minutes, with the possibility of parallel recording of temperature information.

The maximum number of cycles before the appearance of fatigue cracks during testing at the ALF was 420,000 load applications. At the same time, it was found that temperature had the greatest effect on tensile deformations in the range from 140,000 to 240,000 applications, as can be seen from the data presented in Figures 10 and 11.

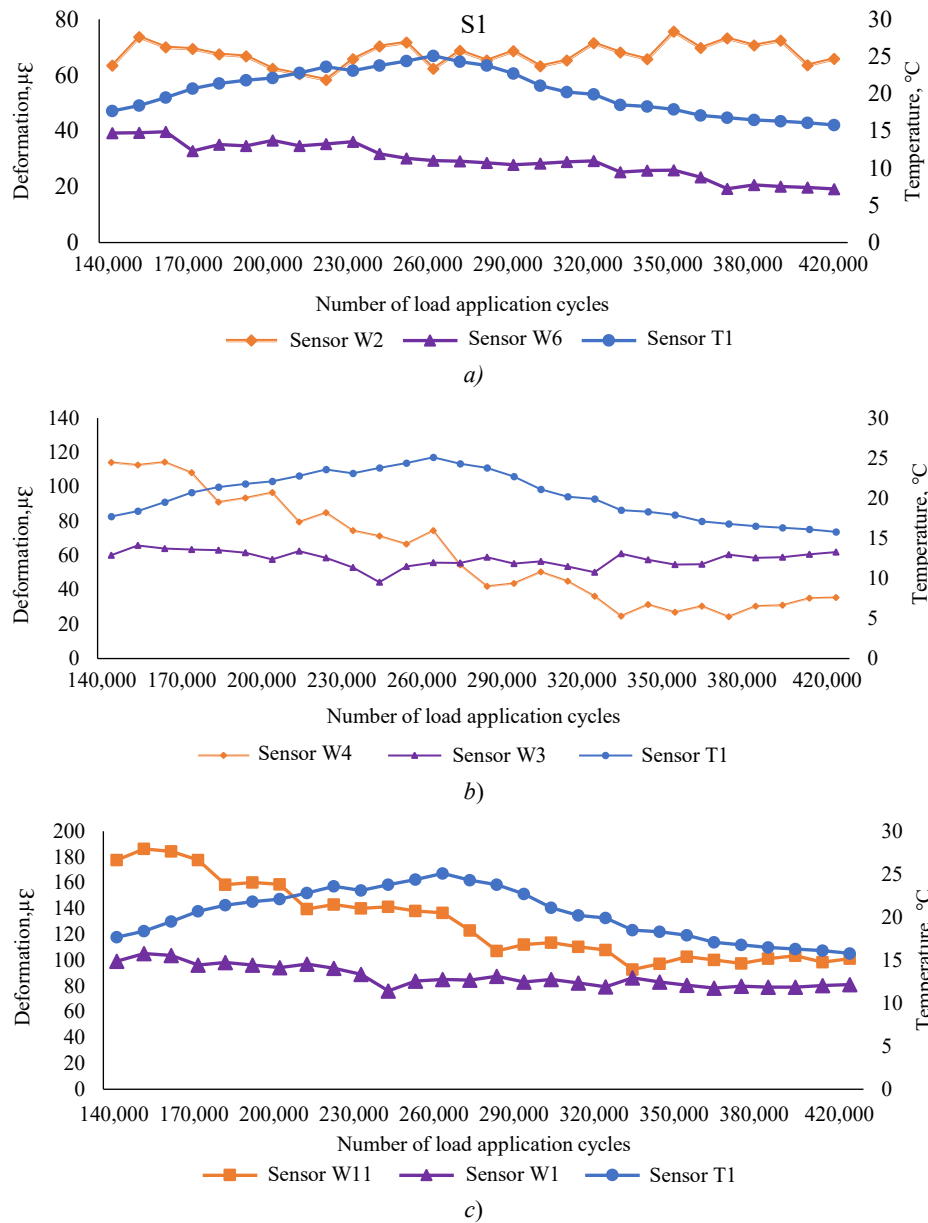


Fig. 10. Strain curve depending on the temperature on the lower face of the lower coating layer and the upper coating layer at different loading times: *a* — structure S1; *b* — structure S2; *c* — structure S3

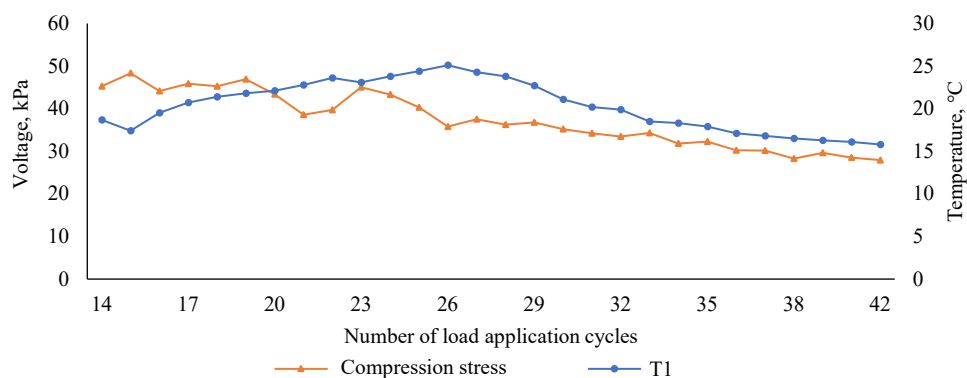


Fig. 11. Maximum stress value change curve in the lower layer of the coating depending on the temperature at different loading times

As can be seen in Figures 10 and 11, the deformation of various layers of the pavement changed depending on temperature at different loading times: in S1 structure, the tensile deformation in the lower part of the upper layer of the pavement was 19.3–39.7 $\mu\epsilon$, and the deformation at the lower boundary of the lower layer of asphalt concrete ranged

from 58.3 to 75.6 $\mu\epsilon$. In S2 structure, the range of deformation variation at the lower boundary of the upper coating layer was 42.5–64.8 $\mu\epsilon$, the deformation range of the lower layer of asphalt concrete was 59.2–115.37 $\mu\epsilon$. Tensile and compressive deformations at the lower boundary of the lower coating layer gradually decreased with increasing loading time and strongly depended on temperature. Changes on the lower face of the lower layer of asphalt concrete were not obvious. In S3 structure, the deformation range in the lower part of the upper coating layer was 76.2–105.2 $\mu\epsilon$, the deformation range on the lower face of the lower layer of asphalt concrete was 92.8–186.2 $\mu\epsilon$. Tensile deformation of the lower coating layer was mainly independent of temperature.

The range of changes in compressive stress at the upper boundary of the base layer was 30.2–48.3 kPa; as the number of loads increased, the change in compressive stress had a high correlation with the trend of temperature change.

Analysis of FWD impact test results. The FWD was used, first of all, to determine the actual values of the elastic modulus of the layers of the road structure and their variation under testing by the ALF in accordance with the backcalculation methodology [25].

A total of six tests were carried out by the FWD. At each test point, measurements were carried out three times at the same load. Then, the average deflection value at the central loading point for the last two impacts was used as a characteristic displacement. The curves of vertical displacement variation at the point of load application depending on the number of cycles of application of the load during accelerated tests are shown in Figure 12.

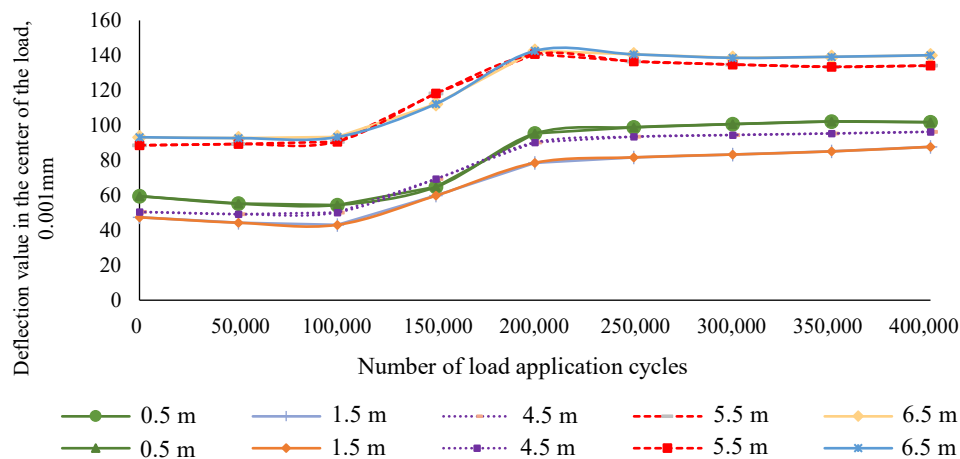


Fig. 12. Deviation curve of various pavement structures depending on the load time

The deflection value in the center of the load application by the FWD gradually grew with increasing number of loads (Fig. 12). Depending on the temperature and loading time during the first 100,000 load cycles, the change in the deflection value was insignificant. The largest change in the magnitude of vertical displacement was observed in the range from 100,000 to 200,000 load applications. After 200,000 load applications, the vertical movement stabilized. Since the pavement structure was affected by temperature and load time, the structural strength of the pavement decreased accordingly, and the amount of vertical displacement increased.

To verify the results of determining the elastic modulus of asphalt concrete layers using the backcalculation technique based on the results of testing by the FWD, additional laboratory examination of asphalt concrete samples was carried out². As a rule, the actual dynamic modulus of elasticity was reduced to a standard value measured at a temperature of 2 °C according to formula 1:

$$E_{20} = E_T \cdot e^{-0.0722(20-T)}, \quad (1)$$

where E_{20} — inversely calculated module of the asphalt concrete layer at 20 °C, MPa; E_T — inversely calculated elastic modulus of the asphalt concrete layer at the actual temperature, MPa; T — temperature, °C.

² AASHTO TP 62-2007 Standard Method of Test for Determining the Percentage of Fracture in Coarse Aggregate [S].(D 5821 – 01 (kashanu.ac.ir))

Figure 13 shows the results of determining the elastic modulus of the asphalt concrete base layer depending on the number of load cycles reproduced during the accelerated testing.

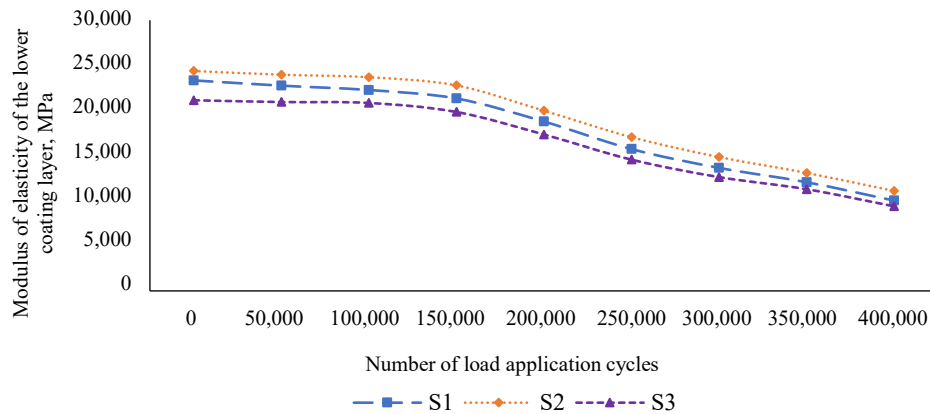


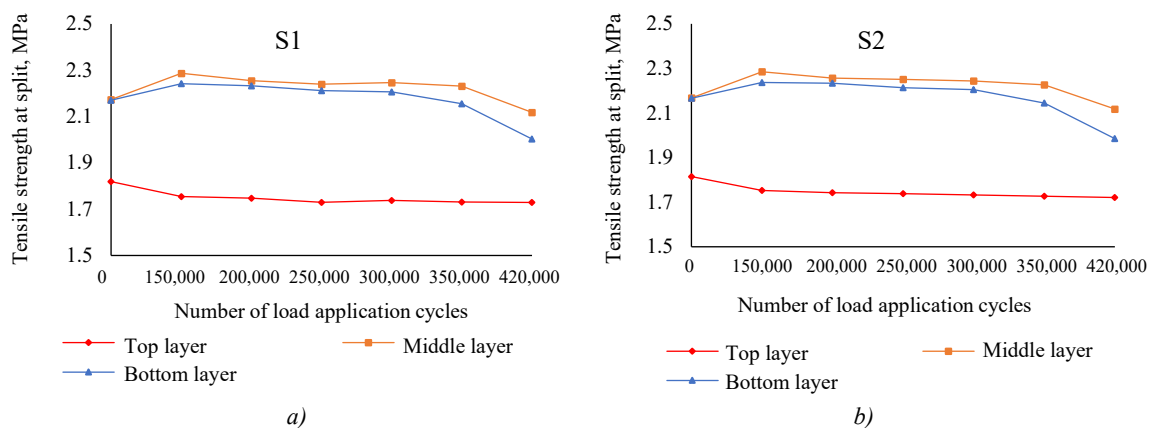
Fig. 13. Variation of dynamic modulus of elasticity of the lower layer of asphalt concrete depending on the number of loading cycles

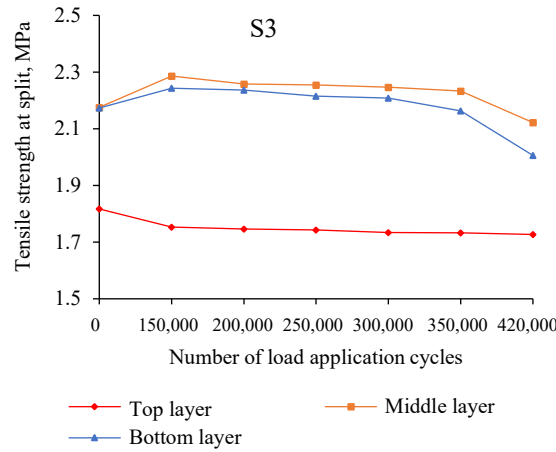
Figure 13 shows that as the number of load applications increased, the module of the lower layer of asphalt concrete of various pavement structures tended to decrease. At the initial stage of the test, 0–100,000 load applications (the standard total calculated axle load was 0–25.6 mln applications), the elastic modulus of the lower layer of asphalt concrete slowly decreased with an increase in the number of load applications (the average decrease was 5.23 %). When the number of load applications exceeded 100,000, the rate of reduction of the elastic modulus of the lower layer of asphalt concrete increased significantly. The modulus of elasticity of the lower layer of asphalt concrete of all structures decreased by an average of 54.87 %.

Split tensile test analysis. As the results of accelerated testing showed, fatigue cracks began to appear by about 350,000 load application cycle. When the load reached 420,000 applications, fatigue cracks were observed on the surface layer of asphalt concrete with an opening width of up to 2 mm, and the test was stopped.

When sampling cores at the locations of cracks, it was found that cracks, as a rule, appeared on the surface of the coating, and did not penetrate into the layers. Most of them were transverse, passing through the rolling bands of the wheel load, and only a small part could be attributed to downward fatigue cracks. According to the results of laboratory tests of asphalt concrete samples selected at the accelerated testing sections, the dependence of the split strength on the number of cycles of the applied load was established.

Figure 14 shows that the tensile strength during the splitting of asphalt concrete mixtures under operation, subjected to different accelerated loading times, changed little. In general, the effect of accelerated loading on the tensile strength during the splitting of the asphalt concrete mixture under operation was insignificant.





c)
Fig. 14. Strength limit for indirect stretching of asphalt concrete mixtures under operation:
a — structure S1; b — structure S2; c — structure S3

Determination of the estimated number of asphalt concrete cycles to failure. At the end of this study, in accordance with the regulatory document of the People's Republic of China JTG D50-2017 “Specifications for Design of Highway Asphalt Pavement”³ and based on the data got by the authors of this study, using the regression analysis method, dependence (2) was obtained for predicting the maximum number of cycles before the onset of fatigue failure. To take into account the influence of the thickness of the asphalt concrete layer package using the regression analysis method and based on the data obtained during accelerated tests, the dependence for the assignment of the correction factor was determined. It is shown in Figure 15.

$$N_f = 0.265 \left(\frac{1}{\varepsilon_t} \right)^{4.51} \left(\frac{1}{E} \right)^{1.42}, \quad (2)$$

$$N_f = C_1 \cdot N_{alf}, \quad (3)$$

where N_f — number of loading cycles on the actual structure of the roadway paving, cycles; N_{alf} — number of loading cycles on the ALF, cycles; ε_t — tensile strain ratio on the lower face of the asphalt concrete layer, $\mu\text{m}\%$; E — elastic modulus of asphalt concrete layer, MPa; C_1 — correction factor between laboratory values and values obtained at a full-scale ALF.

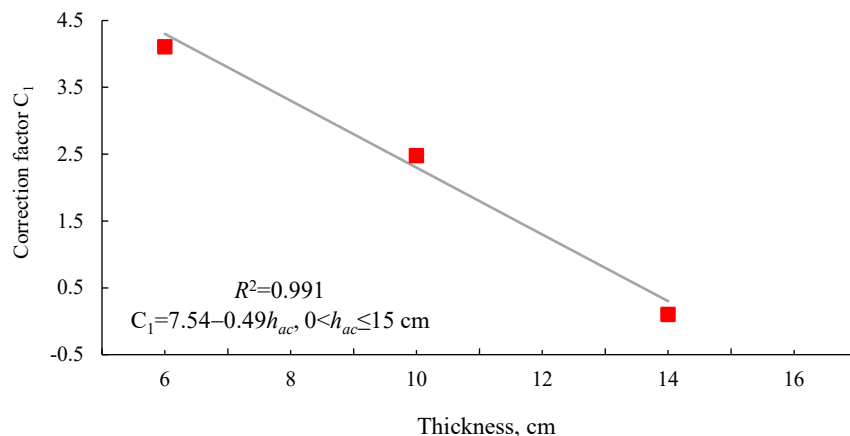


Fig. 15. Relationship between the ALF correction factor and the thickness of the asphalt concrete layer

³ Ministry of Transport of the People's Republic of China. JTG D50-2017 “Specifications for Design of Highway Asphalt Pavement. Ministry of Transport” [S]. 2017. (JTG D50-2017 English PDF (JTGD50-2017) (chinesestandard.net))

The dependence structure corresponds to the general view obtained by the Asphalt institute [14]:

$$N_f = a \left(\frac{1}{\varepsilon} \right)^b \left(\frac{1}{S} \right)^c, \quad (4)$$

where a , b , c — empirical coefficients determined under laboratory or field tests; ε — ultimate deformation at which the tests are carried out; S — material stiffness parameter.

Analysis of mechanical response characteristics. In JTG D50-2017 “Specifications for Design of Highway Asphalt Pavement”, the parameter of fatigue cracking of the bottom layer of asphalt concrete is one of the calculated indicators adopted in the design. Due to the greater rigidity of the bottom layer of asphalt concrete, the greatest tensile deformations are concentrated at its lower boundary, which is confirmed by the results given in this article. In the framework of a numerical experiment, S3 structure is considered as a key control structure for calculating the tensile strain in the lower part of the asphalt concrete pavement. The design scheme of the pavement adopted in the simulation is shown in Figure 16.

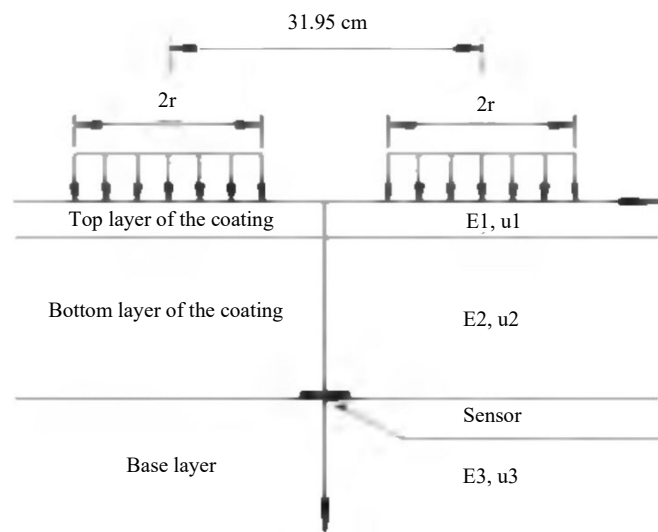


Fig. 16. Mechanical response calculation model according to JTG D50-2017

The calculation of the structure response was carried out on a finite element model of the road structure, while the hypothesis of complete adhesion between all structural layers of the pavement was accepted. The calculation was performed for a paired wheel of a motor vehicle with an axle load of 200 kN and a pressure of 1.1 Mpa [25–27]. When substituting into the mathematical model, the elastic modules of the pavement layers were used as input data, calculated according to the test results by the FWD. The results of comparing the road structure response registered during accelerated tests and calculated using the finite element method (FEM) are shown in Figure 17.

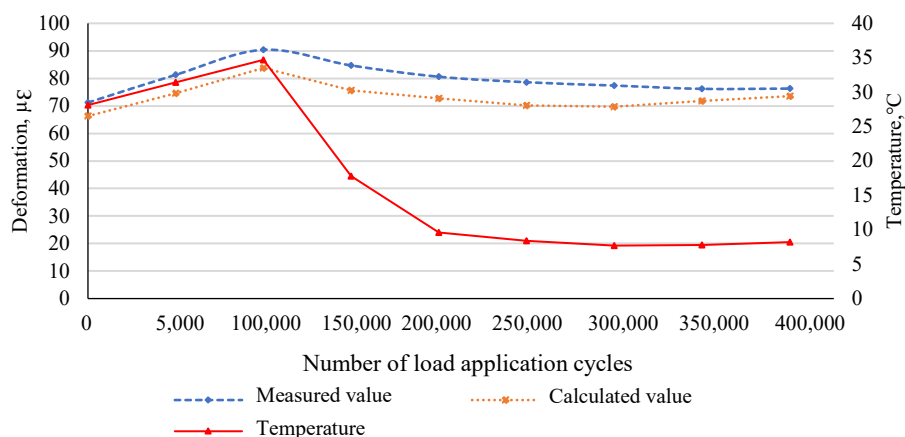


Fig. 17. Comparison of measured and calculated values of the response to deformation of the bottom layer of S3 coating

Judging by the data in Figure 17, due to the influence of ambient temperature and the thickness of the bottom layer of asphalt concrete, the calculated value of deformation in the lower part is slightly less than the measured value of deformation. However, this can be explained by a number of simplifications adopted in the mathematical model. In general, the results of full-scale tests and numerical modeling are quite close and are characterized by similar trends, which indicates the adequacy of both the full-scale testing and the applied methods of numerical modeling.

Discussion and Conclusion. One of the basic results presented in this article and differing from the results of previous studies [3–8, 14, 19, 20] is the conclusion about the prevailing influence of the thickness of the top layer of the base on the amount of the vertical elastic deformation recorded on the surface of the road structure. It was validated by a set of experimental measurements using a dynamic loading unit with FWD Primax 1500. In similar works, it was noted that the combined effect of the thickness of the bottom coating layer and the top base layer had the greatest effect on the amount of elastic deflection on the surface.

Also, within the framework of this study, a comprehensive analysis of the test results at the ALF and numerical experiments based on known models for predicting fatigue failures was carried out. As a result, dependences (2) and (3) were obtained to implement the transition and provide comparability of this outcome. It should be noted that the coefficients obtained in the course of this work for dependence (2) differ from similar values known to us obtained at the MnRoad test site [14] (Fig. 18).

Coefficient	MnRoad dependence	Dependence obtained by the authors
a	0.314	0.265
b	3.291	4.510
c	0.854	1.420

Fig. 18. MnRoad dependence coefficients and those obtained by the authors

Differences in coefficients are largely due to differences in the rules for the selection of asphalt concrete mixtures, as well as regional testing conditions. It should also be noted that these coefficients somewhat tighten the classical performance model, reducing the predicted service life of road clothes, in comparison to the MnRoad model.

Undoubtedly, these results were obtained for a fairly limited sample of experiments and a set of materials according to their physical and mechanical properties. They meet the requirements for asphalt concrete mixtures used in the construction of highways in China, and are quite close to the mixtures used in the Russian Federation. At the same time, it seems promising to use the results obtained. In the future, investigation on calibration of the dependence will be continued taking into account data from test sections of operated highways in the Russian Federation and China.

Laboratory checkout has shown that the split tensile strength practically does not depend on the number of loading cycles of the tested asphalt concrete during accelerated testing.

The results obtained can be applied for further development and improvement of the legal framework of the road industry regulating methods of calculation and prediction of fatigue cracking.

References

1. Ji Xiaoping, Zheng Nanxiang, Niu Sisheng, Meng Shutao, Xu Quanliang. Development of a Rutting Prediction Model for Asphalt Pavements with the Use of an Accelerated Loading Facility. *Road Materials and Pavement Design*. 2015;17(1):1–17. <https://doi.org/10.1080/14680629.2015.1055337>
2. Insoo Yeo, Youngchan Suh, Sungho Mun. Development of Remaining Fatigue Life Model for Asphalt Black Base through Accelerated Pavement Testing. *Construction and Building Materials*. 2008;22(8):1881–1886. <https://doi.org/10.1016/j.conbuildmat.2007.04.015>

3. Chen Shao Xing, Wei Xin Ren. Study Fatigue Performance Predict Model of Asphalt Layer Basement on Accelerated Loading Test. *Advanced Materials Research*. 2011;255–260:3238–3243. <https://doi.org/10.4028/www.scientific.net/AMR.255-260.3238>
4. Zexin Ma, Li-Ping Liu, L-J Sun. Damage and Failure Performance of In-Service Asphalt Mixture Based on Accelerated Loading Test. *Journal of Jilin University*. 2019;49(2):384–391. <https://doi.org/10.13229/j.cnki.jdxbgxb20171109>
5. Shao Xing Chen, Wei Xin Ren. Study Fatigue Performance Predict Model of Asphalt Layer Basement on Accelerated Loading Test. *Advanced Materials Research*. 2011;255:3238–3243. <https://doi.org/10.4028/www.scientific.net/AMR.255-260.3238>
6. TRB's National Cooperative Highway Research Program (NCHRP synthesis 433): Significant Findings from Full Scale Accelerated Pavement Testing. Washington, DC: The National Academies Press; 2012. <https://doi.org/10.17226/22699>
7. Timm DH, Priest AL, McEwen TV. *Design and Instrumentation of the Structural Pavement Experiment at the NCAT Test Track*. Auburn AL: National Center for Asphalt Technology; 2004. 89 p. URL: <https://rosap.nrl.bts.gov/view/dot/38610> (accessed: 20.07.2023).
8. Ji Xiaoping, Zheng Nanxiang, Hou Yueqin, Niu Sisheng. Application of Asphalt Mixture Shear Strength to Evaluate Pavement Rutting with Accelerated Loading Facility (ALF). *Construction and Building Materials*. 2013;41:1–8. <https://doi.org/10.1016/j.conbuildmat.2012.11.111>
9. Uglova EV, Tiraturyan AN, Lyapin AA. Integrated Approach to Studying Characteristics of Dynamic Deformation on Flexible Pavement Surface Using Nondestructive Testing. *PNRPU Mechanics Bulletin*. 2016;(2):111–130. <https://doi.org/10.15593/perm.mech/2016.2.08>
10. Tiraturyan AN, Uglova EV. Assessment of Durability Indicators of Flexible Pavements on the Basis of the Mechanical-Statistical Method. *MATEC Web of Conferences*. 2018;196:01020. <https://doi.org/10.1051/mateconf/201819601020>
11. Uglova EV, Tiraturyan AN, Shilo OA. Prediction of Failure Fatigue Accumulation in Asphalt Concrete Layers of Flexible Pavements. *Russian Journal of Building Construction and Architecture*. 2019;55(3):52–61. <https://doi.org/10.25987/VSTU.2019.55.3.006>
12. Nithin Sudarsanan, Youngsoo Richard Kim. A Critical Review of the Fatigue Life Prediction of Asphalt Mixtures and Pavements. *Journal of Traffic and Transportation Engineering (English Edition)*. 2022;9(5):808–835. <https://doi.org/10.1016/j.jtte.2022.05.003>
13. Sohrab Zarei, Jian Ouyang, Yanqing Zhao. Evaluation of Fatigue Life of Semi-Flexible Pavement with Cement Asphalt Emulsion Pastes. *Construction and Building Materials*. 2022;349:128797. URL: <https://linkinghub.elsevier.com/retrieve/pii/S0950061822024540> (accessed: 22.07.2023).
14. Tanquist B. *Local Road Material Properties and Calibration for MnPAVE Summary Report*. Saint Paul, MN: Minnesota Department of Transportation; 2008. 43 p. URL: <https://www.lrrb.org/media/reports/200856.pdf> (accessed: 20.07.2023).
15. Jian Zou, Roque R, Byron T. Effect of HMA Ageing and Potential Healing on Top-down Cracking Using HVS. *Road Materials and Pavement Design*. 2012;13(3):1–16. <https://doi.org/10.1080/14680629.2012.709177>
16. Zhen Liu, Xingyu Gu, Hua Ren, Zhou Zhou, Xiang Wang, Shi Tang. Analysis of the Dynamic Responses of Asphalt Pavement Based on Full-Scale Accelerated Testing and Finite Element Simulation. *Construction and Building Materials*. 2022;325:126429. <https://doi.org/10.1016/j.conbuildmat.2022.126429>
17. Ze Jiao Dong, Sheng Long Li, Jia Yu Wen, Hong Chun Chen. Asphalt Pavement Structural Health Monitoring Utilizing FBG Sensors. *Advanced Engineering Forum*. 2012;5:339–344. <https://doi.org/10.4028/www.scientific.net/AEF.5.339>
18. Wei Lu, Kayser S, Wellner F. Impact of Surface Temperature on Fatigue Damage in Asphalt Pavement. *Journal of Highway and Transportation Research and Development (English Edition)*. 2013;7(3):1–6. <https://doi.org/10.1061/JHTRCQ.0000324>
19. Lin Wang, Jincheng Wei, Wenjuan Wu, Xiaomeng Zhang, Xizhong Xu, Xiangpeng Yan. Technical Development and Long-Term Performance Observations of Long-Life Asphalt Pavement: A Case Study of Shandong Province. *Journal of Road Engineering*. 2022;2(4):369–389. <https://doi.org/10.1016/j.jreng.2022.11.001>
20. Jinting Wu, Fen Ye, Yinting Wu. Modulus Evolution of Asphalt Pavement Based on Full-Scale Accelerated Pavement Testing with Mobile Load Simulator. *International Journal of Pavement Engineering*. 2014;16(7):1–11. <https://doi.org/10.1080/10298436.2014.943213>

21. Yong Pen, Lijun Sun, Yongjiu Shi. Factors Affecting the Splitting Strength of Asphalt Mixture. *Journal of Jilin University: Engineering Edition*. 2007;37(6):1304–1307. URL: https://www.researchgate.net/publication/290298136_Factors_affecting_splitting_strength_of_asphalt_mixture (accessed: 20.07.2023).
22. Lu Xue-yuan, Sun Li-jun. Factors Affecting Splitting Strength for AC-13 Modified Asphalt Mixture and Marshall Performance Standard Correlation. *Journal of Jilin University: Engineering Edition*. 2010;40(03):676–682. URL: <http://xuebao.jlu.edu.cn/gxb/EN/abstract/abstract10100.shtml> (accessed: 20.07.2023).
23. Yong Chun Qin, Sui Yuan Wang, Wei Zeng, Xiao Pei Shi, Jian Xu, Song Chang Huang. The Effect of Asphalt Binder Aging on Fatigue Performance of Evotherm WMA. *Advanced Materials Research*. 2012;535–537:1686–1692. <https://doi.org/10.4028/www.scientific.net/AMR.535-537.1686>
24. Castro M, Sánchez JA. Estimation of Asphalt Concrete Fatigue Curves — A Damage Theory Approach. *Construction and Building Materials*. 2008;22(6):1232–1238.
25. Uglova EV, Tiraturyan AN. Interlayer Bond Evaluation in the Flexible Pavement Structures Using a Nondestructive Testing Method. *Procedia Engineering*. 2016;150:1791–1796. <https://doi.org/10.1016/j.proeng.2016.07.172>
26. Nazarian S, Alvarado G. Impact of Temperature Gradient on Modulus of Asphaltic Concrete Layers. *Journal of Materials in Civil Engineering*. 2006;18(4):492–499. [https://doi.org/10.1061/\(ASCE\)0899-1561\(2006\)18:4\(492\)](https://doi.org/10.1061/(ASCE)0899-1561(2006)18:4(492))
27. Shuhua Wu, Huaxin Chen, Jiupeng Zhang, Zhonghua Zhang. Effects of Interlayer Bonding Conditions between Semi-Rigid Base Layer and Asphalt Layer on Mechanical Responses of Asphalt Pavement Structure. *International Journal of Pavement Research and Technology*. 2017;10(3):274–281. <https://doi.org/10.1016/j.ijprt.2017.02.003>

Received 01.08.2023

Revised 14.08.2023

Accepted 18.08.2023

About the Authors:

Ni Guangcong, Engineer of the Department of Civil Engineering and Architecture, Shan Dong JiaoTong University (5001, Haitang Road, Jinan City, Shandong Province, 250023, China), [ScopusID](#), [ResearcherID](#), [ORCID](#), ngc931123@163.com

Artem N. Tiraturyan, Dr.Sci. (Eng.), Associate Professor, Professor of the Motorways Department, Don State Technical University (1, Gagarin sq., Rostov-on-Don, 344003, RF), [ResearcherID](#), [ScopusID](#), [AuthorID](#), [ORCID](#), tiraturjan@list.ru

Evgeniya V. Uglova, Dr.Sci. (Eng.), Professor of the Motorways Department, Don State Technical University (1, Gagarin sq., Rostov-on-Don, 344003, RF), [ResearcherID](#), [ScopusID](#), [AuthorID](#), [ORCID](#), uglova.ev@yandex.ru

Andrey V. Vorobev, Engineer of the Motorways Department, Don State Technical University (1, Gagarin sq., Rostov-on-Don, 344003, RF), [ResearcherID](#), [ORCID](#), andreyvorobev19@mail.ru

Claimed contributorship:

Ni Guangcong: basic concept formulation, research objectives and tasks computational analysis.

AN Tiraturyan: academic advising, analysis of research results, formulation of conclusions.

EV Uglova: academic advising, analysis of research results, correction of the conclusions.

AV Vorobev: preparation and revision of the text, formulation of conclusions.

Conflict of interest statement: the authors do not have any conflict of interest.

All authors have read and approved the final manuscript.

Поступила в редакцию 01.08.2023

Поступила после рецензирования 14.08.2023

Принята к публикации 18.08.2023

Об авторах:

Ни Гуанцунг, инженер кафедры гражданского строительства и архитектуры Шаньдунского транспортного университета (КНР, провинция Шаньдун, г. Цзинань), [ScopusID](#), [ResearcherID](#), [ORCID](#), ngc931123@163.com

Артем Николаевич Тиратурян, доктор технических наук, доцент, профессор кафедры автомобильных дорог Донского государственного технического университета (344003, РФ, г. Ростов-на-Дону, пл. Гагарина, 1), [ResearcherID](#), [ScopusID](#), [AuthorID](#), [ORCID](#), tiraturjan@list.ru

Евгения Владимировна Углова, доктор технических наук, профессор кафедры автомобильных дорог Донского государственного технического университета (344003, РФ, г. Ростов-на-Дону, пл. Гагарина, 1), [ResearcherID](#), [ScopusID](#), [AuthorID](#), [ORCID](#), uglova.ev@yandex.ru

Андрей Викторович Воробьев, инженер кафедры автомобильных дорог Донского государственного технического университета (344003, РФ, г. Ростов-на-Дону, пл. Гагарина, 1), [ResearcherID](#), [ORCID](#), andreyvorobyev19@mail.ru

Заявленный вклад соавторов:

Ни Гуанцунг — формирование основной концепции, цели и задачи исследования, проведение расчетов.

А.Н. Тиратурян — научное руководство, анализ результатов исследований, формирование выводов.

Е.В. Углова — научное руководство, анализ результатов исследований, корректировка выводов.

А.В. Воробьев — подготовка и доработка текста, формирование выводов.

Конфликт интересов: авторы заявляют об отсутствии конфликта интересов.

Все авторы прочитали и одобрили окончательный вариант рукописи.

MECHANICS



UDC 624.04

Original article

<https://doi.org/10.23947/2687-1653-2023-23-3-257-268>

Buckling of Rectangular Plates under Nonlinear Creep

Serdar B. Yazyev , Anton S. Chepurnenko  

Don State Technical University, Rostov-on-Don, Russian Federation

 anton_chepurnenk@mail.ru

Abstract

Introduction. The task of analyzing the stability of plates and shells under creep conditions is critical for structural elements made of materials with the property of aging, which are under the action of long-term loads, since the loss of stability can occur abruptly and long before the exhaustion of the strength resource of the material. Currently, the issues of joint consideration of geometric nonlinearity and creep in the problems of buckling plates remain poorly studied, existing software systems do not provide such calculations. The objective of this work is to develop an algorithm for calculating the stability of rectangular plates with initial deflection, which are subjected to loads in the middle plane, taking into account geometric nonlinearity and creep.

Materials and Methods. When obtaining the resolving equations, the geometric and static equations of the theory of flexible elastic plates were taken as the basis. Physical equations were derived from the assumption that total strains were equal to the sum of elastic strains and creep deformations. Finally, the problem was reduced to a system of two differential equations, in which the desired functions were the stress and deflection functions. The resulting system of equations was solved numerically using the finite-difference method in combination with the method of successive approximations and the Euler method. As the boundary conditions for the stress function, the frame analogy was used, as in the case of a plane problem of elasticity theory.

Results. The solution to the problem for a plate compressed in one direction by a uniformly distributed load has been presented. The nature of the growth of displacements at different load rates and initial deflection was studied. It has been established that when the vertical displacements reach values comparable to the thickness of the plate, their growth rate begins to decay even at a load greater than the long-term critical one.

Discussion and Conclusion. The results of stability analysis using the developed algorithm show that the growth of plate deflection under the considered boundary conditions is limited, stability loss is not observed at any load values not exceeding the instantaneous critical one. This indicates the possibility of long-term safe operation of such structures with a load less than instant critical one.

Keywords: stability, creep, plate, geometric nonlinearity, physical nonlinearity, initial imperfections, finite-difference method

Acknowledgements: the authors would like to thank the editorial board and the reviewers for their attentive attitude to the article and for the specified comments that improved the quality of the article.

For citation. Yazyev SB, Chepurnenko AS. Buckling of Rectangular Plates under Nonlinear Creep. *Advanced Engineering Research (Rostov-on-Don)*. 2023;23(3):257–268. <https://doi.org/10.23947/2687-1653-2023-23-3-257-268>

Выпучивание прямоугольных пластин при нелинейной ползучести

С.Б. Языев , А.С. Чепурненко  

Донской государственный технический университет, г. Ростов-на-Дону, Российская Федерация

 anton_chepurnenk@mail.ru

Аннотация

Введение. Задача анализа устойчивости пластин и оболочек в условиях ползучести актуальна для элементов конструкций из материалов, обладающих свойством старения, находящихся под действием длительных нагрузок, поскольку потеря устойчивости может происходить резко и задолго до исчерпания прочностного ресурса материала. Вопросы совместного учета геометрической нелинейности и ползучести в задачах выпучивания пластин в настоящее время остаются слабо изученными, существующие программные комплексы не позволяют выполнить такой расчёт. Целью настоящей работы выступает разработка алгоритма расчета на устойчивость прямоугольных пластинок с начальной погибью, испытывающих действие нагрузок в срединной плоскости с учетом геометрической нелинейности и ползучести.

Материалы и методы. При получении разрешающих уравнений в основу положены геометрические и статические уравнения теории гибких упругих пластин. Физические уравнения выводятся из предположения, что полные деформации равны сумме упругих деформаций и деформаций ползучести. Окончательно задача была сведена к системе из двух дифференциальных уравнений, в которых в качестве искомых функций выступают функция напряжений и прогиба. Решение полученной системы уравнений выполнялось численно с помощью метода конечных разностей в сочетании с методом последовательных приближений и методом Эйлера. В качестве граничных условий для функции напряжений используется рамная аналогия, как в случае плоской задачи теории упругости.

Результаты исследования. В рамках поставленной цели разработан алгоритм расчета и представлено решение задачи для пластины, сжимаемой в одном направлении равномерно распределенной нагрузкой. Исследован характер роста перемещений при различной величине нагрузки и начальной погиби. Установлено, что при достижении вертикальными перемещениями величин, соизмеримых с толщиной пластинки, скорость их роста начинает затухать даже при нагрузке больше длительной критической.

Обсуждение и заключение. Результаты анализа устойчивости с использованием разработанного алгоритма показывают, что рост прогиба пластины при рассмотренных граничных условиях ограничен, потеря устойчивости не наблюдается при любых значениях нагрузки, не превосходящих мгновенную критическую. Это говорит о возможности длительной безопасной эксплуатации таких конструкций при нагрузке менее мгновенной критической.

Ключевые слова: устойчивость, ползучесть, пластина, геометрическая нелинейность, физическая нелинейность, начальные несовершенства, метод конечных разностей

Благодарности: авторы выражают благодарность редакции и рецензентам за внимательное отношение к статье и указанные замечания, которые позволили повысить ее качество.

Для цитирования. Языев С.Б., Чепурненко А.С. Выпучивание прямоугольных пластин при нелинейной ползучести. *Advanced Engineering Research (Rostov-on-Don)*. 2023;23(3):257–268. <https://doi.org/10.23947/2687-1653-2023-3-257-268>

Introduction. Much attention is paid to the stability analysis of thin-walled structures in the form of plates and shells, since such structures are widely used in construction and other branches of technology [1–3]. One of the challenges in the field of calculating plates and shells is the analysis of their stress-strain state under creep conditions, which is confirmed by a significant number of works published recently on this problem in domestic and foreign sources. Thus, in [4–8], the issues of buckling under creep of composite thin-walled structures were investigated. In [9], the problem of stability of functionally gradient plates was considered, taking into account the dependence of material properties on temperature. In [10], stochastic analysis methods were applied to the problem of buckling composite plates. In [11–17], the issues of stability of viscoelastic plates and shells under the influence of dynamic and tracking loads were discussed, and [18] dealt with plates of medium thickness, taking into account the dependence of material properties on time. Mathematical difficulties arising in solving these problems led to the fact that numerous researchers limited themselves to linear laws of viscoelastic deformation or considered the case of steady-state creep. The finite element method opens

up great possibilities in solving the problems of calculating plates and shells taking into account creep. However, modern computational complexes, such as ANSYS, Abaqus, LIRA, etc., contain a limited set of rheological models applicable to specific materials in a fixed range of stresses and temperatures. There is a need for alternative calculation methods suitable for arbitrary laws of viscoelastic deformation, including nonlinear ones.

This work was aimed at constructing a system of resolving equations for the problem of buckling rectangular plates with nonlinear viscoelastic properties under the action of forces in the middle plane, taking into account large displacements, as well as an algorithm for its solution. Note that the problem of the stability of structural elements, taking into account creep, cannot be solved as a problem of pure stability. Its solution requires the presence of disturbances in the form of initial irregularities. Generally, the initial imperfections are given in the form of the initial loss or eccentricities of the application of loads.

Materials and Methods. Let us consider the calculation method on the example of a plate with an initial deflection $w_0(x,y)$, compressed by a distributed load p [kN/m] in the x -axis direction and having a hinge support along the contour (Fig. 1).

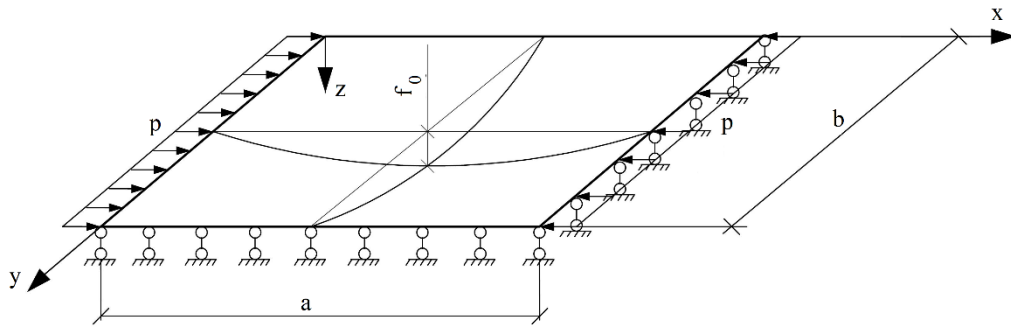


Fig. 1. Computational scheme

In the case under consideration, in the presence of creep, if compared to the theory of elastic flexible plates, the difference manifests itself only in the form of physical equations. Total deformations can be presented as the sum of deformations of the middle plane (passing into the surface) and bending deformations caused by changes in the curvature of the middle surface:

$$\varepsilon_x = \varepsilon_x^0 - z \frac{\partial^2 w}{\partial x^2}; \varepsilon_y = \varepsilon_y^0 - z \frac{\partial^2 w}{\partial y^2}; \gamma_{xy} = \gamma^0 - 2z \frac{\partial^2 w}{\partial x \partial y}, \quad (1)$$

where ε_x and ε_y — total linear deformations; γ_{xy} — total angular deformations; ε_x^0 and ε_y^0 — linear deformations of the middle surface; γ^0 — angular deformations of the middle surface.

For deformations of the middle surface, the equation of continuity of deformations can be written [19]:

$$\frac{\partial^2 \varepsilon_x^0}{\partial y^2} + \frac{\partial^2 \varepsilon_y^0}{\partial x^2} - \frac{\partial^2 \gamma^0}{\partial x \partial y} = \left(\frac{\partial^2 (w + w_0)}{\partial x \partial y} \right)^2 - \frac{\partial^2 (w + w_0)}{\partial x^2} \frac{\partial^2 (w + w_0)}{\partial y^2} - \left[\left(\frac{\partial^2 w_0}{\partial x \partial y} \right)^2 - \frac{\partial^2 w_0}{\partial x^2} \frac{\partial^2 w_0}{\partial y^2} \right]. \quad (2)$$

For materials with viscoelastic properties, total deformations can be represented as:

$$\varepsilon_x = \frac{1}{E} (\sigma_x - \nu \sigma_y) + \varepsilon_x^*; \varepsilon_y = \frac{1}{E} (\sigma_y - \nu \sigma_x) + \varepsilon_y^*; \gamma_{xy} = \frac{2(1+\nu)}{E} \tau_{xy} + \gamma_{xy}^*, \quad (3)$$

where $\varepsilon_x^*, \varepsilon_y^*, \gamma_{xy}^*$ — creep deformations; E — modulus of elasticity; ν — Poisson's ratio; $\sigma_x, \sigma_y, \tau_{xy}$ — values of stress components in the corresponding directions.

Having expressed the stress components in (3) through deformations, we write down the physical relations in the inverse form:

$$\sigma_x = \frac{E}{1-\nu^2} (\varepsilon_x + \nu \varepsilon_y - (\varepsilon_x^* + \nu \varepsilon_y^*)); \sigma_y = \frac{E}{1-\nu^2} (\varepsilon_y + \nu \varepsilon_x - (\varepsilon_y^* + \nu \varepsilon_x^*)); \tau_{xy} = \frac{E}{2(1+\nu)} (\gamma_{xy} - \gamma_{xy}^*). \quad (4)$$

The relationship of internal force factors and stresses is determined by integral relations:

$$N_x = \int_{-h/2}^{h/2} \sigma_x dz; N_y = \int_{-h/2}^{h/2} \sigma_y dz; S = \int_{-h/2}^{h/2} \tau_{xy} dz; M_x = \int_{-h/2}^{h/2} \sigma_x z dz; M_y = \int_{-h/2}^{h/2} \sigma_y z dz; H = \int_{-h/2}^{h/2} \tau_{xy} z dz, \quad (5)$$

where N_x and N_y — linear longitudinal forces; S — linear shear forces; M_x and M_y — linear bending moments; H — linear torques; h — plate thickness.

Next, we substitute (1) in (4), as well as (4) in (5). As a result, we get:

$$\begin{aligned} N_x &= \frac{Eh}{1-\nu^2} (\varepsilon_x^0 + \nu \varepsilon_y^0) - N_x^*; N_y = \frac{Eh}{1-\nu^2} (\varepsilon_y^0 + \nu \varepsilon_x^0) - N_y^*; S = \frac{Eh}{2(1+\nu)} \gamma^0 - S^*; \\ M_x &= -D \left(\frac{\partial^2 w}{\partial x^2} + \nu \frac{\partial^2 w}{\partial y^2} \right) - M_x^*; M_y = -D \left(\frac{\partial^2 w}{\partial y^2} + \nu \frac{\partial^2 w}{\partial x^2} \right) - M_y^*; H = -D(1-\nu) \frac{\partial^2 w}{\partial x \partial y} - H^*, \end{aligned} \quad (6)$$

where $D = \frac{Eh^3}{12(1-\nu^2)}$ — cylindrical rigidity of the plate, $N_x^* = \frac{E}{1-\nu^2} \int_{-h/2}^{h/2} (\varepsilon_x^* + \nu \varepsilon_y^*) dz$,

$$N_y^* = \frac{E}{1-\nu^2} \int_{-h/2}^{h/2} (\varepsilon_y^* + \nu \varepsilon_x^*) dz, S^* = \frac{E}{2(1+\nu)} \int_{-h/2}^{h/2} \gamma_{xy}^* dz,$$

$$M_x^* = \frac{E}{1-\nu^2} \int_{-h/2}^{h/2} (\varepsilon_x^* + \nu \varepsilon_y^*) z dz, M_y^* = \frac{E}{1-\nu^2} \int_{-h/2}^{h/2} (\varepsilon_y^* + \nu \varepsilon_x^*) z dz, H^* = \frac{E}{2(1+\nu)} \int_{-h/2}^{h/2} \gamma_{xy}^* z dz.$$

Values $N_x^*, N_y^*, S^*, M_x^*, M_y^*, H^*$ have the dimension of internal forces and determine the contribution of creep deformations to the redistribution of forces.

Static equations of the flexible plate theory have the form [19]:

$$\begin{aligned} \frac{\partial N_x}{\partial x} + \frac{\partial S}{\partial y} &= 0; \frac{\partial S}{\partial x} + \frac{\partial N_y}{\partial y} = 0; \\ \frac{\partial^2 M_x}{\partial x^2} + 2 \frac{\partial^2 H}{\partial x \partial y} + \frac{\partial^2 M_y}{\partial y^2} + N_x \frac{\partial^2 (w + w_0)}{\partial x^2} + N_y \frac{\partial^2 (w + w_0)}{\partial y^2} + 2S \frac{\partial^2 (w + w_0)}{\partial x \partial y} + q &= 0. \end{aligned} \quad (7)$$

Here, q — normal load on the surface of the plate, which is zero in this problem.

It is possible to satisfy the first two static equations using the Airy stress functions, introduced by the formulas:

$$N_x = \frac{\partial^2 \Phi}{\partial y^2}; N_y = \frac{\partial^2 \Phi}{\partial x^2}; S = -\frac{\partial^2 \Phi}{\partial x \partial y}. \quad (8)$$

After substituting the last three equalities from (6) into the last static equation in (7) and taking into account (8), we obtain the first resolving equation:

$$D \nabla^4 w = q + q^* + \frac{\partial^2 \Phi}{\partial x^2} \frac{\partial^2 (w + w_0)}{\partial y^2} + \frac{\partial^2 \Phi}{\partial y^2} \frac{\partial^2 (w + w_0)}{\partial x^2} - 2 \frac{\partial^2 \Phi}{\partial x \partial y} \frac{\partial^2 (w + w_0)}{\partial x \partial y}, \quad (9)$$

$$\text{where } q^* = - \left(\frac{\partial^2 M_x^*}{\partial x^2} + 2 \frac{\partial^2 H^*}{\partial x \partial y} + \frac{\partial^2 M_y^*}{\partial y^2} \right).$$

To obtain the second resolving equation, it is required to express the deformation of the median surface from (6):

$$\begin{aligned} \varepsilon_x^0 &= \frac{N_x - \nu N_y + N_x^* - \nu N_y^*}{Eh} = \frac{1}{Eh} \left(\frac{\partial^2 \Phi}{\partial y^2} - \nu \frac{\partial^2 \Phi}{\partial x^2} + N_x^* - \nu N_y^* \right); \\ \varepsilon_y^0 &= \frac{N_y - \nu N_x + N_y^* - \nu N_x^*}{Eh} = \frac{1}{Eh} \left(\frac{\partial^2 \Phi}{\partial x^2} - \nu \frac{\partial^2 \Phi}{\partial y^2} + N_y^* - \nu N_x^* \right); \\ \gamma^0 &= \frac{2(1+\nu)}{Eh} (S + S^*) = \frac{2(1+\nu)}{Eh} \left(-\frac{\partial^2 \Phi}{\partial x \partial y} + S^* \right). \end{aligned} \quad (10)$$

Substituting (10) into (2), we get:

$$\begin{aligned} \frac{1}{Eh} \nabla^4 \Phi &= \left(\frac{\partial^2 (w + w_0)}{\partial x \partial y} \right)^2 - \left(\frac{\partial^2 w_0}{\partial x \partial y} \right)^2 - \frac{\partial^2 (w + w_0)}{\partial x^2} \frac{\partial^2 (w + w_0)}{\partial y^2} + \frac{\partial^2 w_0}{\partial x^2} \frac{\partial^2 w_0}{\partial y^2} + \frac{1}{Eh} (2(1+\nu) \frac{\partial^2 S^*}{\partial x \partial y} + \\ &+ \nu \left(\frac{\partial^2 N_x^*}{\partial x^2} + \frac{\partial^2 N_y^*}{\partial y^2} \right) - \frac{\partial^2 N_x^*}{\partial y^2} - \frac{\partial^2 N_y^*}{\partial x^2}). \end{aligned} \quad (11)$$

Thus, for the problem under consideration, a system of resolving equations is obtained from two fourth-order differential equations (9) and (11). Equations (9) and (11) are nonlinear. In the resulting equations, values Φ and w are functions of the coordinates x, y , and time t . Explicitly, there is no time in these equations, the time dependence is laid down in creep deformations $\varepsilon_x^*, \varepsilon_y^*, \gamma_{xy}^*$, which are taken into account by the introduction of integral quantities $N_x^*, N_y^*, S^*, M_x^*, M_y^*, H^*$.

For the calculation scheme shown in Figure 1, the boundary conditions are written as:

$$\begin{aligned} \text{at } x = 0, x = a : N_x = \frac{\partial^2 \Phi}{\partial y^2} = -p; S = -\frac{\partial^2 \Phi}{\partial x \partial y} = 0; w = 0; M_x = 0; \\ \text{at } y = 0, y = b : N_y = \frac{\partial^2 \Phi}{\partial x^2} = 0; S = -\frac{\partial^2 \Phi}{\partial x \partial y} = 0; w = 0; M_y = 0. \end{aligned} \quad (12)$$

Equation (11) for small displacements, in the case of a plate made of elastic material, is a biharmonic equation that is used to solve the plane problem of the theory of elasticity in stresses. Frame analogy can serve as the boundary conditions for the stress function for the biharmonic equation. The plate contour is considered as a frame, and the stress function on the contour are equal to the bending moment M in it, and its derivative along the normal to the contour is the longitudinal force N . Plots M and N in the frame can be constructed in one of the basic systems of the force method (BSFM). The basic system, as well as the diagrams of the bending moment and longitudinal force in the frame are shown in Figure 2.

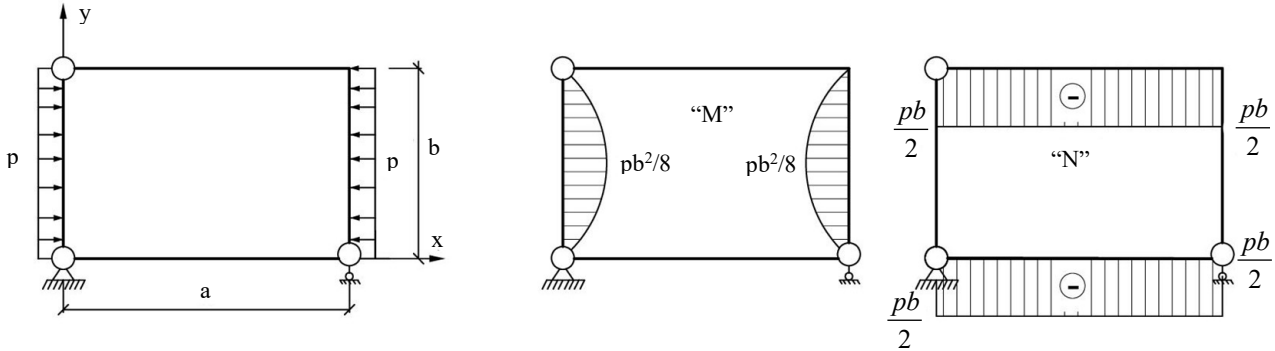


Fig. 2. BSFM and diagrams of the bending moment and longitudinal forces

If the vertical displacements do not exceed a quarter of the plate thickness, then it is possible to assume the forces in the middle surface independent of the coordinates x and y ($N_x = -p, N_y = S = 0$) and use the linearized equation for calculations:

$$D\nabla^4 w + p \frac{\partial^2 w}{\partial x^2} = q^* - p \frac{\partial^2 w_0}{\partial x^2}. \quad (13)$$

The analytical solution to the system of equations (9) and (11) is associated with great difficulties. The authors propose to solve this system numerically. The finite-difference method (FDM) was used in combination with the method of successive approximations. The Euler method was applied to determine creep deformation in the time domain. As the first stage, the solution for the elastic plate was performed. Load p was applied stepwise with small steps. At the initial load values, deflections w_1 were calculated by solving the simplified equation (13). Then, the calculated values w_1 were substituted into the differential equation (11). This provided determining the stress function. The next step was to solve the differential equation (9) using the known values of function Φ , which made it possible to determine the nodal values of deflections w'_1 . After that, the values $(11 w_2 = (w_1 + w'_1)/2)$ were substituted into equation (11). The iterative process was repeated at each step until the relative discrepancy with the norms of the vectors of the nodal values of deflections w_i and w'_i was greater than the specified value (the authors assumed it to be equal to 0.1 %). For the second load step, the initial value w_1 in each node was the final result obtained in the first step. The calculation technique in the time domain, taking into account creep, was similar. The time interval, at which the process was investigated, was divided into steps Δt . In the case of setting the law of viscoelastic deformation in differential form, the values of creep deformations at step $t + \Delta t$ were calculated on the basis of the known rate of their growth at time t using the Euler approximation:

$$\varepsilon_{t+\Delta t}^* = \varepsilon_t^* + \frac{\partial \varepsilon^*}{\partial t} \Delta t. \quad (14)$$

The block diagram of the creep calculation algorithm is shown in Figure 3.

Note that the system of equations (9) and (11) provides using schemes of a higher order of accuracy, e.g., the fourth-order Runge-Kutta method. At the same time, to achieve the same accuracy of the results, you can set noticeably large

time steps. However, with an increase in the step, there is a chance of not catching the effects of unsteady creep at the initial moments of time. And with the same time step, the Runge-Kutta method, in comparison to the Euler method, requires four times more operations to be performed.

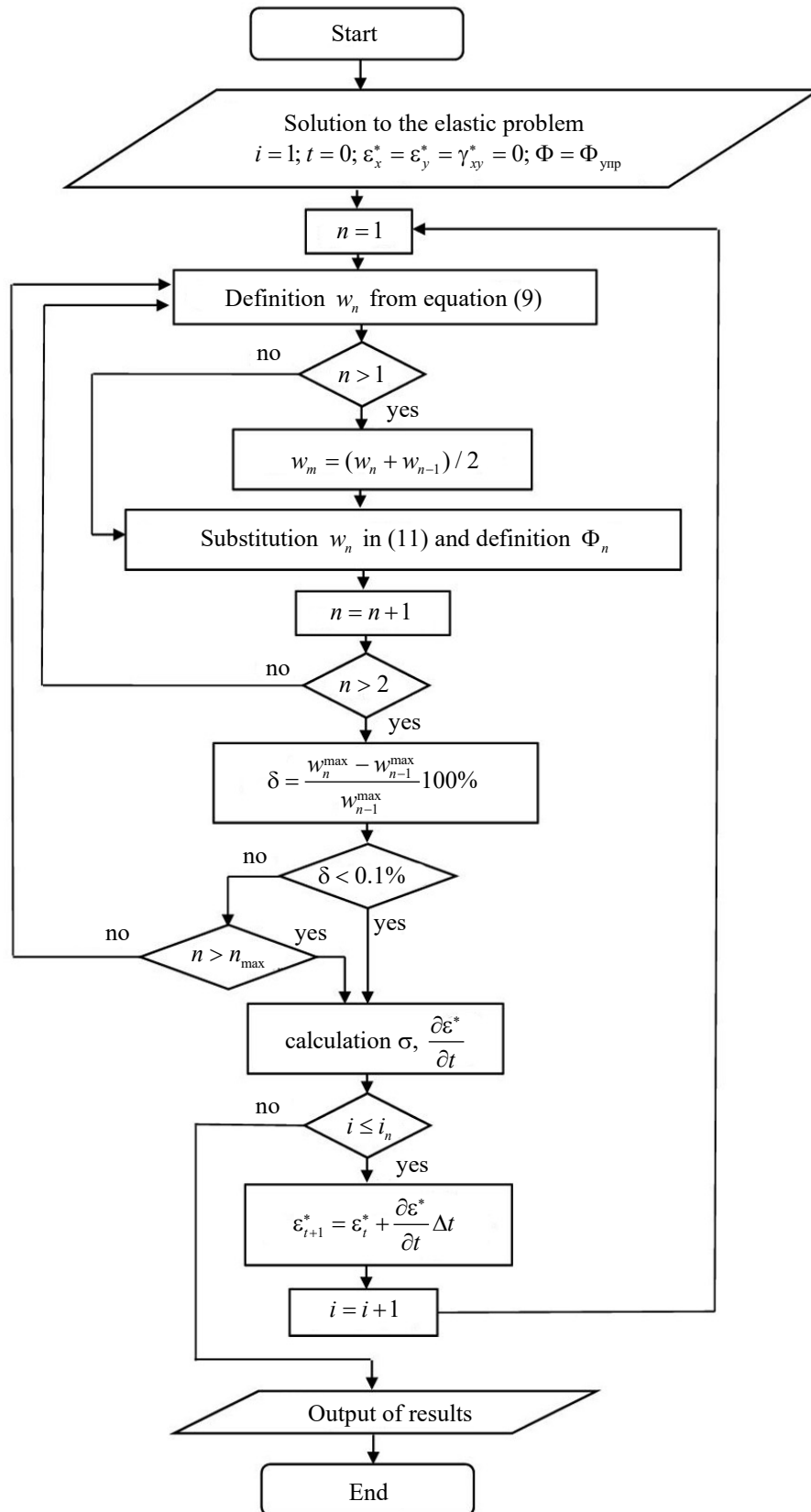


Fig. 3. Block diagram of the creep calculation algorithm

Research Results. A polyvinyl chloride polymer plate with dimensions $a = 2$ m, $b = 2$ m, $h = 1$ cm at $E = 1480$ MPa, $\nu = 0.3$ was considered. The nonlinear Maxwell-Gurevich equation was adopted as the law determining the rate of creep strain growth:

$$\begin{aligned} \frac{\partial \varepsilon_{ij}^*}{\partial t} &= \frac{f_{ij}^*}{\eta^*}, \quad i = x, y, \quad j = x, y; \\ f_{ij}^* &= \frac{3}{2} (\sigma_{ij} - \sigma_0 \delta_{ij}) - E_\infty \varepsilon_{ij}^*; \\ \eta^* &= \eta_0^* \exp \left(-\frac{|f_{max}^*|}{m^*} \right); \quad f_{max}^* = \left| \frac{3}{2} (\sigma_{rr} - \sigma_0) - E_\infty \varepsilon_{rr}^* \right|_{max}, \end{aligned} \quad (15)$$

where δ_{ij} — Kronecker symbol; $\sigma_0 = J_1 / 3$, $J_1 = \sigma_x + \sigma_y$ — first invariant of the stress tensor; η_0^* , E_∞ and m^* — rheological parameters of the material, called the initial relaxation viscosity, the modulus of high elasticity, and the modulus of velocity.

Indices rr in formula (15) indicate the direction of the primary stresses.

For PVC, the authors took the values of rheological parameters from [20]: $E_\infty = 5.99 \cdot 10^3$ MPa, $m^* = 12.6$ MPa, $\eta_0^* = 5.44 \cdot 10^7$ MPa·s. The shape of the initial deflection $w_0(x, y)$ was taken in accordance with the first form of the loss of stability of the plate made of elastic material:

$$w_0(x, y) = f_0 \sin \frac{\pi x}{a} \sin \frac{\pi y}{b}. \quad (16)$$

For a plate made of elastic material without initial imperfections, the critical load, in the case of the whole ratio of sides a/b , was determined from the formula [19]:

$$p_{kp} = \frac{4\pi^2 D}{b^2}. \quad (17)$$

To verify the developed calculation algorithm, the first step was to solve the elastic test problem and compare the results to the calculation in the finite element LIRA-CAD package (Fig. 4). The value of the arrow of the initial deflection f_0 was set to 0.15 mm. The grid size when using the FDM was 20×20 , the number of load steps was 200. When calculating in the LIRA-CAD PC, the plate was divided by triangular finite elements with a triangulation step of 0.1 m. The load step size was assumed to be the same as when using the FDM. The value of the critical load for the elastic plate, calculated from formula (17), was 1340 N/m. Table 1 shows a comparison of vertical displacements in the center of the plate for different load values obtained by the author's method and using the finite element method (FEM). The deflections calculated using two alternative methods are quite close, except for the load of 1330 N/m. The deviation at this load value can be explained by the fact that when approaching the critical load, the movements rush to infinity.

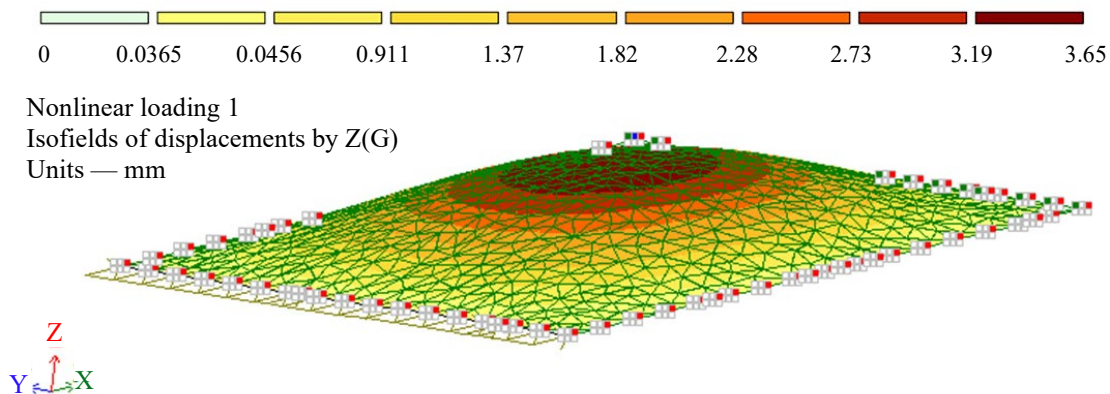


Fig. 4. Isofield of vertical displacements in LIRA-CAD PC ($p = 1330$ N/m)

Table 1

Comparison of calculation results using the author's method and with the help of FEM

$p, \text{ N/m}$	$w \cdot 10^3, \text{ mm}$	
	LIRA-CAD	the authors' method
133	16	16
266	37	37
399	63	63
532	98	99
665	146	148
798	218	221
931	336	342
1,064	562	578
1,197	1,163	1229
1,330	3,646	4,229

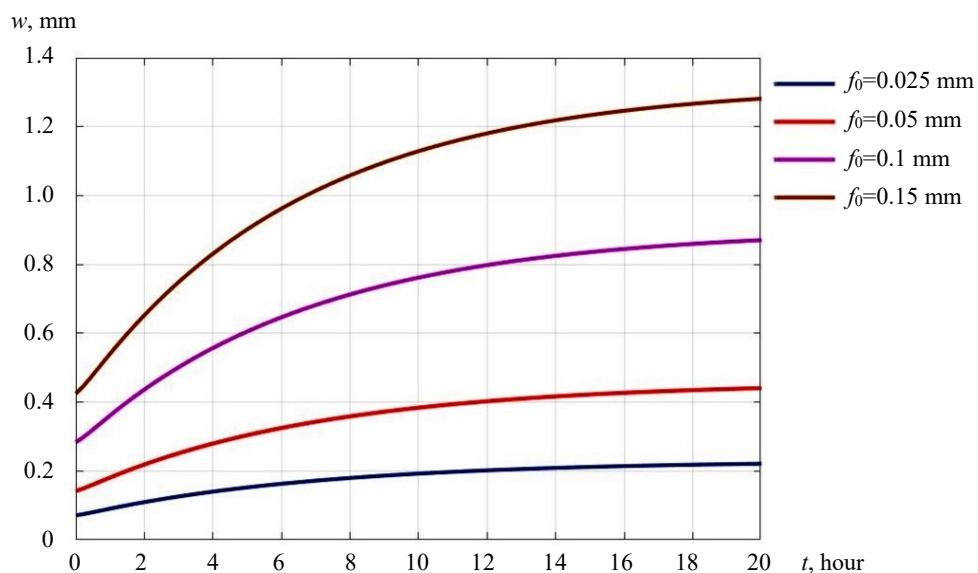
In [21], the possibility of transition from the solution of the elastic problem of calculating plates to the solution at the end of the creep process is shown. The value of the long-term critical load p_∞ can be obtained by replacing the cylindrical stiffness D of the elastic plate with the long-term cylindrical stiffness D_∞ , which is determined from the formula:

$$D_\infty = \frac{\alpha h^3}{12(\alpha^2 - \beta^2)}, \quad (18)$$

where $\alpha = \frac{1}{E} + \frac{1}{E_\infty}$; $\beta = \frac{\nu}{E} + \frac{1}{2E_\infty}$.

For viscoelastic rods and round plates, it has been previously established that in case $p < p_\infty$, the growth of displacements in time slows down, and the deflection arrow comes to a finite value. If $p = p_\infty$, deflections grow at a constant rate. At $p > p_\infty$, the rate of deflection growth increases.

The authors also analyzed the nature of the growth of deflections over time for $p < p_\infty$, $p = p_\infty$ and $p > p_\infty$ for different values of the maximum initial loss f_0 . The deflection curves over time in the center of the plate at $p = 0.9 p_\infty$, $p = p_\infty$ and $p = 1.1 p_\infty$ are shown respectively in Figures 5–7.

Fig. 5. Deflection curves over time in the center of the plate at $p = 0.9 p_\infty$

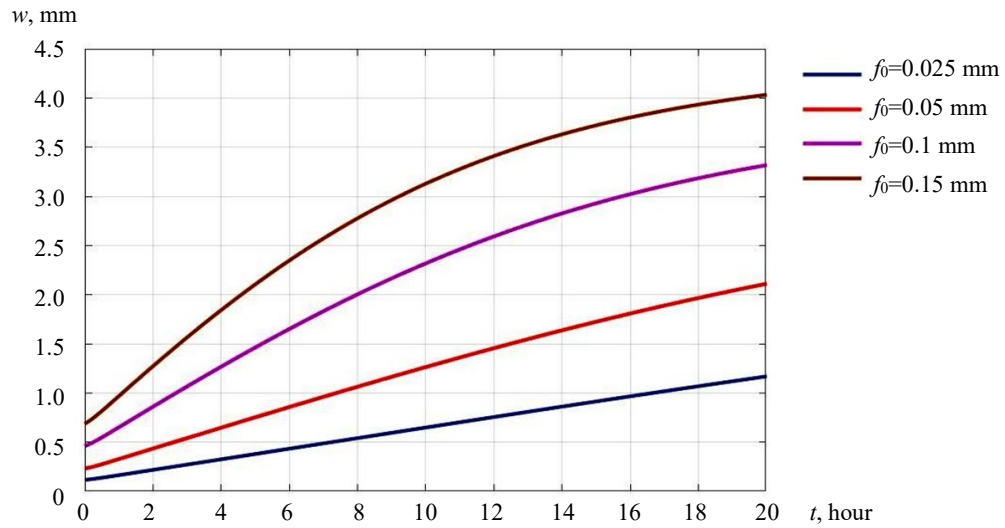


Fig. 6. Deflection curves over time in the center of the plate at $p = p_{\infty}$

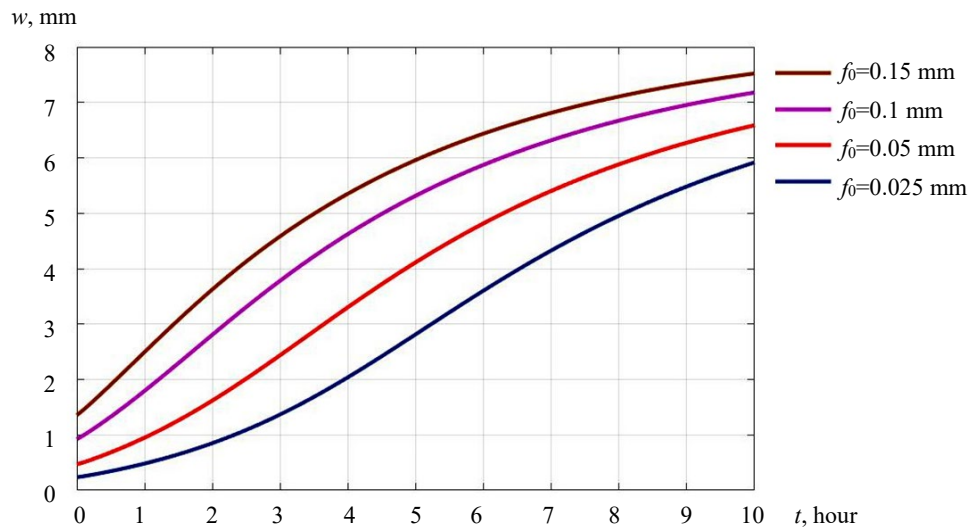


Fig. 7. Deflection curves over time in the center of the plate at $p = 1.1 p_{\infty}$

Discussion and Conclusion. It can be seen from Fig. 5 that at $p < p_{\infty}$, the deflection arrow always comes to the final value, regardless of the values of the initial imperfections. At the same time, at $p \geq p_{\infty}$, the pattern of deflection growth obtained in [21] occurs only with small displacements. When deflections reach values exceeding about a quarter of the plate thickness, the rate of deformation growth begins to decrease even in the case of loads exceeding the long-term critical one. It should also be noted that there is a complete absence of a section with an increasing rate of displacement growth for plates with large initial curvatures. The identified effects can be explained by the redistribution of efforts N_x , N_y , S in the middle surface.

Summarizing the above, we can conclude that the vertical movements of the plate pivotally supported along the contour, under the action of a compressive load on one axis, always come to a final value if the load does not exceed the instantaneous critical one. In other words, with the considered fastening and loading, the plate is in stable equilibrium under creep conditions.

The obtained equations and the calculation algorithm make it possible to calculate plates made of arbitrary viscoelastic materials for any fastening options. The law of the relationship between stresses and creep deformations can also be set arbitrarily.

References

1. Yankovskii AP. Refined Deformation Model for Metal-Composite Plates of Regular Layered Structure in Bending under Conditions of Steady-State Creep. *Mechanics of Composite Materials*. 2017;52(6):715–732. <https://doi.org/10.1007/s11029-017-9622-7>
2. Yankovskii AP. The Steady Creeping Difficulty Reinforced the Metal-Composite Plates Loaded in the Plane. *Mathematical Models and Computer Simulations*. 2010;22(8):55–66. URL: https://www.mathnet.ru/php/archive.phtml?wshow=paper&jrnid=mm&paperid=3007&option_lang=rus (accessed: 18.05.2023).
3. Khoroshun LP, Babich DV. Ustoichivost' pryamougol'nykh plastin iz sloistogo kompozitnogo materiala pri dlitel'noi povrezhdaemosti komponentov. *Prikladnaya mekhanika*. 2010;46(12):67–75. (In Russ.)
4. Zhongyu Lu, Guijun Xian, Khuram Rashid. Creep Behavior of Resin Matrix and Basalt Fiber Reinforced Polymer (BFRP) Plate at Elevated Temperatures. *Journal of Composites Science*. 2017;1(1):3. <https://doi.org/10.3390/jcs1010003>
5. Pawlus D. Stability of Three-Layered Annular Plate with Composite Facings. *Applied Composite Materials*. 2017;24(1):141–158. <https://doi.org/10.1007/s10443-016-9518-z>
6. Rouzegar J, Gholami M. Creep and Recovery of Viscoelastic Laminated Composite Plates. *Composite Structures*. 2017;181:256–272. <https://doi.org/10.1016/j.compstruct.2017.08.094>
7. Gräfe M, Dietsch P, Winter S. CLT under In-Plane Loads: Investigation on Stress Distribution and Creep. In: *Proc. INTER International Network on Timber Engineering Research*. Karlsruhe: Timber Scientific Publishing; 2018. P. 289–306. URL: <https://mediatum.ub.tum.de/doc/1533836/document.pdf> (accessed: 18.05.2023).
8. Pawlus D. Dynamic Behaviour of Three-Layered Annular Plates with Viscoelastic Core under Lateral Loads. *Journal of Theoretical and Applied Mechanics*. 2015;53(4):775–788. <https://doi.org/10.15632/jtam-pl.53.4.775>
9. Sharma K. Elastoplastic Stability and Failure Analysis of FGM Plate with Temperature Dependent Material Properties under Thermomechanical Loading. *Latin American Journal of Solids and Structures*. 2017;14(7):1361–1386. <https://doi.org/10.1590/1679-78253747>
10. Kumar RR, Mukhopadhyay T, Pandey KM, Dey S. Stochastic Buckling Analysis of Sandwich Plates: The Importance of Higher Order Modes. *International Journal of Mechanical Sciences*. 2019;152:630–643. <https://doi.org/10.1016/j.ijmecsci.2018.12.016>
11. Kosheleva E. Dynamic Stability of a Viscoelastic Plate. *MATEC Web of Conferences*. 2017;117:00086. <https://doi.org/10.1051/mateconf/201711700086>
12. Abramovich H. *Stability and Vibrations of Thin-Walled Composite Structures*. Cambridge: Woodhead Publishing; 2017. 770 p.
13. Kirsanov MN. Buckling of a Plate of Nonlinear Rheological Material with Variable Loading. *Bulletin of the Tatar State Humanitarian and Pedagogical University*. 2011;24:19–22. URL: <https://cyberleninka.ru/article/n/vypuchivanie-plastiny-iz-nelineynogo-reologicheskogo-materiala-pri-peremennom-nagruzhenii> (accessed: 18.05.2023).
14. Abdikarimov RA, Zhgutov VM. Geometrically Nonlinear Mathematical Simulation the Viscoelastic Gently Sloping Variable-Thickness Shells' Dynamic Steadiness. *Magazine of Civil Engineering*. 2011;(6):12–22. <https://cyberleninka.ru/article/n/geometricheski-nelineynoe-matematicheskoe-modelirovanie-dinamicheskoy-ustoychivosti-vyazkouprugih-pologih-obolochek-peremennoy/viewer> (accessed: 18.05.2023).
15. Abdikarimov RA, Khudayarov BA. Dinamicheskaya ustoichivost' vyazkouprugikh gibkikh plastin peremennoi zhestkosti pri osevom szhatii. *Prikladnaya mekhanika*. 2014;50(4): 41–51. (In Russ.)

16. Abdikarimov RA, Verlan AF, Goroshko IO. Chislennoe issledovanie dinamicheskoi ustoichivosti vyazkouprugikh ortotropnykh pryamougol'nykh plastin s peremennoi zhestkost'yu. *Моделювання та інформаційні технології*. 2011;60:10–17. (In Russ.)
17. Robinson MTA, Adali S. Nonconservative Stability of Viscoelastic Plates Subject to Triangularly Distributed Follower Loads. *Journal of Theoretical and Applied Mechanics*. 2017;55(3):1015–1027. <https://doi.org/10.15632/jtam-pl.55.3.1015>
18. Jafari N, Azhari M. Stability Analysis of Arbitrarily Shaped Moderately Thick Viscoelastic Plates Using Laplace–Carson Transformation and a Simple HP Cloud Method. *Mechanics of Time-Dependent Materials*. 2017;21(3):365–381. <https://doi.org/10.1007/s11043-016-9334-8>
19. Chepurnenko AS, Yazyev BM, Savchenko AA. Calculation for the Circular Plate on Creep Considering Geometric Nonlinearity. *Procedia Engineering*. 2016;150:1680–1685. <https://doi.org/10.1016/j.proeng.2016.07.150>
20. Chepurnenko AS, Andreev VI, Beskopylny AN, Yazyev BM. Determination of Rheological Parameters of Polyvinylchloride at Different Temperatures. *MATEC Web of Conferences*. 2016;67:06059. <https://doi.org/10.1051/mateconf/20166706059>
21. Andreev VI, Yazyev BM, Chepurnenko AS. Axisymmetric Bending of a Round Elastic Plate in Case of Creep. *Vestnik MGSU*. 2014;(5):16–24. URL: <https://cyberleninka.ru/article/n/osimmetrichnyy-izgib-krugloy-gibkoy-plastinki-pri-polzuchesti> (accessed: 18.05.2023).

Received 29.06.2023

Revised 27.07.2023

Accepted 01.08.2023

About the Authors:

Serdar B. Yazyev, Dr.Sci. (Eng.), Associate Professor, Associate Professor of the Structural Mechanics and Theory of Structures Department, Don State Technical University (1, Gagarin sq., Rostov-on-Don, 344003, RF), [ScopusID](#), [AuthorID](#), [ORCID](#), russiangel@mail.ru

Anton S. Chepurnenko, Dr.Sci. (Eng.), Associate Professor, Professor of the Structural Mechanics and Theory of Structures Department, Don State Technical University (1, Gagarin sq., Rostov-on-Don, 344003, RF), [ResearcherID](#), [ScopusID](#), [AuthorID](#), [ORCID](#), anton_chepurnenk@mail.ru

Claimed contributorship:

SB Yazyev: basic concept formulation, research objective and tasks, calculation analysis, text preparation, formulation of conclusions.

AS Chepurnenko: analysis of the research results, revision of the text, correction of conclusions.

Conflict of interest statement: the authors do not have any conflict of interest.

All authors have read and approved the final manuscript.

Поступила в редакцию 29.06.2023

Поступила после рецензирования 27.07.2023

Принята к публикации 01.08.2023

Об авторах:

Сердар Батырович Языев, доктор технических наук, доцент, доцент кафедры строительной механики и теории сооружений Донского государственного технического университета (344003, РФ, г. Ростов-на-Дону, пл. Гагарина, 1), [ScopusID](#), [AuthorID](#), [ORCID](#), russiangel@mail.ru

Антон Сергеевич Чепурненко, доктор технических наук, доцент, профессор кафедры строительной механики и теории сооружений Донского государственного технического университета (344003, РФ, г. Ростов-на-Дону, пл. Гагарина, 1), [ResearcherID](#), [ScopusID](#), [AuthorID](#), [ORCID](#), anton_chepurnenk@mail.ru

Заявленный вклад соавторов:

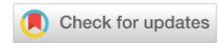
С.Б. Языев — формирование основной концепции, цели и задачи исследования, проведение расчетов, подготовка текста, формирование выводов.

А.С. Чепурненко — анализ результатов исследований, доработка текста, корректировка выводов.

Конфликт интересов: авторы заявляют об отсутствии конфликта интересов.

Все авторы прочитали и одобрили окончательный вариант рукописи.

MACHINE BUILDING AND MACHINE SCIENCE



UDC 621.817

Original article

<https://doi.org/10.23947/2687-1653-2023-23-3-269-282>

Optimization of Geometric Characteristics of Cycloidal Profiles of Gerotor Hydraulic Machines

 Sergey O. Kireev  , Alexey R. Lebedev , Marina V. Korchagina 

Don State Technical University, Rostov-on-Don, Russian Federation

✉ kireevso@yandex.ru

Abstract

Introduction. The performance and reliability of gerotor hydraulic machines depend on the geometry of the cycloidal gearing profile. The existing methods of calculating and optimizing the profile parameters are cumbersome, multi-criteria and difficult for practical application. Therefore, the problem of creating the methodology for calculating the parameters of the gerotor machine profile suitable for engineering calculations at the stage of conceptual design is a challenge. In this regard, the objective of this work was to modernize the methodology for designing the geometry of the profiles of the end section of hypocycloidal gears used in gerotor hydraulic machines, and to analyze the possibilities of their optimization during preliminary design. In the course of the study, the Mathcad computer mathematics system was used; numerical experiments were carried out to study the influence of geometric profile parameters on the performance and operability of the gerotor hydraulic machine, based on the data obtained and analyzed; recommendations for the design of optimal profiles of the end section of gerotor hydraulic machines were developed.

Materials and Methods. Materials included known methods of profile parameters calculation, based on application of classical formulas of hypocycloidal equidistant used for outlining profiles of teeth of working elements of gerotor machines. The basic research method was modeling the gerotor machine profile using Mathcad computer mathematics system. Calculated data were obtained for the selected ranges of varying parameters, processed through the univariate regression analysis.

Results. An algorithm for analyzing the tooth profile smoothness was developed. Two target parameters were defined: the cross-sectional area of the end profile, which affects the productivity; the smallest reduced radius of contact that determines operability of the working body. A technique for calculating the target parameters at the early stage of design was proposed. A number of optimal values of profile parameters according to the criteria of productivity and operability of gerotor machine was obtained. The dependences providing the optimum values of profile parameters at the stage of designing were constructed.

Discussion and Conclusion. The developed methodology makes it possible to obtain an assessment of the performance and operability of the gerotor hydraulic machine at the design stage of the working body. The research results can be used in mechanical engineering when designing gerotor hydraulic machines in order to improve their technical and operational characteristics.

Keywords: hydraulic machine, gerotor gearing, hypocycloid, rotor, stator, contact, open area

Acknowledgements: the authors would like to thank all the parties to the agreement for their assistance in conducting bench tests.

Funding information. The research was carried out within the framework of the state-funded R&D AAAA20-120012190068-8 “Study. modeling and development of innovative designs of machinery and equipment of oil and gas fields”.

For citation. Kireev SO, Lebedev AR, Korchagina MV. Optimization of Geometric Characteristics of Cycloidal Profiles of Gerotor Hydraulic Machines. *Advanced Engineering Research (Rostov-on-Don)*. 2023;23(3):269–282. <https://doi.org/10.23947/2687-1653-2023-23-3-269-282>

Оптимизация геометрических характеристик циклоидальных профилей героторных гидромашин

С.О. Киреев  , А.Р. Лебедев , М.В. Корчагина 

Донской государственный технический университет, г. Ростов-на-Дону, Российская Федерация

 kireevso@yandex.ru

Аннотация

Введение. Производительность и надежность работы героторных гидромашин зависит от геометрических параметров профиля циклоидального зацепления. Существующие методики расчета и оптимизации параметров профиля громоздкие, многокритериальные, сложные для практического применения. Поэтому актуальной представляется проблема создания методики расчета параметров профиля рабочего органа героторной машины, пригодной для инженерных расчетов на этапе эскизного проектирования. В связи с этим целью данной работы является модернизация методики проектирования геометрии профилей торцевого сечения гипоциклоидальных зубчатых зацеплений, используемых в героторных гидравлических машинах, и анализ возможностей их оптимизации при предварительном проектировании. В ходе исследования была использована система компьютерной математики Mathcad, проведены численные эксперименты для изучения влияния геометрических параметров профилей на производительность и работоспособность героторной гидравлической машины. На основе полученных и проанализированных данных выработаны рекомендации по проектированию оптимальных профилей торцевого сечения героторных гидравлических машин.

Материалы и методы. Материалы включают в себя известные методики расчета параметров профиля, основанные на применении классических формул эквидистант гипоциклоид, используемых для очерчивания профилей зубьев рабочих органов героторных машин. Основным методом исследования — моделирование профиля героторной машины с помощью системы компьютерной математики Mathcad. Получены расчетные данные для выбранных диапазонов варьируемых параметров, обработанные методом регрессионного однофакторного анализа.

Результаты исследования. Разработан алгоритм анализа гладкости профилей зубьев. Определены два целевых параметра: площадь сечения торцевого профиля, влияющая на производительность, и наименьший приведенный радиус контакта, определяющий работоспособность рабочего органа. Предложена методика по расчету целевых параметров на ранней стадии проектирования. Получен ряд оптимальных значений параметров профиля по критериям производительности и работоспособности героторной машины. Построены зависимости, позволяющие установить оптимальные значения параметров профиля на стадии проектирования.

Обсуждение и заключение. Разработанная авторами методика дает возможность на этапе проектирования рабочего органа получить оценку производительности и работоспособности героторной гидромашин. Результаты исследований могут быть использованы в машиностроении при проектировании героторных гидромашин для улучшения их технико-эксплуатационных характеристик.

Ключевые слова: гидравлическая машина, героторное зацепление, гипоциклоида, ротор, статор, контакт, площадь живого сечения

Благодарности: авторы выражают благодарность всем участникам договора за помощь в проведении стендовых испытаний.

Финансирование. Работа выполнена в рамках госбюджетной НИОКР АААА–А20–120012190068–8 «Исследование, моделирование и разработка инновационных конструкций машин и оборудования нефтегазовых промыслов».

Для цитирования. Киреев С.О., Лебедев А.Р., Корчагина М.В. Оптимизация геометрических характеристик циклоидальных профилей героторных гидромашин. *Advanced Engineering Research (Rostov-on-Don)*. 2023;23(3):269–282. <https://doi.org/10.23947/2687-1653-2023-23-3-269-282>

Introduction. Gerotor hydraulic machines are increasingly being used in the construction and operation of oil and gas wells. The reason is their structural and operational advantages, the primary of which are low delivery unevenness for pumps or torque for motors, compact overall dimensions.

In the scientific literature, a large place is occupied by studies devoted to the operation of gerotor hydraulic machines. The strong geometric effects of the rotor profile on the performance and reliability of screw gerotor hydraulic

machines were noted by D. and F. Baldenko [1]. The basic unit of such a machine is a multithread screw gerotor mechanism — a cylindrical planetary gear train of internal gearing, consisting of a stator and a rotor, with a difference in the number of teeth equal to one. The stator profile in the end section contacts the rotor profile, forming closed platforms. The authors also analyzed the technology of manufacturing gears.

R. Iyer, V. Jatti and others investigated the feasibility of mathematical models in the design of screw pumps [2]. They also presented the results of modeling various sizes of twin-screw pumps when pumping water, a mixture of water and air. Hong-Seok Park and Xuan-Phuong Dang proposed a CAD model optimization process using the results of CAE modeling and Mathcad calculations [3]. Other authors (A. Lebedev, S. Kireev, M. Korchagina, S. Vlaskin, A. Efimov) noted in their publications the effectiveness of designing various objects and processes based on parametrization and subsequent optimization of the design according to one or more target parameters [4–6].

In their work, F.D. Baldenko and Yang Yao have emphasized that the open area does not depend on the relative position of the rotor and stator profiles and determines the pump performance. They analyzed the effect of dimensionless geometric profile parameters on the open area [7].

Jie Chen, He Liu, Fengshan Wang, Guocheng Shi, Gang Cao and Hengan Wu developed a finite element model of the working body of a screw pump with a surface drive for the oil and gas industry [8]. Based on the results of modeling and experimental tests, they concluded that the gaps in the coupling and the thickness of the stator were the two key factors affecting the optimized target parameter — the volumetric efficiency of the pump.

New data were obtained by J. Gamboa, A. Olivet and S.H. Espin when modeling the working body of a multilobe screw pump [9]. These authors determined a significant relationship between the sliding clearance area and the pressure drop associated with the mechanical properties of the stator material.

Yang Yao and F. Baldenko investigated the effect of dimensionless coefficients of the end profile of a gerotor hydraulic machine on the characteristics of cycloid engagement, which provided optimization based on geometric and kinematic criteria [10]. I.A. Lyagov, F.D. Baldenk, A.V. Lyagov, V.U. Yamaliev and A.A. Lyagova proposed a methodology for selecting the optimal configuration of power sections when designing sectional downhole motors, noting the urgency of the problem of reducing the overall parameters of the screw pump length [11].

Yu.A. Korotaev, A.N. Alpatov, A.V. Sobolev and others have come to the conclusion that the most effective is mesh profiling from the initial contour of the rail outlined by the equidistant shortened cycloid [12]. With regard to the profiles obtained from the equidistant of an ordinary hypocycloid, the authors pointed out their major drawback: they were built as special and did not provide for tension in the engagement. Yu.A. Korotaev and D.A. Goldobin drew attention to the problem associated with the need to increase the performance of screw pumps, and the resulting unacceptable rigidity conditions under the production of stators and rotors [13].

A.F. Minikaev, V.A. Pronin, D.V. Zhignovskaya, Yu.L. Kuznetsov, F.D. Baldenko, A.E. Kovalenok developed a methodology for studying the stress-strain state of the stator during contact interaction with the rotor of a screw working body of a hydraulic machine using CAE modeling. They have stated that the classical Hertz theory of contact interaction cannot be applied to determine contact stresses in the rotor and stator due to a number of features: change in the curvature of the contacting surfaces of the rotor and stator; different thickness of the elastic lining along the circumference of the housing; presence of preload in a pair; complex planetary motion of the rotor, accompanied by a combination of friction rolling and sliding; displacement of the radial force vector relative to the normal at the point of contact.

Summing up the review of scientific publications on the design of a gerotor hydraulic machine, it should be noted that most researchers in this field strive to improve the efficiency of this machine by increasing the open area and reducing the overall dimensions of the working body. Optimal results were achieved by applying and varying the coefficients of off-centroidness, tooth shape, relative sliding speed, rail displacement, etc. Calculation methods were cumbersome, they were difficult to apply in practice. End profiles were built, as a rule, on the basis of shortened hypocycloids, which caused problems with providing kinematic accuracy of movement, contact interaction of the rotor and stator. Some authors (Yu.A. Korotaev, A.N. Alpatov, A.V. Sobolev, et al.) pointed out the impossibility of creating tension in the case of using an ordinary hypocycloid, but tension could be created through changing the equidistant distance of the rotor and stator profiles.

Materials and Methods. To obtain profiles of the rotor and stator in the end section of the working body of the gerotor hydraulic machine, we specify the following set of initial parameters (Fig. 1):

- 1) R_k — profile contour radius, which determines the diameter of circle C_1 , describing the profile of the stator (mm).

In fact, this parameter assigns the radial dimension of the gerotor machine, which is particularly important in the oil and gas industry when the projected object needs to be placed, e.g., in the trunk of the production well column;

- 2) z_1 — number of rotor teeth;

- 3) R_r — radius of the roller, which determines the distance of the equidistant line of the rotor and stator profiles relative to the corresponding hypocycloids (mm);
 4) Δ — tension in the coupling of the rotor and stator (mm).

Recall the principle of formation of hypocycloidal engagement profiles, which consists in the fact that inside circle C_2 (base circle of the stator hypocycloid), circle C_3 (base circle of the rotor hypocycloid) rolls without sliding. The center of circle C_3 is always at distance e (eccentricity) from the center of circle C_2 .

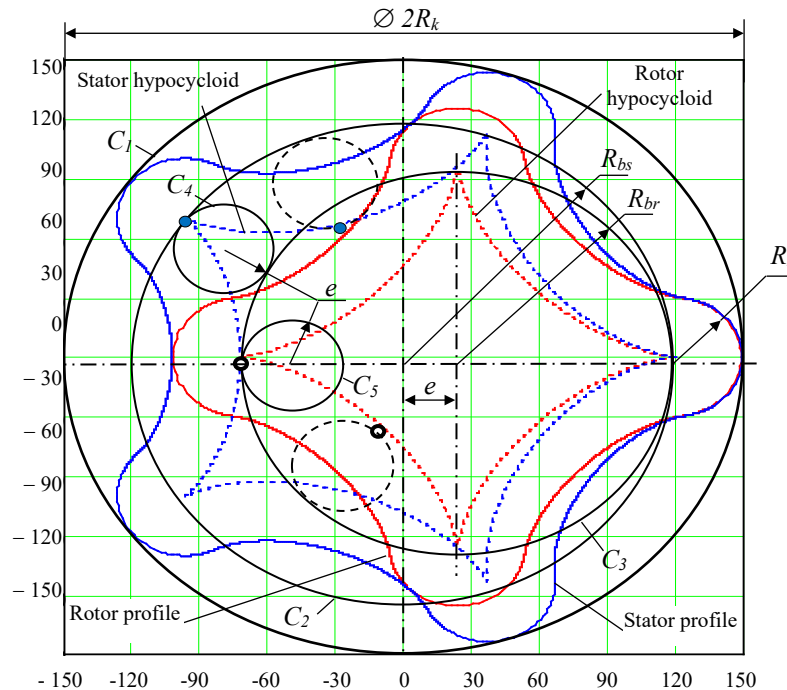


Fig. 1. Diagram of formation of the hypocycloidal profile of the end section of the working body of the gerotor machine,
 $z_1 = 4$, $R_k = 150$ mm, $R_r = 30$ mm

Inside circle C_3 , circle C_5 (generating circle of the rotor hypocycloid), one point of which forms the rotor hypocycloid, rolls without sliding. Inside circle C_2 , circle C_4 (generating circle of the stator hypocycloid), one point of which forms the stator hypocycloid, rolls without sliding. Note that the radii of circles C_5 and C_4 are equal to eccentricity e . The rotor and stator profiles are formed as equidistant lines deposited at distance R_r from the corresponding hypocycloids.

In this setting, the rotor and stator profiles provide an ideal contact under eccentric rotation of the rotor. When required to provide tension/clearance in the engagement, the equidistant distance R_r for the rotor profile should be changed by Δ .

Let us move on to the mathematical description of the method of forming the profiles of the end section of the rotor and stator. The number of stator teeth is equal to

$$z_2 = z_1 + 1. \quad (1)$$

The radius of the base circle of the stator hypocycloid R_{bs} is determined from the condition (Fig. 1):

$$R_{bs} = R_k - R_r. \quad (2)$$

We determine eccentricity e of the transmission from the condition that the length of circle C_2 is equal to integer z_2 of the lengths of generating circle C_4 with radius e :

$$2pR_{bs} = 2pez_2,$$

then,

$$e = R_{bs} / z_2. \quad (3)$$

Note that for $z_1 = 1$ (Moineau mechanism) according to other formulas:

$$e = R_k / 3uR_r = 2e, \text{ if } z_1 = 1. \quad (4)$$

The radius of the base circle of the rotor hypocycloid R_{br} is equal to (Fig. 1):

$$R_{br} = R_{bs} - e. \quad (5)$$

We introduce a function to determine the radius of the base circle of the rotor or stator, fulfilling conditions (2) and (5):

$$R(z) = R_k - R_r - e \cdot (z_2 - z). \quad (6)$$

Parametric formulas of the hypocycloid of the rotor and stator in the Cartesian coordinate system XOY:

$$\begin{aligned} x(\varphi, z) &= R(z) \cdot \left[(1 - 1/z) \cos(\varphi/z) + (a/z) \cos((1 - 1/z)\varphi) \right] \\ y(\varphi, z) &= R(z) \cdot \left[(1 - 1/z) \sin(\varphi/z) - (a/z) \sin((1 - 1/z)\varphi) \right] \end{aligned} \quad (7)$$

where z — number of branches of the hypocycloid of rotor z_1 or stator z_2 , a — velocity factor of the hypocycloid. In the case of an ordinary hypocycloid in theory, $a = 1$. However, in practical calculations using computer mathematics systems (Mathcad. MATLAB) at $a = 1$, difficulties arise with calculating equidistant profiles of the rotor and stator. Therefore, in the model, we assume $a = 0.99$, which is quite justified to achieve our goals; φ — rotation angle of the radius vector drawn from the origin to each point of the hypocycloid. If the hypocycloid must be constructed from N_p points, then

$$\varphi(i, z) = 2 \cdot \pi \cdot i \cdot z / N_p, \quad i = 0 \dots N_p. \quad (8)$$

The profiles of the rotor and stator are determined from the well-known equidistant trajectory formulas relative to the hypocycloids of the rotor or stator at distance R_r taking into account the tension in the coupling Δ .

$$\begin{aligned} X_p(\varphi, z, \Delta) &= x(\varphi, z) + (R_r + \Delta) \cdot \frac{\partial y(\varphi, z)}{\partial \varphi} / \sqrt{\left(\frac{\partial y(\varphi, z)}{\partial \varphi} \right)^2 + \left(\frac{\partial x(\varphi, z)}{\partial \varphi} \right)^2} \\ Y_p(\varphi, z, \Delta) &= y(\varphi, z) - (R_r + \Delta) \cdot \frac{\partial x(\varphi, z)}{\partial \varphi} / \sqrt{\left(\frac{\partial y(\varphi, z)}{\partial \varphi} \right)^2 + \left(\frac{\partial x(\varphi, z)}{\partial \varphi} \right)^2} \end{aligned} \quad (9)$$

During transmission operation, the center of the rotor moves along a circle with radius e and rotates by angle $\alpha = 0 \dots 2\pi$. At the same time, all points of the rotor make an additional rotation by angle ψ , determined by the function

$$\psi(\alpha) = \alpha \cdot (1 - z_2 / z_1). \quad (10)$$

The rotor rotation model is described by parametric coordinate transformation functions when moving and rotating an object:

$$\begin{aligned} X_v(\alpha, \varphi, \Delta) &= e \cdot \cos(\alpha) + X_p(\varphi, z_1, \Delta) \cos(\psi(\alpha)) - Y_p(\varphi, z_1, \Delta) \sin(\psi(\alpha)) \\ Y_v(\alpha, \varphi, \Delta) &= e \cdot \sin(\alpha) \cdot \text{if}(z_1 = 1, 0, 1) + X_p(\varphi, z_1, \Delta) \sin(\psi(\alpha)) + Y_p(\varphi, z_1, \Delta) \cos(\psi(\alpha)) \end{aligned} \quad (11)$$

In expression (11), a conditional function is applied that zeroes the movement along Y axis in the case of rectilinear movement of the rotor in the stator cavity at $z_1 = 1$.

The experience of using this technique has shown that the equidistant profiles of the rotor and stator with an increase in the equidistant distance or radius of the roller R_r can lose smoothness. This occurs at the points of transition from the equidistant circle to the equidistant hypocycloid. Figure 2 shows the problem of loss of smoothness of the stator profile line in the vicinity of ± 1 mm from the transition point of equidistant lines.

In mathematics, the formula for the function smoothness criterion given in parametric form is known. For the stator profile, such a function has the form

$$F_s(p, z) = \frac{\partial Y_p(p, z, 0)}{\partial p} / \frac{\partial X_p(p, z, 0)}{\partial p}, \quad (12)$$

where $z = z_2$;

p — angle of the radius vector of the stator profile point.

It should be noted that function F_s behaves unstable in the entire range $\varphi(i, z_2)$, and it is quite difficult to find any features of its behavior at the transition point of equidistant lines of interest to us. Therefore, the behavior of function F_s was studied only in the vicinity of the transition point when the angular parameter changes

$$p = \pi / z_2 - m \dots \pi / z_2 + m, \quad (13)$$

where m — angle of deviation from the angle of the radius vector of the transition point.

$$m = 2 \cdot p \cdot u, \quad (14)$$

where u — part of the angular sector of the stator profile to study smoothness in the vicinity of the transition point. Value u (for $z_2 = 2 \dots 12$) is determined from the empirical formula

$$u = 0.12 - 0.01 \cdot (z_2 - 1). \quad (15)$$

Figure 2 shows that with an increase in the radius of the roller in the vicinity of the transition point of equidistant lines, the stator profile turns from smooth to self-intersecting. The behavior of function F_s also changes, and when the self-intersection effect of the profile appears, a loop occurs (Fig. 2 c).

This effect is taken as a basis for the stator profile smoothness control algorithm proposed by the authors of the article (Fig. 3). It should be noted that, judging by numerous measurements, if the stator smoothness criterion is met, then the smoothness of the rotor profile does not need to be checked, since it is built on a hypocycloid with a smaller value of the radius of the base circle.

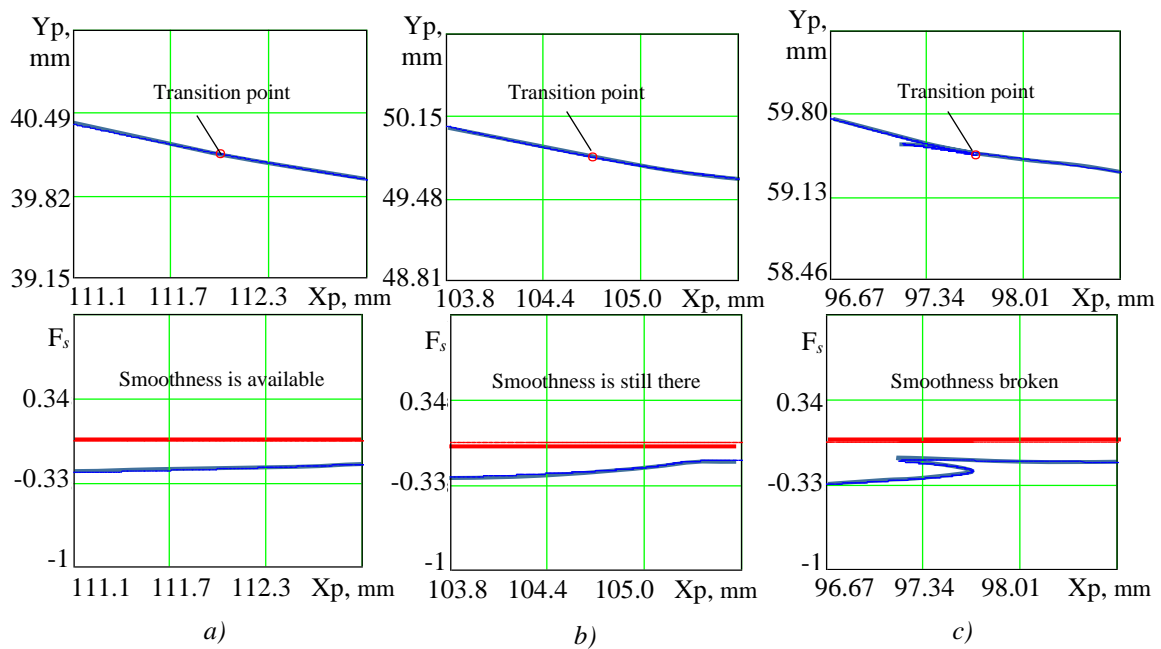


Fig. 2. Stator profile in the vicinity of ± 1 mm from the transition point of equidistant lines (upper graph) and values of function F_s (lower graph) at $z_1 = 3$ and $R_k = 150$ mm, for R_r : a — 40 mm; b — 50 mm; c — 60 mm

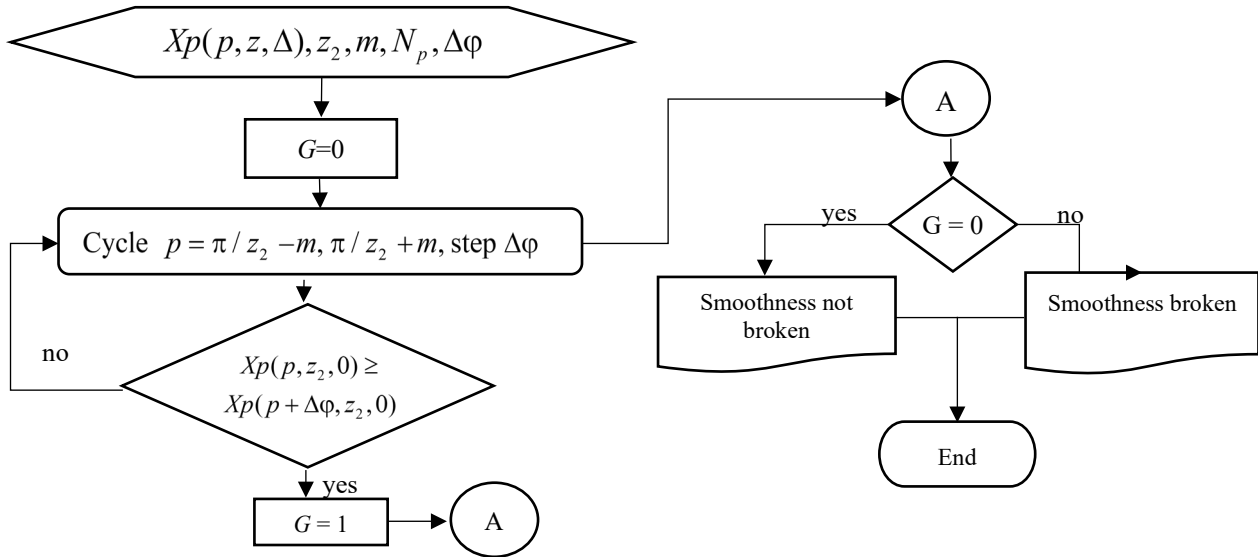


Fig. 3. Algorithm scheme for monitoring the stator profile smoothness

Control of the stator profile smoothness should always be carried out when designing the geometry of the end section of the gerotor machine. In order to study the parameter of the maximum radius of roller $R_{r\max}$, below which the smoothness of the curve was not violated, the authors conducted a series of numerical experiments where various values of the contour radius R_k and the numbers of rotor teeth z_1 were specified.

The first target parameter of this study is the open area of the working body S . This parameter is included in the formula for feeding the gerotor machine, and it determines its performance. With the available parametric functions describing the profiles of the rotor and stator, the task of determining S is reduced to calculating the difference in the areas of the parametric curves of stator S_s and rotor S_r (9). The formula for the area of the parametric curve is known from mathematics; therefore, in the authors' methodology, it looks like this:

$$S = S_s - S_r = \int_0^{z_2 \cdot 2\pi} \left(X_p(p, z_2, 0) \cdot \frac{\partial Y_p(p, z_2, 0)}{\partial p} \right) dp - \int_0^{z_1 \cdot 2\pi} \left(X_p(p, z_1, \Delta) \cdot \frac{\partial Y_p(p, z_1, \Delta)}{\partial p} \right) dp \quad (16)$$

The second target parameter of the study is the reduced radius ρ_{np} of curvature at the contact interaction of the rotor and the stator. Recall that according to Hertz theory, when two cylindrical surfaces come into contact, the reduced radius is calculated, which is in the denominator in the contact stress formula. Consequently, the magnitude of the contact stresses, along with the physical and mechanical parameters of the materials of the contacting surfaces, has the largest value at the lowest value of the reduced radius ρ_{np} , determined from the formula:

$$\rho_{np} = (\rho_r \cdot \rho_s) / (\rho_r + \rho_s). \quad (17)$$

where ρ_r — radius of the equidistant circle of the rotor, equal to parameter R_r ; ρ_s — radius of the stator profile curve.

Note that if $\rho_s > 1$, then the numerator in formula (17) always grows faster than the denominator; therefore, the smallest value $\rho_{np\min}$ is completely determined by the parameter of the smallest radius of the stator $\rho_{ct\min}$.

In the end section of the working body of the gerotor machine, at any rotation angle of the rotor, continuous contact of its equidistant circle and a complex curve of the stator profile is made. Based on the results of observations of the contact interaction dynamics, it can be concluded that the greatest stresses occur at the transition points of the equidistant hypocycloids in the equidistant circumference of the stator profile. Consequently, the smallest radius of the stator profile line $\rho_{ct\min}$ is also located in the transition zone of equidistant lines and determined by the formula known from mathematics:

$$\rho_{cm\min}(p) = \frac{\left[\left(\frac{\partial X_p(p, z_2, 0)}{\partial p} \right)^2 + \left(\frac{\partial Y_p(p, z_2, 0)}{\partial p} \right)^2 \right]^{\frac{3}{2}}}{-\left(\frac{\partial X_p(p, z_2, 0)}{\partial p} \right) \cdot \left(\frac{\partial^2 Y_p(p, z_2, 0)}{\partial p^2} \right) + \left(\frac{\partial^2 X_p(p, z_2, 0)}{\partial p^2} \right) \cdot \left(\frac{\partial Y_p(p, z_2, 0)}{\partial p} \right)}. \quad (18)$$

where $\rho = \pi / z_2$ angular parameter of the stator profile point at the junction of equidistant lines. In case of loss of smoothness of the stator line, parameter $\rho_{cr \min}$ tends to zero.

The technique described above was implemented in the Mathcad system of mathematical calculations. When performing calculations, the hypocycloid velocity factor $a=0.99$, $N_p = 40,000$.

At the first stage of research, it was planned to study the maximum radius of roller $R_{r \max}$, at which the stator profile line smoothness criterion G was zero. Variable parameters — contour radius R_k (100, 150, 200 mm) and the number of rotor teeth z_1 (from 1 to 7). Calculations were performed with a sequential increase in parameter R_r from 5 mm until the smoothness criterion G was triggered. The investigated parameter $R_{r \max}$ was fixed with an accuracy of 1 mm.

At the second stage, a series of calculations were carried out to study the effect of the roller radius R_r (from 5 mm to $R_{r \max}$), the number of rotor teeth z_1 (from 2 to 7) and the contour radius R_k (100, 150, 200 mm) on the open area S and the minimum reduced contact radius $\rho_{np \min}$.

The described method of calculating the profile geometry of the end section of the working body of the gerotor machine can be implemented in any other programming system or in a computer mathematics system.

Research Results. The data of numerical experiments to determine the parameter of the maximum radius of roller $R_{r \max}$, at which the stator profile line smoothness is preserved, are shown in Table 1.

Table 1

Maximum radius of roller $R_{r \max}$ (mm) at different contour radii R_k (mm)

z_1	$R_k = 100$	$R_k = 150$	$R_k = 200$
1	66.6	100	133
2	45	68	91
3	27	41	55
4	20	31	40
5	15	23	31
6	12	19	25
7	10	16	21

Based on the data in Table 1, graphs were constructed (Fig. 4 a). It can be seen that the estimated parameter $R_{r \max}$ grows proportionally with increasing contour radius R_k . We introduce into consideration the relative parameter $R_o = R_{r \max} / R_k$, whose graph is presented in Figure 4 b.

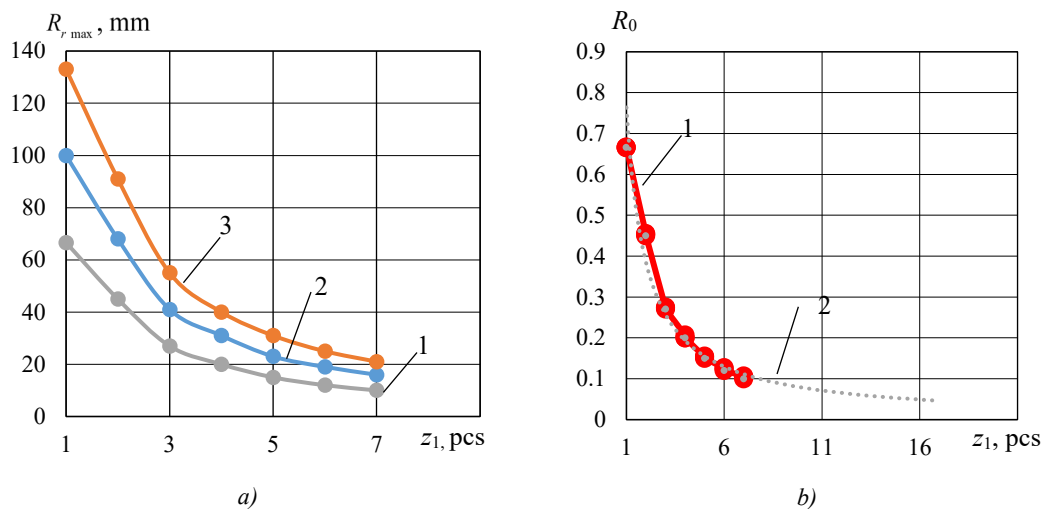


Fig. 4. Dependence of maximum radius of the roller on the number of teeth of the rotor:

a — $R_{r \max}$ and R_k : 1 — 100 mm; 2 — 150 mm; 3 — 200 mm; b — R_o (1) and trend line (2) with extrapolation to $z_1 = 16$

The empirical formula from which it is possible to determine the maximum allowable radius of roller $R_{r\max}$, has the form:

$$R_o = 0.768z_1^{-0.996} \quad (19)$$

At $z_1 = 15$, $R_k = 150$ mm, $R_o = 0.0517$ mm, $R_{r\max} = 7.76$ mm, the profile smoothness is achieved at $R_r = 7.5$ mm.

At $z_1 = 10$, $R_k = 200$ mm, $R_o = 0.0775$ mm, $R_{r\max} = 15.5$ mm, the profile smoothness is achieved at $R_r = 15.5$ mm.

Thus, we can conclude about the satisfactory accuracy of empirical formula (19) for predicting the maximum allowable parameter $R_{r\max}$.

It should be noted that formula (19) was obtained at the values of the velocity factor $a = 0.99$. A decrease in a causes the smoothness of the profile with a more significant increase in parameter R_r . However, the shape of the cycloidal engagement tooth changes, and the conditions of contact interaction between the rotor and the stator are violated, specifically, in those places where the rotor should touch the stator with the sides of the teeth. Calculations show that at $a = 0.99$ and $R_r = 38$ mm, the smoothness criterion is at the limit of feasibility. Though at $a = 0.90$ and $R_r = 38$ mm, good smoothness of the stator profile is achieved, but the kinematic contact of the parts of the working body of the machine is disrupted, which can be restored only by a special selection of the values of the hypocycloid parameters of the rotor and stator. Therefore, the study of the influence of the velocity factor on parameter $R_{r\max}$ is beyond the scope of this research.

Table 2 presents the data of calculations of the target parameters of the studies for the number of rotor teeth $z_1 = 3$ at different values of contour radii. The obtained values of the open area S and the minimum reduced contact radius $\rho_{np\min}$ in the last two columns of Table 2 are given in a dimensionless form for ease of analysis.

Table 2

Calculation data of target parameters at $z_1=3$

R_r , mm	$\rho_{np\min}$, mm	S , mm ²	$S/\max(S)$	$\rho_{np\min}/\max(\rho_{np\min})$
$R_k = 150$ mm				
5	4.72	18,038	0.9712	0.2656
10	8.83	18,256	0.983	0.4969
15	12.28	18,415	0.9915	0.6911
20	14.98	18,513	0.9968	0.843
25	16.85	18,572	1	0.9482
30	17.77	18,530	0.9977	1
35	17.63	18,450	0.9934	0.9921
40	16.28	18,307	0.9857	0.9162
$R_k = 200$ mm				
10	9.14	32,275	0.9786	0.3857
20	16.37	32,738	0.9926	0.6909
30	21.36	32,982	1	0.9015
35	22.9	32,980	0.9999	0.9664
40	23.69	32,943	0.9988	0.9998
45	23.695	32,844	0.9958	1
50	22.82	32,685	0.991	0.9631
55	20.98	32,466	0.9844	0.8854
$R_k = 100$ mm				
5	4.57	8,068	0.9773	0.3857
10	8.18	8,184	0.9914	0.6903

R_r , mm	$\rho_{np \min}$, mm	S , mm ²	$S/\max(S)$	$\rho_{np \min} / \max(\rho_{np \min})$
$R_k = 150$ mm				
13	9.83	8,225	0.9964	0.8295
15	10.68	8,245	0.9988	0.9013
17	11.32	8,255	1	0.9553
20	11.85	8,235	0.9976	1
24	11.64	8,189	0.992	0.9823

Figure 5 shows graphs of variation in the target parameters of studies at $z_1=3$. It is easily seen on them that with an increase in the radius of roller R_r , there is a slight change in the open area S and a sufficiently strong change in the reduced contact radius, whose maximum value falls on a fairly narrow range R_r . This is of the greatest interest to the designer, since in this case, the contact stresses are minimal. Calculations for other values z_1 (from 2 to 7) showed approximately the same qualitative picture as in Figure 5.

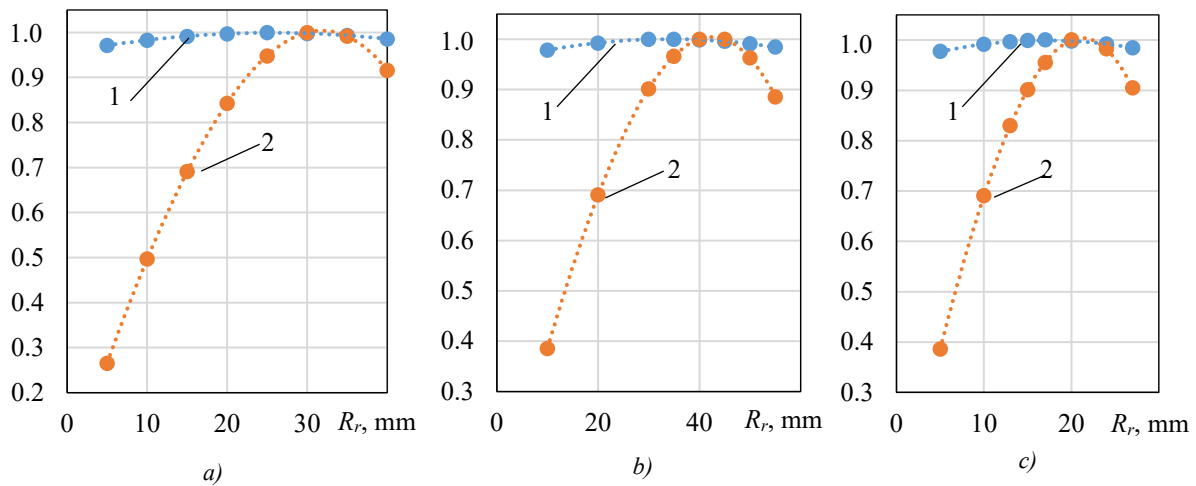


Fig. 5. Dependences of the target parameters of the study on the radius of roller R_r at $z_1 = 3$. a = 0.99. $\Delta = 0$: 1 — $S/\max(S)$; 2 — $\rho_{np \min} / \max(\rho_{np \min})$ (Table 2); R_k , mm: a — 150; b — 200; c — 100 mm

Table 3 shows the calculation data of the optimal radii of rollers $R_{r \text{ opt}}$ for various parameters z_1 and R_k . As a result of the analysis, it turned out that parameters $R_{r \text{ opt}}$ and R_k for one z_1 change almost the same. Therefore, if you enter the parameter of the relative optimal radius of the roller

$$R_{ro} = R_{r \text{ opt}} / R_k, \quad (20)$$

then, with the help of a single-factor dependence of $R_{ro} = f(z_1)$ -type, it is possible to determine the optimal radius of roller R_r at the preliminary stage of designing the working body of the gerotor machine.

As a result of similar reasoning, for parameters S and $\rho_{np \min}$, given in Table 3, dimensionless parameters of the relative reduced radius of contact $\rho_{np o}$ and relative open area $\rho_{np \min}$ were also introduced (Table 3):

$$S_o = S / R_k^2; \rho_{np o} = \rho_{np \min} / R_k \quad (21)$$

New relative values are also presented in Table 3.

Table 3

Optimal radii $R_{r\ opt}$ and relative engagement parameters

R_k , mm	z_1	$R_{r\ opt}$, mm	S , mm ²	$\rho_{np\ min}$, mm	R_{ro}	$\rho_{np\ o}$	S_o
200	2	68	36,103	43.2	0.340	0.216	0.903
150	2	51	20,318	32.2	0.340	0.215	0.903
100	2	34	9,015	21.65	0.340	0.217	0.902
100	3	21	8,235	11.85	0.210	0.119	0.824
150	3	32	18,530	17.8	0.213	0.119	0.824
200	3	42	32,800	23.1	0.210	0.116	0.820
200	4	28	30,015	15.32	0.140	0.077	0.750
150	4	21	16,880	11.5	0.140	0.077	0.750
100	4	14	7,495	7.63	0.140	0.076	0.750
100	5	10	6,860	5.35	0.100	0.054	0.686
150	5	15	15,441	8.1	0.100	0.054	0.686
200	5	20	27,452	10.81	0.100	0.054	0.686
150	7	9	13,050	4.7	0.060	0.031	0.580
200	7	12	22,100	6.2	0.060	0.031	0.582
100	7	6	5,780	3.2	0.060	0.032	0.578

It should be noted that all newly introduced relative values with a high degree of confidence obey approximating formulas that include one factor — the number of rotor teeth z_1 .

The formula for the relative optimal radius of roller R_{ro} has the form

$$R_{ro} = 0.9331 \cdot z_1^{-1.392} \quad (R^2 = 0.9965), \quad (22)$$

where R^2 — value of the approximation accuracy.

The formula for the relative reduced contact radius $\rho_{np\ o}$ has the form

$$\rho_{np\ o} = 0.635 \cdot z_1^{-1.534} \quad (R^2 = 0.9995). \quad (23)$$

The formula of the relative open area S_o has the form

$$S_o = 1.0175 - 0.0641 z_1 \quad (R^2 = 0.9911). \quad (24)$$

Let us consider an example of the application of the results obtained in the design of the geometry of the end section profile of the gerotor machine. We specify the following set of initial data: contour radius $R_k = 120$ mm, number of rotor teeth $z_1 = 4$, tension in the coupling $\Delta = 0$ mm (empirical formulas are obtained at zero tension). The relative optimal radius of roller R_{ro} according to formula (22):

$$R_{ro} = 0.9331 \cdot 4^{-1.392} = 0.135.$$

Absolute value of the roller radius $R_r = R_{ro} \cdot R_k = 0.135 \cdot 120 = 16.2$ mm.

Relative reduced contact radius $\rho_{np\ o}$ from formula (23):

$$\rho_{np\ o} = 0.635 \cdot 4^{-1.534} = 0.076.$$

Absolute value of the minimum reduced contact radius

$$\rho_{np\ min} = r_{np\ o} R_k = 0.076 \cdot 120 = 9.12 \text{ mm}.$$

Relative open area S_o from formula (24):

$$S_o = 1.0175 - 0.0641 \cdot 4 = 0.761.$$

Absolute value of the open area

$$S = S_o \cdot R_k^2 = 0.761 \cdot 120^2 = 10,958 \text{ mm}^2.$$

Mathcad calculations give the following values: $S = 10,820 \text{ mm}^2$, $\rho_{np \min} = 9.167 \text{ mm}$. As can be seen in this example, empirical formulas accurately predict the basic parameters of the geometry of the end section of the gerotor machine.

Discussion and Conclusion. The conducted research was aimed at solving the problem of improving the working bodies of gerotor hydraulic machines. It sufficiently corresponds to the works of domestic and foreign authors [10–15]. The key difference is that when constructing the rotor and stator profiles, ideal hypocycloids are used, providing the greatest kinematic accuracy of movement and contact interaction of the engagement elements. It was proposed to solve the well-known problem of providing tension in the coupling with respect to the difference in the parameters of the roller radius. A special algorithm was developed to control the smoothness of the profiles [12]. The optimal geometry of the profile, as in [10], was proposed to be determined on the basis of the maximum open area of the working body of the gerotor machine. But at the same time, the reduced contact radius should also have the largest value, as a guarantee of the lowest contact stresses. In this study, based on a large number of calculations using a purpose-built Mathcad program, in the range of rotor teeth z_1 from 2 to 7 and contour diameter R_k from 100 to 200 mm, optimal values of the equidistant hypocycloid distance, or roller radii R_r , at which the best combination of the reduced contact radius and the open area of the working body of the gerotor was achieved. It turned out that the introduction of relative values of the radius of the roller, the open area, and the reduced contact radius provided obtaining absolute values of the same magnitudes for any contour radius within the established ranges using simple empirical dependences at an early stage of design.

The developed technique makes it possible to evaluate the performance and operability of the gerotor machine at the design stage of the rotor and stator profiles. In the future, similar studies can be carried out for epicycloid and mixed engagements in gerotor hydraulic machines.

The research results can be used in mechanical engineering under the design of gerotor hydraulic machines to improve their operating characteristics.

References

1. Baldenko DF, Baldenko FD. Single-Screw Hydraulic Machines in the Oil and Gas Industry: Fields of Application and Development Prospects. *Petroleum & Petrochemical Engineering Journal*. 2019;3(5):000207. <https://doi.org/10.23880/ppej-16000207>
2. Ramakrishnan Balaji Iyer, Jatti VK, Yeshpal Yadav, Anurag Verma, Jaimin Desai, Dewan CP. Design Optimization of CAD Model. *Materials Today: Proceedings*. 2017;4(8):7357–7364. <https://doi.org/10.1016/j.matpr.2017.07.065>
3. Hong-Seok Park, Xuan-Phuong Dang. Structural Optimization Based on CAD–CAE Integration and Metamodeling Techniques. *Computer-Aided Design*. 2010;42(10):889–902. <https://doi.org/10.1016/j.cad.2010.06.003>
4. Lebedev A, Kireev S, Korchagina M, Lubinec V. Improvement of Design of Device for Production of Cycloidal Pinion Gear. In: M Shamtsyan, M Pasetti, A Beskopylny (eds). *Robotics, Machinery and Engineering Technology for Precision Agriculture. Smart Innovation, Systems and Technologies*. Vol. 247. P. 223–236. Singapore: Springer; 2022. https://link.springer.com/chapter/10.1007/978-981-16-3844-2_24
5. Korchagina M, Lebedev A, Kireev S, Vlaskin S. Model of Hole Mandrel Process in Tubular Workpieces. In book: A Guda (ed) *Networked Control Systems for Connected and Automated Vehicles*. Vol. 509. P. 1541–1550. Cham: Springer; 2022. https://doi.org/10.1007/978-3-031-11058-0_156
6. Lebedev A, Kireev S, Korchagina M, Efimov A. Optimization of Structure Parameters of Semi-Trailer-Tank for Hydraulic Fracturing of Formation. In book: A Guda (ed) *Networked Control Systems for Connected and Automated Vehicles*. Vol. 510. Cham: Springer; 2023. https://doi.org/10.1007/978-3-031-11051-1_178
7. Baldenko FD, Yang Yao. The Study of the Chambers Area of the Working Bodies of Single-Screw Hydraulic Machines. *Drilling and Oil Magazine*. 2020;(6):24–29. <https://burneft.ru/archive/issues/2020-06/24>
8. Jie Chen, He Liu, Fengshan Wang, Guocheng Shi, Gang Cao, Hengan Wu. Numerical Prediction on Volumetric Efficiency of Progressive Cavity Pump with Fluid-Solid Interaction Model. *Journal of Petroleum Science and Engineering*. 2013;109:12–17. <https://doi.org/10.1016/j.petrol.2013.08.019>
9. Gamboa J, Olivet A, Espin S. New Approach for Modeling Progressive Cavity Pumps Performance. *Journal of Petroleum Technology*. 2003;56(5):51–53. <https://doi.org/10.2118/84137-MS>

10. Yang Yao, Baldenko F. Optimization of Cycloidal Gearing Geometric Parameters of Positive Displacement Motors. *Equipment and Technologies for Oil and Gas Complex*. 2021;(6):22–26. [https://doi.org/10.33285/1999-6934-2021-6\(126\)-22-26](https://doi.org/10.33285/1999-6934-2021-6(126)-22-26)
11. Lyagov I, Baldenko F, Lyagov A, Yamaliev V, Lyagova A. Methodology for Calculating Technical Efficiency of Power Sections in Small-Sized Screw Downhole Motors for the “Perfobur” System. *Journal of Mining Institute*. 2019;240:694–700. <https://doi.org/10.31897/pmi.2019.6.694>
12. Korotaev YuA, Alpatov AN, Sobolev AV, Myalitsin NYu. Investigation of the Systematic Error of Gerotor Mechanism Action Profiled from the Initial Rack Contour. *Izvestiya Tula State University*. 2017;8(1):112–120.
13. Korotaev YuA, Goldobin DA. Designing and Calculation Peculiarities of the Multiple-Thread Screw-Type Gerotor Machines of the Multiphase Pumps. *Izvestiya Tula State University*. 2016;8(2):175–182.
14. Minikaev AF, Pronin VA, Zhignovskaya DV, Kuznetsov YuL. The Use of Computer Modelling for the Development of the Working Bodies’ Profiles for Screw Single-Rotor Compressor. *Journal of International Academy of Refrigeration*. 2018;(1):61–66. <https://doi.org/10.17586/1606-4313-2018-17-1-61-66>
15. Baldenko FD, Kovalenok AE. Komp'yuternoe modelirovanie kontaktnogo vzaimodeystviya rabochikh organov odnovintovykh gidravlicheskh mashin. *Neftegaz Territory*. 2014;10:18–27. (In Russ.)

Received 29.05.2023

Revised 21.06.2023

Accepted 26.06.2023

About the Authors:

Sergey O. Kireev, Dr.Sci. (Eng.), Professor, Head of the Oil and Gas Complex Machinery and Equipment Department, Don State Technical University (1, Gagarin sq., Rostov-on-Don, 344003, RF), [ResearcherID](#), [ScopusID](#), [ORCID](#), [AuthorID](#), kireevso@yandex.ru

Alexey R. Lebedev, Cand.Sci. (Eng.), Associate Professor of the Oil and Gas Complex Machinery and Equipment Department, Don State Technical University (1, Gagarin sq., Rostov-on-Don, 344003, RF), [ResearcherID](#), [ScopusID](#), [ORCID](#), [AuthorID](#), alex-diplom@mail.ru

Marina V. Korchagina, Cand.Sci. (Eng.), Associate Professor of the Oil and Gas Complex Machinery and Equipment Department, Don State Technical University (1, Gagarin sq., Rostov-on-Don, 344003, RF), [ResearcherID](#), [ScopusID](#), [ORCID](#), [AuthorID](#), ms.korchaginamv@mail.ru

Claimed contributorship:

SO Kireev: basic concept formulation, research objectives and tasks, academic advising.

AR Lebedev: computational analysis, text preparation, analysis of the research results, formulation of conclusions.

MV Korchagina: revision of drawings and text, correction of conclusions.

Conflict of interest statement: the authors do not have any conflict of interest.

All authors have read and approved the final manuscript.

Поступила в редакцию 29.05.2023

Поступила после рецензирования 21.06.2023

Принята к публикации 26.06.2023

Об авторах:

Сергей Олегович Киреев, доктор технических наук, профессор, заведующий кафедрой машин и оборудования нефтегазового комплекса Донского государственного технического университета (344003, РФ, г. Ростов-на-Дону, пл. Гагарина, 1), [ResearcherID](#), [ScopusID](#), [ORCID](#), [AuthorID](#), kireevso@yandex.ru

Алексей Романович Лебедев, кандидат технических наук, доцент кафедры машин и оборудования нефтегазового комплекса Донского государственного технического университета (344003, РФ, г. Ростов-на-Дону, пл. Гагарина, 1), [ResearcherID](#), [ScopusID](#), [ORCID](#), [AuthorID](#), alex-diplom@mail.ru

Марина Валерьевна Корчагина, кандидат технических наук, доцент кафедры машин и оборудования нефтегазового комплекса Донского государственного технического университета (344003, РФ, г. Ростов-на-Дону, пл. Гагарина, 1), [ResearcherID](#), [ScopusID](#), [ORCID](#), [AuthorID](#), ms.korchaginamv@mail.ru

Заявленный вклад соавторов:

С.О. Киреев — формирование основной концепции, цели и задачи исследования, научное руководство.

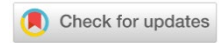
А.Р. Лебедев — проведение расчетов, подготовка текста, анализ результатов исследований, формирование выводов.

М.В. Корчагина — доработка рисунков и текста, корректировка выводов.

Конфликт интересов: авторы заявляют об отсутствии конфликта интересов.

Все авторы прочитали и одобрили окончательный вариант рукописи.

MACHINE BUILDING AND MACHINE SCIENCE



UDC 62-522.7

Original article

<https://doi.org/10.23947/2687-1653-2023-23-3-283-295>

Investigation of Dynamic Characteristics of an Automated Position Long-Stroke Pneumatic Actuator of Fabrication System

Daniil A. Korotych , Valentin S. Sidorenko , Sergey P. Prikhodko

Don State Technical University, Rostov-on-Don, Russian Federation

✉ daniilberuk@gmail.com

Abstract

Introduction. Long-stroke movements in automated pneumatic drives account for a significant number of executive movements in coordinate tables, automated warehouses, cutting machines, etc. Long-stroke movements degrade the dynamic quality and positioning of the drive. This is due to the friction of the piston and the nonlinear characteristics of the compressed gas flow in significant volumes of the pressure and drain cavities of the cylinder. Thus, it seems promising to create an automated position pneumatic actuator for long-stroke movements. This will increase the productivity of processes while providing the declared accuracy. The objective of the work is to obtain a mathematical model and dependences of the critical parameters of the proposed automated position long-stroke pneumatic drive of fabrication system in the areas of acceleration, steady-speed movement, deceleration, and braking.

Materials and Methods. The basis for calculations and modeling was the scheme of two trajectories of movement from point A to point E, taking into account the forces expended on these processes. The optimal displacement was determined using the Portnyagin's principle (i.e., optimal performance). Proportional drive control was presented as a method of achieving the result. For long-stroke drive movements, schematic solution and design scheme were visualized in detail (presented as drawings). An original jet sensor with an internal pneumatic connection and a pneumo-mechanic discrete-proportional device for the control loop performance were proposed. The mathematical model included the movement and braking of the piston, the balance of mass flow, the pressure at points, and the control loop. The system of equations was solved by the Runge-Kutta method in the SimInTech software product. Based on the results of the study of a generalized mathematical model, the dependences of changes in the kinematic, power and pneumatic properties of the drive were constructed in real time during a typical positioning cycle. The information was summarized and presented as a set of graphs.

Results. The mathematical model was formed according to a set of calculations. It took into account the dependences characteristic of the movement of the piston of the pneumatic cylinder. The balance of mass flow was investigated by the equations of gas flow during compression in the chamber, through distributors and chokes, in the discharge and drain cavities and in the control device. Inequalities describing the pressures at the points and the control loop were considered. A complex mathematical model was solved in the SimInTech software environment by the Runge-Kutta method with a variable integration step. A fragment of the program was selected as one of the illustrations. It showed that the software used the following indicators for calculations: target and reduced coordinates; absolute gas constant; coefficients of spring stiffness, resistance, adiabatic and viscous friction in the piston; compressor pressure; mass of the moving parts of the pneumatic actuator; strength of external resistances; diameters of the pipeline, the pneumatic cylinder piston and the braking device; length of the stroke of the cylinder piston; area of piston cavities and throttles; length of the pipeline and its internal volume. Thus, the program manipulated a significant set of data, which made it possible to obtain meaningful and adequate results. The relationship of blocks and diagrams used in solving the model

was schematically shown. We are talking about graphs of movements, areas, pressures, velocities and temperatures. Blocks with the program text and intended for integration were used. Thus, a mathematical model of an automated pneumatic drive of the fabrication system and the dependences of the basic parameters of its operation were obtained. The graphs indicated that the operating mechanism of the pneumatic actuator properly followed the proposed trajectory.

Discussion and Conclusion. The research results allowed us to consider several stages of long-stroke movement of the drive, to determine the time frame of these processes (from 0 to 0.65s), as well as changes in pressure and speed of movement of the pneumatic cylinder carriage recorded in these intervals. There were five such stages: acceleration, steady-speed movement, deceleration, movement with positioning speed, and braking. Further research will focus on optimizing the system to reduce the duration and maintain accurate positioning under external influences.

Keywords: long-stroke pneumatic actuator, jet control system, mechatronic module, pneumatic sensor, pneumatic actuator positioning, SimInTech software environment, Runge-Kutta method

Acknowledgements: the authors would like to thank the editors and reviewers for their attentive attitude to the article and comments that made it possible to improve its quality.

For citation. Korotych DA, Sidorenko VS, Prikhodko SP. Investigation of Dynamic Characteristics of an Automated Position Long-Stroke Pneumatic Actuator of Fabrication System. *Advanced Engineering Research (Rostov-on-Don)*. 2023;23(3):283–295. <https://doi.org/10.23947/2687-1653-2023-23-3-283-295>

Научная статья

Исследование динамических характеристик автоматизированного позиционного длинноходового пневмопривода технологического оборудования

Д.А. Коротыч  , В.С. Сидоренко , С.П. Приходько 

Донской государственный технический университет, г. Ростов-на-Дону, Российская Федерация

 daniilberuk@gmail.com

Аннотация

Введение. На длинноходовые перемещения в автоматизированных пневмоприводах приходится значительное количество исполнительных движений в координатных столах, на автоматизированных складах, раскройных машинах и т. д. Длинноходовые перемещения ухудшают динамическое качество и позиционирование привода. Это обусловлено трением поршня и нелинейными характеристиками потока сжатого газа в значительных объемах напорной и сливной полостей цилиндра. Таким образом, представляется перспективным создание автоматизированного позиционного пневмопривода для длинноходовых перемещений. Это позволит повысить производительность процессов при обеспечении заявленной точности. Цель работы — получение математической модели и зависимостей основных параметров предложенного автоматизированного позиционного длинноходового пневмопривода технологического оборудования на участках разгона, движения с установившейся скоростью, замедления и торможения.

Материалы и методы. Базой для расчетов и моделирования стала схема двух траекторий перемещения из точки А в точку Е с учетом сил, затраченных на эти процессы. Оптимальное перемещение определили с помощью принципа Портягина (то есть оптимального быстродействия). Пропорциональное управление приводом представлено как метод достижения результата. Для длинноходовых перемещений привода детально визуализированы (представлены как рисунки): схематическое решение и расчетная схема. Предложены оригинальный струйный датчик с внутренней пневматической связью и пневмомеханическое дискретно-пропорциональное устройство для быстродействия контура управления. Математическая модель включает движение и торможение поршня, баланс массовых расходов, давление в точках и контур управления. Систему уравнений решали методом Рунге — Кутты в программном продукте «Симинтех» (Simintech). По итогам исследования обобщенной математической модели построили зависимости изменения кинематических,

силовых и пневматических свойств привода в реальном времени при типовом цикле позиционирования. Информацию суммировали и представили как совокупность графиков.

Результаты исследования. Математическая модель сформирована по комплексу расчетов. Она учитывает зависимости, характерные для движения поршня пневмоцилиндра. Баланс массовых расходов исследуется по уравнениям расхода газа при сжатии в камере, через распределители и дроссели, в нагнетательной и сливной полостях и в управляющем устройстве. Рассмотрены неравенства, описывающие давления в точках и контур управления. Сложная математическая модель решалась в программной среде «Симинтех» (Simintech) методом Рунге — Кутты с изменяемым шагом интегрирования. Фрагмент работы программы выбран в качестве одной из иллюстраций. Он показывает, что софт задействует для расчетов такие показатели, как: заданная и приведенные координаты; универсальная газовая постоянная; коэффициенты жесткости пружины, сопротивления, адиабаты и вязкого трения в поршне; давление компрессора; массу подвижных частей пневмопривода; силу внешних сопротивлений; диаметры трубопровода, поршня пневмоцилиндра и тормозного устройства; протяженность хода поршня цилиндра; площади поршневых полостей и дросселей; длину трубопровода и его внутренний объем. Таким образом, программа оперирует значительным комплексом данных, что дает возможность получить существенные и адекватные результаты. Схематически показана взаимосвязь блоков и диаграмм, использованных при решении модели. Речь идет о графиках перемещений, площадей, давлений, скоростей и температур. Используются блоки с текстом программы и предназначенные для интегрирования. Таким образом получены математическая модель автоматизированного пневмопривода технологического оборудования и зависимости основных параметров его работы. Графики свидетельствуют о том, что исполнительный механизм пневмопривода должным образом следует предложенной траектории.

Обсуждение и заключение. Итоги работы позволяют рассмотреть несколько этапов длинноходового перемещения привода, определить временные рамки этих процессов (от 0 до 0,65 сек), а также фиксируемые в данные промежутки изменения давления и скорости движения каретки пневмоцилиндра. Таких этапов пять: разгон, движение с установившейся скоростью, замедление, движение со скоростью позиционирования и торможение. Дальнейшие исследования будут сосредоточены на оптимизации системы для сокращения продолжительности и поддержания точного позиционирования при внешних воздействиях.

Ключевые слова: длинноходовой пневмопривод, струйная система управления, мехатронный модуль, пневматический датчик, позиционирование пневмопривода, программная среда «Симинтех», метод Рунге — Кутты

Благодарности: авторы выражают благодарность редакции и рецензентам за внимательное отношение к статье и замечания, которые позволили повысить ее качество.

Для цитирования. Коротыч Д.А., Сидоренко В.С., Приходько С.П. Исследование динамических характеристик автоматизированного позиционного длинноходового пневмопривода технологического оборудования. *Advanced Engineering Research (Rostov-on-Don)*. 2023;23(3):283–295. <https://doi.org/10.23947/2687-1653-2023-23-3-283-295>

Introduction. The performance of the drives is determined by the accuracy of positioning and the speed of movement of the coordinates in different operating cycles. Modern fabrication systems are often equipped with automatic pneumatic actuators, which are characterized by long-stroke movements. These are, e.g., gantry resistance welding machines, coordinate tables, and cutting devices.

Modern positioning pneumatic actuators for long-stroke movements in fabrication equipment provide a speed of up to 30 mm/s and an accuracy of ~1 % of the travel length. Customized actuators provide positioning accuracy of 0.4 % at speeds up to 100 mm /s. Note that the trajectory of movements is formed by the compressed air flow control in pressure or drain pipelines and the pneumatic cylinder sides. In long-stroke drives, the length of such sides reaches 3 m. Complex thermodynamic processes and compressibility in air flows are the key factors limiting the increase in accuracy [1–3].

Thus, it is necessary to increase the productivity of the working and engineering processes of the equipment while providing the declared accuracy. In this case, it seems promising to create an automated positioning pneumatic actuator

for long-stroke movements. The new solution should take into account such characteristics of the pneumatic actuator as speed, weight-size parameters, explosionproof, and fire protectability [2, 4].

The objective of the work is to obtain a mathematical model and dependences of the key parameters of the proposed automated positioning long-stroke pneumatic drive of industrial equipment in the areas of acceleration, steady-speed movement, deceleration, and braking.

Materials and Methods. Figure 1 shows schematically the transport problem of moving from point A to point E along two trajectories. The forces expended on each of the movements are taken into account. The suboptimal movement $ABCDE$ (trapezoid) with a simple control algorithm is realized in time $T_{n1} \gg T_{n2} \rightarrow \min$.

The optimal displacement AFE (bell) was obtained by solving the optimal speed based on the Portnyagin's principle $T_{n2} \rightarrow \min, \Delta L \leq |\Delta L_{\max}|$. The result was achieved with more complex proportional control of the drive. The trajectory of movement provided the accuracy of switching motion controls along path L_{ny} .

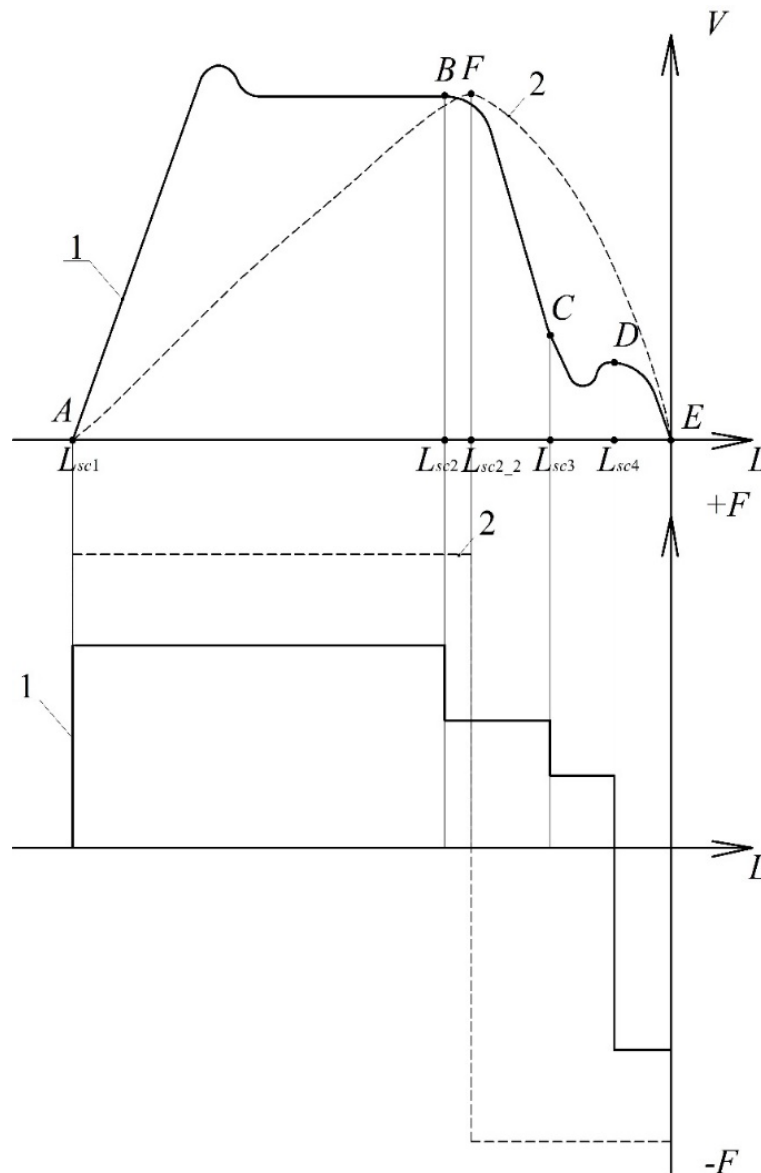


Fig. 1. Movement trajectories: 1 — suboptimal $ABCDE$; 2 — optimal AFE

In the description of trajectory 1, the switching points are indicated in Latin letters: A — for acceleration of the drive; B — for deceleration; C — for positioning speed; D — for stopping. In sections AB and BC , initial acceleration and braking are provided up to the positioning speed V_{n3} and further stopping by the braking device $\Delta L_2 \leq |\Delta L_{\max}|$.

When moving along the second trajectory, *A* — switching to acceleration of the drive; *F* — switching to stop.

An original jet sensor with an internal pneumatic connection and a pneumo-mechanical discrete-proportional device are proposed, which provides increasing the control circuit speed, since feedback in known analogues reduces the accuracy of the main engine by about 10–15 % during long strokes [4–6].

A schematic solution of a pneumatic positioning drive for long-stroke movements is shown in Figure 2. The drive operates in accordance with the suboptimal motion trajectory determined in the optimal speed problem for a given positioning accuracy. Here, ПЦ1 — rodless pneumatic cylinder of long-stroke movements, which carries out the main motion; ПЦ2, ПЦ3 — brake pneumatic cylinders that fix the drive; CA — jet sensor that determines the coordinate of movement, acceleration of the drive, its speed and force; P1 — pneumatic distributor with electropneumatic control, it controls the supply to the jet sensor; P2 — main control distributor; P3 — distributor with pneumatic control, it controls the operation of pneumatic brake cylinders; Г1–Г4 — mufflers responsible for pressure relief into the atmosphere; ДД — pressure sensor receiving data from the jet sensor; ПЛК — logic controller; ШД — stepper motor controlling the distributor spool; БПВ — air-preparation unit; ДР1, ДР2 — throttle with check valve, used to regulate the speed of the rodless pneumatic cylinder of long-stroke movements of the main motion [7].

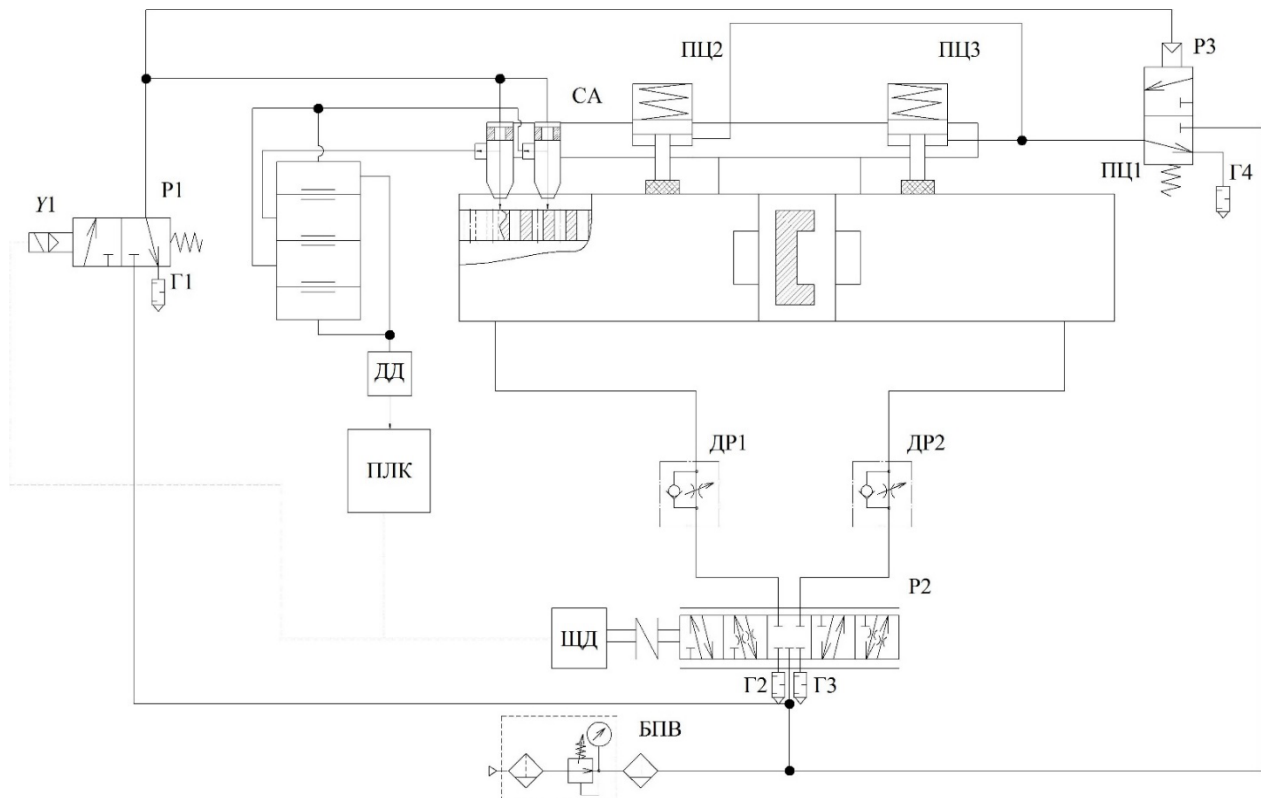


Fig. 2. Circuit design proposal of an automated positioning long-stroke pneumatic actuator

The drive contains a control system that monitors the position of the carriage of a rodless pneumatic cylinder, slows down when approaching the specified coordinates, and sends a signal to the braking gear [1, 4, 7].

The speed is increased by the introduction of a discrete proportional control device. Signals generated by the control loop are used for control. The device is made in the form of two nozzles and contains compensation measurements.

Research Results. The design scheme of the pneumatic drive of long-stroke movements is shown in Figure 3.

Here, ПЦ1 — rodless pneumatic cylinder of long-stroke coordinate movements, carrying out the main motion; ПЦ2, ПЦ3 — brake pneumatic cylinders that fix the drive during a stop in the desired position; CA — jet sensor that determines the coordinate of movement, acceleration of the drive, its speed and force; P1 — pneumatic distributor with electropneumatic control, it controls the supply to the jet sensor; P2 — main control distributor; P3 — distributor with pneumatic control, it controls the operation of brake pneumatic cylinders; Г1–Г4 — mufflers responsible for pressure relief into the atmosphere; ДР1–ДР2 — throttle with a check valve, which serves to regulate the speed of a rodless

pneumatic cylinder of long-stroke movements of the main motion; $\Delta\Delta$ — pressure sensor receiving data from a jet sensor; S — piston area of a rodless pneumatic cylinder of long-stroke coordinate displacements; $P1$ – $P5$ — investigated pressures at points 1–5; $T1$ – $T5$ — investigated temperatures at points 1–5; $F_{\text{тр}}$ — friction force in a rodless pneumatic cylinder of long-stroke displacements; F_{BT} — viscous friction force in a rodless pneumatic cylinder of long-stroke displacements; F_{BH} — external force in the rodless pneumatic cylinder of long-stroke movements; x — travel of the carriage of the rodless pneumatic cylinder of long-stroke movements; V — travel speed of the rodless pneumatic cylinder carriage; C_{np} — spring rate of brake pneumatic cylinders; m — mass to be moved; P_{r} — pressure in brake cylinders; P_y — pressure in the control channel; $f1$ – $f4$ — areas of the through sections; P_a — atmospheric pressure; d_{31} – d_{33} — diameters of distributor spools; $C_{\text{пп1}}$ – $C_{\text{пп3}}$ — spring rate of distributors 1–3; x_{p1} – x_{p4} — displacement of distributor spools 1–4; V_{p1} – V_{p4} — travel speed of distributor spools 1–4; $F_{\text{эм1}}$ – $F_{\text{эм2}}$ — force of the distributor control electromagnet 1–2; P_m — compressor pressure; T_m — temperature generated by the compressor.

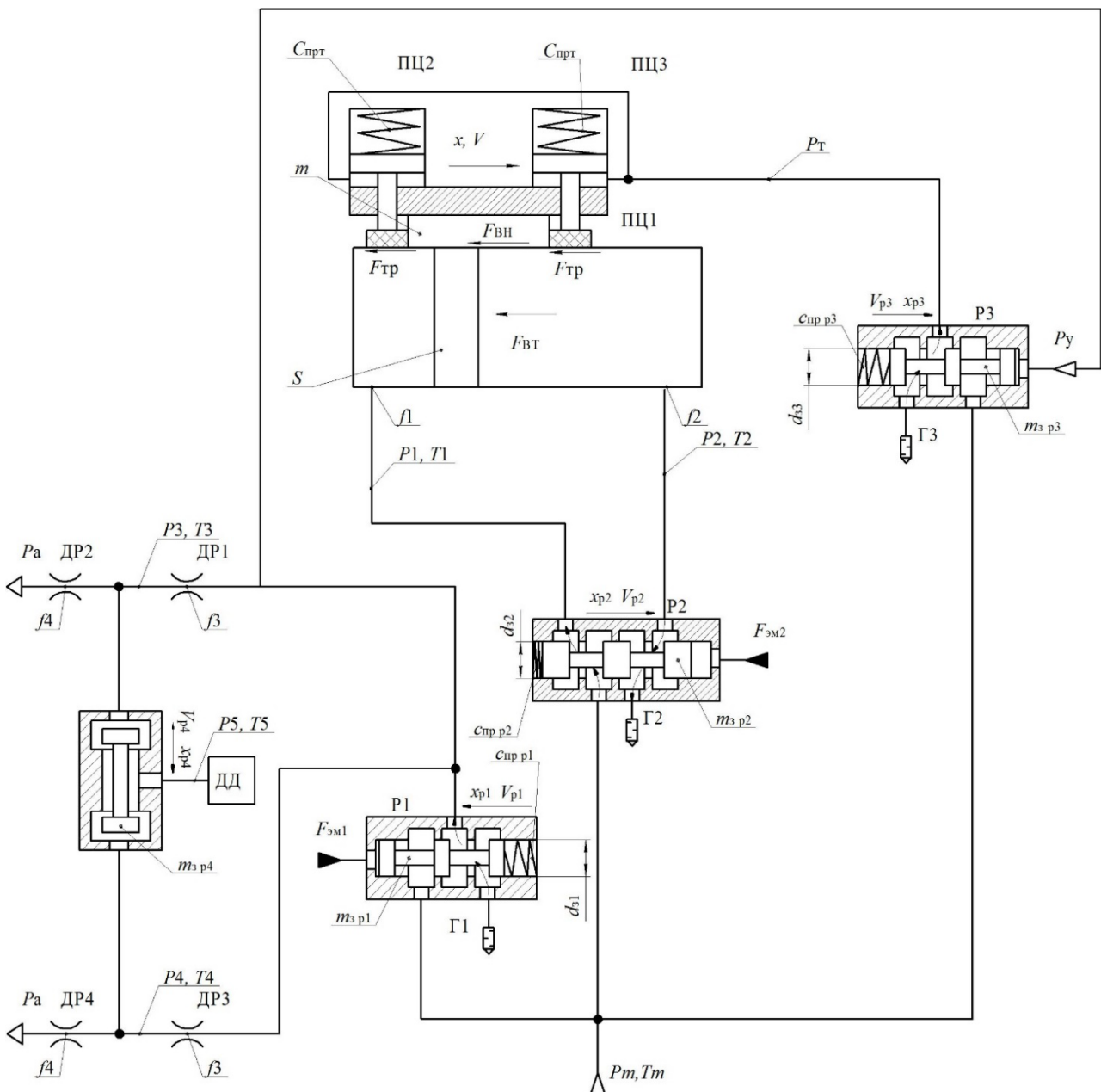


Fig. 3. Diagram of the automated pneumatic drive of long-stroke movements of the industrial equipment

The mathematical model was formed with the following assumptions [8–12]:

- pressure of the compressed air source remained constant over time;
- thermodynamic process of gas behavior in a pneumatic system was adiabatic;
- description of pneumatic devices used the ideal gas model, since the pressure of the pneumatic system did not exceed 10 bar;
- leaks were not taken into account;
- viscous friction force was proportional to the velocity;
- expense ratio was recognized experimentally through identification;
- mass of the moving part was constant;
- force at the output link of the pneumatic drive was constant.

1. Equation of motion of the pneumatic cylinder piston [1, 4]:

$$m \frac{d^2 x}{dt^2} = S \cdot (p_1 - p_2) - F_{BH} - k_{BT} \cdot \frac{dx}{dt} - F_{mp} \cdot \text{sign} \frac{dx}{dt} - \alpha \cdot F_m. \quad (1)$$

Here, S — area of the piston of the discharge and drain sides of the rodless pneumatic cylinder of long-stroke coordinate movements of the main motion, m^2 ; P_1, P_2 — air pressure in the discharge and drain sides of the pneumatic cylinder, Pa; F_{BH} — external forces, N; k_{BT} — viscosity friction coefficient; F_{mp} — friction force, N; α — Boolean parameter: $\alpha = 0$ at $p_5 \leq p_{atm}$ and $\alpha = 1$ at $p_5 \geq p_{atm}$; p_5 — pressure in the control channel, Pa; p_{atm} — atmospheric pressure, Pa [12–14]; m — mass of the moving parts of the drive, kg; F_T — braking force, N.

$$F_m = \mu \cdot c_{np\ m} \cdot (x_{0m} - x_m), \quad (2)$$

where $c_{np\ m}$ — spring rate of the pneumatic cylinder of the brake; μ — friction ratio.

2. Equation of motion of the piston of the braking pneumatic cylinder:

$$m \frac{d^2 x_m}{dt^2} = c_{np\ m} \cdot (x_{0m} - x_m) - S_m \cdot p_m - F_{BH\ T} - k_{BT\ T} \cdot \frac{dx_m}{dt}. \quad (3)$$

Here, $c_{np\ T}$ — spring rate of the brake pneumatic cylinder; x_{0T} — coordinate of the initial compression; S_T — effective area of the piston of the drain side of the brake pneumatic cylinder, m^2 ; P_M — air pressure, respectively, in the discharge side of the brake pneumatic cylinder, Pa; $F_{BH\ T}$ — external forces, N; $k_{BT\ T}$ — viscosity friction coefficient.

3. Mass expenditure balance equations:

$$G_{p2}(t) - G_{m1}(t) + G_{c\&c}(t) = 0, \quad (4)$$

$$G_{m2}(t) - G_{p3}(t) - G_{dp}(t) + G_{c\&c}(t) = 0, \quad (5)$$

$$G_{dp1}(t) - G_{dp2}(t) - G_{yy1}(t) + G_{c\&c}(t) = 0, \quad (6)$$

$$G_{dp3}(t) - G_{dp4}(t) - G_{yy2}(t) + G_{c\&c}(t) = 0, \quad (7)$$

$$G_{yy}(t) - G_{py4}(t) + G_{c\&c}(t) = 0. \quad (8)$$

Here, $G_{c\&c}(t)$ — gas mass flow rate under compression in the chamber; $G_{p2}(t), G_{p3}(t)$ — mass flow through distributors; $G_{m1}(t)$ and $G_{m2}(t)$ mass flow rate in the discharge and drain chambers of a rodless pneumatic cylinder of long-stroke movements; $G_{dp}(t), G_{dp1}(t), G_{dp2}(t), G_{dp3}(t), G_{dp4}(t)$ — mass flow through throttles in the drain line, at the inlet to the nozzle unit of the jet sensor and at the outlet of the nozzle unit; $G_{yy1}(t), G_{yy2}(t), G_{yy}(t), G_{py4}(t)$ — mass flow rate in the control channels of the control device, at the outlet of the control device, distributor of brake pneumatic cylinders [7].

$$G_{c\&c}(t) = \frac{\rho \cdot \pi \cdot V}{4 \cdot E \cdot R \cdot T} \cdot \frac{dp}{dt}, \quad (9)$$

where $\rho = 1.288 \text{ kg/m}^3$ — air density; V — volume of the chamber; $R = 287 \text{ J/(kg}\cdot\text{k)}$ — gas constant; E — volume modulus of elasticity of air; T — temperature at the point; $\frac{dp}{dt}$ — pressure variation at the point [6].

$$G_{m1}(t) = \frac{W_1}{k \cdot R \cdot T} \cdot \frac{dp_1}{dt}, \quad (10)$$

$$G_{m2}(t) = \frac{W_2}{k \cdot R \cdot T} \cdot \frac{dp_2}{dt}, \quad (11)$$

where W_1 and W_2 — current volumes in the pressure and drain sides of the base pneumatic cylinder, m³; k — adiabatic exponent (for air, $k = 1.4$).

4. Pressure equations in points:

$$\frac{dp_1}{dt} = \frac{k \cdot f_1 \cdot \sqrt{R \cdot T_M}}{S(x + x_{01}) \sqrt{\xi_1}} \cdot \sqrt{p_M^2 - p_1^2} - \frac{k \cdot f_3 \cdot \sqrt{R \cdot T_M}}{S(x + x_{01}) \sqrt{\xi_2}} \cdot \left(\frac{p_3}{p_1}\right)^{\frac{k-1}{2k}} \cdot \sqrt{p_1^2 - p_3^2} - \frac{k \cdot p_1}{x + x_{01}} \cdot \frac{dx}{dt}, \quad (12)$$

$$\frac{dp_2}{dt} = -\frac{k \cdot f_2 \cdot \sqrt{R \cdot T_M}}{S(L - x + x_{02}) \sqrt{\xi_2}} \cdot \left(\frac{p_2}{p_a}\right)^{\frac{k-1}{2k}} \cdot \sqrt{p_2^2 - p_a^2} + \frac{k \cdot p_2}{L - x + x_{02}} \cdot \frac{dx}{dt}, \quad (13)$$

$$\frac{dp_3}{dt} = \frac{k \cdot f_3 \cdot \sqrt{R \cdot T_3}}{W_1 \cdot \sqrt{\xi_3}} \cdot \sqrt{p_1^2 - p_3^2} - \frac{k \cdot f_4 \cdot \sqrt{R \cdot T_4}}{W_2 \cdot \sqrt{\xi_4}} \cdot \left(\frac{p_3}{p_a}\right)^{\frac{k-1}{2k}} \cdot \sqrt{p_3^2 - p_a^2}, \quad (14)$$

$$\frac{dp_4}{dt} = \frac{k \cdot f_5 \cdot \sqrt{R \cdot T_5}}{W_3 \cdot \sqrt{\xi_5}} \cdot \sqrt{p_1^2 - p_4^2} - \frac{k \cdot f_6 \cdot \sqrt{R \cdot T_6}}{W_4 \cdot \sqrt{\xi_6}} \cdot \left(\frac{p_4}{p_a}\right)^{\frac{k-1}{2k}} \cdot \sqrt{p_4^2 - p_a^2}, \quad (15)$$

$$\frac{dp_5}{dt} = \frac{k \cdot f_6 \cdot \sqrt{R \cdot T_7}}{W_5 \cdot \sqrt{\xi_7}} \cdot \sqrt{p_5^2 - p_a^2}. \quad (16)$$

Here, k — adiabatic exponent; R — gas constant, J/kg · K; T_M — air temperature in the main line, K; P_a — atmospheric pressure, Pa; $P_1 - P_5$ — pressure in the flow parts of the pipeline, Pa; $W_1 - W_5$ — volumes of the flow parts, m³; $\xi_1 - \xi_7$ — resistance values in the line; $f_1 - f_6$ — areas of the flow sections of the pipeline, m²; L — maximum stroke of the piston, m; x_{01}, x_{02} — ratio of the initial volumes of the pneumatic actuator to the useful area of the piston side of the pneumatic cylinder, m; $\frac{dx}{dt}$ — piston speed, m/s.

5. Control loop equations.

Equation of motion of the distributor spool 1:

$$m_{3p1} \frac{d^2 x_{31}}{dt^2} = c_{np1} \cdot x_{31} - F_{c1} \cdot \text{sign}\left(\frac{dx_{31}}{dt}\right) - F_{y1} \cdot \left(\frac{dx_{31}}{dt}\right) - F_{3m1}. \quad (17)$$

Equation of motion of the distributor spool 2:

$$m_{3p2} \frac{d^2 x_{32}}{dt^2} = c_{np2} \cdot x_{32} - F_{c2} \cdot \text{sign}\left(\frac{dx_{32}}{dt}\right) - F_{y2} \cdot \left(\frac{dx_{32}}{dt}\right) - F_{3m2}. \quad (18)$$

Equation of motion of the distributor spool 3:

$$m_{3p3} \frac{d^2 x_{33}}{dt^2} = S_{p3} \cdot p_y - c_{np2} \cdot x_{33} - F_{c3} \cdot \text{sign}\left(\frac{dx_{33}}{dt}\right) - F_{y1} \cdot \left(\frac{dx_{33}}{dt}\right). \quad (19)$$

Equation of motion of the distributor spool 4:

$$m_{3p4} \frac{d^2 x_{34}}{dt^2} = S_{p4} \cdot p_3 - S_{p4} \cdot p_4 - F_{c4} \cdot \text{sign}\left(\frac{dx_{34}}{dt}\right) - F_{y4} \cdot \left(\frac{dx_{34}}{dt}\right). \quad (20)$$

Here, S_p — area of the distributor spool end face, m²; P_3, P_4, P_y — pressure in the control channels, Pa; F_c — resistance forces to the movement of the distributor spool, N; F_y — reaction forces of stops, N; F_{3m} — force of the electromagnet acting on the distributor spool, N; c_{np} — spring compression ratio, N/m; m_{3p} — weight of the distributor spool, kg.

To solve the mathematical model, SimInTech software product was used. We applied the Runge–Kutta method with a variable integration step (Fig. 4–5).

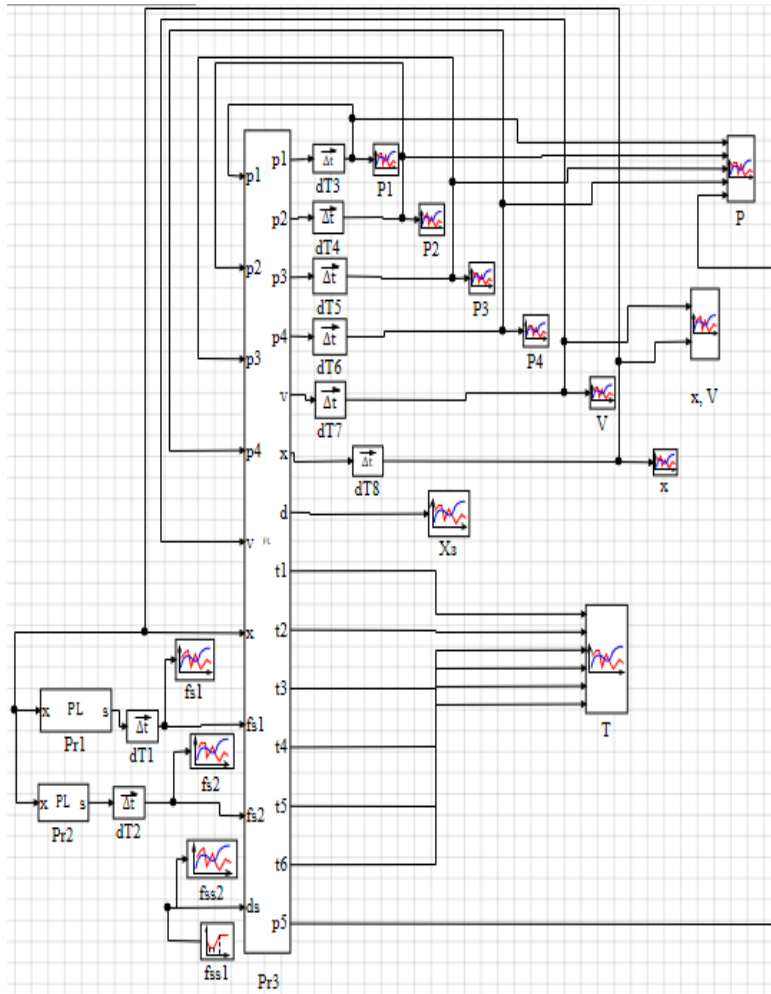


Fig. 4. Model fragment in SimInTech program

Here, $P_{r1}-P_{r3}$ — blocks with the program text; f_{s1}, f_{s2} — graphs of the output of areas 1 and 2 of the jet sensor throttle; f_{ss1} — block of the problem of the areas of the flow sections of the jet sensor; f_{ss2} — graphs of the output of the areas of the flow sections of the jet sensor; $dT1-dT8$ — integration blocks; $P1-P4$ — graphs of the output of the received pressures at points 1–4; P — general schedule for the output of all pressures; V — graph of the obtained speed output of the rodless pneumatic cylinder carriage; x — graph of the received movement output of the rodless pneumatic cylinder carriage; x, V — general graph of the output of the received movement and the speed of the rodless pneumatic cylinder carriage; T — graphs of the output of the obtained temperatures; X_3 — graph of the received movement output of the control distributor spool.

```

1  input p1, p2, p3, p4, V, x, fs1, fs2, ds;
2  output p1, p2, p3, p4, V, x, d, T1, T2, T3, T4, T5, T6, p5;
3  init p1=100000, p2=100000, p3=100000, p4=100000, V=0, x=0;
4  xk=0.31;
5  R=287;
6  Tm=293;
7  ks1=65;
8  ks2=100;
9  ks3=70;
10 ks4=70;
11 d3=0.001;
12 d5=0.006;
13 pm=6*10^5;
14 pa=1.01325*10^5;
15 k=1.4;
16 x01=0.008;
17 x02=0.008;
18 m=6;
19 Fvn=20;
20 dtr1=0.005;
21 dtr2=0.005;
22 D=0.04;
23 Dt=0.04;
24 kv=320;
    
```

a)

```

- L=0.4;
- S=(pi*D^2)/4;
- St=(pi*Dt^2)/4;
- kt=0.4
begin
30 if x<xk+0.0577 then
- p6=0
- else
- p6=pm
- end
begin
- if x>=0.363 then
- p5=pm
- else
- p5=0
40 end
- N=p5*St;
- Ft=kt*N;
begin
- if x<xk then
- d2=0.008
- else
- d2=0.0004
- end;
    
```

b)

```

begin
  if x<xk+0.0577 then
    d=ds
  else
    d=d2=0
  end;
begin
  if x<xk then
    f5=0
  else
    f5=(pi*d5^2)/4
  end;
  f1=(pi*d^2)/4;
  f2=(pi*d2^2)/4;
  f3=(pi*d3^2)/4;
  Ltr=0.01;
  cpr=500000;
  W1=Ltr*((pi*dtr1^2)/4);
  W2=Ltr*((pi*dtr2^2)/4);
begin
  if L<x then Fy=(cpr*(x-L))
  else
    if (L>=x) or (x>=0) then Fy=0
    else if x<0 then Fy=cpr*x
  end
end
end
begin
  if p3>=600000 then p3=600000;
end
begin
  if p3<=pa then p3=pa;
end
begin
  if p4<=pa then p4=pa;
end
  T1=(p1/pm)^((k-1)/k)*Tm;
  T2=(p2/pm)^((k-1)/k)*Tm;
  T3=(pm/pm)^((k-1)/k)*Tm;
  T4=(p3/pm)^((k-1)/k)*Tm;
  T5=(pm/pm)^((k-1)/k)*Tm;
  T6=(p4/pm)^((k-1)/k)*Tm;
  G11=(k*f1*sqrt(R*Tm)/(S*(x+x01)*sqrt(ks1)))*sqrt(abs(pm^2-p1^2));
  G12=(k*f3*sqrt(R*T3)/(S*(x+x01)*sqrt(ks2)))*sqrt(abs(p1^2-p3^2));
  G13=(k*f3*sqrt(R*T5)/(S*(x+x01)*sqrt(ks2)))*sqrt(abs(p1^2-p4^2));
  G14=(k*f1/(x+x01))*V;
  G22=(k*f2*sqrt(R*T2)/(S*(L-x+x02)*sqrt(ks2)))*sqrt(abs(p2^2-pa^2));
  G22=(k*f2/(L-x+x02))*V;
  G31=(k*f3*sqrt(R*T3)/(W1*sqrt(ks3)))*sqrt(p1^2-p3^2);
  G32=(k*f3*sqrt(R*T4)/(W2*sqrt(ks4)))*sqrt(p3^2-pa^2);
  G41=(k*f3*sqrt(R*T5)/(W1*sqrt(ks3)))*sqrt(p1^2-p4^2);
  G42=(k*f3*sqrt(R*T6)/(W2*sqrt(ks4)))*sqrt(p4^2-pa^2);
  p1'=G11-G12-G13-G14;
  p3'=G21-G22;
  p4'=G41-G42;
  x'=V;
  V'=(S*(p1-p2)-Fvn*sign(V)-kvt*V-Fy-Ft*sign(V))/m;
end

```

Fig. 5. Programming block in SimInTech: *a* — part of the source data; *b* — part of the logical functions; *c* — part of the assignment of variables; *d* — skeletal code

The study of the generalized mathematical model of the proposed drive made it possible to obtain graphs of the behavior of the drive during acceleration, deceleration, and stop (Fig. 6), describing the changes in kinematic, power and pneumatic properties of the drive during a typical positioning cycle in real time [15].

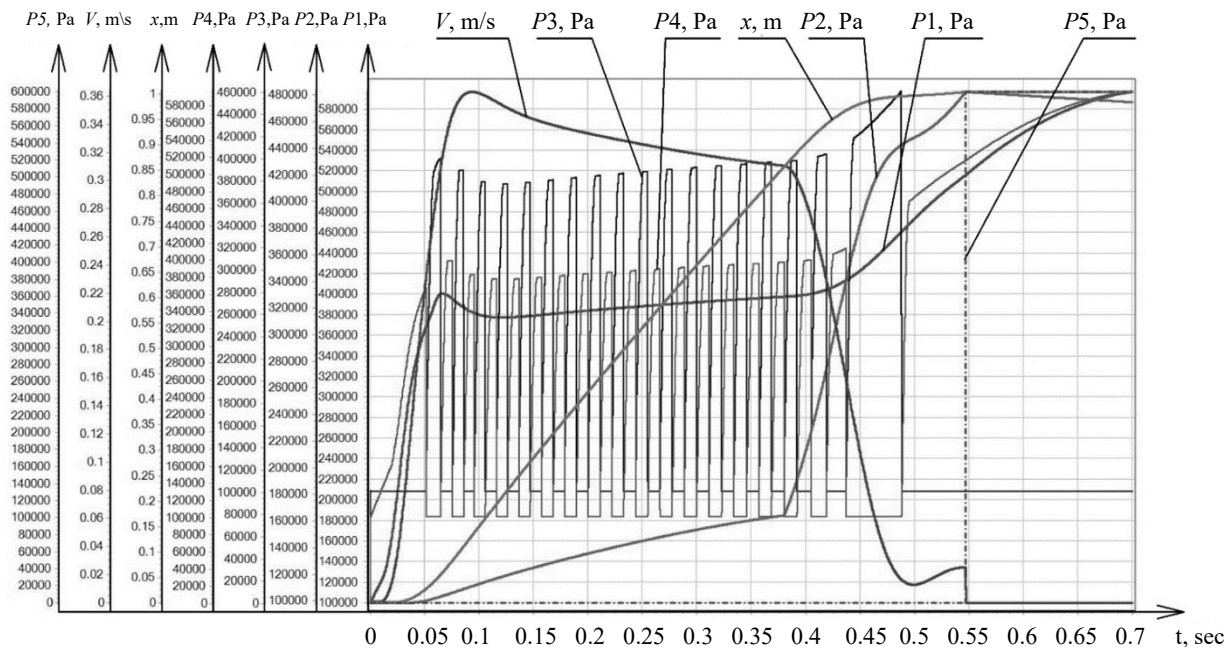


Fig. 6. A set of graphs based on the data of a generalized mathematical model

Discussion and Conclusion. The graph shows a long-stroke movement along the trajectory proposed in Figure 1. The operation of the drive consists of several stages.

1. 0–0.1 sec. Acceleration. The pressure in the pressure side increases to 4 bar, the pneumatic cylinder carriage speed — 1 m/s.

2. 0.1–0.38 sec. Movement at a steady speed. Pressure in the discharge side — about 3.8 bar. Pressure in the drain line increases to 1.6 bar, the pneumatic cylinder carriage speed — 0.85 m/s.

3. 0.38–0.5 sec. Slowing down. Pressure in the pressure and drain sides increases. The pneumatic cylinder carriage speed decreases to 0.075 m/s.

4. 0.5–0.65 sec. Movement with the speed of positioning. Pressure in the pressure and drain sides increases, the pneumatic cylinder carriage speed — 0.075 m/s.

5. 0.65 sec. Switching to braking, activation of an external braking gear.

The graphs obtained confirm that the long-stroke movements of the pneumatic actuator are performed in accordance with the proposed trajectory (Fig. 1), and the control system functions properly. Further research will focus on optimizing the system to reduce the duration and maintain accurate positioning under external influences.

References

1. Korotych DA, Sidorenko VS. Pozitsionnaya sistema upravleniya dlinnokhodovymi pnevmoprivodami. In: *Proc. XXIII Int. Sci.-Tech. Conf. of students and postgraduates "Hydraulic Machines, Hydraulic Drives and Hydropneumodynamics", dedicated to the 100th anniversary of Boris T. Emtsev, Dr.Sci. (Eng.), Honored Professor of MEI, Honorary Academician of Water Sciences*. Moscow: Izd-vo "Mir nauki"; 2019. P. 157–163. URL: <https://www.elibrary.ru/item.asp?id=41599329> (accessed: 04.05.2023). (In Russ.)
2. Jihong Wang, Gordon T. Energy Optimal Control of Servo-Pneumatic Cylinders through Nonlinear Static Feedback Linearization. *Journal of Dynamic Systems, Measurement, and Control*. 2012;134(5):051005. <https://doi.org/10.1115/1.4006084>
3. Dao The Anh. Pozitsionnyi pnevmoprivod povyshennogo bystrodeistviya i tochnosti. Cand.Sci. (Engineering) diss. Rostov-on-Don; 2016. 206 p. URL: <https://viewer.rsl.ru/ru/rsl01008559478> (accessed: 04.05.2023). (In Russ.)
4. Sidorenko VS, Korotych DA, Grishenko VI, Kharchenko AN. Simulation of Pneumatic Actuator Position System for Long Stroke Mounting Movements. *IOP Conference Series: Materials Science and Engineering*. 2021;1029:012039. <https://doi.org/10.1088/1757-899X/1029/1/012039>
5. Gallyamov ShR, Starikov KV, Celishev VA. Experimental Research of Characteristics of the Pneumatic Actuator FESTO with Proportional Allocation of the Expenditure. *Vestnik UGATU*. 2011;15(1(41)):26–33. URL: <http://journal.ugatu.su/index.php/Vestnik/article/view/900> (accessed: 04.05.2023).
6. Mosadegh B, Polygerinos P, Keplinger Ch, Wennstedt S, Shepherd RF, Gupta U, et al. Pneumatic Networks for Soft Robotics that Actuate Rapidly. *Advanced Functional Materials*. 2014;24(15):2163–2170. <https://doi.org/10.1002/adfm.201303288>
7. Dao The Anh, Sidorenko VS. The Study of the Dynamical System High-Speed Pneumatic Robot Position. *Fundamental Research*. 2015;(7–2):285–292. URL: <https://fundamental-research.ru/ru/article/view?id=38687> (accessed: 06.05.2023).
8. Dolgov GA. Kombinirovannyi pnevmoprivod povorotno-delitel'nykh mekhanizmov povyshennogo bystrodeistviya i tochnosti. In: *Proc. XXIII Int. Sci.-Tech. Conf. of students and postgraduates "Hydraulic Machines, Hydraulic Drives and Hydropneumodynamics", dedicated to the 100th anniversary of Boris T. Emtsev, Dr.Sci. (Eng.), Honored Professor of MEI, Honorary Academician of Water Sciences*. Moscow: Izd-vo "Mir nauki"; 2019. P. 119–126. (In Russ.)
9. Lemesenko M, Molev M, Golovin I. Hydraulic Technological Machines with Adaptive Drive Structure. *MATEC Web of Conferences*. 2018;224:02087. <https://doi.org/10.1051/mateconf/201822402087>
10. Dao T.A., Sidorenko V.S., Dymochkin D.D. Study on positioning accuracy of automated pneumatic drive with an outer brake. *Vestnik of Don State Technical University*. 2015;15(4):46–53. (In Russ.) <https://doi.org/10.12737/16077>
11. Gorin A, Tokmakov N, Kyznetsov I. Substantiation of Parameters of Machine with Volumetric Hydraulic Drive for Formation of Wells in Ground. In: *Proc. 5th International Conference on Industrial Engineering (ICIE)*. Cham: Springer; 2019. P. 1315–1323. URL: https://link.springer.com/chapter/10.1007/978-3-030-22063-1_139 (accessed: 04.05.2023).
12. Vardhan A, Dasgupta K, Mishra SK. Dynamic Analysis of a Closed-Circuit Hydraulic Drive System Used in the Rotary Head of Blasthole Drilling Machine Using MATLAB-Simulink Environment. In: *Proceedings of the Institution of Mechanical Engineers, Part I: Journal of Systems and Control Engineering*. 2019;233(6):702–719. <https://doi.org/10.1177/0959651818808870>

13. Obukhova EN, Grishchenko VI, Dolgov GA. Formalization of Dynamic Model of Pneumatic Drive with Variable Structure. *MATEC Web of Conferences*. 2018;226:02022. <https://doi.org/10.1051/mateconf/201822602022>
14. Seppe Terryn, Joost Brancart, Dirk Lefeber, Guy Van Assche, Bram Vanderborght. Self-Healing Soft Pneumatic Robots. *Science Robotics*. 2017;2(9):4268. <https://www.science.org/doi/10.1126/scirobotics.aan4268> (accessed: 04.05.2023).
15. Obukhova EN, Popov AN. Synergetic Synthesis of Nonlinear Adaptive Control for Pneumatic Drives. In: *Proc. IV Int. Conf. on Control in Technical Systems (CTS)*. New York: IEEE; 2021. <https://doi.org/10.1109/CTS53513.2021.9562786>

Received 01.06.2023

Revised 28.06.2023

Accepted 07.07.2023

About the Authors:

Daniil A. Korotych, Teaching assistant and Postgraduate student of the Hydraulics, Hydropneumodynamics and Heat Management Department, Don State Technical University (1, Gagarin sq., Rostov-on-Don, 344003, RF), [ScopusID](#), [ORCID](#), [ResearcherID](#), [Автор ID](#), daniilberuk@gmail.com

Valentin S. Sidorenko, Dr.Sci. (Eng.), Professor of the Hydraulics, Hydropneumodynamics and Heat Management Department, Don State Technical University (1, Gagarin sq., Rostov-on-Don, 344003, RF), [ScopusID](#), [ORCID](#), [ResearcherID](#), [Автор ID](#), vsidorenko@donstu.ru

Sergey P. Prikhodko, Teaching assistant and Postgraduate student of the Hydraulics, Hydropneumodynamics and Heat Management Department, Don State Technical University (1, Gagarin sq., Rostov-on-Don, 344003, RF), [ScopusID](#), [ORCID](#), [ResearcherID](#), [Автор ID](#), sergey.161.96@gmail.com

Claimed Contributorship:

DA Korotych: preparation of the text, development of the mathematical model, modeling in the program, analysis of research results.

VS Sidorenko: academic advising, basic concept formulation, research objectives and tasks.

SP Prikhodko: design and revision of the text, correction of the conclusions.

Conflict of interest statement: the authors do not have any conflict of interest.

All authors have read and approved the final manuscript.

Поступила в редакцию 01.06.2023

Поступила после рецензирования 28.06.2023

Принята к публикации 07.07.2023

Об авторах:

Даниил Андреевич Коротыч, ассистент и аспирант кафедры гидравлики, гидропневмоавтоматики и тепловых процессов Донского государственного технического университета (344003, РФ, г. Ростов-на-Дону, пл. Гагарина, 1), [ScopusID](#), [ORCID](#), [ResearcherID](#), [Автор ID](#), daniilberuk@gmail.com

Валентин Сергеевич Сидоренко, доктор технических наук, профессор кафедры гидравлики, гидропневмоавтоматики и тепловых процессов Донского государственного технического университета (344003, РФ, г. Ростов-на-Дону, пл. Гагарина, 1), [ScopusID](#), [ORCID](#), [ResearcherID](#), [Автор ID](#), vsidorenko@donstu.ru

Сергей Павлович Приходько, ассистент и аспирант кафедры гидравлики, гидропневмоавтоматики и тепловых процессов Донского государственного технического университета (344003, РФ, г. Ростов-на-Дону, пл. Гагарина, 1), [ScopusID](#), [ORCID](#), [ResearcherID](#), [Автор ID](#), sergey.161.96@gmail.com

Заявленный вклад соавторов:

Д.А. Коротыч — подготовка текста, составление математической модели, моделирование в программе, анализ результатов исследования.

В.С. Сидоренко — научное руководство, формирование основной концепции, цели и задач исследования.

С.П. Приходько — оформление и доработка текста, корректировка выводов.

Конфликт интересов: авторы заявляют об отсутствии конфликта интересов.

Все авторы прочитали и одобрили окончательный вариант рукописи.

INFORMATION TECHNOLOGY, COMPUTER SCIENCE AND MANAGEMENT



UDC 57.087

Original article

<https://doi.org/10.23947/2687-1653-2023-23-3-296-306>

GATCGGenerator: New Software for Generation of Quasirandom Nucleotide Sequences

Olga Yu. Kiryanova¹ , Ravil R. Garafutdinov² , Irek M. Gubaydullin³ , Aleksei V. Chemeris² 

¹ Ufa State Petroleum Technological University, Ufa, Russian Federation

² Institute of Biochemistry and Genetics, Ufa Federal Research Center, RAS, Ufa, Russian Federation

³ Institute of Petrochemistry and Catalysis, RAS, Ufa, Russian Federation

✉ olga.kiryanova27@gmail.com

Abstract

Introduction. In recent decades, knowledge about DNA has been increasingly used to solve biological problems (calculations using DNA, long-term storage of information). Principally, we are talking about cases when it is required to select artificial nucleotide sequences. Special programs are used to create them. However, existing generators do not take into account the physicochemical properties of DNA and do not allow obtaining sequences with a pronounced “non-biological” structure. In fact, they generate sequences by distributing nucleotides randomly. The objective of this work is to create a generator of quasirandom sequences with a special nucleotide structure. It should take into account some physicochemical features of nucleotide structures, and it will be involved in storing non-biological information in DNA.

Materials and Methods. A new GATCGGenerator software for generating quasirandom sequences of nucleotides was described. It was presented as SaaS (from “software as a service”), which provided its availability from various devices and platforms. The program generated sequences of a certain structure taking into account the guanine-cytosine (GC) composition and the content of dinucleotides. The performance of the new program algorithm was presented. The requirements for the generated nucleotide sequences were set using a chat in Telegram, the interaction with the user was clearly shown. The differences between the input parameters and the specific nucleotide structures obtained as a result of the program were determined and generalized. Also, the time costs of generating sequences for different input data were given in comparison. Short sequences differing in type, length, GC composition and dinucleotide content were studied. The tabular form shows how the input and output parameters are correlated in this case.

Results. The developed software was compared to existing nucleotide sequence generators. It has been established that the generated sequences differ in structure from the known DNA sequences of living organisms, which means that they can be used as auxiliary or masking oligonucleotides suitable for molecular biological manipulations (e.g., amplification reactions), as well as for storing non-biological information (images, texts, etc.) in DNA molecules. The proposed solution makes it possible to form specific sequences from 20 to 5,000 nucleotides long with a given number of dinucleotides and without homopolymer fragments. More stringent generation conditions remove known limitations and provide the creation of quasirandom sequences of nucleotides according to specified input parameters. In addition to the number and length of sequences, it is possible to determine the GC composition, the content of dinucleotides, and the nature of the nucleic acid (DNA or RNA) in advance. Examples of short sequences differing in length, GC composition and dinucleotide content are given. The obtained 30-nucleotide sequences were tested. The absence of 100 % homology with known DNA sequences of living organisms was established. The maximum coincidence was observed for the generated sequences with a length of 25 nucleotides (similarity of about 80 %). Thus, it has been proved that GATCGGenerator can generate non-biological nucleotide sequences with high efficiency.

Discussion and Conclusion. The new generator provides the creation of nucleotide sequences *in silico* with a given GC composition. The solution makes it possible to exclude homopolymer fragments, which improves qualitatively the physicochemical stability of sequences.

Keywords: GATCGGenerator, nucleotide sequences generator, synthetic nucleic acids, random sequences, data storage in DNA, steganography, NYRN-oligonucleotides, calculations with DNA, cryptography, DNA-tagging in hydrology

Acknowledgements: the authors would like to thank the reviewers for valuable comments that contributed to the improvement of the article.

Funding information. The research is done on RFFI grant no. 20–07–00222.

For citation. Kiryanova OYu, Garafutdinov RR, Gubaydullin IM, Chemeris AV. GATCGGenerator: New Software for Generation of Quasirandom Nucleotide Sequences. *Advanced Engineering Research (Rostov-on-Don)*. 2023;23(3):296–306. <https://doi.org/10.23947/2687-1653-2023-23-3-296-306>

Научная статья


GATCGGenerator: новый генератор для создания квазислучайных нуклеотидных последовательностей

О.Ю. Кирьянова¹ , Р.Р. Гарафутдинов² , И.М. Губайдуллин³ , А.В. Чемерис² 

¹ Уфимский государственный нефтяной технический университет, г. Уфа, Российская Федерация

² Институт биохимии и генетики — обособленное структурное подразделение Федерального государственного бюджетного научного учреждения «Уфимский федеральный исследовательский центр», г. Уфа, Российская Федерация

³ Институт нефтехимии и катализа — обособленное структурное подразделение Федерального государственного бюджетного научного учреждения «Уфимский федеральный исследовательский центр», г. Уфа, Российская Федерация

 olga.kiryanova27@gmail.com

Аннотация

Введение. В последние десятилетия знания о ДНК все шире применяются для решения небологических задач (вычисления с помощью ДНК, долговременное хранение информации). В первую очередь речь идет о случаях, когда необходимо подобрать искусственные нуклеотидные последовательности. Для их создания используются специальные программы. Однако существующие генераторы не учитывают физико-химические свойства ДНК и не позволяют получать последовательности с явно выраженной «небиологической» структурой. Фактически они генерируют последовательности, распределяя нуклеотиды случайным образом. Целью данной работы является создание генератора квазислучайных последовательностей с особой нуклеотидной структурой. Он должен учитывать некоторые физико-химические особенности нуклеотидных структур и будет задействован при хранении небологической информации в ДНК.

Материалы и методы. Описано новое программное обеспечение GATCGGenerator для генерации квазислучайных последовательностей нуклеотидов. Оно предоставляется как SaaS (от англ. software as a service — программное обеспечение как услуга), что обеспечивает его доступность с разных устройств и платформ. Программа генерирует последовательности определенной структуры с учетом гуанин-цитозинового (GC) состава и содержания динуклеотидов. Представлена работа алгоритма новой программы. Требования к сгенерированным нуклеотидным последовательностям заданы с помощью чата в «Телеграм» (Telegram), наглядно показано взаимодействие с пользователем. Определены и обобщены различия входных параметров и получаемых в результате работы программы конкретных нуклеотидных структур. Также в сопоставлении даны временные затраты генерации последовательностей при различных входных данных. Изучены короткие последовательности, различающиеся по типу, длине, GC-составу и содержанию динуклеотидов. В табличном виде показано, как в этом случае соотносятся входные и выходные параметры.

Результаты исследования. Созданное программное обеспечение сравнили с существующими генераторами нуклеотидных последовательностей. Установлено, что генерируемые последовательности отличаются по структуре от известных ДНК-последовательностей живых организмов, а значит, могут быть использованы в качестве вспомогательных или маскирующих олигонуклеотидов, пригодных для молекулярно-биологических

манипуляций (например — реакции амплификации), а также для хранения в молекулах ДНК небологической информации (изображений, текстов и т. д.). Предложенное решение дает возможность формировать специфические последовательности длиной от 20 до 5 000 нуклеотидов с заданным числом динуклеотидов и без гомополимерных участков. Более жесткие условия генерации снимают известные ограничения и позволяют создавать квазислучайные последовательности нуклеотидов по заданным входным параметрам. Кроме количества и длины последовательностей можно заранее определить GC-состав, содержание динуклеотидов и природу нуклеиновой кислоты (ДНК или РНК). Приводятся примеры коротких последовательностей, различающихся по длине, GC-составу и содержанию динуклеотидов. Полученные 30-нуклеотидные последовательности прошли проверку. Установлено отсутствие 100-процентной гомологии с известными ДНК-последовательностями живых организмов. Максимальное совпадение наблюдалось для сгенерированных последовательностей длиной 25 нуклеотидов (сходство около 80 %). Таким образом доказано, что GATCGGenerator может с высокой эффективностью генерировать небологические нуклеотидные последовательности.

Обсуждение и заключение. Новый генератор позволяет создавать нуклеотидные последовательности *in silico* с заданным GC-составом. Решение дает возможность исключить гомополимерные фрагменты, что качественно улучшает физико-химическую стабильность последовательностей.

Ключевые слова: GATCGGenerator, генератор нуклеотидных последовательностей, синтетические нуклеиновые кислоты, случайные последовательности, хранение данных в ДНК, стеганография, NYRN-олигонуклеотиды, вычисления с помощью ДНК, криптография, ДНК-метчики в гидрологии

Благодарности: авторы выражают признательность рецензентам за ценные замечания, способствовавшие улучшению статьи.

Финансирование. Работа выполнена в рамках гранта РФФИ 20–07–00222.

Для цитирования. Кирьянова О.Ю., Гарафутдинов Р.Р., Губайдуллин И.М. Чемерис А.В. GATCGGenerator: новый генератор для создания квазислучайных нуклеотидных последовательностей. *Advanced Engineering Research (Rostov-on-Don)*. 2023;23(3):296–306. <https://doi.org/10.23947/2687-1653-2023-23-3-296-306>

Introduction. DNA is a unique biopolymer that provides storage, transmission and reproduction of genetic information in living organisms. DNA molecules consist of four types of nucleotides containing nitrogenous bases: adenine (A), guanine (G), cytosine (C), thymine (T). Their possible combinations provide nucleotide sequences forming functional genetic elements. In molecular biology and genetics, the basic investigations are carried out on nucleotide sequences of living organisms, but there is an increasing need to create artificial sequences, especially, when solving non-biological tasks (e.g., DNA calculations [1, 2], storage in DNA [3], cryptography [4], DNA tags in hydrology [5], etc.).

It is expected that by the end of 2040, the volume of information will reach several yottabytes (10^{24}), which requires its structuring and storage. Both of these processes affect significantly the consumption of energy resources, as well as the production of storage devices and peripheral devices (hard drives, solid-state drives). To store such an amount of information, more than 10^9 kg of extra pure silicon is required [6], which may not be enough. The solution is seen in using the principles of DNA to work with large-scale amounts of data.

Nucleotide sequences are easily digitized by assigning the corresponding binary codes to individual nucleotides [7–11] or blocks of nucleotides [12–14]; therefore, text, graphic or multimedia files can be converted into nucleotide sequences [15–18]. Artificial nucleotide sequences can be made manually or generated using special software (DNA generators), depending on the tasks being solved. Some DNA generators were developed as independent applications,

others — as part of software packages designed to solve general [19]^{1, 2, 3, 4, 5} or specific tasks [20]. As a rule, DNA generators are developed on the basis of combinatorial approaches and produce random sequences of a given length of guanine-cytosine (GC) composition. However, such software solutions do not take into account the chemical properties of nucleotides and do not provide obtaining sequences with a certain structure (e.g., without homopolymer sites or long repeating motifs). Therefore, the sequences created by such generators cannot always be reproduced in the laboratory. Moreover, such sequences may be identical to DNA fragments existing in nature, which introduces ambiguity when trying to encode information of a non-biological nature.

The presented work is aimed at creating a generator of nucleotide sequences of a special structure that can be used when encoding text, graphic and other information in DNA molecules.

Materials and Methods. The criteria that should be kept in mind when creating sequences were defined. The need to vary the GC composition, set a certain number of dinucleotides, and exclude homopolymer sites in sequences was taken into account.

A team of authors has developed the GATCGGenerator program in Python 3.6 (Anaconda distribution)⁶. To create a bot⁷ in Telegram, Numpy 1.19 [21] and the Python GATCGGenerator library were used. The solution was provided as SaaS (from “software as a service”), which opened up the possibility of access from different devices and platforms.

Input parameters included the number of sequences, their length, GC composition, and dinucleotide content. The generator excluded repeats with a length of two nucleotides more than four times. The result was presented as a CSV file, which contained the following information: sequence, GC composition, and the number of all nucleotides.

Repeats and homopolymer fragments were stored as a separate list. First, a sequence of four elements was randomly generated (`random.choice(nuc)`, where `nuc = 'ACGT'`). Then the search for repetitions was performed. If there was at least one item from the list, a new random generation was performed. Next, the GC and NN composition was calculated. If the NN composition did not match the user-defined range, the paired nucleotide was replaced randomly and the GC composition was recalculated. If the sequence matched the input parameters, it was written to a set of sequences.

Below is the operation of the program algorithm.

Type, GCmin, GCmax — range of possible GC content, NNmin, NNmax — range of possible dinucleotide content
NN%, N — quantity, S — sequence, l — sequence length, count — total number of sequences

Pseudocode

Start

Input (Type, GC, NN, N)

Comprehension of a list of repeating motifs, homopolymer sites `rep.list`

Count = 0

sequences = set()

IF $i \leq N$?

 IF (`rep.list(k) ⊂ S`)?

 Return to **step 1**.

 ELSE

$NN = \text{len}(\text{DI_REGEX.findall}(\text{"join}(S))$

$NN_perc = (NN \times 2 / l) \times 100$

 IF $NNmin \leq NN_perc \leq NNmax$

$GC = S.\text{count}('G') + S.\text{count}('C') / l \times 100$

 IF $GCmin \leq GC \leq GCmax$

 IF `type == DNA`

Step 2.

$A_perc = S.\text{count}('A') / l \times 100$

¹ Nucleotide Sequence Generator. nucleotide-generator.herokuapp.com. URL: <https://nucleotide-generator.herokuapp.com/> (accessed: 01.12.2022).

² DNA Sequence Tools: Random Sequence Generator. molbiotools.com. URL: <http://www.molbiotools.com/randomsequencegenerator.html> (accessed: 01.12.2022).

³ Random DNA Sequence Generator. faculty.ucr.edu. URL: <http://www.faculty.ucr.edu/~mmaduro/random.htm> (accessed: 02.12.2022).

⁴ Random DNA Sequence GenScript. genscript.com. URL: https://www.genscript.com/sms2/random_dna.html (accessed: 04.12.2022).

⁵ Random DNA Generator. Computer software. URL: <http://54.235.254.95/cgi-bin/gd/gdRandDNA.cgi> (accessed: 04.12.2022).

⁶ Anaconda. Anaconda Inc. anaconda.com. URL: <https://www.anaconda.com/> (accessed: 20.01.2023).

⁷ Python telegram bot. github.com. URL: <https://github.com/python-telegram-bot/python-telegram-bot> (accessed: 01.12.2022).

```

G_perc = S.count('G') / 1 × 100
C_perc = S.count('C') / 1 × 100
T_perc = S.count('T') / 1 × 100
U_perc = S.count('U') / 1 × 100
Count = count + 1
sequences.add(S)
ELSE S = S.replace('T', 'U')
Step 2.)
ELSE
    Return to step 1.
ELSE
    Random replacement of the second repeated character,
    GC = S.count('G') + S.count('C') / 1 × 100
Output Sequences: (S, GC%, NN%, A%, G%, C%, T/U%)
End

```

The requirements for the generated nucleotide sequences were set using Telegram chat. An example of user interaction is shown in Figure 1.

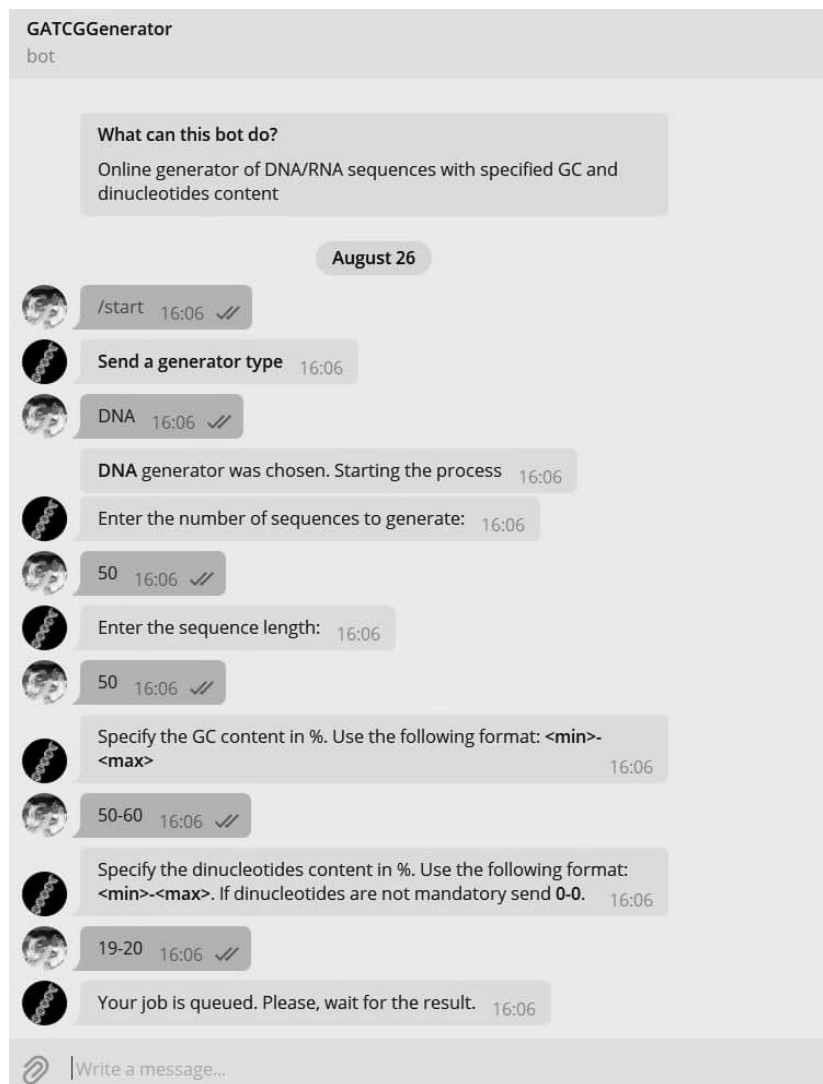


Fig. 1. Example of a user chat in Telegram

In the framework of the presented work, the functionality of random sequence generators and GATCGGenerator were compared. The differences between the input parameters and the specific nucleotide structures obtained as a result of the program were determined (Table 1).

Table 1

Comparison of GATCGGenerator functionality to other nucleotide sequence generators

	GATCGGenerator [20]	Nucleotide Sequence Generator ⁸	DNA Sequence Tools: Random Sequence Generator ⁹	Random DNA Sequence Generator ¹⁰	Random DNA Sequence ¹¹	Random DNA Generator ¹²
Maximum length (nucleotides)	5,000	1,000,000			10,000	1,000
Number of sequences	100	1			1; 10; 50; 100	100
Input GC composition (%)	+	−	+		−	+ (*)
GC composition (%)	interval		number		−	number
Input NN composition (%)		−				
No homopolymer sites						
Sequence type	DNA/RNA	DNA	DNA/RNA / Protein	DNA		
Output of results	.CSV file	Text on the screen				
(*) User enters AT composition						

GATCGGenerator has a broader functionality, it allows the user to specify the number of dinucleotides, create sequences without extended homopolymer sites and repeats that affect the success of the experiment. In existing generators, it is only possible to vary the GC composition.

The program created by the authors of this research generates a given number of quasi-random sequences of nucleotides that do not have homology with natural DNA, but are suitable for molecular biological manipulations.

Research Results. GATCGGenerator allows you to generate specific DNA or RNA sequences from 20 to 5,000 nucleotides long, containing a given number of dinucleotides and not containing homopolymer sites (no more than two identical nucleotides located side by side). More stringent generation conditions can cause a long selection of sequences. As an example, we give a small range of possible content of guanine and cytosine and dinucleotides (e.g., GC composition 45–50 % and NN composition 10–20 %). The operating period of the program for various input data is shown in Table 2.

Table 2

Sequence generation time for different inputs

Data inputs				Time (s)
Length	Number	GC, %	NN, %	
20	10	50–60	20–50	3.45
30	10	50–60	20–50	3.91
20	10	50–60	40–50	9.74
30	10	50–60	40–50	9.53
30	10	40–50	20–20	8.80
1,000	100	45–50	40–50	11.49
2,000	100	45–50	10–20	240.25
5,000	100	50–60	20–50	11.57

GATCGGenerator, through more stringent sequence generation conditions, removes the limitations of known DNA generators and creates quasi-random sequences of nucleotides depending on the indicated input parameters. You can specify the required number of sequences, their length, GC composition and dinucleotide content, as well as the nature of the nucleic acid (DNA or RNA). Specifically, sequences created by GATCGGenerator can be used in DNA steganography, applied to protect and transmit information through hiding the message content in the nucleotide sequence [3].

The proposed software solution (GATCGGenerator) provides obtaining a set of quasi-random sequences of nucleotides depending on user-defined input parameters (type of nucleic acid, sequence length, GC and dinucleotide composition). GATCGGenerator excludes the presence of any nucleotide repeats and homopolymer sites longer than three elements. The generated sequences can be used as service or masking sequences (e.g., in DNA steganography) and are suitable for any non-biological enzymatic manipulations. It is possible to generate numerous artificial nucleotide sequences and use them to create a universal oligotheca suitable for multiple encoding of non-biological data and their long-term storage.

The data presented in Table 3 summarizes the results of the program. For a certain type of nucleic acid (in this case, DNA), the following data is shown: the content of dinucleotides (NN %), the number of generated sequences, their length (nucleotides — nt), and GC composition.

Table 3

Examples of short sequences differing in length, GC composition, and dinucleotide content (%)

Input parameters					Nucleotide sequence, 5'→3'	Output parameters		
Type	Number	Length, nt	GC, %	NN, %*		Length, nt	GC, %	NN, %*
DNA	5	30	41–50	20	CTGG**TATATCGGAATCATATCGCGCAGTGT	30	46.7	20.0
					AATCAGCTAGTAGGACGCAGTAGTGAATCA	30	43.3	20.0
					GAATGTAGTCCTAGGCACATACTACGTAGC	30	46.7	20.0
					AGTTGCACTGAAGTCTATGATCTGGCATGC	30	46.7	20.0
					GACACACTACTATGGACGTGAGGCAC TTAC	30	50.0	20.0
	TCAGCTCAGCGCCAATCGAGCTTATAGTGC		30		53.3	20.0		
	GAGGCTATCGTCAAGCATAGACCGTGTGCT		30		53.3	20.0		
	GACTCAGTAGCTGCTCCGGACATACAGCCT		30		56.7	20.0		
	TCGCGCGTTAGACTTAGGTCTCATCGCAGC		30		56.7	20.0		
	ACGCTCACAGGAGTTCGCATCGAACGATGC		30		56.7	20.0		
	5	41–50	0	ACGACAGTGATATAGCACGACGTGCTCATA	30	46.7	0.0	
				GACTACATCTGATAGTACACGTGCTGCACT	30	46.7	0.0	
				TCTATCTCTGCTAGAGCGCTCGTCACTCTA	30	50.0	0.0	
				TCTGATCTACTATAGCGATACGTGAGAGTG	30	43.3	0.0	
				ACACATATATCGACGCACGCGTCGTAGTAC	30	50.0	0.0	
	5	50	41–60	20	TGCATGACCATGCTTGCGGTAGACATTCA GACGCGCGAATAGTAGGACGA	50	52.0	20.0
					GCATACGAGTGGCATAACATATTAGACTAT ACGGTAGTGATATGGTGCAA	50	42.0	20.0
					CTGAGACTCCTCTCTGTGGAGCTCCTAGTA CCGTACGCGTGCTCTGAAG	50	58.0	20.0
					CTGTGTGAACATACGATGCATTCTCATCTC GGTATGGCTGAAGTGCACAT	50	46.0	20.0
					GCGCTGACGTCATGGTTCATACCAATGTA GCATGATGTGCGATAGGCACA	50	50.0	20.0

* NN shows the fraction (%) of the dinucleotides contained in the nucleotide sequence.

** Dinucleotides are highlighted in bold.

* NN shows the fraction (%) of the dinucleotides contained in the nucleotide sequence.

** Dinucleotides are highlighted in bold.

The obtained 30-nucleotide sequences were tested using the Blast tool from NCBI. The absence of 100% homology with known DNA sequences of living organisms was identified. The maximum coincidence was observed for the generated sequences with a length of 25 nucleotides (similarity is about 80 %). This indicates the ability of the GATCGGenerator to generate non-biological nucleotide sequences with high efficiency. It can be assumed that the sequences generated in this way do not have an absolute coincidence with the nucleotide fragments of living organisms.

In this case, special DNA-oligonucleotides of artificial origin containing informative and service parts can be used as a convenient information carrier. Recently, the authors of this work have proposed the use of NYRN-oligonucleotides [14] consisting of:

- internal part (YR)_n encoding the encrypted information;
- service (auxiliary) parts S1 and S2 flanking sequence (YR)_n (Fig. 2).

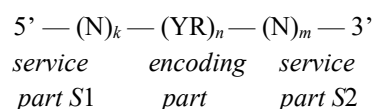


Fig. 2. Structure of NYRN-oligonucleotides: N — degenerate nucleotides; Y — pyrimidines (C or T); R — purines (A or G); *k, n, m* — indices corresponding to the length of the part

The length of the sites (*n*, *k* and *m*) may vary, but the structure of the service parts should provide the successful course of amplification reactions (length more than 18 nt, 40–60 % GC composition, absence of homopolymer sites and repeats). GATCGGenerator allows including NN dinucleotides containing identical paired nucleotides (e.g., AA, GG, CC, TT or UU for RNA), which can increase the specificity of molecular hybridization of nucleic acids.

Discussion and Conclusion. Thus, based on the results of the scientific investigation performed, a software solution (GATCGGenerator) has been proposed, which, in comparison to traditional approaches, assumes more stringent conditions for generating sequences. Due to this feature, the limitations of known DNA generators are removed, and quasi-random sequences of nucleotides are formed depending on the specified input parameters. The obtained 30-nucleotide sequences were studied. The test allowed us to establish the absence of 100 % homology with known DNA sequences of living organisms. The generated sequences with a length of 25 nucleotides coincided as much as possible (by about 80 %).

Note also that in order to hide information in NYRN-oligonucleotides, it is required to mix them with masking DNA. Masking sequences should be similar to sequences of NYRN-oligonucleotides, so that when trying to read hidden information, it would be impossible to recognize them without key sequences. The addressee should know the key sequences — primers to the service sites of NYRN-oligonucleotides. The addressee can decipher the transmitted message by isolating informative nucleotide sequences using a polymerase chain reaction followed by sequencing. A set of NYRN- and masking oligonucleotides can be easily obtained using GATCGGenerator, synthesized, and then stored as an oligotheca. To do this, it is enough to determine the optimal NYRN-oligonucleotides with subsequent filling of the oligotheca. In the future, it is planned to conduct laboratory experiments in order to test the proposed method of storing non-biological information and checking the viability of oligotheca obtained using the generator.

References

1. Malinetski GG, Mitin NA, Naumenko SA. Nanobiology and Synergetics. Problems and Ideas. Part 2. *Keldysh Institute Preprints*. 2005;29:1–26. URL: <http://mi.mathnet.ru/ipmp722> (accessed: 01.06.2023).
2. Katz E. (ed) *DNA- and RNA-Based Computing Systems*, 1st ed. Weinheim: Wiley-VCH; 2021. 408 p.
3. Ceze L, Nivala J, Strauss K. Molecular Digital Data Storage Using DNA. *Nature Reviews Genetics*. 2019;20:456–466. <https://doi.org/10.1038/s41576-019-0125-3>
4. Kaundal AK, Verma AK. DNA Based Cryptography: A Review. *International Journal of Information and Computation Technology*. 2014;4(7):693–698.
5. Aquilanti L, Clementi F, Landolfo S, Nanni T, Palpacelli S, Tazioli A. A DNA Tracer Used in Column Tests for Hydrogeology Applications. *Environmental Earth Sciences*. 2013;70:3143–3154. <https://doi.org/10.1007/s12665-013-2379-y>
6. Zhirnov V, Zadegan RM, Sandhu GS, Church GM, Hughes W. Nucleic Acid Memory. *Nature Materials*. 2016;15:366–370. <https://doi.org/10.1038/nmat4594>

7. Yetisen AK, Davis J, Coskun AF, Church GM, Seok Hyun Yun. Bioart. *Trends in Biotechnology*. 2015;33(12):724–734. <https://doi.org/10.1016/j.tibtech.2015.09.011>
8. Na D. DNA Steganography: Hiding Undetectable Secret Messages within the Single Nucleotide Polymorphisms of a Genome and Detecting Mutation-Induced Errors. *Microbial Cell Factories*. 2020;19(128):1–9. <https://doi.org/10.1186/s12934-020-01387-0>
9. Shuhong Jiao, Goutte R. Code for Encryption Hiding Data into Genomic DNA of Living Organisms. In: *Proc. 9th International Conference on Signal Processing*. Beijing: IEEE; 2008. P. 2166–2169. <https://doi.org/10.1109/ICOSP.2008.4697576>
10. Masanori Arita. Writing Information into DNA. In book: N Jonoska, G Păun, G Rozenberg (eds). *Aspects of Molecular Computing. Lecture Notes in Computer Science*. Berlin, Heidelberg: Springer; 2004. P. 23–35. https://doi.org/10.1007/978-3-540-24635-0_2
11. Church GM, Yuan Gao, Sriram Kosuri. Next-Generation Digital Information Storage in DNA. *Science*. 2012;337(6102):1628. <https://doi.org/10.1126/science.1226355>
12. KA Schouhamer Immink, Kui Cai. Design of Capacity-Approaching Constrained Codes for DNA Based Storage Systems. *IEEE Communications Letters*. 2018;22(2):224–228. <https://doi.org/10.1109/LCOMM.2017.2775608>
13. Nozomu Yachie, Kazuhide Sekiyama, Junichi Sugahara, Yoshiaki Ohashi, Masaru Tomita. Alignment-Based Approach for Durable Data Storage into Living Organisms. *Biotechnology Progress*. 2007;23(2):501–505. <https://doi.org/10.1021/bp060261y>
14. Garafutdinov RR, Sakhabutdinova AR, Slominsky PA, Aminev FG, Chemeris AV. A New Digital Approach to SNP Encoding for DNA Identification. *Forensic Science International*. 2020;317:110520. <https://doi.org/10.1016/j.forsciint.2020.110520>
15. Ailenberg M, Rotstein OD. An Improved Huffman Coding Method for Archiving Text, Images, and Music Characters in DNA. *BioTechniques*. 2009;47(3):747–754. <https://doi.org/10.2144/000113218>
16. Doricchi A, Platnich CM, Gimpel A, Horn F, Earle M, Lanzavecchia G, et al. Emerging Approaches to DNA Data Storage: Challenges and Prospects. *ACS Nano*. 2022;16(11):17552–17571. <https://doi.org/10.1021/acsnano.2c06748>
17. Sakhabutdinova AR, Mikhailenko KI, Garafutdinov RR, Kiryanova OYu, Sagitova MA, Sagitov AM, et al. Non-Biological Application of DNA Molecules. *Biomics*. 2019;11(3):344–377. <https://doi.org/10.31301/2221-6197.bmcs.2019-28>
18. Garafutdinov RR, Chemeris DA, Sakhabutdinova AR, Chemeris AV, Kiryanova OYu, Mikhaylenko CI. Encoding of Non-Biological Information for its Long-Term Storage in DNA. *Biosystems*. 2022;215–216:104664. <https://doi.org/10.1016/j.biosystems.2022.104664>
19. Kiryanova OYu, Kiryanova II, Garafutdinov RR, Chemeris DA, Gubaidullin IM. *GATCGGenerator*. Certificate of Software Registration No. RU 2021667097. 2021. (In Russ.)
20. Borzov EA, Marakhonov AV, Ivanov MV, Drozdova PB, Baranova AV, Skoblov MYu. RANDTRAN: Random Transcriptome Sequence Generator that Accounts for Partition Specific Features in Eukaryotic mRNA Datasets. *Molecular Biology*. 2014;48:749–756. <https://doi.org/10.1134/S0026893314050021>
21. Harris CR, Millman KJ, van der Walt SJ, Gommers R, Virtanen P, Cournapeau D, et al. Array Programming with NumPy. *Nature*. 2020;585:357–362. <https://doi.org/10.1038/s41586-020-2649-2>

Received 07.06.2023

Revised 29.06.2023

Accepted 03.07.2023

About the Authors:

Olga Yu. Kiryanova, Teaching assistant of the Department of Digital Technologies and Modeling, Ufa State Aviation Technical University (1, Kosmonavtov St., Ufa, 450064, RF), [Researcher ID](#), [ScopusID](#), [ORCID](#), [AuthorID](#), olga.kiryanova27@gmail.com

Ravil R. Garafutdinov, Cand.Sci. (Chemistry), Head of the Laboratory of Physico-Chemical Methods of Analysis of Biopolymer, Institute of Biochemistry and Genetics — a separate structural subdivision of the Ufa Federal Research Centre, RAS (71, Oktyabrya Av., Ufa, 450054, Bashkortostan Rep., RF), [ScopusID](#), [ORCID](#), [AuthorID](#), garafutdinovr@mail.ru

Irek M. Gubaydullin, Dr.Sci. (Phys.-Math.), Professor, Head of the Laboratory of Mathematical Chemistry, Institute of Petrochemistry and Catalysis — a separate structural subdivision of the Ufa Federal Research Centre, RAS (141, Oktyabrya Av., Ufa, 450075, Bashkortostan Rep., RF), [ScopusID](#), [ORCID](#), [AuthorID](#), irekmars@mail.ru

Aleksei V. Chemeris, Dr.Sci. (Biology), Professor, Chief Research Fellow, Institute of Biochemistry and Genetics — a separate structural subdivision of the Ufa Federal Research Centre, RAS (71, Oktyabrya Av., Ufa, 450054, Bashkortostan Rep., RF), [ScopusID](#), [ORCID](#), [AuthorID](#), chemeris@anrb.ru

Claimed Contributorship:

OYu Kiryanova: software development, text preparation, calculations, formulation of conclusions.

RR Garafutdinov: consulting on the subject area, software testing, revision of the text, correction of the conclusions.

IM Gubaydullin: academic advising, correction of the conclusions, revision of the text.

AV Chemeris: formulation of the basic concept, research objectives and tasks; analysis of the research results, revision of the text, correction of the conclusions.

Conflict of interest statement: the authors do not have any conflict of interest.

All authors have read and approved the final manuscript.

Поступила в редакцию 07.06.2023

Поступила после рецензирования 29.06.2023

Принята к публикации 03.07.2023

Об авторах:

Ольга Юрьевна Кирьянова, ассистент кафедры цифровых технологий и моделирования Уфимского государственного нефтяного технического университета (РФ, 450064, Уфа, ул. Космонавтов, 1), [Researcher ID](#), [ScopusID](#), [ORCID](#), [AuthorID](#), olga.kiryanova27@gmail.com

Равиль Ринатович Гарафутдинов, кандидат химических наук, заведующий лабораторией физико-химических методов анализа биополимеров Института биохимии и генетики — обособленного структурного подразделения Федерального государственного бюджетного научного учреждения «Уфимский федеральный исследовательский центр» (РФ, 450054, Уфа, пр. Октября, 71), [ScopusID](#), [ORCID](#), [AuthorID](#), garafutdinovr@mail.ru

Ирек Марсович Губайдуллин, доктор физико-математических наук, профессор, заведующий лабораторией математической химии Института нефтехимии и катализа — обособленного структурного подразделения Федерального государственного бюджетного научного учреждения «Уфимский федеральный исследовательский центр» (РФ, 450075, Уфа, пр. Октября, 141), [ScopusID](#), [ORCID](#), [AuthorID](#), irekmars@mail.ru

Алексей Викторович Чемерис, доктор биологических наук, профессор, главный научный сотрудник Института биохимии и генетики — обособленного структурного подразделения Федерального государственного бюджетного научного учреждения «Уфимский федеральный исследовательский центр» (РФ, 450054, Уфа, пр. Октября, 71), [ScopusID](#), [ORCID](#), [AuthorID](#), chemeris@anrb.ru

Заявленный вклад соавторов:

О.Ю. Кирьянова — разработка программного обеспечения, подготовка текста, расчеты, формулировка выводов.

Р.Р. Гарафутдинов — консультирование по предметной области, тестирование ПО, доработка текста, корректировка выводов.

И.М. Губайдуллин — научное руководство, корректировка выводов, доработка текста статьи.

А.В. Чемерис — формирование основной концепции, целей и задач исследования, анализ результатов исследования, доработка текста, корректировка выводов.

Конфликт интересов: авторы заявляют об отсутствии конфликта интересов.

Все авторы прочитали и одобрили окончательный вариант рукописи.

INFORMATION TECHNOLOGY, COMPUTER SCIENCE AND MANAGEMENT



<https://doi.org/10.23947/2687-1653-2023-23-3-307-316>

Original article

Sensitivity of Diffusion-Weighted Image Combined with T2 Turbo Inversion Recovery Magnitude Sequence and as an Alternative to Contrast-Enhanced MRI in the Detection of Perianal Fistula

Noor Fadhil Baqir[✉]¹, Rasha Sabeeh Ahmed¹ , Khaleel Ibraheem Mohsen²

¹ College of Medicine, Al-Nahrain University, Baghdad, Iraq

² National Cancer Research Center, University of Baghdad, Baghdad, Iraq

✉ lavendrtechnologist2017@gmail.com

Abstract

Introduction. Perianal fistula rapidly develops an abscess, requiring surgical decompression. However, simple cases must be managed. However, for patients with renal insufficiency, MRI with contrast is contraindicated. It is proposed to use diffusion-weighted images that can diagnose anal fistulae, showing areas of high signal intensity (inflammatory tissues). The aim is to determine sensitivity of diffusion-weighted image combined with T2 turbo inversion recovery magnitude and as an alternative technique to contrast-enhanced MRI using clinical examination as a reference.

Materials and Methods. Study included fifty patients with a clinical diagnosis of perianal fistula. MRI sequences were T2 turbo inversion recovery magnitude in oblique coronal and axial planes, diffusion-weighted image, and T1 weighted image turbo spin echo (fat suppression) pre- and post-administration of contrast agents in oblique axial planes. Three radiologists evaluated the MR imaging data using a questionnaire of parameters that necessitated a binary response, “yes” or “no” answer.

Results. Diffusion-weighted image combined with axial T2 turbo inversion recovery magnitude sequence had 96.7 %. All raters agreed that it is sensitive enough to correctly identify perianal fistula with a moderate Kappa agreement ($k = 0.586$) and $p\text{-value} < 0.001$. The mean value of rater's responses was 76.7 % represents sensitivity of diffusion-weighted images + T2 turbo inversion recovery magnitude as an alternative technique to T1-enhanced contrast with moderate ($k = 0.553$) agreement between raters and $P\text{-value} < 0.001$.

Discussion and Conclusion. Diffusion-weighted images and T2 turbo inversion recovery magnitude sequences exhibit comparable efficacy to T1-enhanced contrast sequences in detecting perianal fistula. This may be an option for patients with renal impairment who cannot receive an MRI contrast.

Keywords: magnetic resonance imaging; diffusion-weighted image; T1-enhanced contrast

Acknowledgements: the authors would like to thank the Editorial board and the reviewers for their attentive attitude to the article and for the specified comments that improved the quality of the article.

For citation. Noor Fadhil Baqir, Rasha Sabeeh Ahmed, Khaleel Ibraheem Mohsen. Sensitivity of Diffusion-Weighted Image Combined with T2 Turbo Inversion Recovery Magnitude Sequence and as an Alternative to Contrast-Enhanced MRI in the Detection of Perianal Fistula. *Advanced Engineering Research (Rostov-on-Don)*. 2023;23(3):307–316. <https://doi.org/10.23947/2687-1653-2023-23-3-307-316>

Чувствительность диффузионно-взвешенного изображения в сочетании с последовательностью восстановления турбо-инверсии T2 в качестве альтернативы МРТ с контрастным усилением при обнаружении параректального свища

Noor Fadhil Baqir ¹, Rasha Sabeeh Ahmed¹ , Khaleel Ibraheem Mohsen²

¹ Медицинский колледж, университет Аль-Нахрейн, Багдад, Ирак

² Национальный онкологический центр, Багдадский университет, Багдад, Ирак

 javendrtechnologist2017@gmail.com

Аннотация

Введение. Параректальный свищ быстро переходит в абсцесс, требующий хирургической декомпрессии. Тем не менее, простые случаи подлежат лечению. Однако, для пациентов с почечной недостаточностью МРТ с контрастированием противопоказана. Предлагается применение диффузионно-взвешенного изображения, которое способно диагностировать анальные свищи, показывая на снимках области с высокой интенсивностью сигнала (очаг воспаления). Цель работы заключается в том, чтобы определить степень чувствительности изображения диффузионной спектральной томографии в сочетании с величиной восстановления турбо-инверсии T2 и возможность применения данного метода в качестве альтернативного метода МРТ с контрастным усилением, используя клиническое обследование в качестве стандарта сравнения.

Материалы и методы. В ходе работы были обследованы 50 пациентов с клиническим диагнозом «параректальный свищ». Последовательности МРТ представляли собой турбо-инверсию T2 с величиной восстановления в косых коронарных и аксиальных плоскостях, изображение диффузионной МРТ и взвешенное изображение быстрого спин-эха (жироподавление) до и после введения контрастных веществ в косые аксиальные плоскости. Три радиолога оценили данные МРТ, используя анкету параметров, которая требовала бинарного ответа, ответа «да» или «нет».

Результаты исследования. Диффузионно-взвешенное изображение в сочетании с последовательностью восстановления аксиальной турбо-инверсии T2 показало 96,7 %. Все эксперты согласились с тем, что данный метод, показавший умеренное согласие Каппа ($k = 0,586$) и значение $p < 0,001$, достаточно чувствителен для того, чтобы верно идентифицировать параректальный свищ. Среднее значение экспертной оценки составило 76,7 %. Это подтверждает, что чувствительность предложенного метода – диффузионно-взвешенные изображения + величина восстановления турбо-инверсии T2 – является альтернативой методу контрастного усиления T1 с умеренным ($k = 0,553$) согласием между экспертами и значением $P < 0,001$.

Обсуждение и заключение. Диффузионно-взвешенные изображения и последовательности величин восстановления при турбо-инверсии T2 демонстрируют сравнимую эффективность с последовательностями контрастного усиления T1 для обнаружения параректального свища. Предложенный метод может служить вариантом для пациентов с почечной недостаточностью, которым противопоказана МРТ с контрастированием.

Ключевые слова: магнитно-резонансная томография, диффузионно-взвешенное изображение, контрастное усиление T1

Благодарности: авторы благодарят редакцию и рецензентов за внимательное отношение к статье и за указанные замечания, позволившие улучшить качество статьи.

Для цитирования. Noor Fadhil Baqir, Rasha Sabeeh Ahmed, Khaleel Ibraheem Mohsen. Sensitivity of Diffusion-Weighted Image Combined with T2 Turbo Inversion Recovery Magnitude Sequence and as an Alternative to Contrast-Enhanced MRI in the Detection of Perianal Fistula. *Advanced Engineering Research (Rostov-on-Don)*. 2023;23(3): 307–316. <https://doi.org/10.23947/2687-1653-2023-23-3-307-316>

Introduction. Perianal fistula is a rare condition that is difficult to treat and is associated with patient morbidity. It is the connection between the mucosal lining of the anal canal and the perianal epidermis [1]. The rate of occurrence is approximately two times higher in males than in females. The male-female ratio is 2:1. Perianal discharge that comes and goes, itchiness, discomfort, fever, and localized pain are the most typical symptoms [2]. Perianal fistula is associated with the rapid development of an abscess, necessitating timely surgical intervention for decompression. Consequently, the management of uncomplicated cases is crucial [3]. The treatment of anal fistula involves the excision of the primary fistula opening, any associated tracts, and any supplementary openings while ensuring the preservation of continence [4]. This requires accurate identification of the fistula's internal opening and any secondary abscesses or extensions. Imaging techniques, including magnetic resonance imaging (MRI), are increasingly important in perianal fistula diagnosis [5, 6] because they provide the most precise and reliable data regarding the anatomical characteristics of the fistula tract and its

association with the anal sphincter muscles. Providing these specific details by MRI has enhanced surgical success rates and reduced the likelihood of recurrence in perianal fistulas [7, 8]. T2-weighted with fat suppression (Turbo spin echo or turbo inversion recovery magnitude) MRI is very good at showing a fistula track. Still, some reports have pointed out how hard it is to distinguish between real abscesses that need to be drained by surgery and inflamed masses that cannot be drained and need anti-inflammatory medicine. Gadolinium chelate-enhanced T1-weighted MR scans are often used as a tool to help solve problems [9, 10]. Post-contrast MR imaging is the optimal sequence for detecting and characterizing perianal fistula. It is considered the gold standard by various institutions [5, 11].

Nonetheless, using gadolinium contrast agents increases expenses and duration and poses a risk of nephrogenic systemic fibrosis in patients already experiencing renal insufficiency. In addition, several studies have found evidence of gadolinium accumulation in the brain's deep nuclei after repeated contrast agent injections [1, 12, 13]. In recent years, Diffusion-Weighted Imaging (DWI) has provided high differentiation between pathological lesions, such as cancer or inflammatory processes, and the adjacent normal tissue [14]. DWI is a technique that captures variations in water mobility resulting from interactions with macromolecules, cell membranes, and changes in the tissue environment. Therefore, inflammatory tissues may also demonstrate limited diffusivity, resulting in the appearance of high signal areas on DWI, which takes advantage of this property. This sequence has the potential to be helpful in the diagnosis of anal fistulae [15, 16].

Moreover, Diffusion-Weighted Imaging can be integrated into customary Magnetic Resonance Imaging (MRI) scans of the perianal fistula, as it removes the need for a contrast agent, has shorter sequence duration, and does not necessitate additional equipment. The diffusion-weighted imaging technique has a naturally low spatial resolution, one of the method's drawbacks. Therefore, the T2 turbo inversion recovery magnitude (TIRM) sequence was added to DWI to assess the perianal fistula to overcome these drawbacks [16, 17]. In the T2 TIRM imaging technique, the fistulous tracts are commonly visualized as highly intense linear structures [18]. Additionally, it should be noted that pus, fluid, and granulation tissue manifest as areas of high signal intensity against a background of low signal intensity fat [6, 19].

Boruah et al. [20] evaluated the efficacy of diffusion-weighted magnetic resonance imaging (MRI) as a diagnostic tool for perianal fistulae. The study consisted of 47 participants diagnosed with perianal fistula. The MRI results were correlated with the clinical evaluation or the surgical findings. The performance of DWI alone was inferior to that of T2W imaging. Nevertheless, the most notable outcome was the assessment of combined DWI-T2W images, despite the lack of statistical significance compared to DWI or T2W images individually.

Gu et al. [21] explored an alternative technique comparable to Gadolinium-contrast enhancement to assess any morphological changes in the preoperative evaluation of anal fistulas. The study comprised 46 individuals who had received a diagnosis of anal fistula. The gold standard for comparison will involve outcomes derived from surgical pathology. The utilization of FS T2-weighted and diffusion-weighted imaging exhibited similar effectiveness when compared to FS T1-weighted contrast-enhanced imaging for evaluating changes in the morphology of anal fistulas.

This study aims to determine the sensitivity of diffusion-weighted images combined with T2 turbo inversion recovery magnitude (TIRM) and as an alternative technique to contrast-enhanced MRI using the clinical examination as a gold standard reference.

Patients and Methods. The study was carried out between December 2022 and May 2023 at the MRI department of the oncology teaching hospital located in Medical City, Baghdad, Iraq. The research was carried out as a cross-section and utilized a non-randomized design. After a thorough clinical evaluation of each patient, the surgical outpatient clinics sent fifty patients who were thought to have perianal fistulas to the MRI department. Each participant gave their informed written agreement, and the institution's ethical committee gave its stamp of approval before the study was carried out.

The inclusion criteria for this study include adult patients, regardless of gender, who have been diagnosed with a perianal fistula during a clinical examination and have been referred from outpatient surgical clinics.

The exclusion criteria for this study include individuals who fall into specific categories, namely children, pregnant women, and patients who are contraindicated for MRI examinations. This includes patients with cardiac pacemakers or metallic shells and those who experience claustrophobia.

The MRI examinations were performed using 1.5 T scanners (Magnetom Aera, Siemens Healthcare, Germany) equipped with a phased-array surface coil comprising 18 channels. There was no requirement for patient preparation before the examination. During the MRI, patients take a supine position on the examination table, with a phased array surface coil positioned over their pelvic region. It is crucial to ensure correct orientation when using magnetic resonance imaging (MRI) for imaging the anal canal. The planning of the images is performed with the assistance of a sagittal T2-weighted localizer that passes through the middle of the patient. The oblique transverse and coronal sections are orthogonally and parallel to the anal sphincter.

The following MRI sequence parameters were utilized for this investigation: T2 TIRM in the coronal oblique plane (TR/TE: 5000/50, slice thickness: 3 mm, flip angle: 140°, interstice gap: 20 %, number of slices: 34, FOV: 390mm, matrix size: 384×288, signal averages: 1, inversion time (TI): 160 s, acquisition time: 2:27 (min: sec)). T2 TIRM performed in

the oblique axial plane (TR/TE: 5040/50 ms, slice thickness: 3 mm, interstice gap: 20 %, flip angle: 140°, number of slices: 36, FOV: 380 mm, matrix size: 384×234, signal averages: 1; inversion time (TI): 160 s, acquisition time: 2:02 (min: sec). Single shot echo planar imaging (EPI) imaging (DWI) in an oblique axial plane (TR/TE: 2600/70, FOV: 380mm, distance factor: 20 %, slice thickness: 3 mm number of slices: 30, matrix size: 128×128, b-value 50–400–800 with signal averages of 1 for 50, 3 for 400, and 800, acquisition time: 2:22 (min: sec)). And T1 FS TSE in an oblique axial plane before and after administration of contrast agent (TR/TE: 619/20, slice thickness: 3mm, number of slices: 27, interstice gap: 20 %, flip angle: 160°, FOV: 239 mm, signal averages: 1, matrix size: 192×163, acquisition time: 1:55 (min: sec)).

Three radiologists, each with an advanced radio diagnosis degree and over five years of experience in MRI reporting, were carefully selected for employment at the oncology teaching hospital based on their superior rankings among other radiologists. Furthermore, these individuals consistently produce a substantial volume of over 40 reports per week. They were provided information regarding the patient's clinical suspicion of perianal fistula while unaware of the surgical and prior MRI reports. The radiologists reviewed the MR imaging data sets using a questionnaire of parameters requiring a binary response (yes or no) as follows:

- Diffusion-weighted image (3mm slice thickness) combined with T2 TIRM;
- Diffusion-weighted image replaces T1 enhanced contrast with fat suppression.

The data were inputted, categorized, and examined using the SPSS (statistical package for social sciences) software program version 26. The data were presented using frequencies and percentages. A significance level of 0.05 or lower was used to determine statistical significance. The study employed the Fleiss kappa test to evaluate the reliability and inter-rater agreement among multiple raters.

Results. The findings of this study were derived from the analysis of a sample of fifty individuals who presented with a perianal fistula as determined through clinical assessment. Most individuals diagnosed with anal fistula were male, comprising 82 % of the cases, while females constituted the remaining 18 % as shown in Figure 1. The mean age of the entire patient population was 39.80 years, and the standard deviation was 12.46 years.

According to the prepared questionnaire, the three rater's responses about the best visualization of perianal fistula by diffusion-weighted image combined with T2 TIRM and as an alternative method to T1 enhanced contrast. The frequency distribution of the three raters is demonstrated in Table 1. The three raters' responses according to the constructed questionnaire; regarding the best visualization of the perianal fistula compared to the positive clinical examination (standard reference) is represented in Fig. 2.

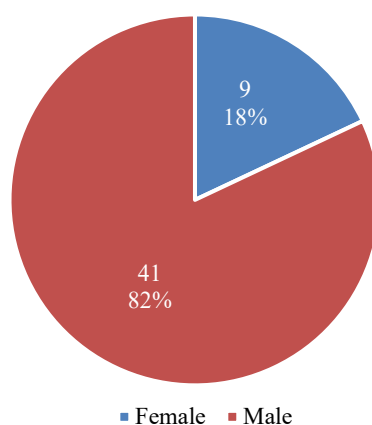


Fig. 1. Frequency distribution of the gender for the 50 participant patients

Table 1

Frequency and percentage of DWI+T2 TIRM and DWI as an alternative to T1 enhanced contrast images for three raters

	DWI+T2 TIRM freq. (%)	DWI image as an alternative to T1 enhanced contrast freq. (%)
Rater 1	47(94 %)	37(74 %)
Rater 2	49(98 %)	36(72 %)
Rater 3	49(98 %)	42(84 %)
Total	50 (100 %)	

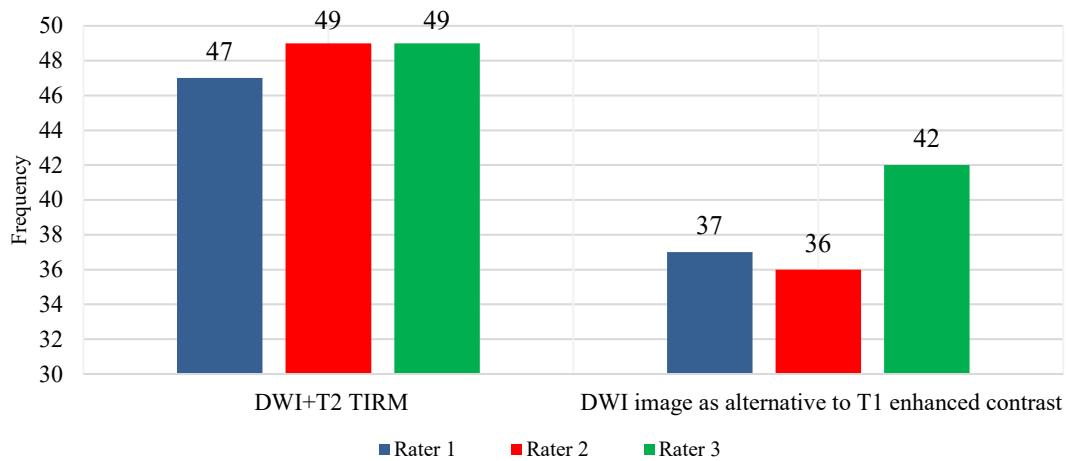


Fig. 2. Bar chart frequency distribution of the raters' opinions about using diffusion-weighted image combined with T2 TIRM and as an alternative to T1 enhanced contrast in detecting perianal fistula

The average of the three raters for detecting cases of perianal fistula by each reported MRI sequence is demonstrated in Fig. 3. It was found that DWI+ axial T2 TIRM had a higher percentage (96.7 %), which corresponded to the sensitivity of this sequence in the detection of true cases of perianal fistula by the three raters. The average of raters' answers for replacing the T1 FS TSE enhanced contrast with DWI in detecting anal fistula was 76.7 % (sensitivity of DWI +T2 TIRM as an alternative technique to T1 enhanced contrast). The inter-rater kappa agreement was performed to test the reliability of the questionnaire used to evaluate MRI sequences obtained for the visualization of 50 patients clinically diagnosed with perianal fistula, as shown in Table 2. A significant (P -value<0.001) moderate ($k=0.586$) agreement was found for the question related to the use of optimized DWI + T2 TIRM. Also, significant (P -value<0.001) moderate ($k=0.553$) agreement between raters when asked to use DWI versus T1 enhanced contrast.

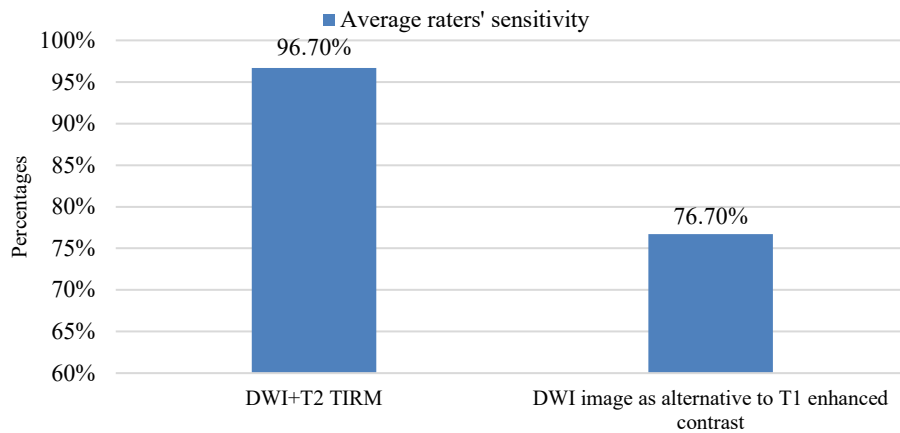


Fig. 3. Bar chart of overall average sensitivity of the raters' opinions (%) about using different MRI sequences in detecting anal fistula

Table 2

Inter-rater reliability and overall agreement between radiologists in the diagnosis of anal fistula among 50 patients

Sequence used	Kappa	95% CI	P-value
DWI versus T1 enhanced contrast	0.553	0.548–0.558	<0.001
DWI + T2 TIRM	0.586	0.581–0.591	<0.001

DWI diffusion-weighted image, TIRM turbo inversion recovery magnitude, CI confident interval.

The presence of a perianal fistula can be seen in a variety of MRI sequences, as shown in Fig. 4 and Fig. 5, and Fig. 6 demonstrates the abscess collection of patients with perianal fistula that shows the well-defined restricted diffusion of the abscess and hyper-signal intensity on T2 TIRM as an alternative technique to T1 enhanced contrast.

Discussion. The primary purpose of magnetic resonance imaging (MRI) in the context of perianal fistulas is to establish the extent of the tract, identify any side branches, and determine the presence of deep abscesses, especially at the supra levator level [22]. The utilization of Gadolinium-enhanced T1-weighted images and fat suppression confers distinct advantages in differentiating a fluid-filled tract from an area of inflammation. The wall of the tract displays increased enhancement, whereas the central region exhibits a hypo-intense appearance. Post-contrast gadolinium images exhibit high efficacy in visually representing abscesses [23]. However, the gadolinium contrast agent does have certain limitations. These include an extended duration of magnetic resonance examination, additional costs, the potential deposition of gadolinium contrast in the brain, and contraindications for patients with renal insufficiency (1).

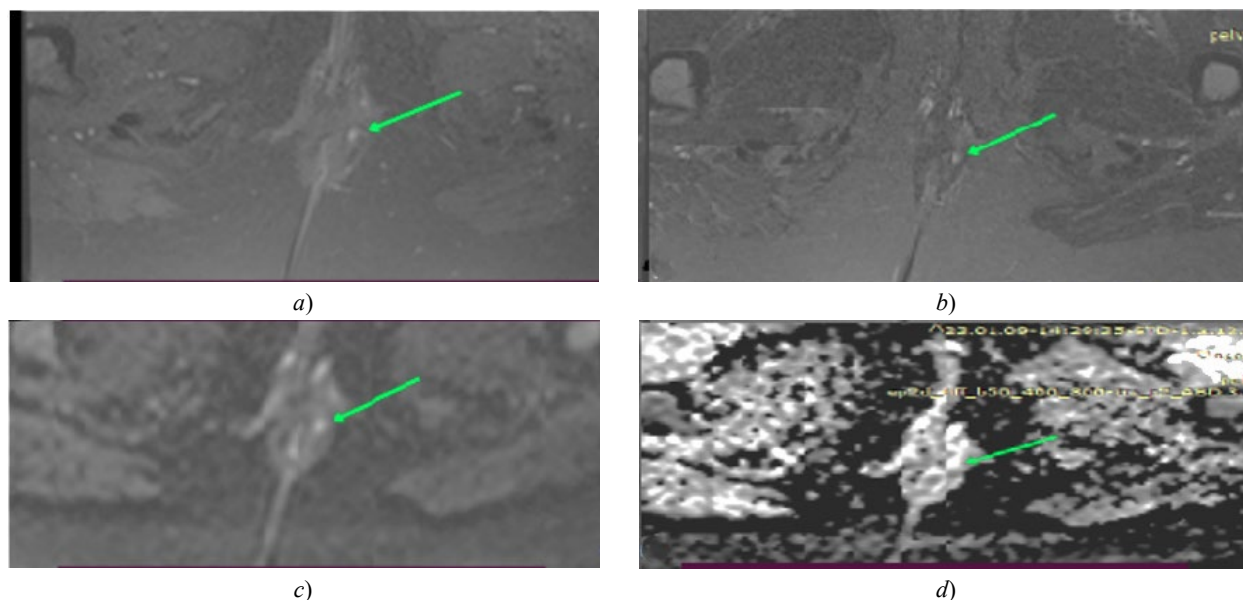


Fig. 4. A 41-year-old female patient presenting with a left-sided supra sphincteric fistula at 2 o'clock (green arrow):
a — shows the T1 FSTSE enhanced contrast; *b* — shows the T2 TIRM;
c — shows the diffusion-weighted image (3 mm slice thickness); *d* — shows the ADC map

Diffusion-weighted imaging has been proposed as a noteworthy alternative due to its ability to identify inflammatory lesions as areas exhibiting high signal intensity. The fistulous tracks demonstrate increased intensity in diffusion-weighted images, whereas the background signal is significantly attenuated. Consequently, the identification and extent of the fistula can be easily determined [24]. One limitation of diffusion-weighted imaging is its inherent drawback of having a relatively low spatial resolution. Diffusion-weighted imaging was not evaluated as an independent variable in our study. In this study, we evaluated the supplementary benefits of the technique in fat-suppressed T2-weighted imaging, specifically T2 TIRM (16). In our study, it was observed that all three raters concurred on the suitability of the majority of images derived from the sequences of Diffusion-Weighted Imaging (DWI) combined with T2 Turbo Inversion Recovery Magnitude (TIRM) to delineate anal fistula. Both rater two and rater three reported a percentage of 98, while rater 1 reported a slightly lower percentage of 94 for the images. Hence, the DWI+T2 TIRM sequence exhibited the highest percentage (96.7 %), aligning with the sensitivity of DWI combined with T2 TIRM compared to the clinical examination as the gold standard. The inter-rater kappa agreement was moderate ($k = 0.586$), with a significant P-value of less than 0.001. It is agreed Fahmy et al. (5) that is conducted a study that revealed a sensitivity of 92.12 % for the detection of perianal fistula when using a combination of diffusion-weighted imaging (DWI) and T2-weighted imaging (T2WI).

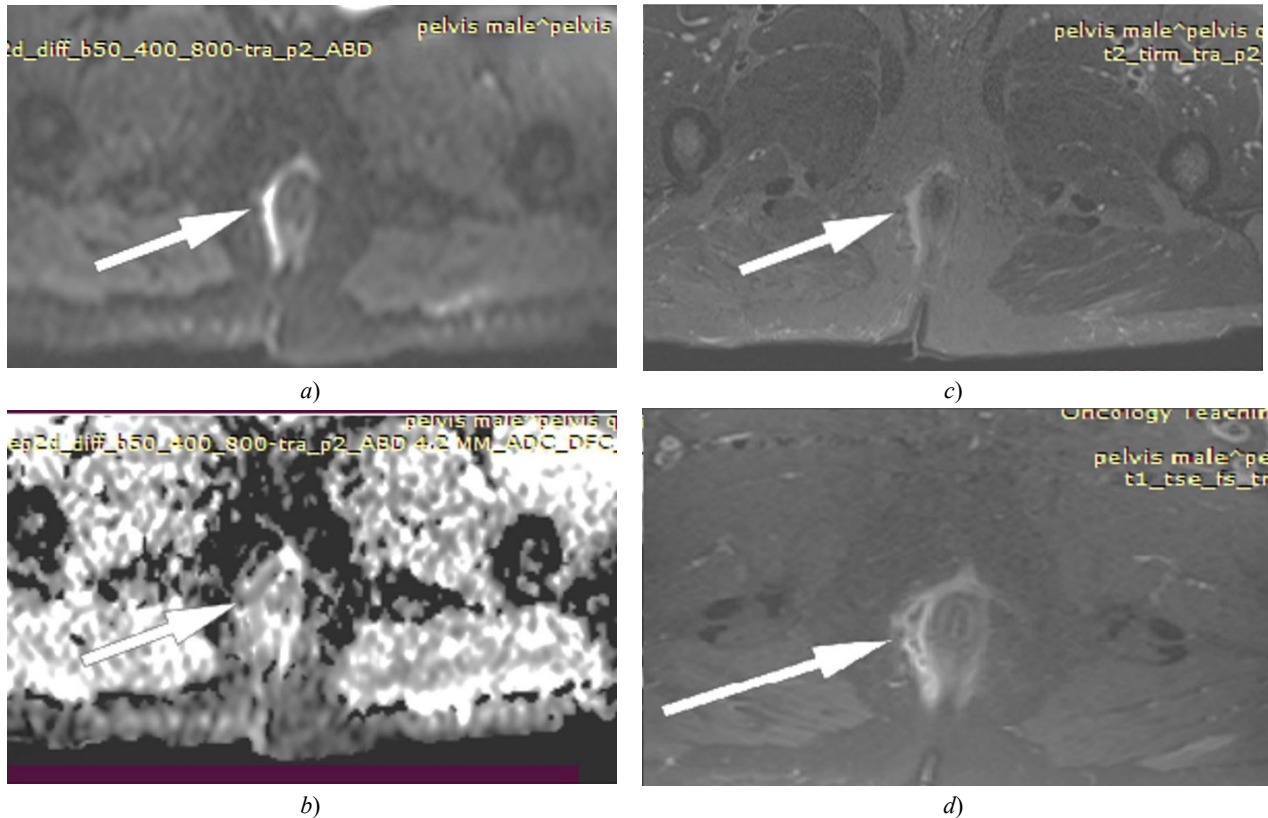


Fig. 5. A 51-year-old male presenting with a right-sided supra sphincteric branching fistula with extensive inflammatory changes and multiple extra sphincteric abscess collections (white arrow): *a* — optimized DWI; *b* — ADC map shows restricted diffusion; *c* — T2 TIRM shows hyper signal intensity; *d* — T1FSTSE post-contrast shows peripheral enhancement. All the images are in the oblique axial plane

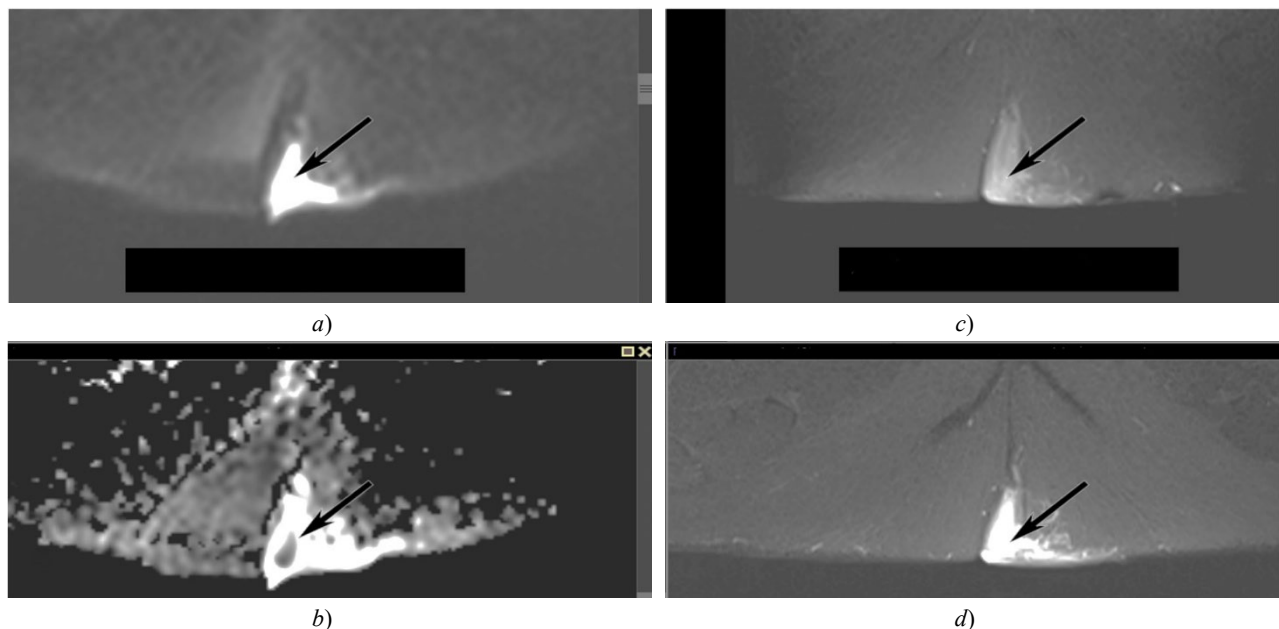


Fig. 6. A 36-year-old male presenting with a left gluteal abscess collection with surrounding significant soft tissue edema (black arrow), *a* — diffusion weighted image; *b* — ADC map shows restricted diffusion; *c* — T1FSTSE post-contrast shows peripheral enhancement; *d* — T2 TIRM shows hyper signal intensity. All the images are in the oblique axial plane

However, they regarded T1-weighted imaging (T1WI) post-contrast as the reference standard for comparison. Additionally, Mohsen and Osman [25] evaluated the combined utilization of diffusion-weighted imaging (DWI) and T2-weighted (T2W) sequences to obtain optimal outcomes. The perianal fistulas and abscesses were accurately diagnosed in 97.8 per cent of cases using T2-weighted imaging (T2WI) and T1-weighted imaging post-contrast (T1WI post-contrast) as the established benchmark. Regarding the sensitivity of DWI combined with T2TIRM as an alternative technique to T1 FS TSE post-contrast, our research revealed that rater 3 said that it is sensitive for 42 (84 %), followed by rater one

and rater two in the same order, who reported 74 % and 72 % of the sensitivity, respectively. Therefore, an average raters' sensitivity of 76.7 %; there was a significant (P-value 0.001 fair ($k=0.370$)) agreement between the three raters in selecting DWI as an alternative to post-contrast sequence for the detection of perianal fistula. Therefore, it reflects the capability of DWI in clearly delineating perianal fistula, making it comparable to contrast enhancement MRI in the detection of perianal fistula and possibly making it superior to contrast enhancement MRI in the detection of perianal fistula by reducing the amount of time an MRI examination takes and by reducing the adverse effects of contrast agents, particularly in patients with renal impairment. Our findings agree with those of Hori et al. (16), who established that there was not a statistically significant difference (p-value less than 0.05) in the sensitivity between combined contrast-enhanced sequences with T2WI and DWI coupled with T2WI. Also, according to the findings of Fahmy and Dawoud (5), the utilization of a combination of diffusion-weighted imaging (DWI) and turbo inversion recovery magnitude (TIRM) is deemed equivalent to the utilization of post-contrast images in the detection of primary and complicated fistula. The application of Diffusion-Weighted Imaging (DWI) has demonstrated its utility in differentiating between abscesses and inflammatory reactions and assessing the extent of disease activity. Active granulation tissue will exhibit enhancement on post-contrast T1-weighted imaging compared to the fluid in the fistula. Rim enhancement indicates an abscess, while diffuse enhancement is typical of granulation tissue (5). In comparison, diffusion-weighted imaging is a technique that depicts changes in the mobility of water molecules caused by their interactions with cell membranes, macromolecules, and environmental changes in the tissue. On diffusion-weighted imaging (DWI), inflammatory tissues may exhibit reduced diffusivity, resulting in hyper-intense signal regions [26]. The apparent diffusion coefficient (ADC) values observed in abscesses are estimated to be lower than those in healthy tissues. As reported in the scientific literature, this is due to pus, which inhibits the unrestricted diffusion of water molecules (9). As inflammatory tissues typically demonstrate enhanced signal intensity, diffusion-weighted imaging may hold promise as a diagnostic sequence for anal fistulas (6).

Our study has the limitation of not making a quantitative comparison by calculating ADC values in the diffusion-weighted images to diagnose active and inactive perianal fistula compared with the T1 enhanced contrast because of the overloaded work in the institution where the study was conducted. Therefore, we recommend future research to evaluate the ADC value of diffusion-weighted images to diagnose active and inactive perianal fistula compared with the T1 enhanced contrast with a larger sample size.

Conclusion. The sensitivity of diffusion-weighted images in conjunction with T2 turbo inversion recovery magnitude (TIRM) sequences demonstrates a similar level of effectiveness as T1 enhanced contrast sequences in identifying and assessing perianal fistula. This combination of imaging techniques may serve as a viable alternative, particularly for individuals with renal impairment who are contraindicated to administer MRI contrast agents.

References

1. Cattapan K, Chulroek T, Kordbacheh H, Wancharoenrungs D, Harisinghani M. Contrast- vs. Non-Contrast Enhanced MR Data Sets for Characterization of Perianal Fistulas. *Abdominal Radiology*. 2019;44:446–455. <https://doi.org/10.1007/s00261-018-1761-3>
2. Gurung G. 3T MR Imaging Evaluation of Perianal Fistulas: an Initial Experience in Nepal. *Journal of Society of Surgeons of Nepal*. 2016;19(1):25–30. URL: <https://api.semanticscholar.org/CorpusID:199464071> (accessed: 10.04.2023).
3. Singh K, Singh N, Thukral C, Singh KP, Bhalla V. Magnetic Resonance Imaging (MRI) Evaluation of Perianal Fistulae with Surgical Correlation. *Journal of Clinical and Diagnostic Research (JCDR)*. 2014;8(6):RC01–04. <https://doi.org/10.7860/JCDR/2014/7328.4417>
4. Kee Ho Song. New Techniques for Treating an Anal Fistula. *Journal of the Korean Society of Coloproctology*. 2012;28(1):7–12. <https://doi.org/10.3393/jksc.2012.28.1.7>
5. Fahmy DM, Dawoud MG. Value of Diffusion Weighted MRI in Assessment of Simple and Complicated Perianal Fistula. *The Egyptian Journal of Radiology and Nuclear Medicine*. 2017;48(3):553–562. <https://doi.org/10.1016/j.ejrnm.2017.03.010>
6. Jaime de Miguel Criado, Laura Garcia del Salto, Patricia Fraga Rivas, Luis Felipe Aguilera del Hoyo, Leticia Gutiérrez Velasco, M Isabel Díez Pérez de las Vacas, et al. MR Imaging Evaluation of Perianal Fistulas: Spectrum of Imaging Features. *RadioGraphics*. 2012;32(1):175–194. <https://doi.org/10.1148/rg.321115040>
7. Akyel NG, Akın K, Kösehan D, Köktener A. Perianal Fistula Imaging: A Comparison between Two-Channel Superficial Flex Coil and Eight-Channel Body Coil. *Polish Journal of Radiology*. 2019;84:e430–e435. <https://doi.org/10.5114/pjr.2019.89906>
8. Omer HK, Jalab HA, Hasan AM, Tawfiq NE (eds.) Combination of Local Binary Pattern and Face Geometric Features for Gender Classification from Face Images. In: *Proc. 9th IEEE International Conference on Control System*,

- Computing and Engineering (ICCSCE). New York City, NY: IEEE; 2019. <https://doi.org/10.1109/ICCSCE47578.2019.9068593>
9. Dohan A, Eveno C, Oprea R, Pautrat K, Placé V, Pocard M, et al. Diffusion-Weighted MR Imaging for the Diagnosis of Abscess Complicating Fistula-in-ano: Preliminary Experience. *European Radiology*. 2014;24:2906–2915. <https://doi.org/10.1007/s00330-014-3302-y>
 10. Hasan AM, Meziane F, Aspin R, Jalab HA (eds). MRI Brain Scan Classification Using Novel 3-D Statistical Features. In: *Proceedings of the Second International Conference on Internet of Things, Data and Cloud Computing*. New York, NY: ACM; 2017. P. 1–5. <https://doi.org/10.1145/3018896.3036381>
 11. Jiyeon Baik, Seung Ho Kim, Yedaun Lee, Jung-Hee Yoon. Comparison of T2-Weighted Imaging, Diffusion-Weighted Imaging and Contrast-Enhanced T1-Weighted MR Imaging for Evaluating Perianal Fistulas. *Clinical Imaging*. 2017;44:16–21. <https://doi.org/10.1016/j.clinimag.2017.03.019>
 12. Marckmann P, Skov L, Rossen K, Dupont A, Damholt MB, Heaf JG, et al. Nephrogenic Systemic Fibrosis: Suspected Causative Role of Gadodiamide Used for Contrast-Enhanced Magnetic Resonance Imaging. *Journal of the American Society of Nephrology*. 2006;17(9):2359–2362. <https://doi.org/10.1681/ASN.2006060601>
 13. Cansu A, Bekircavusoglu S, Oguz S, Bulut E, Fidan S. Can Diffusion Weighted Imaging Be Used as an Alternative to Contrast-Enhanced Imaging on Magnetic Resonance Enterography for the Assessment of Active Inflammation in Crohn Disease. *Medicine*. 2020;99(8):e19202. <https://doi.org/10.1097/MD.00000000000019202>
 14. Yoshizako T, Wada A, Takahara T, Kwee TC, Nakamura M, Uchida K, et al. Diffusion-Weighted MRI for Evaluating Perianal Fistula Activity: Feasibility Study. *European Journal of Radiology*. 2012;81(9):2049–2053. <https://doi.org/10.1016/j.ejrad.2011.06.052>
 15. Cavusoglu M, Duran S, Cılız DS, Tufan G, Çetin HH, Ozsoy A, et al. Added Value of Diffusion-Weighted Magnetic Resonance Imaging for the Diagnosis of Perianal Fistula. *Diagnostic and Interventional Imaging*. 2017;98(5):401–408. <https://doi.org/10.1016/j.diii.2016.11.002>
 16. Hori M, Oto A, Orrin S, Suzuki K, Baron RL. Diffusion-Weighted MRI: A New Tool for the Diagnosis of Fistula in ano. *Journal of Magnetic Resonance Imaging*. 2009;30(5):1021–1026. <https://doi.org/10.1002/jmri.21934>
 17. Hilal SR, Hasan HS, Hasan AM. Magnetic Resonance Imaging Breast Scan Classification Based on Texture Features and Long Short-Term Memory Model. *NeuroQuantology*. 2021;19(7):41–47. <https://doi.org/10.14704/nq.2021.19.7.NQ21082>
 18. Balcı S, Onur MR, Karaosmanoğlu AD, Karçaaltıncaba M, Akata D, Konan A, et al. MRI Evaluation of Anal and Perianal Diseases. *Diagnostic and Interventional Radiology*. 2019;25(1):21–27. <https://doi.org/10.5152/dir.2018.17499>
 19. Hasan AM, Qasim AF, Jalab HA, Ibrahim RW. Breast Cancer MRI Classification Based on Fractional Entropy Image Enhancement and Deep Feature Extraction. *Baghdad Science Journal*. 2022;20(1):0221. <https://doi.org/10.21123/bsj.2022.6782>
 20. Boruah DK, Hazarika K, Ahmed H, Borah KK, Borah S, Malakar S, et al. Role of Diffusion-Weighted Imaging in the Evaluation of Perianal Fistulae. *Indian Journal of Radiology and Imaging*. 2021;31(01):091–101. <https://doi.org/10.1055/s-0041-1729673>
 21. Chao Gu, Yu Wang, Lixia Lai, Weiwei Han, Jiansheng Li, Haichang Xing, et al. A Comparable Method to Gd-contrast Enhancement in the Preoperative Evaluation of Anal Fistula. *Medicine*. 2019;98(44):e17807. <https://doi.org/10.1097/MD.00000000000017807>
 22. Jean AA, Reddy AK, Elavarasi JA, Siddhartha N. Assessment of Role of Diffusion-Weighted Imaging in the Evaluation of Perianal Fistulae. *International Journal of Academic Medicine and Pharmacy*. 2023;5(3):461–464. <http://dx.doi.org/10.47009/jamp.2023.5.3.99>
 23. Khera PS, Badawi HA, Afifi AH. MRI in Perianal Fistulae. *Indian Journal of Radiology and Imaging*. 2010;20(01):53–57. <https://doi.org/10.4103/0971-3026.59756>
 24. Sharma A, Yadav P, Sahu M, Verma A. Current Imaging Techniques for Evaluation of Fistula in ano: a Review. *Egyptian Journal of Radiology and Nuclear Medicine*. 2020;51(1):1–18. <https://doi.org/10.1186/s43055-020-00252-9>
 25. Mohsen LA, Osman NM. Diffusion-Weighted Imaging in the Evaluation of Perianal Fistula and Abscess. *Egyptian Journal of Radiology and Nuclear Medicine*. 2020;51:1–9. <https://doi.org/10.1186/s43055-020-00193-3>
 26. Yoshizako T, Kitagaki H. A Pictorial Review of the Impact of Adding Diffusion-Weighted MR Imaging to Other MR Sequences for Assessment of Anal Fistulae. *Japanese Journal of Radiology*. 2013;31:371–376. <https://doi.org/10.1007/s11604-013-0204-x>

Received 26.05.2023

Revised 22.06.2023

Accepted 28.06.2023

About the Authors:

Noor F. Baqir, BSc. (Radiological Engineering), College of Medical and Health Techniques, Middle Technical University (Muasker, Al Rashid Street, Baghdad, Iraq), MRI technologist, Oncology Teaching Hospital in Medical City, Baghdad, Iraq. lavendrtechnologist2017@gmail.com

Rasha S. Ahmed, BSc. (Physics), M.Sc. (Atomic Physics), Mustansiriyah University, Iraq, Ph.D. (Nuclear Physics), Baghdad University, Professor at Physiology and Medical Physics Department, College of Medicine, Al-Nahrain University (Al-Jadria, Baghdad, 10072, Iraq). [ScopusID](#), [ResearcherID](#), [ORCID](#), rasha.sabeehahmed@colmed-alnahrain.edu.iq

Khaleel I. Mohson, MD, Assistant Professor of the Radiology Department, Head of Clinical Department, National Cancer Research Center, University of Baghdad (Al-Jadria, Baghdad, 10072, Iraq). khalelcabm@gmail.com

Claimed contributorship:

NF Baqir: experimental base, samples and equipment; computational analysis; discussion of the results, and writing—original draft.

RS Ahmed: planning and organization of experiments; analysis of the results obtained; correction of the conclusions.

KI Mohson: academic advising; basic concept formulation; research objectives and tasks; discussion of the results; text preparation; formulation of conclusions.

Conflict of interest statement: the authors declare that they do not have any conflict of interest.

All authors have read and approved the final manuscript.

Об авторах:

Noor F. Baqir, бакалавр наук (радиологическая инженерия), Колледж медицины и оздоровительных технологий Среднего технического университета, Ирак (Muasker, Al Rashid Street, Baghdad, Iraq), технолог МРТ в Учебной онкологической больнице в Медицинском городке, Багдад, Ирак, lavendrtechnologist2017@gmail.com

Rasha S. Ahmed, бакалавр наук (физика), магистр наук (атомная физика), Университет Мустансирия, Ирак, доктор философии (ядерная физика), Багдадский университет, профессор кафедры физиологии и медицинской физики в Медицинском колледже Университета Аль-Нахрейн, Багдад, Ирак (Al-Jadria, Baghdad, 10072, Iraq), [Scopus ID](#), [Researcher ID](#), [ORCID](#), rasha.sabeehahmed@colmed-alnahrain.edu.iq

Khaleel I. Mohson, доктор медицинских наук, доцент кафедры радиологии, руководитель клинического отделения Национального центра исследования рака, Багдадский университет, Ирак (Al-Jadria, Baghdad, 10072, Iraq), khalelcabm@gmail.com

Заявленный вклад соавторов:

N.F. Baqir — экспериментальная база, образцы и оборудование; проведение расчетов; обсуждение результатов; написание чернового варианта статьи.

R.S. Ahmed — планирование и организация экспериментов; анализ полученных результатов; корректировка выводов.

K.I. Mohson — научное руководство; формирование основной концепции; цели и задачи исследования; обсуждение результатов; подготовка текста; формулирование выводов.

Конфликт интересов: авторы заявляют об отсутствии конфликта интересов.

Все авторы прочитали и одобрили окончательный вариант рукописи.

INFORMATION TECHNOLOGY, COMPUTER SCIENCE AND MANAGEMENT



UDC 004.9

Original article

<https://doi.org/10.23947/2687-1653-2023-23-3-317-328>

3D Human Motion Capture Method Based on Computer Vision

Artem D. Obukhov , Denis L. Dedov , Ekaterina O. Surkova , Irina L. Korobova 

Tambov State Technical University, Tambov, Russian Federation

[✉ obuhov.art@gmail.com](mailto:obuhov.art@gmail.com)

Abstract

Introduction. The analysis of approaches to tracking the human body identified problems when capturing movements in a three-dimensional coordinate system. The prospects of motion capture systems based on computer vision are noted. In existing studies on markerless motion capture systems, positioning is considered only in two-dimensional space. Therefore, the research objective is to increase the accuracy of determining the coordinates of the human body in three-dimensional coordinates through developing a motion capture method based on computer vision and triangulation algorithms.

Materials and Methods. A method of motion capture was presented, including calibration of several cameras and formalization of procedures for detecting a person in a frame using a convolutional neural network. Based on the skeletal points obtained from the neural network, a three-dimensional reconstruction of the human body model was carried out using various triangulation algorithms.

Results. Experimental studies have been carried out comparing four triangulation algorithms: direct linear transfer, linear least squares method, L2 triangulation, and polynomial methods. The optimal triangulation algorithm (polynomial) was determined, providing an error of no more than 2.5 pixels or 1.67 centimeters.

Discussion and Conclusion. The shortcomings of existing motion capture systems were revealed. The proposed method was aimed at improving the accuracy of motion capture in three-dimensional coordinates using computer vision. The results obtained were integrated into the human body positioning software in three-dimensional coordinates for use in virtual simulators, motion capture systems and remote monitoring.

Keywords: motion capture, virtual reality, triangulation, computer vision, machine learning

Acknowledgements: the authors would like to thank the Editorial board of the journal and the reviewer for their professional analysis and recommendations for correcting the text of the article.

Funding information. The research was done on grant of the Russian Science Foundation No. 22–71–10057, <https://rscf.ru/project/22-71-10057/>

For citation. Obukhov AD, Dedov DL, Surkova EO, Korobova IL. 3D Human Motion Capture Method Based on Computer Vision. *Advanced Engineering Research (Rostov-on-Don)*. 2023;23(3):317–328. <https://doi.org/10.23947/2687-1653-2023-23-3-317-328>

Метод трехмерного захвата движений человека на основе компьютерного зрения

А.Д. Обухов , Д.Л. Дедов , Е.О. Суркова , И.Л. Коробова 

Тамбовский государственный технический университет, г. Тамбов, Российская Федерация

✉ obuhov.art@gmail.com

Аннотация

Введение. Проведенный анализ существующих подходов к отслеживанию тела человека выявил наличие проблем при захвате движений в трехмерной системе координат. Отмечена перспективность систем захвата движений на основе компьютерного зрения. В существующих исследованиях по безмаркерным системам захвата движений рассматривается позиционирование только в двумерном пространстве. Поэтому целью исследования являлось повышение точности определения координат человеческого тела в трехмерных координатах за счет разработки метода захвата движения на основе компьютерного зрения и алгоритмов триангуляции.

Материалы и методы. Представлен метод захвата движений, включающий калибровку нескольких камер и формализацию процедур обнаружения человека в кадре с использованием сверточной нейронной сети. На основе полученных от нейронной сети скелетных точек осуществляется трехмерная реконструкция модели тела человека с использованием различных алгоритмов триангуляции.

Результаты исследования. Проведены экспериментальные исследования по сравнению четырех алгоритмов триангуляции: прямого линейного переноса, линейного метода наименьших квадратов, L2 триангуляции и полиномиального методов. Определен оптимальный алгоритм триангуляции (полиномиальный), обеспечивающий погрешность не более 2,5 пикселей или 1,67 сантиметров.

Обсуждение и заключение. Выявлены недостатки существующих систем захвата движения. Предложенный метод направлен на повышение точности захвата движений в трехмерных координатах с использованием компьютерного зрения. Полученные результаты интегрированы в программное обеспечение позиционирования тела человека в трехмерных координатах для удаленного мониторинга, использования в виртуальных тренажерах и системах захвата движений.

Ключевые слова: захват движений, виртуальная реальность, триангуляция, компьютерное зрение, машинное обучение

Благодарности: авторы выражают благодарность редакционной коллегии журнала и рецензенту за профессиональный анализ и рекомендации по корректировке текста статьи.

Финансирование. Исследование выполнено за счет гранта Российского научного фонда № 22–71–10057, <https://rscf.ru/project/22-71-10057/>

Для цитирования. Обухов А.Д., Дедов Д.Л., Суркова Е.О., Коробова И.Л. Метод трехмерного захвата движений человека на основе компьютерного зрения. *Advanced Engineering Research (Rostov-on-Don)*. 2023;23(3):317–328. <https://doi.org/10.23947/2687-1653-2023-23-3-317-328>

Introduction. Significant progress has currently been made in the domain of computer vision. Technologies have been developed to solve the problems of detecting objects, determining their state, geometric evaluation of the space depicted on the frame, and a lot more. As a result, computer vision has become widespread in various spheres of human activity, ranging from healthcare and education to entertainment. A rather promising direction is the use of computer

vision technologies for three-dimensional reconstruction and positioning of various objects, including people. There is fairly large number of systems for determining the absolute position of a person in space, which can be divided into the following categories.

- Systems using inertial sensors and providing the determination of the amount of their movement, as well as the change of angles between them, which involves the use of gyroscopes and accelerometers [1]. A well-known representative of this category is the Noitom Mocap Perception Neuron [2], which includes up to 32 inertial sensors.

- Laser position tracking systems based on the use of base stations installed on opposite sides of the room and emitting infrared rays, which provide accurate determination of the position and orientation of sensors in space. An example of such systems is a virtual reality kit from HTC [3], which have an error of up to 0.1 mm.

- Systems using magnetic sensors [4] based on the use of a magnetic field to capture human movement, which assume the presence of wearable sensors on the user's body. This category includes Polhemus Liberty — a portable electromagnetic motion tracking system, considered one of the fastest (sampling rate — 240 Hz).

- Marker-based optical systems determine the position of objects by markers using a set of cameras. An example is Vicon, which has a fairly low error: the average absolute errors of marker tracking are 0.15 mm in static tests, and 0.2 mm (with corresponding angular errors of 0.3°) in dynamic tests [5].

- Marker-free optical systems based on the use of computer vision and machine learning. Examples of such technologies are Open space, MediaPipe, Movenext. With their help, human movements can be tracked with an accuracy of up to 30 mm [6].

After analyzing the listed categories of motion capture systems, it can be concluded that most of the solutions used to recognize human actions and movements involve various wearable devices, such as sensors or gloves. Most of these devices are bulky due to the large number of sensors and the need for a wired connection. Some systems have high accuracy, but they cannot be used due to the size or the presence of electromagnetic interference [7]. Inertial systems have a number of problems associated with the accumulation of errors, which limits their use only to relative positioning in space.

Therefore, optical systems for recognizing and tracking user actions are well regarded. To get information about the actions and position of the user, frames obtained from the camera are used. Among optical systems, it is worth noting those that use markers (the user may be wearing special clothes or certain labels fixed on him), which makes it difficult to use them under real conditions. They are more applicable to specially prepared premises (e.g., film studios).

Systems that do not use any markers allow users to interact more freely with the environment and are more suitable for use under real conditions. The significant disadvantages of systems in this line include relatively low accuracy, unreliability, and low performance. To a great extent, this may be due to the shortcomings of computer vision algorithms used to recognize a person in the frame, as well as the following reasons: the variability of a person's appearance and lighting conditions, partial occlusions owing to the layering of objects in the scene, the complexity of the human skeletal structure.

As a rule, the operation of marker-free motion capture systems is based on an algorithm for evaluating a person's posture. Approaches to solving the problem of assessing a person's posture can be divided into top-bottom and bottom-up. In top-bottom approaches, first there is a detection of people in the frame, then an assessment of the pose of each person found. Algorithms that relate to the bottom-up approach, at the first stage, search for body parts in the frame, then group them into poses. As a rule, convolutional neural networks are used for this task, such as YOLO (You Look Only Once) [8], SSD (Single Shot Detection) [9], R-CNN (Region CNN) [10], and others. They provide the recognition of numerous different objects, including a person or individual body parts with high accuracy. However, one of the disadvantages of the solutions listed above is their low performance and slow operation. To solve this problem, there

are special frameworks (MoveNet [11], MediaPipe [12], OpenPose [13]) that also use neural networks optimized for real-time operation.

It should be noted that the above algorithms, technologies and approaches of marker-free motion capture systems provide positioning in two-dimensional space, which makes it difficult both to determine the distance to objects and their sizes, and to track complex movements when, e.g., the user's hands are hidden by his body. Existing solutions in the field of stereo cameras can be effective, but they are not very accurate when the object is significantly removed from the camera, which happens when tracking the entire human body. In addition, they do not solve the problem of occlusions. Thus, the major line of research is the development of a method of motion capture using multiple cameras and computer vision technologies. When implementing multi-camera motion capture systems, the problem of combining objects from several images inevitably arises, i.e., the need to perform triangulation. Among the triangulation methods, linear and iterative linear algorithms can be distinguished.

Linear triangulation is the most common approach to performing reconstruction of objects in three-dimensional space, including such methods as linear-proportional method, linear least squares method, direct linear transformation, which differ in varying degrees of resistance to noise [14].

Iterative linear methods are a more robust version of linear triangulation. Conventional linear methods may be less accurate when solving problems of triangulation of a set of points, since in this case, the minimized error has no geometric meaning (it does not take into account the shape of the skeleton and the rules for connecting points). The key idea of iterative linear methods is to adaptively change the weights of linear equations in such a way that the weighted equations correspond to errors. Iterative linear methods include L_2 and L_∞ triangulation [15].

Thus, within the framework of this study, the following task was set: to develop a method for capturing human movements that provides positioning the user's body in three-dimensional coordinates with minimal error and using computer vision technologies. The proposed method can be used as a replacement for existing motion capture systems, or as part of other algorithms, e.g., for the subsequent classification of a person's condition. This work was aimed at increasing the accuracy of determining the poses and coordinates of the human body in three-dimensional coordinates by developing motion capture methods based on computer vision. To achieve this goal, it was required to formalize the main stages of the process of capturing points of the human body from several cameras, integrate triangulation algorithms, choosing among them the optimal one from the point of view of accuracy, carry out the software implementation of the proposed method.

Materials and Methods. Solving the problem of 3D positioning of a person in space includes the following main stages:

- preliminary calibration of a set of cameras;
- implementation of human detection procedures in the frame, and calculation of skeletal points;
- calculation of 3D reconstruction of the human body model.

Let us look at them in more detail.

The calibration process involves the camera system taking several pictures of a calibration template, on which it is easy to identify key points with known relative positions in space. After that, internal and external parameters are calculated for each camera. Internal parameters are constant for a particular camera, external parameters depend on the location of the cameras relative to each other [16]. Therefore, this step must be performed before the first use of the camera system in a given location.

To calculate the coordinates of a point in three-dimensional space, it is necessary to know the coordinates of its projection on the images and the projective matrices of the cameras [17]. Projective matrix P of some camera can be represented as a combination of matrices A (containing the internal parameters of the camera) and R (rotation), as

well as the displacement vector T , which describe the change of coordinates from the world coordinate system to the coordinate system relative to the camera:

$$P = A[R | T] = \begin{bmatrix} f_x & 0 & c_x \\ 0 & f_y & c_y \\ 0 & 0 & 1 \end{bmatrix} \begin{bmatrix} r_{11} & r_{12} & r_{13} & t_1 \\ r_{21} & r_{22} & r_{23} & t_2 \\ r_{31} & r_{32} & r_{33} & t_3 \end{bmatrix}, \quad (1)$$

where (x, y) — coordinates of the projection of a 3D point on the image in pixels; (c_x, c_y) — coordinates of the central point of the camera; (f_x, f_y) — focal length in pixels.

At the second stage, it is required to obtain directly the key (skeletal) points of the human body on each of their cameras. To extract skeletal body points from the frame, it is possible to use various machine learning technologies, e.g., MoveNet, MediaPipe, OpenPose, and others [18]. As part of this study, it is proposed to use a highly efficient and productive Pose module from the MediaPipe library. MediaPipe Pose uses machine learning to accurately track a person's body posture, determine 3D landmarks, and mask background segmentation on the entire body from RGB video frames. This approach makes it possible to track up to 33 points and provides real-time operation on most modern devices.

Thus, as part of the second stage, a set of 33 points is formed for each i -th camera:

$$\{x_{ij} = \langle u_{ij}, v_{ij} \rangle \mid j \in \{1, 2, \dots, 33\}, i \in \{1, 2, \dots, K\}\}, \quad (2)$$

where u_{ij} — coordinate of j -th point on X axis in i -th image; v_{ij} — coordinate of j -th point on Y axis in i -th image; K — total number of cameras and images.

At the third stage, the positions of key skeletal points in three-dimensional space are calculated. To obtain data on the position of human skeletal points in space, triangulation is performed — finding the coordinates of a 3D point by the coordinates of its projections. Triangulation is one of the most important challenges in computer vision, its solution is a crucial stage in 3D reconstruction, it affects the accuracy of the entire result [19].

Epipolar geometry is fundamental for the three-dimensional reconstruction of the object points based on the position values of the projections of the points in the images from all cameras. Its main idea is that 3D points in the scene are projected onto lines in the image plane of each camera — epipolar lines. These lines correspond to the intersection of the image plane and the plane passing through the camera centers and the 3D point. This idea provides a condition for finding pairs of corresponding points on two images: if it is known that point x on the plane of the first image corresponds to point x' on the plane of another image, then its projection should lie on the corresponding epipolar line. According to this condition, the following relation will be valid for all corresponding pairs of points $x \leftrightarrow x'$:

$$x'Fx = 0, \quad (3)$$

where F — fundamental matrix having size 3×3 and rank equal to 2.

For some point X , given in three-dimensional space, the following projection formula expressed in homogeneous coordinates is valid:

$$x_i = P_i X, \quad (4)$$

where $x_i = w(u_i, v_i, 1)^T$ — homogeneous coordinates of some point on the plane of the i -th image (obtained from the i -th camera during the second stage), including the position on image u_i (on X axis) and v_i (on Y axis); w — scale factor; P_i — projection matrix of i -th camera obtained at the first stage.

To simplify calculations, the projection matrix of the camera is often presented in the following form:

$$P_i = \begin{bmatrix} p_i^{1T} \\ p_i^{2T} \\ p_i^{3T} \end{bmatrix} (P_i \in \mathbb{R}^{3 \times 4}), \quad (5)$$

where p_i^{jT} — j -th row of matrix P_i .

Therefore, equation (4) can be represented as follows:

$$\begin{aligned} wu_i &= p_i^{1T} X, \\ wv_i &= p_i^{2T} X, \\ w &= p_i^{3T} X. \end{aligned} \quad (6)$$

Since w — scale factor, we obtain the following system of equations:

$$\begin{aligned} u_i p_i^{3T} X - p_i^{1T} X &= 0, \\ v_i p_i^{3T} X - p_i^{2T} X &= 0. \end{aligned} \quad (7)$$

Since X is a homogeneous representation of coordinates in three-dimensional space, then, for their calculation, it is necessary to obtain x_i and P_i for at least two cameras. To solve the system of equations (7), 4 algorithms were considered [14]:

- direct linear transfer (DLT);
- linear least squares method;
- L2 triangulation;
- optimal (polynomial) method.

DLT refers to a linear triangulation algorithm, whose main advantage is the simplicity of its implementation. Specifically, in the OpenCV computer vision library there is a ready-made implementation of this algorithm in the triangulatePoints method.

The linear least squares method also refers to linear ones and consists in the fact that the system of homogeneous equations (7) is reduced to a system consisting of inhomogeneous equations, for whose solution, the least squares method is used.

L2 triangulation is an iterative method of three-dimensional reconstruction, whose solution is reduced to minimizing the reprojection error:

$$\sum_i d(x_i, \hat{x}_i) \rightarrow \min, \quad (8)$$

where x_i — coordinate of the projection of the estimated point in the image; \hat{x}_i — projection coordinate calculated from formula (4) for an already determined spatial point; $d(\bullet)$ — distance between two points.

The algorithm of optimal (polynomial) triangulation refers to non-iterative approaches. To solve it, a sextic polynomial is required. The minimization criterion for performing three-dimensional reconstruction in this method can be defined as follows:

$$\sum_i d(x_i, \lambda_i) \rightarrow \min, \quad (9)$$

where λ_i — epipolar line corresponding to point x_i .

When using a two-camera system, to minimize error (9), the following sequence of actions must be performed:

- parametrize the bundle of epipolar lines in the first image using parameter t . Thus, the epipolar line in the first image can be expressed as $\lambda_0(t)$;
- using fundamental matrix F , calculate the corresponding epipolar line $\lambda_1(t)$ in the second image;
- express the distance function (9) as a function of t ;
- perform a search for value t , at which (9) tends to a minimum.

Using the methods of elementary calculus, it is possible to reduce the solution of the minimization problem to finding the roots of a sextic polynomial. The calculation of the assumed spatial point is performed using the direct linear transfer method (DLT) [17].

Summing up the third stage, we get that after successfully solving system (7) and obtaining the world coordinates of the key points of the target object (human body), the following set of points H is formed:

$$H = \{X_j \mid \forall i (x_{ij} = P_i X_j)\}, \quad (10)$$

where X_j — world coordinates of the skeletal point of the human body obtained after solving the triangulation problem, expressed in centimeters.

Thus, in this study, the optimization problem, when using two cameras, is reduced to finding triangulation method $MT: \{x_{ij}\} \rightarrow H$, in which the reprojection error tends to a minimum:

$$R = \frac{\sum_{i=1}^2 \sum_{j=1}^K d(x_{ij}, \hat{x}_{ij})}{K} \rightarrow \min. \quad (11)$$

Research Results. Optimization problem (11) is solved through performing triangulation of 2D object points obtained from images of several cameras, in the framework of this study — from two cameras using various algorithms listed in the previous section.

The listed triangulation methods were implemented using OpenCV and NumPy libraries. For comparison, the algorithms were integrated into software implementing the method of three-dimensional motion capture. An example of the method for reconstructing the entire human skeleton is shown in Figure 1.

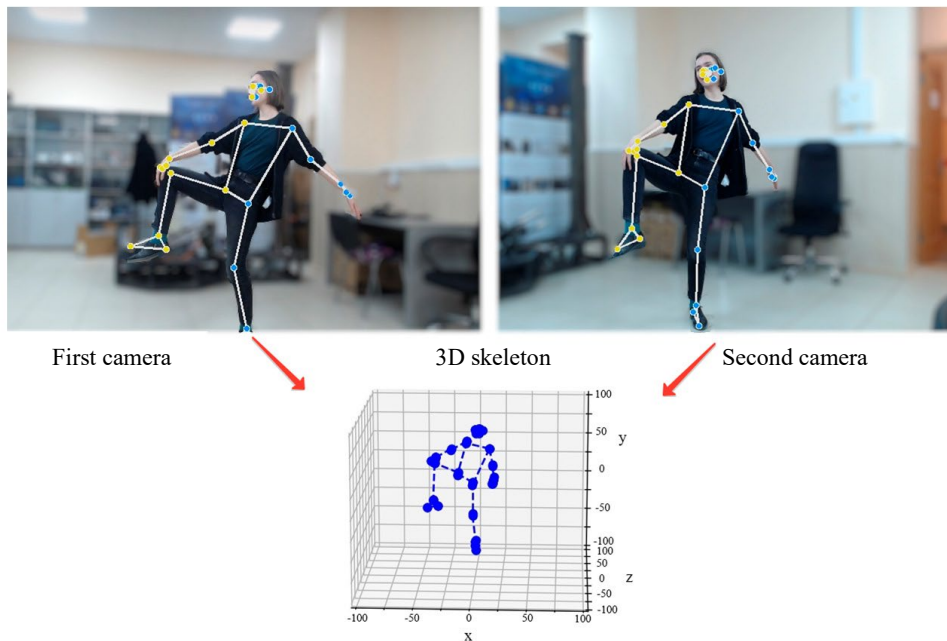


Fig. 1. Example of the method, including recognition of a person on two cameras and construction of a 3D skeleton

Then, these algorithms were compared by the value of the reprojection error function (11) for all points of the skeleton from two images. The comparison of the selected triangulation methods by the error rate, as well as by the time of obtaining a solution (computational complexity) for the entire set of skeleton points was carried out. Summary comparative diagrams are shown in Figure 2.

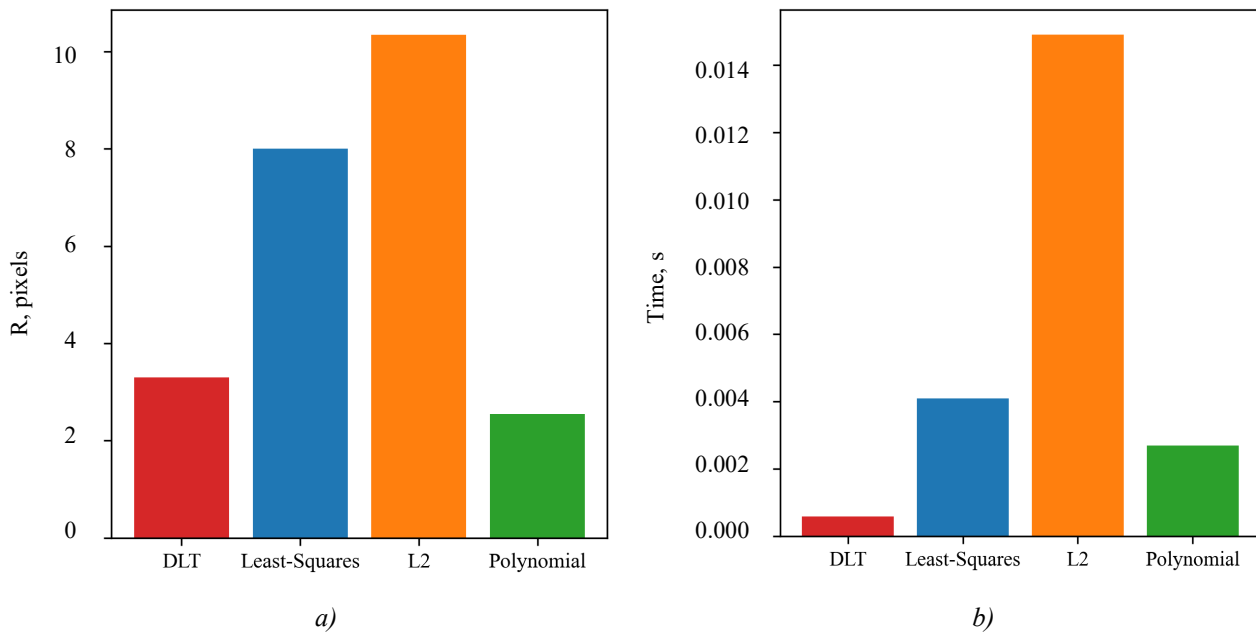


Fig. 2. Comparison of triangulation methods by metrics: *a* — by reprojection error; *b* — by calculation time

A number of experimental tests were also carried out for the selected triangulation methods. Under testing, the calculated lengths of the user's limbs and the absolute deviation of the obtained values from the real ones were measured for each approach. The comparison is presented in Table 1.

Table 1

Comparison of the accuracy of determining the size of limbs in the process of triangulation

Body segment	DLT	Least Squares	L2	Polynomial	Real value
Forearm	25.2 ± 1.6	30.8 ± 0.2	26.6 ± 0.5	24.3 ± 0.4	26
Shin	42.2 ± 2.0	65.3 ± 1.1	44.6 ± 0.7	38.7 ± 1.8	41
Hip	45.7 ± 2.7	59.5 ± 0.49	48.7 ± 1.3	44.1 ± 0.6	45
Average deviation	2.43	14.58	2.26	1.67	0
Presented are the average values (in centimeters) after a sample of 10 measurements \pm standard deviation in the sample					

The developed software includes the following modules:

- for working with input devices (cameras);
- to perform calibration and obtain basic camera parameters;
- to synchronize multiple cameras;
- for object recognition (user's body and arms);
- to analyze the location of the found skeletal points;
- to build real-time visualization.

When implementing the software, the Python programming language, OpenCV and Matplotlib libraries were used. The operation of the system was carried out in several streams: one was responsible for receiving data from cameras, the second — for visualization, the third — for sending the received world coordinates of the human body to external systems or modules. Using a unified protocol with a data package in JSON format provides integrating the software into third-party systems (e.g., Unity game development environments, Unreal Engine, etc.) [20, 21].

Discussion and Conclusion. Let us analyze the results of comparing triangulation algorithms by selected metrics, shown in Figure 2 and in Table 1.

During the comparison, it was found that the optimal algorithm for three-dimensional reconstruction was the polynomial method. The error value was about 2.55 pixels. In real tests, when determining a person's height, the error

was no more than 3 %, taking into account the fact that MediaPipe Pose did not fix the upper point of the head and it was calculated approximately based on the position of the eyes. When measuring limbs, the error ranged from 0.9 cm to 2.3 cm, the average was 1.67 (Table 1). Thus, real tests validate the correctness of the choice of the polynomial method.

Next, we compared the results obtained with existing studies, e.g., described in [22]. The authors also used trained networks (OpenPose) to implement a marker-free human recognition system, a camera calibration procedure, and the extraction of skeletal points, but placed cameras next to each other to simulate stereo vision. This key difference made it possible to recognize human postures within the framework of this study, when some parts of the body overlapped others. In addition, using MediaPipe Pose provided tracking 33 skeletal points, not 18, as in the OpenPose-based method. The obtained error values generally corresponded to existing studies (the best result in [22] was 2 cm), which allowed us to conclude that the proposed approach can be used in practice. Other marker-free systems, e.g., based on Kinect [23], also showed comparable results in terms of measurement error (2–5 cm). Thus, the resulting solution generally corresponded to the accuracy of existing developments.

A comparison of the calculation time of a set of points, shown in Figure 2 on the right, demonstrated that the DLT algorithm provided the highest performance. However, all algorithms showed acceptable results (to provide a speed of 30 and even 60 frames per second). Therefore, this metric was not determinative.

The developed software can be used in various subject areas primarily as a replacement for motion capture systems based on inertial sensors. The advantages of the proposed solution are low economic costs for implementation and accessibility (transition from highly specialized motion capture suits to common camera-based tools), the possibility of parallel capture of body models of several users [24].

The scientific novelty of the research consists in a comprehensive approach to formalizing the process of three-dimensional positioning of a person using computer vision technologies. It includes preliminary calibration of a set of several cameras, formalization of procedures for detecting a person in a frame using an arbitrary neural network to obtain skeletal points, as well as calculation of three-dimensional reconstruction of a human body model using various triangulation algorithms. The study presents all the necessary calculation formulas and detailed steps to achieve the goal — to increase the accuracy of determining the poses and coordinates of the human body in three-dimensional coordinates using computer vision technologies. The theoretical results obtained are quite universal and can be used for the practical implementation of motion capture systems based on various models of neural networks, and not just MediaPipe Pose.

References

1. Lind CM, Abtahi F, Forsman M. Wearable Motion Capture Devices for the Prevention of Work-Related Musculoskeletal Disorders in Ergonomics – An Overview of Current Applications, Challenges, and Future Opportunities. *Sensors*. 2023;23(9):4259. <https://doi.org/10.3390/s23094259>
2. Sers R, Forrester S, Moss E, Ward S, Ma J, Zecca M. Validity of the Perception Neuron Inertial Motion Capture System for Upper Body Motion Analysis. *Measurement*. 2020;149:107024. <http://dx.doi.org/10.1016/j.measurement.2019.107024>
3. Bauer P, Lienhart W, Jost S. Accuracy Investigation of the Pose Determination of a VR System. *Sensors*. 2021;21(5):1622. <http://dx.doi.org/10.3390/s21051622>
4. Irshad MT, Nisar MA, Gouverneur P, Rapp M, Grzegorzec M. AI Approaches towards Prechtl's Assessment of General Movements: A Systematic Literature Review. *Sensors*. 2020;20(18):5321. <http://dx.doi.org/10.3390/s20185321>
5. Merriault P, Dupuis Y, Bouteau R, Vasseur P, Savatier X. A Study of Vicon System Positioning Performance. *Sensors*. 2017;17(7):1591. <https://doi.org/10.3390/s17071591>

6. Nakano N, Sakura T, Ueda K, Omura L, Kimura A, Iino Y, et al. Evaluation of 3D Markerless Motion Capture Accuracy Using OpenPose with Multiple Video Cameras. *Frontiers in Sports and Active Living*. 2020;2:50. <https://doi.org/10.3389/fspor.2020.00050>
7. Coronado E, Fukuda K, Ramirez-Alpizar IG, Yamanobe N, Venture G, Harada K. Assembly Action Understanding from Fine-Grained Hand Motions, a Multi-camera and Deep Learning Approach. In: *Proc. IEEE/RSJ International Conference on Intelligent Robots and Systems (IROS)*. New York, NY: IEEE; 2021. P. 2628–2634. <http://dx.doi.org/10.1109/IROS51168.2021.9636715>
8. Tausif Diwan, Anirudh G, Tembhurne JV. Object Detection Using YOLO: Challenges, Architectural Successors, Datasets and Applications. *Multimedia Tools and Applications*. 2023;82(6):9243–9275. <https://doi.org/10.1007/s11042-022-13644-y>
9. Wei Liu, Anguelov D, Erhan D, Szegedy C, Reed S, Cheng-Yang Fu, et al. SSD: Single Shot MultiBox Detector. In book: Leibe B, Matas J, Sebe N, Welling M (eds). *Computer Vision – ECCV 2016*. Cham: Springer. 2016;9905: 21–37. https://doi.org/10.1007/978-3-319-46448-0_2
10. Bharati P, Pramanik A. Deep Learning Techniques—R-CNN to Mask R-CNN: A Survey. In book: Das A, Nayak J, Naik B, Pati S, Pelusi D (eds). *Computational Intelligence in Pattern Recognition*. New York, NY: Springer. 2020;999:657–668. http://dx.doi.org/10.1007/978-981-13-9042-5_56
11. Bajpai R, Joshi D. MoveNet: A Deep Neural Network for Joint Profile Prediction across Variable Walking Speeds and Slopes. *IEEE Transactions on Instrumentation and Measurement*. 2021;70:1–11. <http://dx.doi.org/10.1109/TIM.2021.3073720>
12. Ghanbari S, Ashtyani ZP, Masouleh MT. User Identification Based on Hand Geometrical Biometrics Using Media-Pipe. In: *Proc. 30th International Conference on Electrical Engineering (ICEE)*. New York, NY: IEEE; 2022. P. 373–378. <http://dx.doi.org/10.1109/ICEE55646.2022.9827056>
13. Weijian Mai, Fengjie Wu, Ziqian Guo, Yuhang Xiang, Gensheng Liu, Xiaobin Chen. A Fall Detection Alert System Based on Lightweight Openpose and Spatial-Temporal Graph Convolution Network. *Journal of Physics: Conference Series*. 2021;2035:012036. <http://dx.doi.org/10.1088/1742-6596/2035/1/012036>
14. Szeliski R. Recognition. In book: *Computer Vision: Algorithms and Applications*. London: Springer; 2011. P. 575–640. https://doi.org/10.1007/978-1-84882-935-0_14
15. Kahl F, Hartley R. Multiple-View Geometry Under the L_∞ -Norm. *IEEE Transactions on Pattern Analysis and Machine Intelligence*. 2008;30(9):1603–1617. <http://dx.doi.org/10.1109/TPAMI.2007.70824>
16. Luhmann T, Fraser C, Maas H-G. Sensor Modelling and Camera Calibration for Close-Range Photogrammetry. *ISPRS Journal of Photogrammetry and Remote Sensing*. 2016;115:37–46. <https://doi.org/10.1016/j.isprsjprs.2015.10.006>
17. Kudinov IA, Pavlov OV, Holopov IS. Implementation of an Algorithm for Determining the Spatial Coordinates and the Angular Orientation of an Object Based on Reference Marks Using Information from a Single Camera. *Computer Optics*. 2015;39(3):413–419. <https://doi.org/10.18287/0134-2452-2015-39-3-413-419>
18. Jen-Li Chung, Lee-Yeng Ong, Meng-Chew Leow. Comparative Analysis of Skeleton-Based Human Pose Estimation. *Future Internet*. 2022;14(12):380. <https://doi.org/10.3390/fi14120380>
19. Jia Chen, Dongli Wu, Peng Song, Fuqin Deng, Ying He Y, Shiyang Pang. Multi-View Triangulation: Systematic Comparison and an Improved Method. *IEEE Access*. 2020;8:21017–21027. <http://dx.doi.org/10.1109/ACCESS.2020.2969082>
20. Obukhov A, Dedov D, Volkov A, Teselkin D. Modeling of Nonlinear Dynamic Processes of Human Movement in Virtual Reality Based on Digital Shadows. *Computation*. 2023;11(5):85. <https://doi.org/10.3390/computation11050085>
21. Abella J, Demircan E. A Multi-Body Simulation Framework for Live Motion Tracking and Analysis within the Unity Environment. In: *Proc. 16th International Conference on Ubiquitous Robots (UR)*. New York, NY: IEEE; 2019. P. 654–659. <http://dx.doi.org/10.1109/URAI.2019.8768659>

22. Zago M, Luzzago M, Marangoni T, De Cecco M, Tarabini M, Galli M. 3D Tracking of Human Motion Using Visual Skeletonization and Stereoscopic Vision. *Frontiers in Bioengineering and Biotechnology*. 2020;8:181. <https://doi.org/10.3389/fbioe.2020.00181>
23. Latorre J, Llorens R, Colomer C, Alcañiz M. Reliability and Comparison of Kinect-Based Methods for Estimating Spatiotemporal Gait Parameters of Healthy and Post-Stroke Individuals. *Journal of Biomechanics*. 2018;72:268–273. <https://doi.org/10.1016/j.jbiomech.2018.03.008>
24. Obukhov AD, Volkov AA, Vekhteva NA, Patutin KI, Nazarova AO, Dedov DL. The Method of Forming a Digital Shadow of the Human Movement Process Based on the Combination of Motion Capture Systems. *Informatics and Automation*. 2023;22(1):168–189. <https://doi.org/10.15622/ia.22.1.7>

Received 18.05.2023

Revised 13.06.2023

Accepted 19.06.2023

About the Authors:

Artem D. Obukhov, Dr.Sci. (Eng.), Associate Professor of the Department of Automated Systems for Decision-Making Support, Tambov State Technical University (1, Leningradskaya St., Tambov, 392036, RF), [ResearcherID](#), [ScopusID](#), [AuthorID](#), [ORCID](#), obuhov.art@gmail.com

Denis L. Dedov, Cand.Sci. (Eng.), Senior Researcher, Tambov State Technical University (116, Sovetskaya St., Tambov, 392000, RF), [ScopusID](#), [AuthorID](#), [ORCID](#), hammer68@mail.ru

Ekaterina O. Surkova, 4th year student of the Department of Automated Systems for Decision-Making Support, Tambov State Technical University (1, Leningradskaya St., Tambov, 392036, RF), [ScopusID](#), [AuthorID](#), [ORCID](#), esur2506@yandex.ru

Irina L. Korobova, Cand.Sci. (Eng.), Head of the Department of Automated Systems for Decision-Making Support, Tambov State Technical University (1, Leningradskaya St., Tambov, 392036, RF), [AuthorID](#), [ORCID](#), ira.sapr.tstu@mail.ru

Claimed contributorship:

AD Obukhov: basic concept formulation, academic advising, formulation of the research objective and tasks, text preparation, formulation of conclusions.

DL Dedov: organization of experimental research, text preparation.

EO Surkova: experimental research, software development.

IL Korobova: analysis of research results, revision of the text.

Conflict of interest statement: the authors do not have any conflict of interest.

All authors have read and approved the final version of the manuscript.

Поступила в редакцию 18.05.2023

Поступила после рецензирования 13.06.2023

Принята к публикации 19.06.2023

Об авторах:

Артём Дмитриевич Обухов, доктор технических наук, доцент кафедры системы автоматизированной поддержки принятия решений Тамбовского государственного технического университета, (392036, РФ, г. Тамбов, ул. Ленинградская, 1), [ResearcherID](#), [ScopusID](#), [AuthorID](#), [ORCID](#), obuhov.art@gmail.com

Денис Леонидович Дедов, кандидат технических наук, старший научный сотрудник Тамбовского государственного технического университета, (392000, РФ, г. Тамбов, ул. Советская, 116), [ScopusID](#), [AuthorID](#), [ORCID](#), hammer68@mail.ru

Екатерина Олеговна Суркова, студентка 4 курса кафедры системы автоматизированной поддержки принятия решений Тамбовского государственного технического университета, (392036, РФ, г. Тамбов, ул. Ленинградская, 1), [ScopusID](#), [AuthorID](#), [ORCID](#), esur2506@yandex.ru

Ирина Львовна Коробова, кандидат технических наук, заведующая кафедрой системы автоматизированной поддержки принятия решений Тамбовского государственного технического университета, (392036, РФ, г. Тамбов, ул. Ленинградская, 1), [AuthorID](#), [ORCID](#), ira.sapr.tstu@mail.ru

Заявленный вклад соавторов:

А.Д. Обухов — формирование основной концепции, научное руководство, формулирование цели и задач исследования, подготовка текста, формирование выводов.

Д.Л. Дедов — организация экспериментальных исследований, подготовка текста.

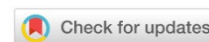
Е.О. Суркова — проведение экспериментальных исследований, разработка программного обеспечения.

И.Л. Коробова — анализ результатов исследования, доработка текста.

Конфликт интересов: авторы заявляют об отсутствии конфликта интересов.

Все авторы прочитали и одобрили окончательный вариант рукописи

INFORMATION TECHNOLOGY, COMPUTER SCIENCE AND MANAGEMENT



UDC 004.272.22

Original article

<https://doi.org/10.23947/2687-1653-2023-23-3-329-339>

Model of a Parallel-Pipeline Computational Process for Solving a System of Grid Equations

 Vladimir N. Litvinov¹ , Nelli B. Rudenko² , Natalya N. Gracheva² 
¹Don State Technical University, Rostov-on-Don, Russian Federation² Azov-Black Sea Engineering Institute, Don State Agrarian University, Zernograd, Russian Federation✉ LitvinovVN@rambler.ru

Abstract

Introduction. Environmental problems arising in shallow waters and caused by both natural and man-made factors annually do significant damage to aquatic systems and coastal territories. It is possible to identify these problems in a timely manner, as well as ways to eliminate them, using modern computing systems. But earlier studies have shown that the resources of computing systems using only a central processor are not enough to solve large scientific problems, in particular, to predict major environmental accidents, assess the damage caused by them, and determine the possibilities of their elimination. For these purposes, it is proposed to use models of the computing system and decomposition of the computational domain to develop an algorithm for parallel-pipeline calculations. The research objective was to create a model of a parallel-conveyor computational process for solving a system of grid equations by a modified alternating-triangular iterative method using the decomposition of a three-dimensional uniform computational grid that takes into account technical characteristics of the equipment used for calculations.

Materials and Methods. Mathematical models of the computer system and computational grid were developed. The decomposition model of the computational domain was made taking into account the characteristics of a heterogeneous system. A parallel-pipeline method for solving a system of grid equations by a modified alternating-triangular iterative method was proposed.

Results. A program was written in the CUDA C language that implemented a parallel-pipeline method for solving a system of grid equations by a modified alternating-triangular iterative method. The experiments performed showed that with an increase in the number of threads, the computation time decreased, and when decomposing the computational grid, it was rational to split into fragments along coordinate z by a value not exceeding 10. The results of the experiments proved the efficiency of the developed parallel-pipeline method.

Discussion and Conclusion. As a result of the research, a model of a parallel-pipeline computing process was developed using the example of one of the most time-consuming stages of solving a system of grid equations by a modified alternating-triangular iterative method. Its construction was based on decomposition models of a three-dimensional uniform computational grid, which took into account the technical characteristics of the equipment used in the calculations. This program can provide you for the acceleration of the calculation process and even loading of program flows in time. The conducted numerical experiments validated the mathematical model of decomposition of the computational domain.

Keywords: parallel algorithm, computational process, grid equations

Acknowledgements: the authors would like to thank the editorial board of the journal and the reviewer for their professional analysis and recommendations for correcting the article.

Funding information. The research was done with the support of the Russian Science Foundation (project No. 21-71-20050).

For citation. Litvinov VN, Rudenko NB, Gracheva NN. Model of a Parallel-Pipeline Computational Process for Solving a System of Grid Equations. *Advanced Engineering Research (Rostov-on-Don)*. 2023;23(3):329–339. <https://doi.org/10.23947/2687-1653-2023-23-3-329-339>

Разработка модели параллельно-конвейерного вычислительного процесса для решения системы сеточных уравнений

В.Н. Литвинов¹  , Н.Б. Руденко² , Н.Н. Грачева² 

¹ Донской государственный технический университет, г. Ростов-на-Дону, Российская Федерация,

² Азово-Черноморский инженерный институт, ДГАУ, г. Зерноград, Российская Федерация

✉ LitvinovVN@rambler.ru

Аннотация

Введение. Экологические проблемы, возникающие на мелководных водоёмах и вызываемые как природными, так и техногенными факторами, ежегодно наносят существенный ущерб аквасистемам и прибрежным территориям. Своевременно определить эти проблемы, а также пути их устранения возможно с использованием современных вычислительных систем. Но проведённые ранее исследования показали, что ресурсов вычислительных систем, использующих только центральный процессор, недостаточно для решения больших научных задач, в частности, по прогнозированию крупных экологических происшествий, оценке нанесенного ими ущерба и определению возможностей их устранения. Для этих целей предлагается использовать модели вычислительной системы и декомпозиции расчётной области для разработки алгоритма параллельно-конвейерных вычислений. Целью данной работы является создание модели параллельно-конвейерного вычислительного процесса для решения системы сеточных уравнений модифицированным попеременно-треугольным итерационным методом с использованием декомпозиции трёхмерной равномерной расчётной сетки, учитывающей технические характеристики используемого для расчетов оборудования.

Материалы и методы. Разработаны математические модели вычислительной системы и расчётной сетки. Модель декомпозиции расчётной области выполнена с учётом характеристик гетерогенной системы. Предложен параллельно-конвейерный метод решения системы сеточных уравнений модифицированным попеременно-треугольным итерационным методом.

Результаты исследования. На языке CUDA C написана программа, реализующая параллельно-конвейерный метод решения системы сеточных уравнений модифицированным попеременно-треугольным итерационным методом. Проведённые эксперименты показали, что с увеличением числа потоков время вычислений уменьшается и при декомпозиции расчётной сетки рациональным является разбиение на фрагменты по координате z на величину, не превышающую 10. Результаты экспериментов подтвердили эффективность разработанного параллельно-конвейерного метода.

Обсуждение и заключения. По итогам проведенных исследований разработана модель параллельно-конвейерного вычислительного процесса на примере одного из самых трудоёмких этапов решения системы сеточных уравнений модифицированным попеременно-треугольным итерационным методом. Её построение основано на моделях декомпозиции трёхмерной равномерной расчётной сетки, учитывающей технические характеристики используемого в расчетах оборудования. Применение программы позволит ускорить процесс расчёта и равномерно по времени загрузить программные потоки. Проведенные численные эксперименты подтвердили математическую модель декомпозиции расчётной области.

Ключевые слова: параллельный алгоритм, вычислительный процесс, сеточные уравнения

Благодарности: авторы выражают благодарность редакционной коллегии журнала и рецензенту за профессиональный анализ и рекомендации для корректировки статьи.

Финансирование. Работа выполнена при поддержке Российского научного фонда (проект № 21–71–20050).

Для цитирования. Литвинов В.Н., Руденко Н.Б., Грачева Н.Н. Разработка модели параллельно-конвейерного вычислительного процесса для решения системы сеточных уравнений. *Advanced Engineering Research (Rostov-on-Don)*. 2023;23(3):329–339. <https://doi.org/10.23947/2687-1653-2023-23-3-329-339>

Introduction. Recently, a number of serious environmental problems have been observed in the Rostov region. These include, in particular, the eutrophication of waters of the Sea of Azov and the Tsimlyansk reservoir, which causes the growth of harmful and toxic species of phytoplankton populations [1]. Engineering works in the waters of rivers and seas cause pollution of adjacent territories, changes in the population structure of biota, and deterioration of reproduction conditions of valuable and commercial fish. Climate change in the south of Russia has led to an increase in the number of cases of flooding of some territories in the area of the Taganrog Bay and the floodplain of the Don River caused by up and down surges. In the last decade, during the summer period, almost complete drainage of the Don

riverbed was observed several times, which led to a complete stop of navigation. To predict the occurrence and development of such cases, to plan ways to address their consequences, to assess the damage caused by them, modern software systems built using high-precision mathematical models, numerical methods, algorithms and data structures are needed [2].

Mathematical models used in predicting natural and man-made disasters are based on systems of partial differential equations, such as Poisson, Navier-Stokes, diffusion-convection-reaction, and thermal conductivity equations. The numerical solution to such systems causes the need for operational storage of large amounts of data (in arrays of various structures) and the solution to systems of grid equations of high dimension exceeding 10^9 . The amount of RAM required to store arrays of data when numerically solving only one Poisson equation for a three-dimensional domain with a dimension of $103 \times 103 \times 103$ by an alternately triangular iterative method is more than 64 GB. In the case of numerical solution to combined tasks, hundreds of gigabytes of RAM are required, which can be accessed only when using supercomputer systems.

An earlier study has shown that the resources of a computing system using only the CPU are not enough to solve such scientific problems [3]. Increasing the GPU power and video memory made it possible to use video adapter resources for calculations [4]. The GPU utilization depends on the application of parallel algorithms to solve computationally intensive problems of aquatic ecology [5–7]. To partially solve the problems of lack of memory and computing power on workstations, you can install additional video adapters in PCI-E X16 slots directly and in PCI-E X1 slots using PCI-E X1–PCI-E X16 adapters. Thus, the number of video adapters installed on one workstation can be increased to 12 [8–11].

Heterogeneous computer systems that provide sharing CPU and GPU resources are becoming increasingly popular in the scientific community. Application of such systems makes it possible to reduce the computation time of scientific problems [12–14]. However, the utilization of a heterogeneous computing environment involves the modernization of mathematical models, algorithms and programs that implement them numerically. A heterogeneous system provides organizing the calculation process in parallel mode. At the same time, fundamental differences in the construction of software systems using CPU and GPU together should be taken into account.

Materials and Methods. We describe the proposed mathematical models of the computational system, the computational grid, as well as the method of decomposition of the computational domain.

Let D be a set of technical characteristics of a computing system, then

$$D = D^1 \cup D^2 \cup D^3, \quad (1)$$

where D^1 — a subset of the characteristics of the central processing units (CPU) of a computing system; D^2 — a subset of the characteristics of video adapters (GPU) of a computing system; D^3 — a subset of RAM characteristics.

$$D^1 = \langle d^{1,1}, d^{1,2}, d^{1,3}, d^{1,4} \rangle, \quad (2)$$

where $d^{1,1}$ — total number of CPU cores; $d^{1,2}$ — number of streams simultaneously processed by one CPU core; $d^{1,3}$ — clock rate, MHz; $d^{1,4}$ — CPU bus frequency, MHz.

$$D^2 = \bigcup_{k_{GPU} \in K_{GPU}} D_{k_{GPU}}^2 = \left\{ d^2 \mid \exists k_{GPU} \in K_{GPU}, d^2 \in D_{k_{GPU}}^2 \right\}, \quad (3)$$

where $K_{GPU} = \{1, \dots, N_{GPU}\}$ — multiple video adapter indices; N_{GPU} — number of computer system video adapters;

k_{GPU} — video adapter index. Each video adapter is represented as a tuple

$$D_{k_{GPU}}^2 = \langle d_{k_{GPU}}^{2,1}, d_{k_{GPU}}^{2,2} \rangle, \quad (4)$$

where $d_{k_{GPU}}^{2,1}$ — amount of video memory of the video adapter with index k_{GPU} , GB; $d_{k_{GPU}}^{2,2}$ — number of streaming multiprocessors.

$$D^3 = \langle d^{3,1}, d^{3,2} \rangle, \quad (5)$$

where $d^{3,1}$ — total amount of RAM, GB; $d^{3,2}$ — clock rate of RAM, MHz.

Let S — a set of software streams involved in the computing process, then

$$\begin{aligned} S &= S^1 \cup S^2, \\ S^1 &= \{1, \dots, N_{S^1}\}, \\ S^2 &= \bigcup_{k_{GPU} \in K_{GPU}} S_{k_{GPU}}^2, \quad S_{k_{GPU}}^2 = \{1, \dots, N_{S_{k_{GPU}}^2}\}, \end{aligned} \quad (6)$$

where S^1 — a subset of program streams implementing the calculation process on the CPU; S^2 — a subset of CUDA streaming blocks implementing the calculation process on GPU streaming multiprocessors; N_{S^1} — number of CPU program streams involved; $S^2_{k_{GPU}}$ — a subset of CUDA streaming blocks that implement the calculation process on GPU streaming multiprocessors with index k_{GPU} ; $K_{GPU} = \{1, \dots, N_{GPU}\}$ — multiple GPU indices; N_{GPU} — number of GPU in the computing system; $N_{S^2_{k_{GPU}}}$ — number of CUDA stream blocks involved that implement the calculation process on GPU stream multiprocessors with index k_{GPU} .

Let E be a set of identifiers of program streams. Then, in order to identify program flows in the computing system, we assign tuple e of two elements to each element of the set of program flows S :

$$\forall s \in S \exists e \in E : e = \langle n_d, n_t \rangle, \quad (7)$$

where n_d — index of a computing device in a computing system; n_t — index of the CPU program stream or GPU streaming unit.

$$n_d = \begin{cases} 0, & s \in S^1 \\ K_{GPU}, & s \in S^2 \end{cases}, \quad (8)$$

$$n_t = \begin{cases} K_{S^1}, & s \in S^1 \\ K_{S^2_{k_{GPU}}}, & s \in S^2_{k_{GPU}} \end{cases}. \quad (9)$$

Let us take the computational domain with the following parameters: l_x — characteristic size on axis Ox ; l_y — on axis Oy ; l_z — on axis Oz . We compare a uniform computational grid of the following type to the specified area:

$$\begin{aligned} W = \{ & \overline{x_i = ih_x}, \overline{y_j = jh_y}, \overline{z_k = kh_z}; \\ & i = \overline{0, n_x - 1}, j = \overline{0, n_y - 1}, k = \overline{0, n_z - 1}; \\ & (n_x - 1)h_x = l_x, (n_y - 1)h_y = l_y, (n_z - 1)h_z = l_z \}, \end{aligned} \quad (10)$$

where h_x, h_y, h_z — steps of the computational grid in the corresponding spatial directions; n_x, n_y, n_z — number of nodes of the computational grid in the corresponding spatial directions.

Then, we represent the set of nodes of the computational grid in the form

$$\begin{aligned} G = \{ & \overline{g_{i,j,k}}, i = \overline{0, n_x - 1}, j = \overline{0, n_y - 1}, k = \overline{0, n_z - 1} \}, \\ & g_{i,j,k} = \langle x_i, y_j, z_k \rangle, \end{aligned} \quad (11)$$

where $g_{i,j,k}$ — computational grid node.

The number of nodes of the computational grid N_G is calculated from formula

$$N_G = n_x \cdot n_y \cdot n_z. \quad (12)$$

By the subsection of the computational grid $G^{k_1} \subset G$ (hereinafter — subsection), we mean a subset of the nodes of the computational grid G .

$$G = \bigcup_{k_1 \in K_{k_1}} G^{k_1} = \{ g^{k_1} \mid \exists k_1 \in K_{k_1}, g^{k_1} \in G^{k_1} \}, \bigcap_{k_1 \in K_{k_1}} G^{k_1} = \emptyset, \quad (13)$$

where $K_{k_1} = \{1, \dots, N_{k_1}\}$ — multiple indices of subsections G^{k_1} of computational grid G ; N_{k_1} — number of subsections G^{k_1} ; $K_{k_1}, N_{k_1} \subset N$; N — set of natural numbers; k_1 — index of subsection G^{k_1} .

Since $G^{k_1} \subset G$, then

$$G^{k_1} = \{ g^{k_1}_{i,\tilde{j},k}, i = \overline{0, n_x - 1}, \tilde{j} = \overline{0, n_y^{k_1} - 1}, k = \overline{0, n_z - 1} \}, \quad (14)$$

where $g^{k_1}_{i,\tilde{j},k}$ — node of subsection k_1 ; sign \sim indicates belonging to the subsection; \tilde{j} — node index of subsection k_1 by coordinate y ; $n_y^{k_1}$ — number of nodes in subsection k_1 by coordinate y .

$$\begin{aligned} g_{i,j,k}^{k_1} &= \langle x_i, y_j, z_k \rangle, \\ x_i &= ih_x, y_j = \left(\sum_{b_1=1}^{k_1-1} n_y^{b_1} + \tilde{j} \right) \cdot h_y, z_k = kh_z, \end{aligned} \quad (15)$$

where $n_y^{b_1}$ — number of nodes by coordinate y of b_1 -th subsection.

Under the block of computational grid G^{k_1, k_2} (hereinafter — block), we mean a subset of the computational grid nodes of subsection G^{k_1} .

$$G^{k_1} = \bigcup_{k_2 \in K_{k_1, k_2}} G^{k_1, k_2} = \left\{ g_{i,j,k}^{k_1, k_2} \mid \exists k_2 \in K_{k_1, k_2}, g_{i,j,k}^{k_1, k_2} \in G^{k_1, k_2} \right\}, \quad \bigcap_{k_2 \in K_{k_1, k_2}} G^{k_1, k_2} = \emptyset, \quad (16)$$

where $K_{k_1, k_2} = \{1, \dots, N_{k_1, k_2}\}$ — multiple indices of block G^{k_1, k_2} of subsection G^{k_1} ; N_{k_1, k_2} — number of blocks G^{k_1, k_2} ;

$K_{k_1, k_2}, N_{k_1, k_2} \subset N$; k_2 — index of block G^{k_1, k_2} of subsection G^{k_1} .

Since $G^{k_1, k_2} \subset G^{k_1}$, then

$$G^{k_1, k_2} = \left\{ g_{i,j,k}^{k_1, k_2}, i = \overline{0, n_x - 1}, j = \overline{0, n_y^{k_1, k_2} - 1}, k = \overline{0, n_z - 1} \right\}, \quad (17)$$

where $g_{i,j,k}^{k_1, k_2}$ — node of block k_1, k_2 ; sign \wedge indicates belonging to the block; \hat{j} — node index of block k_1, k_2 by coordinate y ; $n_y^{k_1, k_2}$ — number of nodes in block k_1, k_2 by coordinate y .

$$\begin{aligned} g_{i,j,k}^{k_1, k_2} &= \langle x_i, y_j, z_k \rangle, \\ x_i &= ih_x, y_j = \left(\sum_{b_1=1}^{k_1-1} \sum_{b_2=1}^{N_{k_1, k_2}} n_y^{b_1, b_2} + \hat{j} \right) \cdot h_y, z_k = kh_z, \end{aligned} \quad (18)$$

where $n_y^{b_1, b_2}$ — number of nodes of block b_1, b_2 .

By a fragment of the computational grid G^{k_1, k_2, k_3} (hereinafter — fragment), we mean a subset of the nodes of the computational grid of block G^{k_1, k_2} of subsection G^{k_1} .

$$\begin{aligned} G^{k_1, k_2} &= \bigcup_{k_3 \in K_{k_1, k_2, k_3}} G^{k_1, k_2, k_3} = \left\{ g_{i,j,k}^{k_1, k_2, k_3} \mid \exists k_3 \in K_{k_1, k_2, k_3}, g_{i,j,k}^{k_1, k_2, k_3} \in G^{k_1, k_2, k_3} \right\}, \\ \bigcap_{k_3 \in K_{k_1, k_2, k_3}} G^{k_1, k_2, k_3} &= \emptyset, \end{aligned} \quad (19)$$

where $K_{k_1, k_2, k_3} = \{1, \dots, N_{k_1, k_2, k_3}\}$ — multiple indices of fragments G^{k_1, k_2, k_3} of block G^{k_1, k_2} of subsection G^{k_1} ; N_{k_1, k_2, k_3} — number of fragments G^{k_1, k_2, k_3} ; $K_{k_1, k_2, k_3}, N_{k_1, k_2, k_3} \subset N$; k_3 — index of fragment G^{k_1, k_2, k_3} of block G^{k_1, k_2} of subsection G^{k_1} .

Each index k_3 of fragment G^{k_1, k_2, k_3} is assigned a tuple of indices $\langle k_4, k_5 \rangle$, designed to store the fragment coordinates in the plane xOz , where k_4 — fragment index by coordinate x ; k_5 — fragment index by coordinate z .

$$k_3 = k_4 + K_{k_4} \cdot k_5, \quad (20)$$

where k_4 — fragment index by coordinate x ; k_5 — fragment index by coordinate z .

Number of fragments G^{k_1, k_2, k_3} of block G^{k_1, k_2} is calculated from the formula

$$K_{k_3} = K_{k_4} \cdot K_{k_5}, \quad (21)$$

where K_{k_4} — number of fragments along axis Ox ; K_{k_5} — number of fragments by coordinate z .

Since $G^{k_1, k_2, k_3} \subset G^{k_1, k_2}$, then

$$G^{k_1, k_2, k_3} = \left\{ \tilde{g}_{\tilde{i}, \tilde{j}, \tilde{k}}, \tilde{i} = \overline{0, \tilde{n}_x - 1}, \tilde{j} = \overline{0, \tilde{n}_y - 1}, \tilde{k} = \overline{0, \tilde{n}_z - 1} \right\}, \quad (22)$$

where $\tilde{g}_{\tilde{i},\tilde{j},\tilde{k}}$ — fragment node; sign \subset indicates belonging to the fragment; \tilde{i}, \tilde{k} — fragment node indices by coordinates x, z ; \tilde{n}_x, \tilde{n}_z — number of nodes of the computational grid in the fragment by coordinates x, z ; \tilde{l}_x, \tilde{l}_z — fragment dimensions by coordinates x, z .

$$\tilde{g}_{\tilde{i},\tilde{j},\tilde{k}} = \langle x_i, y_j, z_k \rangle, \quad x_i = \left(\sum_{b=1}^{k_4-1} \tilde{n}_b + \tilde{i} \right) h_x, \quad y_j = j h_y, \quad z_k = \left(\sum_{b=1}^{k_5-1} \tilde{n}_b + \tilde{k} \right) h_z, \quad (23)$$

where \tilde{n}_b — number of nodes of b -th fragment.

We introduce a set of comparisons of the computational grid blocks to program flows M^1

$$M^1 = \bigcup_{k_1 \in K_{k_1}} \left(\bigcup_{k_2 \in K_{k_2}} M_{k_1, k_2}^1 \right), \quad (24)$$

where M_{k_1, k_2}^1 — element of the set M^1 .

Let M_{k_1, k_2}^1 — mapping block G_{k_1, k_2} to program stream s_{k_1, k_2} , then

$$M_{k_1, k_2}^1 = \langle G_{k_1, k_2}, s_{k_1, k_2} \rangle, \quad (25)$$

where $s_{k_1, k_2} \in S$ — program flow, computing block G_{k_1, k_2} .

In the process of solving hydrodynamic problems on three-dimensional computational grids of large dimension, high-performance computing systems and huge amounts of memory for data storage are needed. The resources of one computing device are not enough for computing and storing a three-dimensional computational grid with all its data. To solve this problem, various methods of decomposition of computational grids followed by the use of parallel calculation algorithms in heterogeneous computing environments are proposed [15].

For the decomposition of the computational grid, it is required to take into account the performance of computing devices involved in calculations. By performance, we mean the number of nodes of the computational grid calculated using a given algorithm per unit of time.

Assume that all computing devices are used for calculations. Then, the total performance of the computing system P_Σ is calculated from the formula

$$P_\Sigma = P_{CPU} \cdot N_{S^1} + \sum_{b=1}^{N_{GPU}} P_{GPU}^b \cdot N_{S^2}^b, \quad (26)$$

where P_{CPU} — performance of a single CPU stream; N_{S^1} — number of program streams implementing the calculation process on the CPU; P_{GPU}^b — GPU performance with index b on a single streaming multiprocessor; $N_{S^2}^b$ — number of CUDA streaming blocks implementing the calculation process on GPU streaming multiprocessors.

Then, the number of nodes of the computational grid n_y^b in the subsection by coordinate y for each GPU with index b can be calculated from the formula

$$n_y^b = \left\lfloor \frac{P_{GPU}^b}{P_\Sigma} \right\rfloor \cdot n_y. \quad (27)$$

In the process of calculating by formula (27), we get the remainder — a certain number of nodes of the computational grid. These nodes will be located in RAM. The number of remaining nodes n_{yL}^b by coordinate y is calculated from the formula:

$$n_{yL}^b = n_y - \sum_{b=1}^{N_{GPU}} n_y^b. \quad (28)$$

To calculate the number of nodes by coordinate y in the blocks of the computational grid processed by GPU streaming multiprocessors, we use the formulas:

$$n_{yGT}^b = \left\lfloor \frac{n_y^b}{N_{s^2}^b - 1} \right\rfloor, \quad b = \overline{1, N_{s^2}^b - 1},$$

$$n_{yGTL}^b = n_y^b - \sum_{b=1}^{N_{s^2}^b - 1} n_{yGT}^b,$$
(29)

where n_{yGT}^b — number of nodes by coordinate y in computational grid blocks processed by GPU streaming multiprocessors with index b , except for the last block; n_{yGTL}^b — number of nodes by coordinate y in the last block of the computational grid processed by GPU streaming multiprocessors with index b .

To calculate the number of nodes of the computational grid by coordinate y in blocks processed by software streams implementing the calculation process on the CPU, we use the formulas

$$n_{yCT} = \left\lfloor \frac{n_y^{CPU}}{N_{s^1} - 1} \right\rfloor,$$

$$n_{yCTL} = n_y^{CPU} - n_{yCT} \cdot (N_{s^1} - 1),$$
(30)

where n_{yCT} — number of nodes of the computational grid by coordinate y , processed by CPU program streams, except the last stream; n_{yCTL} — number of nodes of the computational grid by coordinate y , processed by CPU program streams, in the last stream.

Calculate the number of the computational grid fragments by coordinate y :

$$N_y^f = N_{s^1} + \sum_{b=1}^{N_{GPU}} N_{s^2}^b.$$
(31)

Let the number of fragments N_x^f and N_z^f be specified by coordinates x and z , respectively. Then, the number of nodes of the computational grid by coordinate x is calculated using the formulas

$$n_x^f = \left\lfloor \frac{n_x}{N_x^f - 1} \right\rfloor,$$

$$n_x^{fL} = n_x - n_x^f \cdot (N_x^f - 1),$$
(32)

where n_x^f — number of nodes of the computational grid by coordinate x in all fragments, except the last fragment;

n_x^{fL} — number of nodes of the computational grid by coordinate x in the last fragment.

Similarly, the number of nodes of the computational grid is calculated by coordinate z :

$$n_z^f = \left\lfloor \frac{n_z}{N_z^f - 1} \right\rfloor,$$

$$n_z^{fL} = n_z - n_z^f \cdot (N_z^f - 1),$$
(33)

where n_z^f — number of nodes of the computational grid by coordinate z in all fragments, except the last node; n_z^{fL} — number of nodes of the computational grid by coordinate z in the last fragment.

Let us describe a model of the parallel-pipeline method. Suppose it is necessary to organize a parallel process of computing some function F on M^1 , and the calculations in each fragment G_{k_1, k_2, k_3} depend on the values in neighboring fragments, each of which has at least one of the indices by coordinates x , y , z , and one less than the current one (Fig. 1).

To organize the parallel-pipeline method, we introduce a set of tuples A , that specify correspondences a between the identifiers of program streams e , processing fragments G_{k_1, k_2, k_3} , to the step numbers of the parallel-pipeline method r

$$\forall e \in E \quad \exists a \in A: a = \langle e, G_{k_1, k_2, k_3}, r \rangle,$$
(34)

where $r = \overline{1, N_r}$ — step number of the parallel-pipeline method;

N_r — number of steps of the parallel-pipeline method, calculated from the formula

$$N_r = N_x^f N_z^f + N_y^f - 1. \quad (35)$$

The full load of all calculators in the proposed parallel-pipeline method starts with step $r_{100START} = N_y^f$ and ends at step $r_{100STOP} = N_x^f N_z^f$. At the same time, the total number of steps with a full load of calculators N_{rPAR} will be

$$N_{rPAR} = r_{100STOP} - r_{100START} + 1 = N_x^f N_z^f - N_y^f + 1. \quad (36)$$

The calculation time of some function F by the parallel-pipeline method is written as

$$T_M^1 = \sum_{r=1}^{N_r} \max(T_a), \quad (37)$$

where T_a — vector of values of time spent on processing fragments in parallel mode.

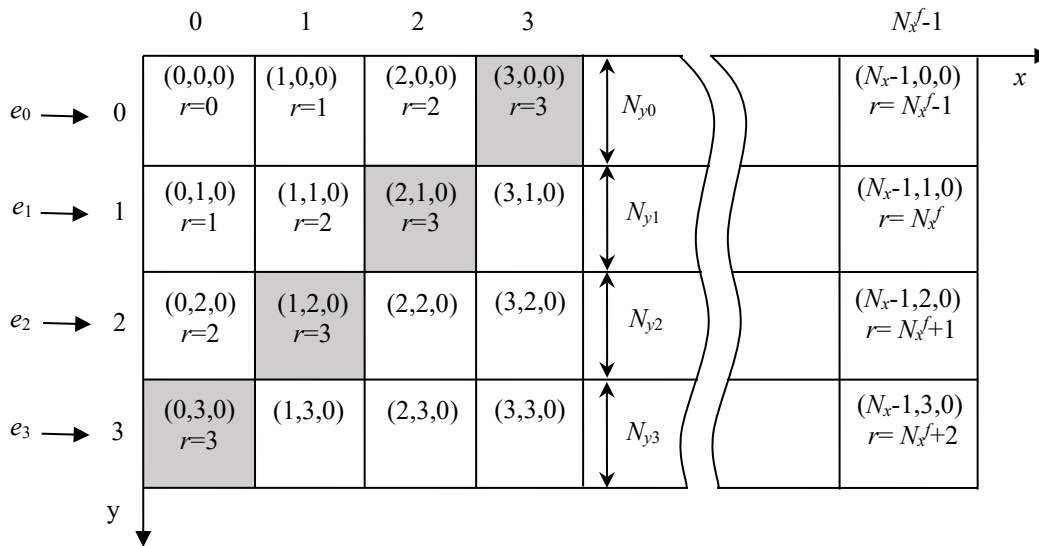


Fig. 1. Parallel-pipelined computing process

Research Results. The computational experiments were carried out on K-60 high-performance computing system of the Keldysh Applied Mathematics Institute, RAS. A GPU section was used, each node of which was equipped with two Intel Xeon Gold 6142 v4 processors, four Nvidia Volta GV100GL video adapters and 768 GB of RAM.

The computational experiment consisted of two stages — preparatory and basic. At the preparatory stage, the correctness of the decomposition of the computational domain into subsections, blocks and fragments was checked by step-by-step comparison of values in the nodes of the initial grid and in fragments obtained as a result of decomposition. Then, the operation of the flow control algorithm during which the time spent on calculating 1, 8, 16 and 32 fragments of the computational grid with a dimension of 50 nodes by spatial coordinates x , y , z , and the same number of CPU streams N_{S1} was checked by the iterative alternating-triangular method in parallel mode. Ten repetitions were performed with the calculation of the arithmetic mean T_a and standard deviation σ . Based on the data obtained, time $T_a^1 = T_a / N_{S1}$, spent by each stream on processing one fragment of the computational grid and acceleration $E = T_a^1(N_{S1}) / T_a^1(1)$, equal to the ratio of the processing time $T_a^1(N_{S1})$ of one fragment N_{S1} by streams to the corresponding processing time by one stream $T_a^1(1)$ was calculated. The experimental data are given in Table 1. The experiment showed that the standard deviation had the smallest value in the case of using 32 parallel CPU streams and was 0.026 ms, i.e., using 32 parallel CPU streams when calculating 32 fragments of the computational grid gave a more uniform time load of program streams, which generally increased the efficiency of the computing node. At the same time, the average value of the calculation of one fragment was 4.14 ms. The dependence of acceleration E on the number of streams turned out to be linear $E = 0.603 + 0.804N_{S1}$, with a coefficient of determination equal to 0.99. We

have found that with an increase in the number of streams, the acceleration of the developed algorithm increases. This indicates the efficient use of the subsystem when working with memory.

Table 1

Results of the preparatory stage of the computational experiment

N_{st}	$\max(T_a)$, ms	σ , ms	T_a , ms	E
1	3.38	0.141	3.38	1.00
8	3.66	0.042	0.46	7.39
16	3.94	0.028	0.25	13.73
32	4.14	0.026	0.13	26.13

At the basic stage of the computational experiment, a three-dimensional computational domain having dimensions of 1,600; 1,600; 200 by spatial coordinates x , y and z , accordingly, was divided into 32 fragments of 50 nodes for each of the coordinates x and y . The division into fragments by coordinate z is given in Table 2. For each decomposition option with a tenfold repetition, the processing time of the entire computational grid was measured by the proposed parallel-conveyor method, and its average value T_{pm} was calculated. Acceleration E_{pm} was calculated as ratio T_{pm} to time T_{sm} of the calculation by sequential version of the algorithm, equal to 6.963 ms. Regression equation $E_{pm} = 7.35 + 1.97 \ln(N_z^f)$ with a determination coefficient equal to 0.94 was obtained. Analysis of the results of the basic stage of the computational experiment showed a significant slowdown in growth E_{pm} at $N_z^f > 10$. Therefore, we conclude that splitting into fragments by coordinate z by an amount not exceeding 10 is optimal.

Table 2

Results of the main stage of the computational experiment

N_z^f	n_z^f	T_{pm} , ms	E_{pm}
1	200	1033.20	6.74
2	100	779.00	8.94
4	50	651.90	10.68
8	25	588.35	11.84
20	10	550.22	12.66

Discussion and Conclusion. As a result of the conducted research, a model of a parallel-pipeline computing process was developed by the example of one of the most intensive stages of solving a system of grid equations by a modified alternating-triangular iterative method. Its construction was based on decomposition models of a three-dimensional uniform computational grid, taking into account the technical characteristics of the equipment used in the calculations.

The results obtained under the computational experiments validated the effectiveness of the developed method. The correctness of the decomposition of the computational domain into subsections, blocks and fragments was also confirmed. The operation of the flow control algorithm was verified. At the same time, it was revealed that the standard deviation had the smallest value in the case of using 32 parallel CPU streams and is 0.026 ms, i.e., using 32 parallel CPU streams when calculating 32 fragments of the computational grid gave a more uniform time load of program streams. Here, the average value of the calculation of one fragment was 4.14 ms.

The results of processing the measurements of the calculation time by the proposed parallel-conveyor method showed a significant slowdown in the growth of acceleration when divided into fragments by coordinate z at $N_z^f > 10$. It was found that splitting into fragments by coordinate z by an amount not exceeding 10 was optimal.

References

- Shiganova TA, Alekseenko E, Kazmin AS. Predicting Range Expansion of Invasive Ctenophore *Mnemiopsis leidyi* A. Agassiz 1865 under Current Environmental Conditions and Future Climate Change Scenarios. *Estuarine, Coastal and Shelf Science*. 2019;227:106347. <https://doi.org/10.1016/j.ecss.2019.106347>
- Sukhinov AI, Chistyakov AE, Nikitina AV, Filina AA, Lyashchenko TV, Litvinov VN. The Use of Supercomputer Technologies for Predictive Modeling of Pollutant Transport in Boundary Layers of the Atmosphere

- and Water Bodies. In book: L Sokolinsky, M Zymbler (eds). *Parallel Computational Technologies*. Cham: Springer; 2019. P. 225–241. [10.1007/978-3-030-28163-2_16](https://doi.org/10.1007/978-3-030-28163-2_16)
3. Rodriguez D, Gomez D, Alvarez D, Rivera S. A Review of Parallel Heterogeneous Computing Algorithms in Power Systems. *Algorithms*. 2021;14(10):275. <https://doi.org/10.3390/a14100275>
 4. Abdelrahman AM Osman. GPU Computing Taxonomy. In ebook: Wen-Jyi Hwang (ed). *Recent Progress in Parallel and Distributed Computing*. London: InTech; 2017. <http://dx.doi.org/10.5772/intechopen.68179>
 5. Parker A. GPU Computing: The Future of Computing. In: *Proceedings of the West Virginia Academy of Science*. Morgantown, WV: WVAS; 2018. Vol. 90 (1). [10.55632/pwvas.v90i1.393](https://doi.org/10.55632/pwvas.v90i1.393)
 6. Nakano Koji. Theoretical Parallel Computing Models for GPU Computing. In book: Ç Koç (ed). *Open Problems in Mathematics and Computational Science*. Cham: Springer; 2014. P. 341–359. [10.1007/978-3-319-10683-0_14](https://doi.org/10.1007/978-3-319-10683-0_14)
 7. Bhargavi K, Sathish Babu B. GPU Computation and Platforms. In book: Ganesh Chandra Deka (ed). *Emerging Research Surrounding Power Consumption and Performance Issues in Utility Computing*. Hershey, PA: IGI Global; 2016. P.136–174. [10.4018/978-1-4666-8853-7.ch007](https://doi.org/10.4018/978-1-4666-8853-7.ch007)
 8. Ebrahim Zarei Zefreh, Leili Mohammad Khanli, Shahriar Lotfi, Jaber Karimpour. 3-D Data Partitioning for 3-Level Perfectly Nested Loops on Heterogeneous Distributed System. *Concurrency and Computation: Practice and Experience*. 2017;29(5):e3976. <https://doi.org/10.1002/cpe.3976>
 9. Fan Yang, Tongnian Shi, Han Chu, Kun Wang. The Design and Implementation of Parallel Algorithm Accelerator Based on CPU-GPU Collaborative Computing Environment. *Advanced Materials Research*. 2012;529:408–412. <https://doi.org/10.4028/www.scientific.net/AMR.529.408>
 10. Varshini Subhash, Karran Pandey, Vijay Natarajan. A GPU Parallel Algorithm for Computing Morse-Smale Complexes. *IEEE Transactions on Visualization and Computer Graphics*. 2022. P. 1–15. [10.1109/TVCG.2022.3174769](https://doi.org/10.1109/TVCG.2022.3174769)
 11. Leiming Yu, Fanny Nina-Paravecino, David R Kaeli, Qianqian Fang. Scalable and Massively Parallel Monte Carlo Photon Transport Simulations for Heterogeneous Computing Platforms. *Journal of Biomedical Optics*. 2018;23(1):010504. <https://doi.org/10.1117/1.JBO.23.1.010504>
 12. Fujimoto RM. Research Challenges in Parallel and Distributed Simulation. *ACM Transactions on Modeling and Computer Simulation*. 2016;26(4):1–29. <https://doi.org/10.1145/2866577>
 13. Qiang Qin, ChangZhen Hu, TianBao Ma. Study on Complicated Solid Modeling and Cartesian Grid Generation Method. *Science China Technological Sciences*. 2014;57:630–636. [10.1007/s11431-014-5485-5](https://doi.org/10.1007/s11431-014-5485-5)
 14. Seyong Lee, Jeffrey Vetter. Moving Heterogeneous GPU Computing into the Mainstream with Directive-Based, High-Level Programming Models. In: *Proc. DOE Exascale Research Conference*. Portland, Or; 2012.
 15. Thoman P, Dichev K, Heller Th, Iakymchuk R, Aguilar X, Hasanov Kh, et al. A Taxonomy of Task-Based Parallel Programming Technologies for High-Performance Computing. *Journal of Supercomputing*. 2018;74(2):1422–1434. <https://doi.org/10.1007/s11431-014-5485-5>

Received 11.07.2023

Revised 14.08.2023

Accepted 18.08.2023

About the Authors:

Vladimir N. Litvinov, Cand.Sci. (Eng.), Associate Professor of the Mathematics and Informatics, Don State Technical University (1, Gagarin sq., Rostov-on-Don, 344003, RF), [ResearcherID](https://orcid.org/0000-0001-9141-1141), [ScopusID](https://scopus.com/authors/details/litvinovvn), [ORCID](https://orcid.org/0000-0001-9141-1141), LitvinovVN@rambler.ru

Nelli B. Rudenko, Cand.Sci. (Eng.), Associate Professor, Associate Professor of the Mathematics and Bioinformatics Department, Azov-Black Sea Engineering Institute, Don State Agrarian University (21, Lenina St., Zernograd, 347740, RF), [ScopusID](https://orcid.org/0000-0001-9141-1141), [ORCID](https://orcid.org/0000-0001-9141-1141), nellyi-rud@yandex.ru

Natalya N. Gracheva, Cand.Sci. (Eng.), Associate Professor of the Mathematics and Bioinformatics Department, Azov-Black Sea Engineering Institute, Don State Agrarian University (21, Lenina St., Zernograd, 347740, RF), [ScopusID](https://orcid.org/0000-0001-9141-1141), [ORCID](https://orcid.org/0000-0001-9141-1141), grann72@mail.ru

Claimed Contributorship:

VN Litvinova: basic concept formulation, research objectives and tasks, development of algorithms for performing a computational experiment, calculation analysis.

NB Rudenko: analysis of research results, drawing conclusions, text preparation.

NN Gracheva: writing program code for performing a computational experiment, preparing illustrations, finalizing the text, correction of the conclusions.

Conflict of interest statement: the authors do not have any conflict of interest.

All authors have read and approved the final manuscript.

Поступила в редакцию 11.07.2023

Поступила после рецензирования 14.08.2023

Принята к публикации 18.08.2023

Об авторах:

Владимир Николаевич Литвинов, кандидат технических наук, доцент кафедры математики и информатики Донского государственного технического университета (344003, РФ, г. Ростов-на-Дону, пл. Гагарина, 1), [ResearcherID](#), [ScopusID](#), [ORCID](#), LitvinovVN@rambler.ru

Нелли Борисовна Руденко, кандидат технических наук, доцент, доцент кафедры математики и биоинформатики Азово-Черноморского инженерного института, ДГАУ (347740, РФ, г. Зерноград, ул. Ленина, 19), [ScopusID](#), [ORCID](#), nelli-rud@yandex.ru

Наталья Николаевна Грачева, кандидат технических наук, доцент кафедры математики и биоинформатики Азово-Черноморского инженерного института, ДГАУ (347740, Ростовская область, г. Зерноград, ул. Ленина, 19), [ScopusID](#), [ORCID](#), grann72@mail.ru

Заявленный вклад соавторов:

В.Н. Литвинов — формирование основной концепции, цели и задачи исследования, разработка алгоритмов для выполнения вычислительного эксперимента, проведение расчетов.

Н.Б. Руденко — анализ результатов исследований, формирование выводов, подготовка текста.

Н.Н. Грачева — написание программного кода для выполнения вычислительного эксперимента, подготовка иллюстраций, доработка текста, корректировка выводов.

Конфликт интересов: авторы заявляют об отсутствии конфликта интересов.

Все авторы прочитали и одобрили окончательный вариант рукописи.